Intense-Field Theory of High Harmonic Generation from Freely Rotating Molecules

Dissertation

zur Erlangung des Doktorgrades der Naturwissenschaften
an der Fakultät für Physik der Universität Bielefeld

vorgelegt von
Abdurrouf
aus Indonesien

Fakultät für Physik
Universität Bielefeld
Deutschland

September 2007

Abdurrouf
Theoretische Atom-, Molekül- und Laserphysik
Fakultät für Physik
Universität Bielefeld
email: rouf@physik.uni-bielefeld.de, a.abdurrouf@googlemail.com

Abdruck der genehmigten Dissertation
zur Erlangung des akademischen Grades
Doktor der Naturwissenschaften (Dr. rer. nat)
der Fakultät für Physik
der Universität Bielefeld
am 26. September 2007 vorgelegt von Abdurrouf
am 22. November 2007 verteidigt und genehmigt.

Gutachter:
Prof. F.H.M. Faisal, Ph.D.
Prof. Dr. J. Schnack

Promotionauschu*β*:
Prof. F.H.M. Faisal, Ph.D.
Prof. Dr. J. Schnack
Prof. Dr. H. Steidl
Prof. Dr. D. Bödeker

Gedruckt auf alterungbeständigem Papier ISO 9706

Preface

This dissertation is submitted to the Faculty of Physics University of Bielefeld, Germany, in order to fulfill the requirements for the doctor degree. The work presented in this dissertation has been carried out in the years 2004-2007 in the Theoretical Atomic, Molecular, and Laser Physics group at the Bielefeld University under the supervision of Prof. F.H.M. Faisal, Ph.D.
A part of the work has been published in the following papers.

- K. Miyazaki, M. Kaku, G. Miyaji, A. Abdurrouf, and F.H.M. Faisal*, Field-Free Alignment of Molecules Observed with High-Order Harmonic Generation*, Phys. Rev. Lett. **95**, 243903 (2005) (chapter 3)
- F.H.M. Faisal, A.Abdurrouf, K. Miyazaki, and G. Miyaji, *Origin of Anomalous Spectra of Dynamic Alignments Observed in* N_2 *and* O_2*,* Phys. Rev. Lett. **98**, 143001 (2007) (chapter 6)
- F.H.M. Faisal and A.Abdurrouf, *Interplay of polarization geometry and rotational dynamics in high harmonic generation from coherently rotating linear molecules,* arXiv:0707.2184v1 (chapter 7)

In addition to some references mentioned at the Bibliography, there are some computer packet program used during the work: GNU Compiler Collection (GCC), GNU Scientific Library (GSL), Suse Linux, FORTRAN 90, Numerical Algorithms Group (NAG) FORTRAN Library, General Atomic and Molecular Electronic Structure System (GAMESS), LYX, Jab Ref Reference Manager; Xmgrace, DISLIN Scientific Plotting Software, and Xfig.

Table of Contents

Preface iii

1 Introduction **1**

1.1 Molecular Alignment 2
1.2 High Harmonic Generation 3
1.3 Pump-probe Experiment 5
1.4 Theoretical Background 6
1.5 Organization of the Work 7

2 Mathematical Formulation **9**

2.1 Intense-field Wavefunction 9
2.2 Molecule Interacting with a Pump- and a Delayed Probe-Pulse 12
2.3 Molecular Wavefunction of the Interacting System: KFR Approximation 14
2.4 Dipole Expectation Value 15
2.5 Dynamic HHG Signal and HHG Transition Operator 17
2.6 HHG Operator 18
2.7 Evaluation the Radial Integration 22
2.8 Comparison with Other Mathematical Model 23

3 Dynamic Alignment **27**

3.1 Solving Schrödinger Equation of the System 27
3.2 Alignment Degree 30
3.3 Type of Alignment 32
3.4 Dynamics Alignment: Some Expectation Values 33
3.5 Periods and Phase of Revival Structures 38
3.6 Beat Frequencies 43
3.7 Temperature Effect 45
3.8 Does Probe Pulse Affect The Dynamic Alignment? 47
3.9 Comparison with Physical Observable 49

4 Application to Diatomic Molecules: Case N_2 and O_2 51
4.1 Explicit Expression of HHG Transition Operator for N_2 and O_2 52
4.1.1 HHG operator $T_e^{(n)}(\theta)$ and dynamic signal for N_2 52
4.1.2 HHG operator $T_e^{(n)}(\theta)$ and dynamic signal for O_2 53
4.2 HHG Spectra 55
4.3 Dynamic Signal 60
4.4 Effect of Initial Temperature 66
4.5 Differential signal 68

5 Application to the Three-atomic Molecule: CO_2 73
5.1 HHG Operator $T_e^{(n)}(\theta)$ for CO_2 75
5.2 HHG Spectrum 79
5.3 Dynamic Signal 79
5.4 Origin of Inverted Modulation Phase 83
5.5 Inverted Modulation in Other Molecules 90

6 Signal in Frequency Domain: Fourier Analysis of Dynamic HHG Signal 95
6.1 Frequency Spectrum of N_2 96
6.2 Frequency Spectrum of O_2 98
6.3 Frequency Spectrum of CO_2 101
6.4 Effect of Initial Temperature 103
6.5 Comparison with Other Theoretical Model: Case O_2 106

7 Dependence of the Dynamic Signal on the Relative Angle Between the Pump and the Probe Polarizations α 109
7.1 Salient Experimental Data 109
7.2 Generalization of the Expression of Dynamic Signal for Arbitrary Relative Polarization Angle α 110
7.3 Harmonic Spectrum 114
7.4 Harmonic Signal as Function of t_d..... 115
7.5 Harmonic Signal as Function of α..... 118
7.6 Harmonic Signal as Function of t_d and α 124
7.7 Comparison with the Planar Model : Case N_2 124
7.8 Application to Adiabatic Alignment... 128

8 Summary and Outlook 131

Bibliography 135

A List of Publication 149

B Field-Free Alignment of Molecules Observed with High-Order Harmonic Generation 151

C Origin of Anomalous Spectra of Dynamic Alignments Observed in N_2 and O_2 157

D Interplay of polarization geometry and rotational dynamics in high harmonic generation from coherently rotating linear molecules 163

E A theory of molecular high harmonic generation from coherently rotating molecules and interpretation of recent pump-probe experiments 169

F Rotational coherence in high-order harmonic generation from monadibatically aligned molecules 173

G Angle-dependent high-harmonic generation from field-free aligned molecules 177

Acknowledgements 181

Selbtändigkeitserklärung 183

List of Tables

1.1 Peak intensity I and wavelength λ corresponding to $\gamma = 1$ for N_2, O_2, and CO_2. 4

3.1 Molecular properties of N_2, O_2, and CO_2 [117, 118, 119, 120, 121] 31

4.1 Explicit form of $d^l_{0m}(\theta)$ required for evaluating Eqs. (4.3) and (4.10) [103, 104] 52

4.2 The molecular properties of N_2 and O_2 used in this work. I_p is ionization potential, B is rotational constant of molecule, $\alpha_\parallel$ and $\alpha_\perp$ are parallel and perpendicular polarizability, and $C^{(m)}_l$'s are angular coefficient of electronic wave function. 55

4.3 The $c^{(n)}_{j,j'}$ and the related expectation values of N_2 for different harmonic order. The coefficients for 19th harmonic order are calculated by using Miyazaki's parameters [71] and *normalized* so that $c^{(19)}_{0,1} = 1$. The coefficients for 23th and 35th harmonic orders are obtained by using Itatani's parameters [70] and *normalized* so that $c^{(23)}_{0,1} = 1$. 61

4.4 The $c^{(n)}_{j,j'}$ and related expectation values of O_2 for 19th harmonic order. The coefficients are *normalized* so that $c_{1,1} = 1$. 65

5.1 Explicit form of $d^l_{0m}(\theta)$ required for evaluating Eq. (5.2) [103, 104, 153] . . . 76

5.2 The molecular properties of CO_2 and O_2 (as a comparison) used in this work. I_p is ionization potential, B is rotational constant of molecule, $\alpha_\parallel$ and $\alpha_\perp$ are parallel and perpendicular polarizability, R_0 is the internuclear distance, and $C^{(m)}_l$'s are angular coefficient of electronic wave function. The $C^{(m)}_l$ for CO_2 are *normalized* so that $C^{(1)}_2$ has the same value for both O_2 and CO_2. 77

5.3 The $c^{(n)}_{j,j'}$ and related expectation values of CO_2 for different harmonic order. The coefficients are *normalized* so that $c_{1,1} = 1$. 82

6.1 All possible frequency arising from $\langle\langle\cos^2\theta\rangle\rangle$, $\left\langle\langle\cos^2\theta\rangle^2\right\rangle$, and $\langle\langle\cos^4\theta\rangle\rangle$ for N_2 whose both odd and even J 's are allowed 97

6.2 All possible frequency arising from $\left\langle\langle\sin^2\cos^2\theta\rangle^2\right\rangle$ for O_2 whose only odd J 's are allowed. The group of frequencies with a weak intensity are noticed with (*). 99

6.3 All possible frequency arising from $\left\langle \left\langle \sin^2 \cos^2 \theta \right\rangle^2 \right\rangle$ for CO_2 whose only even J 's are allowed. The group of frequencies with a weak intensity are noticed with (*). 101

List of Figures

1.1 (a) The HHG process, n photon with frequency ω produce radiation with frequency $\Omega = n\omega$. (b). Description of HHG process in the framework of three-step model, which are (1) ionization, (2) propagation, and (3) recombination. 3

1.2 Schema of pump-probe experiment. The explanation is given in text. 6

2.1 Schematic diagram defining the directions of the molecular axis, $\boldsymbol{R}$, electron position vector $\boldsymbol{r}$, and the pump and probe polarization ($\boldsymbol{\epsilon}_1$, $\boldsymbol{\epsilon}_2 \parallel z-$ axis). The fields are assumed to propagate along the y-axis. 20

3.1 $|a_{J0}(t)|^2$ plotted as a function of time delay after peak of laser pulse, for various initial state, i.e. $\Phi(t=0) = |10\rangle$ (panel a), $\Phi(t=0) = |30\rangle$ (panel b), $\Phi(t=0) = |50\rangle$ (panel c), and $\Phi(t=0) = |70\rangle$ (panel d). The initial states are identified by thick line and *. We use here the laser field (dashed line) of intensity 0.5 $\times 10^{14}\,\mathrm{W/cm^2}$ with FWHM 40 fs subjected to molecule O_2. . . 30

3.2 Alignment of N_2 with pulse intensity of $0.8 \times 10^{14}\mathrm{W/cm^2}$ and initial temperature 300 K. We use pulse duration $\tau = 2.6547\,\mathrm{ps}$ (panel a), $\tau = 24\,\mathrm{fs}$ (panel c), and a combination of $\tau = 2.6547\,\mathrm{ps}$ for left side and $\tau = 24\,\mathrm{fs}$ for right (panel b). Solid (black) line is $\langle\langle\cos^2\theta\rangle\rangle$ (left scale), whereas dashed (blue) line for pulse profile (right scale). Pulse profile for panel c is not shown. The red line shows a period 33

3.3 Dynamics alignment of N_2, O_2, and CO_2 with initial temperature 300 K. We use laser pulse with peak intensity of $0.5 \times 10^{14}\,\mathrm{W/cm^2}$ for O_2 and $0.8 \times 10^{14}\,\mathrm{W/cm^2}$ for N_2 and CO_2 with FWHM 40 fs. 34

3.4 Molecular axis distribution of N_2 (upper panel), O_2 (middle panel), and CO_2 (lower panel). The laser parameters are similar with ones of Fig. 3.3. 35

3.5 Some expectation value of O_2 at 300 K subject to laser field of intensity $0.5 \times 10^{14}\,\mathrm{W/cm^2}$ with FWHM 40 fs. Solid (black) line for $\langle\langle\cos^2\theta\rangle\rangle$, dashed dotted (red) line for $\langle\langle\sin^2\theta\rangle\rangle$, and dashed (blue) line for $\langle\langle\sin^2 2\theta\rangle\rangle$. 37

3.6 The lowest fractional revival of dynamics alignment of O_2 for $\langle\langle \cos^4\theta \rangle\rangle$ at $T_{rev}/12$ (upper panel) and $\langle\langle \cos^6\theta \rangle\rangle$ at $T_{rev}/16$ (lower panel). Note hat these fractional revivals are so small that does not appear in full figure. We use here the pulse of intensity $0.5 \times 10^{14}\,\mathrm{W/cm^2}$ and FWHM 40 fs with initial temperature 300 K. 41

3.7 Revival structure of $\langle\langle \sin^2 2\theta \rangle\rangle$ of O_2, for the total frequency (panel a), with $\Delta J = 0$ only (panel b), with $\Delta J = \pm 2$ only (panel c), and with $\Delta J = \pm 4$ only (panel d). It is clear that the transition with $\Delta J = \pm 4$ has lowest fractional revival at $\frac{1}{8}T_{rev}$. Panel (d) also tells us that the transition with $\Delta J = \pm 4$ has rotational period $\frac{1}{2}T_{rev}$. 42

3.8 Dynamics alignment $\langle\langle \cos^2\theta \rangle\rangle$ of N_2 with same parameter of Fig. 3.3. Panel (a): dynamics for single initial state $|50\rangle$ only (blue) and for all odd J with $J_{max} = 19$ (black). Panel (b): for $|60\rangle$ only (blue) and all even J with $J_{max} = 20$ (black). Panel (c): for all J with $J_{max} = 20$. We use here pulse of intensity $0.8\ \times 10^{14}\,\mathrm{W/cm^2}$ and FWHM 40 fs with initial temperature 300 K. 42

3.9 Fourier transform of dynamics alignment of Fig. 3.3, plotted using Bc as basis frequency (lower scale). Following $4J + 6$ rule for $\langle\langle \cos^2\theta \rangle\rangle$, it is clear that the peak frequencies occur for J odd only for O_2, even only (CO_2), and both even and odd (N_2). The corresponding J values are shown in upper scale. . 44

3.10 Fourier transform of $\langle\langle \sin^2 2\theta \rangle\rangle$ of O_2 : whole frequencies (panel a), beat frequencies coming from transition with $\Delta J = \pm 2$ only (panel b), and beats frequencies coming from transition with $\Delta J = \pm 4$ (panel c). We use here pulse of intensity $0.5 \times 10^{14}\,\mathrm{W/cm^2}$ and FWHM 40 fs with initial temperature 300 K. 45

3.11 Signature of initial temperature of jet gas O_2, on the molecular axis distribution (panel a-b) of O_2, on the expectation value of $\langle\langle \sin^2 2\theta \rangle\rangle$ (panel c-d), and the Fourier spectrum (panel e-f). The molecular distribution on panel a-b are given at various time delay, i.e. at top alignment $t = 5.649\,\mathrm{ps}$ (blue, dashed line), at average alignment $t = 5.812\,\mathrm{ps}$ (green, solid line), and at anti-top alignment $t = 5.975\,\mathrm{ps}$ (red, dotted line). The radii are in same scale. The peak intensity of laser field is $0.5 \times 10^{14}\,\mathrm{W/cm^2}$ with FWHM 40 fs. 46

3.12 Mean energy of O_2 before and after interaction with the laser pulse, for different initial temperature. The peak intensity of laser field is $0.5 \times 10^{14}\,\mathrm{W/cm^2}$ with FWHM 40 fs. 47

3.13 Dynamics alignment of $\langle\langle \cos^2\theta \rangle\rangle$ (upper panel) and $\langle\langle \sin^2 2\theta \rangle\rangle$ (lower panel) of O_2 at 300 K subject to laser pulses of $I_{pump} = 0.8 \times 10^{14}\mathrm{W/cm^2}$ and $I_{probe} = 1.7 \times 10^{14}\mathrm{W/cm^2}$ with FWHM 40 fs. We keep second pulse to interact for 40 fs. 48

4.1 The calculated squared asymptotic wavefunction for N_2 (left panel) and O_2 (right panel). 54

4.2 The contribution of different angular momentum (l_r, l_i) to the whole HHG spectrum of N_2. The quantities in y-axis are $\tilde{a}_{zz}(l_r, l_i; m)$, which is the electronic part of Fourier transform of electronic dipole. We use (probe) pulse of intensity $I_{probe} = 1.7 \times 10^{14}\,\mathrm{W/cm^2}$, wavelength $\lambda = 800\,\mathrm{nm}$, and 36 cycles, corresponding to $\gamma = 0.876$ 57

4.3 The contribution of different angular momentum (l_r, l_i) to the whole HHG spectrum of O_2. The quantities in y-axis are $\tilde{a}_{zz}(l_r, l_i; m)$, which is the electronic part of Fourier transform of electronic dipole. We use (probe) pulse of intensity $I_{probe} = 1.2 \times 10^{14}\,\mathrm{W/cm^2}$, wavelength $\lambda = 800\,\mathrm{nm}$, and 36 cycles, , corresponding to $\gamma = 0.917$ 57

4.4 HHG spectrum of N_2 for various alignment angle. The pulse parameters are equal to those of Fig. 4.2. The arrow shows the cut off position according to the three-step model. 58

4.5 HHG spectrum of O_2 for various alignment angle. The pulse parameters are equal to those of Fig. 4.3. The arrow shows the cut off position according to the three-step model. 58

4.6 Alignment-dependent HHG signal of N_2 for various order. The pulse parameters are equal to those of Fig. 4.2. 59

4.7 Alignment-dependent HHG signal of O_2 for various order. The pulse parameters are equal to those of Fig. 4.3. 59

4.8 Comparison of the experimental (from [69, 71]) and the theoretical dynamic 19th harmonic signal for N_2; pump intensity $I_{pump} = 0.8 \times 10^{14}$ W/cm^2, probe intensity $I_{probe} = 1.7 \times 10^{14}$ W/cm^2; duration 40 fs, wavelength 800 nm, temperature 200 K. 62

4.9 Comparison of the experimental (upper panel) (from [70]) and the theoretical (lower panel) dynamic HHG signal for N_2; pump pulse: $I_{pump} = 0.4 \times 10^{14}$ W/cm^2 and 60 fs; probe pulse: $I_{probe} = 2 \times 10^{14}$ W/cm^2 and 30 fs, wavelength 800 nm, temperature 30 K. 63

4.10 Comparison of the experimental (from [71]) and the theoretical dynamic 19th HHG signal for O_2; pump intensity $I_{pump} = 0.5 \times 10^{14}$ W/cm^2, probe intensity $I_{probe} = 1.2 \times 10^{14}$ W/cm^2; duration 40 fs, wavelength 800 nm, temperature 200 K. 65

4.11 Dynamic 19th harmonic signal of N_2 for various initial temperature . The laser parameters and the initial temperature are similar with Fig. 4.8. 67

4.12 Dynamic 19th harmonic signal of O_2 for various initial temperature. The laser parameters and the initial temperature are similar with Fig. 4.10. 67

4.13 Alignment-dependent HHG signal for single molecule (red, dashed line), molecular distribution (blue, dash-dotted line), and $dS^{(n)}(t_d, \theta_0, \phi = 0^o)$ (green, solid line) calculated at first half revival. (a) N_2 at top signal $t_d = 4.09\,\mathrm{ps}$, (b) N_2 at average signal $t_d = 4.18\,\mathrm{ps}$, (c) N_2 at anti-top signal $t_d = 4.27\,\mathrm{ps}$, (d) O_2 at top signal $t_d = 5.68\,\mathrm{ps}$, (e) O_2 at average signal $t_d = 5.79\,\mathrm{ps}$, and (f) O_2 at anti-top signal $t_d = 5.90\,\mathrm{ps}$. The laser parameters are similar with Figs. 4.8 and 4.10 for N_2 and O_2, respectively. The initial temperature is 200 K. . . . 69

4.14 Differential signal of 19th harmonic as function of both time delay and alignment angle for N_2 (upper panel) and O_2 (lower panel). The laser parameters are similar with Figs. 4.8 and 4.10 for N_2 and O_2, respectively. The initial temperature is 200 K. 71

5.1 The calculated squared asymptotic wavefunction. The left column for CO_2 whereas the right one for O_2, as a comparison. 75

5.2 The contribution of different angular momentum (l_r, l_i) to the whole HHG spectrum of CO_2. The quantities in y-axis are $\tilde{a}_{zz}(l_r, l_i; m = 1)$, which is the electronic part of Fourier transform of electronic dipole. We use (probe) pulse of intensity $I_{probe} = 1.5 \times 10^{14}\,\mathrm{W/cm^2}$, wavelength $\lambda = 800\,\mathrm{nm}$, and 36 cycles, corresponding to $\gamma = 0.876$. The arrows show the position of minima. 78

5.3 HHG spectrum of CO_2 for various alignment angle. The pulse parameters are similar to those of Fig. 5.2 78

5.4 Comparison of the experimental (upper panel) (from [138]) and the theoretical dynamic (middle panel) of 9th HHG signal for CO_2; pump intensity $I = 0.56 \times 10^{14}$ W/cm^2, probe intensity $I = 1.3 \times 10^{14}$ W/cm^2; duration 40 fs, wavelength 800 nm, temperature 300 K. The corresponding alignment degree $\langle\langle\cos^2\theta\rangle\rangle$ is presented in lower panel. 80

5.5 Comparison of the experimental (upper panel) (from [138, 72]) and the theoretical dynamic (middle panel) of 19th HHG signal for CO_2; pump intensity $I = 0.53 \times 10^{14}$ W/cm^2, probe intensity $I = 1.5 \times 10^{14}$ W/cm^2; duration 40 fs, wavelength 800 nm, temperature 300 K. The corresponding alignment degree $\langle\langle\cos^2\theta\rangle\rangle$ is presented in lower panel. 81

5.6 A direct comparison between the spectrum of the top alignment and the one of the anti-top alignment. The term top and anti-top alignment refer to the points a and c in Fig. 5.4. The pulse parameters are similar to those of Fig. 5.5. 84

5.7 (a) A direct comparison between the spectrum of the top alignment and that of the anti-top alignment. (b) The dynamic signal of 21th harmonic order. The laser parameters are equal to the ones in Fig. 5.6, except the probe intensity which is $I = 2 \times 10^{14}\,\mathrm{W/cm^2}$. 85

5.8 Peak of alignment dependence of HHG signal θ_{peak} as a function of harmonic order. The laser parameters are equal to those in Fig. 5.6. 85

5.9 (a) A direct comparison between the spectrum of the top alignment and the one of the anti-top alignment. (b) The dynamic signal of 21th harmonic order. The laser parameters are equal to the one in Fig. 5.6, except the initial temperature, T = 25 K. 86

5.10 Semi-classical HHG spectrum of Fig 5.6 (panel a), Fig 5.7 (panel b), and Fig. 5.9 (panel c). 87

5.11 Peak of alignment dependence of HHG signal θ_{peak} as a function of harmonic order, obtained from Fig. 5.6 (panel a), Fig 5.7 (panel b), and Fig. 5.9 (panel c). 88

5.12 Contribution of individual $\tilde{a}_{zz}(l_r, l_i; m)$ on the whole spectrum. 88

5.13 Molecular-axis distribution (blue, dash-dotted line), alignment-dependent signal (red, dashed line), and differential signal (green, solid line) at first half revival of CO_2. (a) H9 at top signal $t_d = 21.06\,\mathrm{ps}$, (b) H9 at average signal $t_d = 20.80\,\mathrm{ps}$, (c) H9 at anti-top signal $t_d = 21.60\,\mathrm{ps}$, (d) H-19 at top signal $t_d = 21.06\,\mathrm{ps}$, (e) H19 at average signal $t_d = 20.80\,\mathrm{ps}$, and (f) H19 at anti-top signal $t_d = 21.60\,\mathrm{ps}$. The laser parameters are similar with Fig. 5.4. The initial temperature is 300 K. 89

5.14 HHG differential signal for 9th (upper panel) and 19th (lower panel) of CO_2. The laser parameters are similar with Fig. 5.4 and 5.5, for 9th and 19th harmonic, respectively. The initial temperature is 300 K. 91

5.15 (a) Comparison between the dynamic signal of 47th harmonic signal for O_2 and its alignment degree at their first revival, for initial temperature 40 K. Pump intensity $I_{pump} = 1.0 \times 10^{14}\,\mathrm{W/cm^2}$, duration 60 fs; probe intensity $I_{probe} = 3.5 \times 10^{14}\,\mathrm{W/cm^2}$, duration 30 fs, mean wavelength 800 nm. (b) Harmonic signal in (a) for various initial temperature. (c) Harmonic signal in (a) for various pump intensities. (d) Harmonic signal in (a) for various probe intensities. 92

5.16 Left column: harmonic spectra of O_2 (panel a), N_2 (panel b), and ethylene (panel c). Right column: the corresponding alignment dependent signal for interest orders, i.e for O_2 (panel d), N_2 (panel e), and ethylene (panel f). The pulse parameters are given in text. 93

6.1 Comparison of the experimental (from [71]) and theoretical Fourier spectrum of the dynamic 19th harmonic signal for N_2. The spectrum shows series I: $(6, 14, 22, 30, 38, ..)\,Bc$ (blue mark), series II: $(\mathit{10}, \mathit{18}, \mathit{26}, \mathit{34}, \mathit{42}, ..)\,Bc$ (green mark), series III: $(\mathbf{20}, \mathbf{28}, \mathbf{36}, \mathbf{44}, \mathbf{52}, \mathbf{60}, ..)Bc$ (red mark), and series IV: $(\boldsymbol{4}, \boldsymbol{8}, \boldsymbol{12}, \boldsymbol{16}, \boldsymbol{..})Bc$ (violet mark). We use pump pulse of intensity $I_{pump} = 0.8 \times 10^{14}\,\mathrm{W/cm^2}$ and pulse width $FWHM = 40\,\mathrm{fs}$, and probe pulse of intensity $I_{probe} = 1.7 \times 10^{14}\,\mathrm{W/cm^2}$, wavelength $\lambda = 800\,\mathrm{nm}$, and 36 cycles. The initial temperature is 200 K. 98

6.2 Comparison of the experimental (from [71]) and theoretical Fourier spectrum of the dynamic 19th harmonic signal for O_2. The spectrum shows series II: $(\mathit{10}, \mathit{18}, \mathit{26}, \mathit{34}, \mathit{42}, ..)\, Bc$ (green mark), series III: $(\mathbf{20}, \mathbf{28}, \mathbf{36}, \mathbf{44}, \mathbf{52}, \mathbf{60}, ..)\, Bc$ (red mark), and series V: $(\boldsymbol{8}, \boldsymbol{16}, \boldsymbol{24}, \boldsymbol{..})\, Bc$ (brown mark). We use pump pulse of intensity $I_{pump} = 0.5 \times 10^{14}\,\mathrm{W/cm^2}$ and pulse width $FWHM = 40\,\mathrm{fs}$, and probe pulse of intensity $I_{probe} = 1.2 \times 10^{14}\,\mathrm{W/cm^2}$, wavelength $\lambda = 800\,\mathrm{nm}$, and 36 cycles. The initial temperature is 200 K. 100

6.3 Comparison of the experimental (from [138]) and theoretical Fourier spectrum of the dynamic 19th harmonic signal for CO_2. The spectrum is dominated by three main series, i.e. series I: $(6, 14, 22, ..)\, Bc$, series III: $(\mathbf{20}, \mathbf{28}, \mathbf{36}, \mathbf{44}, ..)Bc$, and series V: $(\boldsymbol{8}, \boldsymbol{16}, \boldsymbol{24}, \boldsymbol{..})Bc$. We use pump pulse of intensity $I_{pump} = 0.53 \times 10^{14}\,\mathrm{W/cm^2}$ and pulse width $FWHM = 40\,\mathrm{fs}$, and probe pulse of intensity $I_{probe} = 1.5 \times 10^{14}\,\mathrm{W/cm^2}$, wavelength $\lambda = 800\,\mathrm{nm}$, and 36 cycles. The initial temperature is 300 K. 102

6.4 Theoretical Fourier spectrum of the dynamic 9th harmonic signal for CO_2. The spectrum is dominated by three main series, i.e. series I: $(6, 14, 22, ..)\, Bc$, series III: $(\mathbf{20}, \mathbf{28}, \mathbf{36}, \mathbf{44}, ..)Bc$, and series V: $(\boldsymbol{8}, \boldsymbol{16}, \boldsymbol{24}, \boldsymbol{..})Bc$. We use pump pulse of intensity $I_{pump} = 0.56 \times 10^{14}\,\mathrm{W/cm^2}$ and pulse width $FWHM = 40\,\mathrm{fs}$, and probe pulse of intensity $I_{probe} = 1.23 \times 10^{14}\,\mathrm{W/cm^2}$, wavelength $\lambda = 800\,\mathrm{nm}$, and 36 cycles. The initial temperature is 300 K. There is no experimental spectrum reported. 103

6.5 Calculated spectra for19th harmonic signal of N_2 (panel a) and O_2 (panel b) at Boltzmann temperature 100 K; laser parameters as in Fig. 6.1, for N_2 and, as in Fig. 6.2 for O_2. 104

6.6 Calculated spectra for CO_2 of 9th harmonic (upper panel) and 19th harmonic (lower panel) at Boltzmann temperature 100 K; laser parameters as in Fig. 6.4, for 9th harmonic order and, as in Fig. 6.3 for 19th harmonic order. . . . 105

6.7 Theoretical Fourier spectrum of the dynamic 19th harmonic signal for O_2; pump intensity $I = 0.5 \times 10^{14}\,\mathrm{W/cm^2}$, probe intensity $I = 1.2 \times 10^{14}\,\mathrm{W/cm^2 W/cm^2}$, duration 40 fs, wavelength 800 nm, and temperature 200 K. The calculation was done based on the semi adiabatic model (left-lower panel), the frozen nuclei model of Lin (right-upper panel) , the 'mixture model' of Madsen (right-lower panel). As comparison, the experimental spectrum (left-upper panel) is also shown. 107

7.1 Schematic diagram defining the directions of the molecular axis, $\boldsymbol{R}$, electron position vector $\boldsymbol{r}$, the pump polarization ($\boldsymbol{\epsilon}_1 \parallel z -$ axis), and the probe polarization ($\boldsymbol{\epsilon}_2 \parallel z' -$ axis). The z and z' axes lie on the common x-z plane; the fields are assumed to propagate along the y-axis. 111

7.2 Theoretical harmonic spectra of N_2 for various relative polarization angle, α, at top signal (left panel) and anti-top signal (right panel); pump pulse: $I_{pump} = 0.4 \times 10^{14}$ W/cm^2 and 60 fs; probe pulse: $I_{probe} = 2 \times 10^{14}$ W/cm^2 and 30 fs, wavelength 800 nm, temperature 30 K. 114

7.3 Comparison of experimental (left panel) (from [138]) and calculated (right panel) dynamic 19th harmonic order for N_2 for various relative pump-probe polarization angles, i.e. $\alpha = 0^o$, $\alpha = 45^o$, and $\alpha = 90^o$. The laser parameters are $I_{pump} = 0.8 \times 10^{14}$ W/cm^2, $I_{probe} = 1.7 \times 10^{14}$ W/cm^2, $FWHM = 40$ fs, $\lambda = 800$ nm, and 36 cycles. The initial temperature is 200 K. 116

7.4 Calculated dynamic 19th harmonic order for O_2 for various relative pump-probe polarization angles, i.e. $\alpha = 0^o$, $\alpha = 45^o$, and $\alpha = 90^o$. The laser parameters are $I_{pump} = 0.5 \times 10^{14}$W/cm^2, $I_{probe} = 1.2 \times 10^{14}$W/cm^2, $FWHM = 40$ fs, $\lambda = 800$ nm, and 36 cycles. The initial temperature is 200 K. 117

7.5 Calculated dynamic 9th harmonic order for CO_2 for various relative pump-probe polarization angles, i.e. $\alpha = 0^o$, $\alpha = 45^o$, and $\alpha = 90^o$. The laser parameters are $I_{pump} = 0.56 \times 10^{14}$ W/cm^2, $I_{probe} = 1.3 \times 10^{14}$ W/cm^2, $FWHM = 40$ fs, $\lambda = 800$ nm, and 36 cycles. The initial temperature is 300 K. 117

7.6 Calculated dynamic 19th harmonic order for CO_2 for various relative pump-probe polarization angles. The laser parameters are $I_{pump} = 0.53 \times 10^{14}$ W/cm^2, $I_{probe} = 1.5 \times 10^{14}$ W/cm^2, $FWHM = 40$ fs, $\lambda = 800$ nm, and 36 cycles. The initial temperature is 300 K. 118

7.7 Experimental (left panel) (from [72]) and calculated (right panel) 19th harmonic at peak of its first half-revival (when its alignment degree is maximum) plotted as a function of pump-probe angle α, for N_2 ($t_d = 4.09$ ps), O_2 ($t_d = 5.68$ ps), and CO_2 ($t_d = 21.18$ ps) [72]. The laser parameters for both calculation and experiment are similar with Fig. 7.3 for N_2, Fig. 7.4 for O_2, and Fig. 7.6 for CO_2. 119

7.8 HHG signal near the first half-revival plotted as a function of pump-probe angle α, for N_2, O_2, and CO_2. The solid (black) line for 'top signal', i.e. when its alignment degree $\langle\langle\cos^2\theta\rangle\rangle$ is maximized. The dashed (blue) line for 'anti-top signal', i.e. when its alignment degree is minimum. The dash-dotted (red) line for 'average signal', i.e. when its alignment degree is in average. The observation times for top, average, and anti-top are: (4.09 ps, 4.18 ps, and 4.27 ps) for N_2, (5.680 ps, 5.790 ps, and 5.900 ps) for O_2, and (21.18 ps, 21.38 ps, and 21.58 ps) for CO_2. The pulse parameters are the same as in Fig. 7.3 for N_2, Fig. 7.4 for O_2, Fig. 7.5 for 9th harmonic order of CO_2, and Fig. 7.6 for 19th harmonic order of CO_2. 120

7.9 The modulation depth around first half revival of HHG signal of N_2 (upper panel) and O_2 (lower panel) for various initial temperature. The pulse parameters are similar with Figs. 7.3 and 7.4 for N_2 and O_2, respectively. 121
7.10 The 19th harmonic signal of O_2 near the second eight-revival, plotted as a function of pump-probe angle α. In panel (a), the signal is approximated by its first leading term only (Eq. (7.16)), whereas the true signal is shown in panel (b). The pulse parameters are the same as in Fig. 7.4 123
7.11 The 19th harmonic signal for N_2 (left upper panel) and O_2 (left lower panel) as function of time delay and relative polarization angle between pump and probe pulses. We also show the dynamic signals around their half revival for both N_2 (right upper panel) and O_2 (right lower panel). The pulse parameters are the same as in Figs. 7.3 and 7.4 for N_2 and O_2, respectively. The initial temperature is 200 K. 125
7.12 The HHG signal for CO_2 for 9th (upper panel) and 19th (lower panel) harmonic orders as function of time delay and relative polarization angle between pump and probe pulses. We also show the dynamic signals around their half revival for both 9th (right upper panel) and 19th (right lower panel). The pulse parameters are the same as in Figs. 7.5 and 7.6 for 9th and 19th, respectively. The initial temperature is 300 K. 126
7.13 Comparison between planar model and 3D model, for 19th harmonic of N_2. The pulse parameters are the same as in Fig. 7.3. 127
7.14 Experimental (upper panel) (from [67, 141, 142]) and theoretical (lower panel) dynamic signal of 9th harmonic signal of N_2 for various pump-probe polarizations angle $\alpha = 0^o$ and $\alpha = 90^o$; pump intensity $I = 2 \times 10^{12}$W/cm^2, duration 300 ps; probe intensity, $I = 5 \times 10^{14}$ W/cm^2, duration 70 fs, and wavelength 798 nm; Boltzmann temperature 25 K. 129
7.15 Theoretical 19th harmonic signal of molecule aligned by using turn-off method. (a) Dynamic alignment for various relative polarization angle α. (b) α-dependent HHG signal for various delay time. (c) Fourier spectrum for HHG signal with $\alpha = 0^o$. We use $I_{pump} = 0.8 \times 10^{14}$W/cm^2 with $\tau_{on} = 2.6547$ ps and $\tau_{off} = 24$ fs, $I_{probe} = 1.7 \times 10^{14}$W/cm^2 with $\tau = 24$ fs and wavelength 800 nm, and Boltzmann temperature 200 K. 130

Chapter 1

Introduction

In recent years there have been a lot of interests and progresses in general understanding of the interaction of atoms and molecules with intense laser fields (e.g. reviews [1, 2]). They are stimulated by success of optical pulse engineering in strikingly decreasing the laser pulse duration from a hundred micro second in 1960s down to femtosecond at very high peak power and intensities in modern Ti:sapphire laser system in 2000s [3, 4, 5]. Femtosecond laser technology has enabled us to follow atomic motion in real time, achieve high harmonic generation (HHG), stimulate Raman scattering, as well as exploit the highly nonlinear response of atoms and molecules [6, 7].

Further advances in femtosecond technology also allow one to align molecules and follow their dynamic in so called pump-probe experiments [8]. Molecular alignment and orientation in gaseous phase are of particular interest (see [9, 10]), not less because of their potential and wide range applications, especially for controlling chemical reactions [11]. Recently, the molecular alignment has been also applied for laser assisted isotope separation [12], imaging molecular structure [13], nanoscale design [14], pulse compression [15], and quantum information processing [16]. One of the best candidates for observing dynamic alignment is high harmonic generation (HHG). As reverse, alignment also provides a way of controlling HHG source and enables HHG to provide a powerful source of ultrashort coherent radiation in the xuv region. In this chapter we shortly introduce some concepts that underline this work, by highlighting the recent achievements both in experimental and theoretical sides. While there has been considerable progress in experimental side on the HHG of aligned molecules, there has been much less explanation of them from theoretical view. To overcome this discrepancy is one of the motivations of this work. In particular, we shall develop a detailed ab initio theory of molecular alignment and high harmonic generation in pump-probe experiments, and analyze and interpret a whole class experimental observation in recent years.

1.1 Molecular Alignment

The idea of molecular alignment dates back to 1975, as the possibility molecular alignment induced by a strong non-resonant laser field was first studied theoretically by Zon and Katsnelson [17]. In the same year alignment by formation of rotational wavepackets was demonstrated in the relatively heavy molecule CS_2 [18] by using a 5 ps pulse which is short enough to create a rotational wavepacket that aligns and revives regularly. Aligned and oriented molecules can be also produced by collisions with atoms [19], by 'brute force' orientation with strong electric fields [20], or by using optical infrared radiation [21]. It is important to distinguish between alignment, where molecular axis is preferentially aligned at some relative angle to a space-fixed axis (e.g. an electric field line), and orientation, where the direction in which the molecule is pointing along the alignment axis is also controlled. Orientation degree is quantified by the orientation angle $\cos\theta$, meanwhile alignment degree is quantified by the alignment degree: $\cos^2\theta$.

The current burst in molecular alignment research activities by using intense nonresonant laser pulse was initiated by the work of Friedrich and Herschbach [21] and Seideman [22] in mid-90s. Friedrich and Herscbach [21] developed a simple model of interaction between molecule and nonresonant laser field. The model used the anisotropic polarizability of a (non polar) molecule, to couple the electric field of the intense laser field which give a potential energy. The potential energy contains an angle-dependent term and creates a torque, rotating the molecules to align along the electric field of the laser. The laser induced alignment has the advantage that it is a general method and can be applied to any molecule, because no permanent dipole is required. However, this method could only align but not orient the molecule.

Based on the laser pulse duration, there are three different alignment scenarios. The simplest case was alignment by using a pulse whose duration was longer than the rotational period of molecule [21] (known as adiabatic alignment). In this scenario, a high alignment degree could be reached, but it was lost once the pulse was turned off. The second scenario was alignment by using a pulse shorter than the rotational period of the molecule [23] (known as non-adiabatic alignment or dynamic alignment). This method ensured molecules to align and revive even after the pulse was turned off, but could not reach an alignment degree as high as in adiabatic alignment. The third scenario was a 'turn-off' alignment where a pulse was slowly turned on but rapidly turned off [24]. In fact, the last method could reach higher alignment degree than from the non-adiabatic method and still showed revival effects even after the pulse was turned off.

Since the method of alignment was known, there have been experimental realizations of non-adiabatic alignment of heavy to light molecule, such as I_2 [25], N_2 [26], O_2 [27], CO_2 [28], CO [29], and recently D_2 [30]. Observations were also made for adiabatic alignment of naphthalene [31] and turn-off alignment of CO_2 [32]. In addition there were both theoretical proposal and experimental realization of enhancement of alignments with (i) combination of short pulses [33, 34, 35, 36], (ii) combination of short and long pulses [37], (iii) combination of laser pulse and strong electric field with various ‘tilt’ angle [38, 39, 40, 41], (iv) combination of laser pulse and static octahedral potential [42], and (v) variation of the relative polarization angle between pump and probe pulses [43]. It was also possible to enhance the degree of alignment by varying the temperature of the ensemble [44, 45] and the pulse properties like pulse intensity and pulse duration [46]. Finally, molecular alignment by using elliptic polarization has been proposed [47] and realized for 3-dimensional alignment of polyatomic molecules [48, 49].

1.2 High Harmonic Generation

First observed at the end of the 80’s, high harmonic generation (HHG) is a process in which noble gas atoms are driven by an intense laser field of frequency ω and produce radiation of a higher frequency $\Omega = n\omega$ (Fig. 1.1(a)), where n is an odd number, known as harmonic order [50, 51]. The high harmonic spectrum (harmonic yields as a function of their order) has a number of characteristic features. That is, the harmonic signal exponentially decreases for the low harmonic orders (the so called perturbative region), followed by a harmonic intensity plateau, where the harmonic signal stays roughly constant with increasing harmonic order, before reaching a cut-off, where a rapid exponential decrease of harmonic signal is observed. According to the perturbation theory, one would expect a rapid decrease of harmonic signal with increasing harmonic order [52]. However, at high intensities the observed plateau region and the cut-off of the harmonic was not immediately understood.

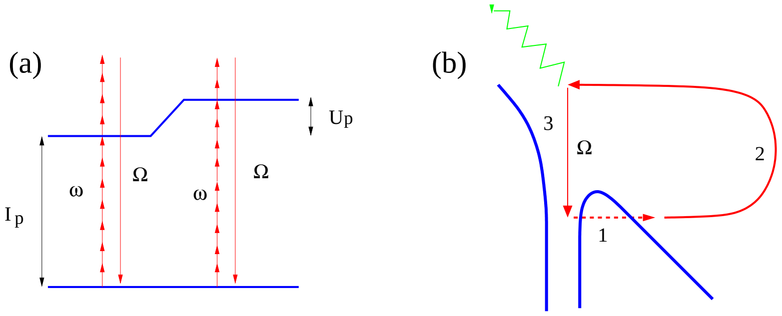

Figure 1.1: (a) The HHG process, n photon with frequency ω produce radiation with frequency $\Omega = n\omega$. (b). Description of HHG process in the framework of three-step model, which are (1) ionization, (2) propagation, and (3) recombination.

The first theoretical breakthrough in understanding of the origin of the plateau of HHG came in 1992 when Krause *et al.* [53] showed, by solving the time-dependent Schrödinger equation (TDSE) numerically, that the position of cut-off in harmonic spectrum is given by the universal law, $n_{cut-off} = (I_p + 3U_p)/\hbar\omega$, where I_p is ionization potential and $U_p = \frac{e^2E^2}{4m\omega^2}$ (where e and m are electric charge and mass of electron, respectively) or $U_p(eV) = 9.33 \times 10^{-14} I(\mathrm{W/cm^2})\lambda^2(\mu\mathrm{m})$ is the so-called ponderomotive energy, which is

Table 1.1: Peak intensity I and wavelength λ corresponding to $\gamma = 1$ for N_2, O_2, and CO_2.

	Keldysh parameter	λ (nm)					
	($\gamma = 1$)	600	700	800	900	1000	1064
N_2 ($I_p = 15.58\,\mathrm{eV}$) $\Rightarrow$		2.31	1.70	1.30	1.03	0.83	0.74
O_2 ($I_p = 12.03\,\mathrm{eV}$) $\Rightarrow$	$I\,(10^{14}\,\mathrm{W/cm^2})$	1.78	1.31	1.01	0.80	0.65	0.57
CO_2 ($I_p = 13.77\,\mathrm{eV}$) $\Rightarrow$		2.05	1.51	1.15	0.91	0.74	0.65

the cycle-averaged kinetic energy of an electron in the laser electric field with peak electric field E . This mean electron-laser interaction energy also raises the ionization potential I_p by U_p, as shown in Fig. 1.1(a). In 1993 Corkum [54] and Kulander *et al.* [55] published a classical/quasiclassical theory, which reproduced the plateau region observed in the experiments. According to their works, the HHG can be broken up into a three-step process: ionization, propagation, and recombination. The model has therefore been named the 'three-step model' or also the 'simple-man's model' due to its striking classical simplicity. In addition, they found classically also the cut-off in the harmonic spectrum to occur at $n_{cut-off} = (I_p + 3.17U_p)/\hbar\omega$. Shortly after the three-step model was introduced, a quantum model was proposed by Lewenstein *et al.* [56] which confirmed the validity of the classical approximation.

The three-step model is quasiclassical, meaning that the quantum aspects, like tunneling and ionization are incorporated into the model but the motion of the electron in the driving laser field is treated classically. The three-step model is shown in Fig. 1.1(b). (1) The electron is born into the continuum through tunnel ionization with zero kinetic energy. (2) The electron is treated as a free classical particle, which is accelerated by the driving laser field thereby accumulating kinetic energy. (3) The high harmonic emission takes place because the electron is attracted back to recombine with the core and emit a single photon with frequency $\Omega = n\omega$. The three-step process repeats every half-cycle of the driving laser field. This periodicity in the time domain results in the frequency domain as separation by twice the frequency of the driving laser field, 2ω. The fundamental frequency appears in the spectrum as a first order ($n = 1$) emission, and the separation by 2ω implies that the HHG signals appear for the odd harmonic orders only.

It should be noted here that the three-step model is applicable only for high intensities laser pulse, characterized with $\gamma < 1$ where $\gamma = \sqrt{\frac{I_p}{2U_p}}$ is the so-called Keldysh parameter [57]. For $\gamma > 1$ or at low intensities the HHG process is explained by multiple absorption of photons and described in the frame of perturbation theory. The typical value of peak intensity I and wavelength λ corresponding to $\gamma = 1$ for N_2, O_2, and CO_2 are given in Tab. 1.1. Higher intensities indicate the tunneling regime whereas the lower ones indicate the multiphoton regime.

The HHG from molecules has been studied experimentally already soon after the discovering of HHG from atoms [58, 59], and found to yield radiation patterns very similar to that of atoms. The further studies however showed some differences on the cut-off position between HHG of molecules and that of atoms with similar potential ionization [60, 61], due to the particular symmetry (e.g. the axial symmetry) of the molecules.

1.3 Pump-probe Experiment

To observe dynamic alignment of molecules, one needs at least two pulses. We start with a pump-pulse to set them in rotational motions and wait for the molecules to be aligned at a later time (a few picoseconds) when they could undergo a 'rotational revival'. A second delayed probe-pulse is then used to generate the observed signal from the aligned molecules. The signal is then measured against the delay time between the two pulses and the rotational alignment is traced out in time.

The first observation on the dynamic alignment was made by Rosca-Pruna and Vrakking [25]. They used a short intense laser pulse to Coulomb explode aligned I_2 molecule and a velocity-map imaging, to study the angular distributions of ion fragments. Later on, similar method was used by Dooley *et al.* for N_2 and O_2 [27] and Lee *et al.* for D_2 [30]. Renard *et al.* probed non-adiabatic alignment of CO_2 [62] and N_2 [63] by measuring transient birefringence, whereas Susmann *et al.* [32] probed turn-off alignment of CO_2 and CS_2 by optical Kerr effect (OKE). Further, it was proposed to detect molecular alignment by Photoelectron Angular Distribution (PAD) [64] and the so-called Above Threshold Ionization (ATI) [65, 66].

Observing molecular alignment by using HHG was first demonstrated in case of adiabatic alignment of N_2, H_2, CS_2 [67], and CO_2 [68]. HHG signal has also been demonstrated as a sensitive tool for probing non-adiabatic alignment in N_2, O_2, and CO_2 [69, 70, 43, 71]. Unlike the Coulomb explosion, detection by HHG is a non-destructive process. Recent observations show that the HHG signal from aligned molecules can be controlled by the relative pump-probe polarization angle [72, 43] and the probe ellipticity [73, 74, 75]. As a reverse case, HHG signal has been used to reconstruct the molecular orbital [13, 76, 77, 78, 5], proton dynamics [79], and molecular dynamics [80]. HHG from aligned molecule signals had also potential application as a source of coherent ultraviolet light and generation of ultrashort attosecond laser pulse [81].

The typical pump-probe experiment set up using HHG as a probe, is depicted in Fig. 1.2. A laser beam is split into two parts by a beam splitter (BS) to separate the pump and probe pulses, with a specific ratio of intensity between them. The probe pulse is then delayed with a controllable delay line system D and, if needed, can be also rotated with a polarizer P. The two pulses is then mixed again with a beam mixer (BM) where the probe pulse is delayed by $2l/c$ from the pump pulse and its polarization is rotated with respect to that of the pump pulse by an angle α, if desired. The pump-probe pulse sequence is focused by a system of lenses (F) and is then subjected to a molecular gas jet: the pump pulse dynamically 'aligns' the molecules whereas the probe pulse generates HHG signal from the aligned molecules. The HHG signal is then recorded by a detector system. Depending on the experimental purpose, the observation of the HHG signal of aligned molecules can be arranged in several different ways.

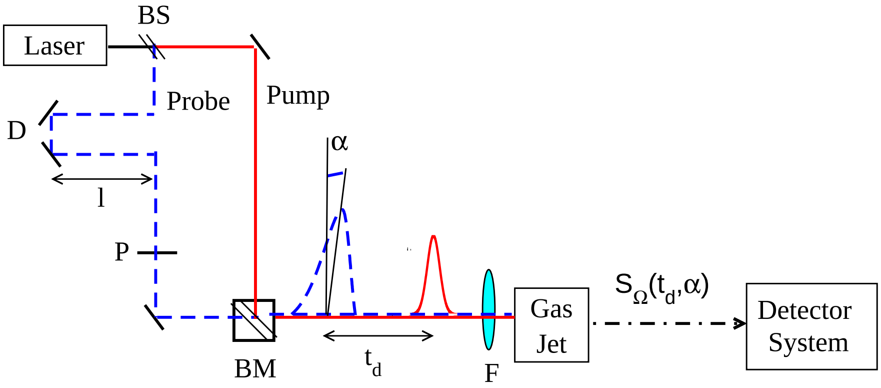

Figure 1.2: Schema of pump-probe experiment. The explanation is given in text.

1. Keeping the delay time between the two pulses fixed, one can measure the harmonic signals for all possible frequencies, and plotting them as a function of emitted frequency in units of the probe laser frequency ω. This gives the well known high harmonic spectrum.
2. Observing the harmonic signal for a fixed frequency (corresponding to a specific order), repeating it for various delay times, and plotting the signal against the delay between two pulses, gives the so called dynamic HHG signal.
3. Observing the harmonic spectrum for various relative polarizations between the two pulses [13], one can obtain information on the angular distribution of the process.
4. In addition, one can Fourier transform the dynamic signal and plot the emission intensity as a function of Bc with B is the rotational constant of molecules. Compared to the dynamic HHG signal, the HHG signal in frequency domain can give a more precise information of the dynamic HHG signal [82].

1.4 Theoretical Background

A first theoretical investigation on HHG of aligned molecules was the dependence of HHG spectrum on the alignment angle (between the polarization of the pump pulse and the molecular axis) of a simple ion H_2^+ and molecule H_2 was made by directly solving the time-dependent Schrödinger equation (TDSE) and introducing a static alignment angle between the molecular axis and the laser polarization axis [83, 84, 85]. Kopold *et al.* [83] and Lappas and Marangos [84] showed a discrepancy of HHG spectrum of H_2^+ between the assumed parallel and the perpendicular molecular axis alignment, relative to the field polarization. Their work was then elaborated by Lein and his coworkers for any alignment angle [85, 86, 68] within a one and a two dimensional model. However, these early models assumed a static angle, that did not change with the time.

Lin and his colleagues [87, 88] and Madsen and Madsen [89] proposed dynamic models which were based on the atomic Lewenstein model [56] by replacing atomic wave function with the molecular wave function of interest and introducing an adiabatic alignment angle between the molecular axis and the laser polarization. They had only a limited success in interpreting the observations and showed qualitative discrepancy with respect to the spectrum of dynamic signal e.g. for O_2 and modulation signal with respect to the relative polarization angles (see [88]).

1.5 Organization of the Work

We develop an *ab initio* intense-field theory of the HHG signals from linear molecules using a short femtosecond (linear polarization) pump pulse, to excite the coherent rotational motion, which is then interrogated by a second probe-pulse.

The rest of the present work is organized as follow. The mathematical formulation for the interaction between the molecule and a delayed sequence of a pump and a probe pulses is presented in chapter 2. The dynamic HHG signal is then derived and expressed in term of an explicit *HHG operator*. The present theory is used to provide a critique of the heuristic models used earlier, at the end of the chapter. Chapter 3 focuses on dynamic alignments, revivals and their periods, beat frequencies, and temperature.

In chapter 4, the theory is applied to diatomic molecules N_2 and O_2. The main topic is the analysis of the dependence of the dynamic signals on the symmetry of the molecular wavefunction. In addition, the differential signal is derived. In chapter 5, the theory is applied to the three-atomic molecule CO_2 where the origin of phenomenon of phase inversion is investigated.

Chapter 6 discusses the signals in the frequency domain obtained by Fourier transforming the time domain signals. The frequency domain provides more precise discrete information and therefore can be used to test the validity of the present theory and the earlier models, more stringently.

In Chapter 7, the theory is generalized for an arbitrary relative angle between the pump and the probe polarizations and is applied to the most recent experiments that depend both on the delay time between the pulses and on the relative angle between their polarizations. We end the chapter by considering the nature of HHG signal in the adiabatic and turn-off case for long pump pulse.

The last chapter 8 summarizes the results and gives a short outlook.

Chapter 2

Mathematical Formulation

This chapter presents a mathematical formulation of intense-field theory for high harmonic generation (HHG) from freely rotating linear molecules. It starts with a review of intense-field wavefunction describing the interaction between a molecule and an intense laser field. The wavefunction is then applied to the interaction between a molecule and a sequence of two (pump and probe) pulses. The emission signal is given by the Fourier transform of the expectation value of the total dipole (c.f. [90]). This is used to derive the dynamic signal which is expressed in term of an HHG operator. The explicit expression of the HHG operator is then derived for the usual parallel set-up of pump and probe polarizations. The theoretical distinctions between the present theory and other ad hoc models are discussed at the end of this chapter.

2.1 Intense-field Wavefunction

The Schrödinger equation of a molecule subject to an external intense laser field is given by

$$i\hbar\frac{\partial}{\partial t}\Psi\left(\boldsymbol{R},\boldsymbol{r},t\right) = H(\boldsymbol{R},\boldsymbol{r},t)\Psi\left(\boldsymbol{R},\boldsymbol{r},t\right) \tag{2.1}$$

with $\boldsymbol{R} = (\boldsymbol{R}_1, ..., \boldsymbol{R}_n)$ are the coordinates of the atomic nuclei and $\boldsymbol{r} = (\boldsymbol{r}_1, ..., \boldsymbol{r}_m)$ are coordinates of the electrons. $H(\boldsymbol{R},\boldsymbol{r},t)$ is the total Hamiltonian of an interacting molecular and laser system and can be written as

$$H(\boldsymbol{R},\boldsymbol{r},t) = H^0(\boldsymbol{R},\boldsymbol{r},t) + V(\boldsymbol{R},\boldsymbol{r},t). \tag{2.2}$$

Above, $H^0(\boldsymbol{R},\boldsymbol{r},t)$ is the reference Hamiltonian and $V(\boldsymbol{R},\boldsymbol{r},t)$ is the interaction with the external laser field.

The solution of Eq. (2.1) can be obtained by using an *ab initio* systematic approximation method known as the ‘intense-field many-body S-matrix theory’ (IMST) [91, 92, 2]. In this approach, the usual perturbation expansion of the transition amplitude of a process was arranged in such a way that the dominant virtual channels, when present, appear already in the leading term of S-matrix series. To this end, the Hamiltonian of the system at the initial time is partitioned as

$$H(t) = H_i^0(t) + V_i(t) \tag{2.3}$$

where $H_i^0(t)$ is the initial unperturbed Hamiltonian, and $V_i(t)$ is the initial interaction with the laser field (for simplicity, the explicit expressions of coordinates are dropped). By using Eq. (2.3), the Schrödinger equation of the interacting system (Eq. (2.1)) can be rewritten as a time-dependent generalization of the Lippman-Schwinger equation

$$\left[i\hbar\frac{\partial}{\partial t} - H_i^0(t)\right]\Psi\left(t\right) = V_i(t)\Psi\left(t\right). \tag{2.4}$$

In integral form, the last equation reads

$$|\Psi(t)\rangle = |\phi_i(t)\rangle + \int_{t_i}^{t_f} dt_1 G\left(t, t_1\right) V_i\left(t_1\right)|\phi_i(t_1)\rangle \tag{2.5}$$

with $t_f > t$. The validity of Eq. (2.5) can be verified by directly substituting it in Eq. (2.4). The first term, $\phi_i(t)$, is a (homogeneous) solution of the Schrödinger equation of unperturbed Hamiltonian $H_i^0(t)$

$$\left[i\hbar\frac{\partial}{\partial t} - H_i^0(t)\right]|\phi_i(t)\rangle = 0. \tag{2.6}$$

The second term, $\int_{t_i}^{t_f} dt_1 G\left(t, t_1\right) V_i\left(t_1\right)|\phi_i(t_1)\rangle$, is a (non homogeneous) solution of the Schrödinger equation of total Hamiltonian $H(t)$. $G(t, t')$ is the total Green's function (or propagator), defined by

$$\left[i\hbar\frac{\partial}{\partial t} - H(t)\right]G(t, t') = \delta(t - t'). \tag{2.7}$$

Next, the final state partition of the Hamiltonian

$$H(t) = H_f^0(t) + V_f(t) \tag{2.8}$$

is introduced, where $H_f^0(t)$ is the final state reference Hamiltonian and $V_f(t)$ is the final-state interaction. The total Green's function is then expanded in terms of the final-state Green's function, $G_f^0(t, t')$, in the form

$$G\left(t, t'\right) = G_f^0\left(t, t'\right) + \int_{t_i}^{t_f} dt_1 G_f^0\left(t, t_1\right) V_f\left(t_1\right) G\left(t_1, t'\right) \tag{2.9}$$

where $G_f^0\left(t, t'\right)$ satisfies

$$\left[i\hbar\frac{\partial}{\partial t} - H_f^0(t)\right]G_f^0(t, t') = \delta(t - t'). \tag{2.10}$$

By inserting the total Green's function (Eq. (2.9)) in the expression for the total wavefunction $|\Psi(t)\rangle$, Eq. (2.5), one obtains

$$\begin{aligned} |\Psi(t)\rangle &= |\phi_i(t)\rangle + \int_{t_i}^{t_f} dt_1 G_f^0\left(t,t_1\right) V_i\left(t_1\right) |\phi_i(t_1)\rangle \\ &\quad + \int_{t_i}^{t_f}\int_{t_i}^{t_f} dt_2 dt_1 G_f^0\left(t,t_2\right) V_f\left(t_2\right) G\left(t_2,t_1\right) V_i\left(t_1\right) |\phi_i(t)\rangle\,. \end{aligned} \tag{2.11}$$

The above form of the wavefunction automatically satisfies the initial state condition (e.g. the molecule in the ground state at initial time t_i)

$$\lim_{t_f \longrightarrow t_i} |\Psi(t)\rangle = |\phi_i(t=t_i)\rangle \tag{2.12}$$

where $\phi_i\left(t_i\right) = e^{-\frac{i}{\hbar}E_i t_i}\phi_i$ is one or a linear combination of the eigenstates, $\{\phi_j\}$, with energy E_j, of unperturbed Hamiltonian of the target Hamiltonian or $H_i\phi_j = E_j\phi_j$. Then by introducing the third (intermediate) partition of the total Hamiltonian

$$H(t) = H_0(t) + V_0(t) \tag{2.13}$$

and the corresponding propagator, $G_0(t,t')$, we expand $G(t,t')$ as

$$G\left(t,t'\right) = G_0\left(t,t'\right) + \int_{t_i}^{t_f} dt_1 G_0\left(t,t_1\right) V_0\left(t_1\right) G_0\left(t_1,t'\right) + ... \tag{2.14}$$

Substitution of Eq. (2.14) in Eq. (2.11) gives the the desired systematic expansion of the wavefunction of the interacting system

$$\Psi(t) = \sum_{j=0}^{\infty} \Psi^{(j)} \tag{2.15}$$

with

$$\left|\Psi^{(0)}\right\rangle = |\phi_i(t)\rangle \tag{2.16}$$

$$\left|\Psi^{(1)}\right\rangle = \int_{t_i}^{t_f} dt_1 G_f^0\left(t,t_1\right) V_i\left(t_1\right) |\phi_i(t_1)\rangle \tag{2.17}$$

$$\left|\Psi^{(2)}\right\rangle = \int_{t_i}^{t_f}\int_{t_i}^{t_f} dt_2 dt_1 G_f^0\left(t,t_2\right) V_f\left(t_2\right) G_0\left(t_2,t_1\right) V_i\left(t_1\right) |\phi_i(t_1)\rangle \tag{2.18}$$

$$\begin{aligned} \left|\Psi^{(n)}\right\rangle &= \int_{t_i}^{t_f} .... \int_{t_i}^{t_f}\int_{t_i}^{t_f} dt_n ...... dt_2 dt_1 \\ &\quad \times G_f^0\left(t,t_n\right) V_f\left(t_n\right) ..... G_0\left(t_3,t_2\right) V_f\left(t_2\right) G_0\left(t_2,t_1\right) V_i\left(t_1\right) |\phi_i(t_1)\rangle \end{aligned} \tag{2.19}$$

2.2 Molecule Interacting with a Pump- and a Delayed Probe-Pulse

The total Hamiltonian of a system consisting of a molecule interacting with a pump pulse (L_1) at a time t and a probe pulse (L_2) at a delayed time $t - t_d$ can be written (in Born-Oppenheimer approximation [93]) as [94],

$$H_{tot}(t) = H_N + V_{N-L_1}(t) + H_e + V_{e-L_2}\left(t - t_d\right) \tag{2.20}$$

where H_N is the nuclear Hamiltonian, $V_{N-L_1}(t)$ is the interaction due to the pump pulse L_1 with the nuclear motion, H_e is the electronic Hamiltonian, and $V_{e-L_2}\left(t - t_d\right)$ is the delayed interaction of the probe pulse L_2 with the active electron. To be noted is that in this approximation, the electronic wavefunction depends parametrically on the nuclear coordinates $\boldsymbol{R}$ such as that its gradient with respect to $\boldsymbol{R}$, and hence the adiabatic couplings, is assumed to be zero.

The laser fields are described in terms of the vector potentials which have the form $\boldsymbol{A}(t) = -c\int \boldsymbol{F}(t)dt$ where $\boldsymbol{F}(t)$ is the electric field of the laser at time t. Thus the interaction Hamiltonians appearing above are (in the usual dipole approximation [52], and for negligible overlap between the pulses) given by

$$V_{N-L_1}(t) = -\boldsymbol{\mu} \cdot \boldsymbol{F}_1(t) - \frac{1}{2}\boldsymbol{F}_1(t) : \boldsymbol{\alpha} : \boldsymbol{F}_1(t) \tag{2.21}$$

where $\boldsymbol{\mu}$ is the permanent dipole moment (if non-zero) and $\boldsymbol{\alpha}$ is the polarizability *tensor* of the molecule; and

$$V_{e-L_2}\left(t - t_d\right) = -\hat{\boldsymbol{d}}_e \cdot \boldsymbol{F}\left(t - t_d\right) \tag{2.22}$$

where $\hat{\boldsymbol{d}}_e$ stands for the electronic dipole *operator.*

Following Eqs. (2.1) and (2.7), the Schrödinger equation of the total system is,

$$i\hbar\frac{\partial}{\partial t}\Psi(t) = H_{tot}(t)\Psi(t), \tag{2.23}$$

where the corresponding Green's function $G(t, t')$ satisfies

$$\left[i\hbar\frac{\partial}{\partial t} - H_{tot}(t)\right] G(t, t') = \delta(t - t')\mathbf{1} \tag{2.24}$$

We note first that the slow nuclear motion driven by the pump pulse can be described in terms of the solutions of the Schrödinger equation

$$i\hbar\frac{\partial}{\partial t}\Phi_{JM}(t) = \left(H_N + V_{N-L_1}(t)\right)\Phi_{JM}(t). \tag{2.25}$$

They are obtained in practice by solving the coupled time dependent differential equations satisfied by the expansion coefficients $a_{JM}(t)$ of $|\Phi_{JM}(t)\rangle$ [95], where

$$|\Phi_{J_0M_0}(t)\rangle = \sum_{JM} a_{JM}^{J_0M_0}(t)e^{-\frac{i}{\hbar}E_{JM}t}\,|JM\rangle\,, \tag{2.26}$$

in which the basis functions are given by the angular momentum eigenfunctions, $|JM\rangle$. The linear differential equations of interest are

$$i\hbar\frac{\partial}{\partial t}a_{JM}^{J_0M_0}(t) = \sum_{J'M'}\left\langle JM\left|V_{N-L_1}(t)\right|J'M'\right\rangle a_{J'M'}^{J_0M_0}(t) \tag{2.27}$$

Physically, a fundamental solution $|\Phi_{J_0M_0}(t)\rangle$ of Eq. (2.25), obtained from Eqs. (2.27) and (2.26), is a rotational wave-packet state that uniquely evolves from an initially occupied rotational eigenstate, $|J_0M_0\rangle$, of the unperturbed nuclear motion. The wave-packet solutions are linearly independent, and like the eigenstates $|J_0M_0\rangle$ of H_N, form a complete set:

$$\sum_{J_0M_0}|\Phi_{J_0M_0}(t)\rangle\,\langle\Phi_{J_0M_0}(t)| = \mathbf{1}. \tag{2.28}$$

The electronic motion arising from the interaction of the active electron with an intense probe pulse L_2, is governed by the electronic Green's function $G_e(t,t')$, which satisfies the equation,

$$\left\{i\hbar\frac{\partial}{\partial t} - \left(H_e + V_{e-L_2}\left(t-t_d\right)\right)\right\}G_e(t,t') = \delta(t-t')\mathbf{1}. \tag{2.29}$$

The above equation can be solved in the form

$$\begin{aligned} G_e\left(t-t'\right) &= -\frac{i}{\hbar}\theta\left(t-t'\right)\sum_{j,\boldsymbol{p}}\left|\phi_j^{(+)}\right\rangle e^{-\frac{i}{\hbar}E_j^+t}\left|\boldsymbol{p}\left(t-t_d\right)\right\rangle \\ &\quad\times e^{-\frac{i}{\hbar}\int_{t'-t_d}^{t-t_d}\left(p^2(u)/2m\right)du}\left\langle\boldsymbol{p}\left(t'-t_d\right)\right|e^{\frac{i}{\hbar}E_j^+t'}\left\langle\phi_j^{(+)}\right| \end{aligned} \tag{2.30}$$

where j runs over all the ionic electronic states $\left|\phi_j^{(+)}\right\rangle$, with eigenvalues E_j^+, and $\boldsymbol{p}(t)$ stands for the instantaneous electron momenta in the presence of the field, as defined by 'minimum coupling prescription' (e.g. [90, 93])

$$\boldsymbol{p}(t) \equiv \boldsymbol{p} - \frac{e\boldsymbol{A}(t)}{c} \tag{2.31}$$

where $\boldsymbol{p}$ is the free momenta of the electron. The validity of Eq. (2.30) can be verified by substituting it in Eq. (2.29) and using the completeness relation of the Volkov wavefunctions $|\phi_v\left(\boldsymbol{p}\left(t\right)\right)\rangle$,

$$\sum_{\boldsymbol{p}}\langle\boldsymbol{r}\left|\phi_v(\boldsymbol{p}(t))\right\rangle\left\langle\phi_v\left(\boldsymbol{p}\left(t\right)\right)\right|\boldsymbol{r}\rangle = \mathbf{1}, \tag{2.32}$$

which are defined by

$$\langle \boldsymbol{r} \, | \phi_v(\boldsymbol{p}(t)) \rangle = e^{\frac{i}{\hbar}\boldsymbol{p}(t)\cdot\boldsymbol{r}} e^{-\frac{i}{\hbar}\int^t \left(p^2(u)/2m\right) du}, \tag{2.33}$$

and $\Sigma_{\boldsymbol{p}} \equiv \frac{\int d^3p}{(2\pi\hbar)^3}$. Note that the Volkov-wavefunctions account for the interactions of a free electron with the laser field to all orders in the vector potential (or electric field) strengths. Finally, by using Eqs. (2.28) and (2.30), the total Green's function $G_f^0(t,t')$ of the system is obtained:

$$\begin{aligned} G_f^0(t,t') &= -\frac{i}{\hbar}\theta(t-t') \sum_{j\boldsymbol{p}JM} \left|\phi_j^{(+)}\right\rangle \left|\phi_v^{(-)}(\boldsymbol{p}(t-t_d)\right\rangle \left|\Phi_{JM}(t)\right\rangle \\ &\quad \times e^{-\frac{i}{\hbar}E_j^+(t-t')} \left\langle \Phi_{JM}(t')\right| \left\langle \phi_v^{(-)}(\boldsymbol{p}(t'-t_d)\right| \left\langle \phi_j^{(+)}\right| \end{aligned} \tag{2.34}$$

The validity of Eq. (2.34) can be verified by substituting it directly in Eq. (2.24), and neglecting the derivatives of the electronic orbitals with respect to the nuclear coordinates $\boldsymbol{R}$ (Born-Oppenheimer approximation).

2.3 Molecular Wavefunction of the Interacting System: KFR Approximation

We require the total wavefunction of the system satisfying the initial condition i.e. with (i) the nuclear motion prepared (by the pump laser L_1) in a rotational wave-packet state $|\Phi_{J_0M_0}(t)\rangle$ evolving from the unperturbed angular momentum state $|J_0M_0\rangle$, and (ii) the active electron in the ground electronic state, $e^{-\frac{i}{\hbar}E_0 t}\left|\phi_e^{(0)}\right\rangle$, where the energy of the initial molecular state is E_0. The initial state of the whole system is,

$$\left|\Psi^{(0)}\,(t)\right\rangle = e^{-\frac{i}{\hbar}E_0 t}\left|\phi_e^{(0)}\right\rangle \left|\Phi_{J_0M_0}(t)\right\rangle \tag{2.35}$$

Using the Green's function (Eq. (2.34)), the wavefunction of the system interacting with the probe laser L_2, can be written using the expansion of Eq. (2.15) as

$$\left|\Psi_{KFR}(t)\right\rangle = \left|\Psi^{(0)}(t)\right\rangle + \left|\int_0^t dt' G_f^0(t,t') V_{e-L_2}\left(t'-t_d\right) \Psi^{(0)}(t')\right\rangle + ... \tag{2.36}$$

The neglect of the higher terms in the expansions consists of molecular generalization of the well-known KFR (Keldysh-Faisal-Reiss)-approximation first introduced for atoms [57, 96, 97]. Note that the presence of the Volkov Green's function $G_f^0(t,t')$ (Eq. (2.34)) allows for the laser-electron interaction of all orders. The above wavefunction (Eq. (2.36)) is now used to derive an analytical expression for the expectation value of the dipole operator of the system.

2.4 Dipole Expectation Value

We now derive the total dipole expectation value, $D(t)$, of the electronic dipole operator $\hat{\boldsymbol{d}}_e$, of the molecule and specify the approximations used to arrive at the result. Within the first order KFR approximation (Eq. (2.36)), the dipole expectation value is defined as

$$\begin{aligned} D(t) &= \left\langle \Psi_{KFR}(t) \left| \hat{\boldsymbol{d}}_e \right| \Psi_{KFR}(t) \right\rangle \\ &= \left\{ \left\langle \Psi^{(0)}(t) \left| \hat{\boldsymbol{d}}_e \right| \Psi^{(0)}(t) \right\rangle \right. \\ &\quad \left. + \left\langle \Psi^{(0)}(t) \left| \hat{\boldsymbol{d}}_e \right| \int_0^t dt' G_f^0(t,t') V_{e-L_2}\left(t'-t_d\right) \Psi^{(0)}(t') \right\rangle + c.c. \right\} + ... \\ &\simeq \left\langle \Psi^{(0)}(t) \left| \hat{\boldsymbol{d}}_e \right| \int_0^t dt' G_f^0(t,t') V_{e-L_2}\left(t'-t_d\right) \Psi^{(0)}(t') \right\rangle + c.c. \end{aligned} \tag{2.37}$$

In above, the term $\left\langle \Psi^{(0)}(t) \left| \hat{\boldsymbol{d}}_e \right| \Psi^{(0)}(t) \right\rangle$ is zero due to the parity of electronic wavefunction. The term $\left\langle \Psi^{(0)}(t) \left| \hat{\boldsymbol{d}}_e \right| \int_0^t dt' G_f^0(t,t') V_{e-L_2}\left(t'-t_d\right) \Psi^{(0)}(t') \right\rangle$ (reading from right to left) describes the electron propagating from the initial states $\Psi^{(0)}(t')$, interacting with the laser field V_{e-L_2} at $t'-t_d$, going into intermediate Volkov through the propagator $G(t,t')$, and then at the later time t recombining to parent ion when a harmonic photon is created. The *c.c.* stands for the complex conjugate of the term preceding it, $c.c. = \left\langle \int_0^{t'} dt G_f^{0*}(t,t') V_{e-L_2}\left(t-t_d\right) \Psi^{(0)}(t) \left| \hat{\boldsymbol{d}}_e \right| \Psi^{(0)}(t') \right\rangle$. We have neglected here the quadratic term on the right hand side, consistent with the lowest order KFR-approximation. However, if needed, one can improve the $D(t)$ expression by going to the higher terms systematically using Eq. (2.15). Further, by the following mathematical steps: (i) substituting the total Green's function of Eq. (2.34) in total dipole expression of Eq. (2.37), (ii) neglecting the interaction of the inactive electrons with the probe laser field L_2 and the small deviation from unity of the overlap of the inactive neutral and the residual-ion orbitals i.e. $\left\langle \phi_e^{(+)} \mid \phi_e^{(1,2,..N_e-1)} \right\rangle \approx 1$, and (iii) taking the wavefunction of Eq. (2.35) as an initial state for the whole system, we may simplify the expression above as

$$\begin{aligned} D(t) &= -\frac{i}{\hbar} \sum_{j\boldsymbol{p}JM} \left\langle \Phi_{J_0M_0}(t) \right| \left\langle \phi_e^{(0)} \left| \hat{\boldsymbol{d}}_e \right| \boldsymbol{p}(t-t_d) \right\rangle \\ &\quad \times \left| \phi_j^+ \right\rangle \left| \Phi_{JM}(t) \right\rangle e^{-\frac{i}{\hbar}(E_j^+ - E_0)(t-t')} \int_0^t dt' e^{-\frac{i}{\hbar}\int_{t'-t_d}^{t-t_d}\left(p^2(u)/2m\right)du} \left\langle \Phi_{JM}(t') \right| \left\langle \phi_j^+ \right| \\ &\quad \times \left\langle \boldsymbol{p}(t'-t_d) \left| V_{e-L_2}\left(t'-t_d\right) \right| \phi_e^{(0)} \right\rangle \left| \Phi_{J_0M_0}(t') \right\rangle + c.c. \end{aligned} \tag{2.38}$$

Changing the variable $t' \rightarrow t' + t_d$, and similarly, $t \rightarrow t + t_d$, and noting that the free evolution of the molecular wave packet at $(t+t_d)$ is $\Phi_{J_0M_0}\left(t+t_d\right) = e^{-\frac{i}{\hbar}H_N t}\Phi_{J_0M_0}\left(t_d\right)$, and similarly, at $(t'+t_d)$ is $\Phi_{J_0M_0}\left(t'+t_d\right) = e^{-\frac{i}{\hbar}H_N t'}\Phi_{J_0M_0}\left(t_d\right)$, and keeping only the dominant contribution from the ground state of the molecular ion, we may rewrite Eq. (2.38) as

$$\begin{aligned} D(t;t_d) \quad \simeq \quad & -\frac{i}{\hbar}\sum_{\boldsymbol{p}JM} \left\langle \Phi_{J_0M_0}\left(t_d\right) \right| e^{\frac{i}{\hbar}H_N t} \left\langle \phi_e^{(0)} \left| \hat{\boldsymbol{d}}_e \right| \boldsymbol{p}(t') \right\rangle \left| \phi_0^+ \right\rangle \\ & \times \left| \Phi_{JM}\left(t_d\right) \right\rangle e^{-\frac{i}{\hbar}H_N t} \int_{t_d}^{t_d+t} dt' e^{-\frac{i}{\hbar}\int_{t'}^{t}\left[p^2(u)/2m + (E_0^+ - E_0)\right]du} e^{\frac{i}{\hbar}H_N t'} \left\langle \Phi_{JM}(t_d) \right| \\ & \times \left\langle \phi_0^+ \right| \left\langle \boldsymbol{p}(t') \left| V_{e-L_2}(t') \right| \phi_e^{(0)} \right\rangle e^{-\frac{i}{\hbar}H_N t'} \left| \Phi_{J_0M_0}\left(t_d\right) \right\rangle + c.c. \end{aligned} \tag{2.39}$$

where H_N is the nuclear (rotational) Hamiltonian, and $E_0^+ - E_0 = E_B$, where E_B is the binding energy of the active electron. Assuming adiabatic condition (e.g. [93, 98])

$$Max \left|\Delta E_{J,J'}\right| \ll E_B, \hbar\Omega \tag{2.40}$$

and/or

$$\frac{H_N}{\hbar}\Delta t_p \approx \frac{\left|\Delta E_{J,J'}\right|}{\hbar}\Delta t_p \ll 1 \tag{2.41}$$

where Δt_p is of the order of the duration of the probe pulse, and using the completeness relation of Eq. (2.28), the dipole expectation value (Eq. (2.39)) reads

$$\begin{aligned} D\left(t;t_d\right) \quad = \quad & -\frac{i}{\hbar}\sum_{\boldsymbol{p}} \left\langle \Phi_{J_0M_0}\left(t_d\right) \right| \left\langle \phi_e^{(0)} \left| \hat{\boldsymbol{d}}_e \right| \boldsymbol{p}(t) \right\rangle \\ & \times \int_{t_d}^{t_d+t} dt' e^{-\frac{i}{\hbar}\int_{t'}^{t}\left[p^2(u)/2m + E_B\right]du} \\ & \times \left\langle \boldsymbol{p}(t') \left| V_{e-L_2}(t') \right| \phi_e^{(0)} \right\rangle \left| \Phi_{J_0M_0}\left(t_d\right) \right\rangle + c.c. \end{aligned} \tag{2.42}$$

Or simply it can be written as:

$$D\left(t;t_d\right) = \left\langle \Phi_{J_0M_0}(t_d) \left| D_e\left(t;t_d\right) \right| \Phi_{J_0M_0}(t_d) \right\rangle + c.c. \tag{2.43}$$

with $D_e\left(t;t_d\right)$ arises only from the electronic part of the total dipole expectation value $D\left(t;t_d\right)$ and is given by:

$$D_e\left(t;t_d\right) = -\frac{i}{\hbar}\sum_{\boldsymbol{p}} \left\langle \phi_e^{(0)} \left| \hat{\boldsymbol{d}}_e \right| \boldsymbol{p}(t) \right\rangle \int_{t_d}^{t_d+t} dt' e^{-\frac{i}{\hbar}S(p,t,t')} \left\langle \boldsymbol{p}(t') \left| V_{e-L_2}(t') \right| \phi_e^{(0)} \right\rangle + c.c. \tag{2.44}$$

where the action $S(t,t')$ is given by

$$\begin{aligned} S(p,t,t') \quad & = \quad \int_{t'}^{t} (\boldsymbol{p}(u)^2/2 + E_B)du \\ & = \quad \int_{t'}^{t} \left[\frac{1}{2m}\left(p - \frac{e}{c}A(t'')\right)^2 + E_B\right] dt'' \end{aligned} \tag{2.45}$$

Thus, within the approximations of Eq. (2.42), we arrive at an expression of the time dependent of the total dipole expectation value for the molecular case that is analogous to the well-known Lewenstein model obtained for the case of an atom [56].

2.5 Dynamic HHG Signal and HHG Transition Operator

According to semiclassical procedure, the amplitude for the harmonic emission from a pure state is proportional to the modulus square of the Fourier transform of dipole moment [90, § 9.1]. The dynamic signal for the emission of the HHG for a given frequency $\Omega = n\omega$ and delay time t_d is therefore given by the absolute square of the Fourier transform (*F.T.*) of the total dipole expectation value $D\left(t;t_d\right)$ (Eq. (2.42)). In the atomic case, Eq. (2.44) reduces to the popular Lewenstein model [56]. For a thermal mixture of a molecular ensemble, the dynamic signal for a given frequency $\Omega = n\omega$ and delay time t_d can be obtained by averaging the signal, over the distribution of the initially pure unperturbed rotational eigenstates $|J_0 M_0\rangle$, at a given initial temperature T:

$$S^{(n)}\left(t_d\right) = \sum_{J_0 M_0} \rho(J_0) \left|\left[F.T.\left(D\left(t,t_d\right)\right)\right](n\omega)\right|^2 \tag{2.46}$$

with $\rho(J_0) = \frac{1}{Z_P} e^{-E_{J_0}/kT}$ where k is the Boltzmann constant, T is the temperature, E_{J_0} is the rotational energy of the eigen state $|J_0 M_0\rangle$, and $Z_p = \sum_{J_0}(2J_0+1)e^{-E_{J_0}/kT}$ is the rotational partition function. It can be seen from Eq. (2.43) that $D\left(t,t_d\right)$ consists of the nuclear rotational wave function $\Phi_{J_0 M_0}\left(t_d\right)$ and the electronic part $D_e\left(t;t_d\right)$. Due to the independence of nuclear rotational wave function $\Phi_{J_0 M_0}\left(t_d\right)$ on t, the *F.T.* of $D\left(t,t_d\right)$ over t can now be expressed as

$$\left[F.T.\left(D\left(t,t_d\right)\right)\right](n) = \left\langle \Phi_{J_0 M_0}\left(t_d,\theta\right) \left|\left[F.T.\left(D_e\left(t;t_d\right)\right)\right](n\omega)\right| \Phi_{J_0 M_0}\left(t_d,\theta\right)\right\rangle + c.c. \tag{2.47}$$

Here, we write explicitly the dependence of instantaneous nuclear wave function $\Phi_{J_0 M_0}\left(t_d,\theta\right)$ on the alignment angle θ. Then, we define a new operator

$$T_e^{(n)}(\theta) = \left[F.T.\left(D_e\left(t;t_d\right)\right)\right](n\omega). \tag{2.48}$$

$T_e^{(n)}(\theta)$ can be viewed as *HHG transition operator* whose matrix element with respect to the rotational wave-packet become responsible for the signal. In above, $T_e^{(n)}(\theta)$ depends on θ through electronic ground state $\phi_e^{(0)}$ appears in $D_e\left(t;t_d\right)$ which is defined in Eq. (2.44). Finally, the dynamic signal at delay time t_d can be obtained by substituting Eq. (2.47) in Eq. (2.46)

$$S^{(n)}\left(t_d\right) = \sum_{J_0 M_0} \rho(J_0) \left|\left\langle \Phi_{J_0 M_0}\left(t_d,\theta\right) \left| T_e^{(n)}(\theta) \right| \Phi_{J_0 M_0}\left(t_d,\theta\right)\right\rangle\right|^2 \tag{2.49}$$

It is important to note that the expression of dynamic signal (Eq. (2.49)), which is obtained from the adiabatic hypotheses, differs from the other ad hoc models obtained by using fully frozen nuclei assumption [88, 89]. The comparison will be discussed at the end of this chapter.

2.6 HHG Operator: for Parallel Set-up of Pump and Probe Polarizations

We now proceed to obtain an explicit expression of the HHG transition operator $T_e^{(n)}(\theta)$ given by Eq. (2.48) and hence we need to evaluate the electronic dipole $D_e\left(t;t_d\right)$ given by Eq. (2.44). We first consider the most common experimental geometry in which the pump and probe polarizations are chosen to be parallel. It is convenient to take the space fixed polar axis (z-axis) along the common direction of the polarizations. Let the molecular axis point in the direction $\hat{\boldsymbol{R}}(\theta,\phi)$. We evaluate the triple-integral over the components of the momentum $\boldsymbol{p}$ in Eq. (2.44) by the stationary phase method [99, 56], for which the derivative of the action $S(t,t')$ with respect to p is put equal to zero

$$\nabla_{\boldsymbol{p}} S(p,t,t') \equiv 0. \tag{2.50}$$

The stationary value of momentum is then given by

$$\boldsymbol{p}_{st}(t,t') = \frac{e}{c\left(t'-t\right)} \int_{t'}^{t} \boldsymbol{A}(t'')dt'' \tag{2.51}$$

whereas the corresponding stationary value of the action is given by,

$$S_{st}(t,t') = \int_{t'}^{t} \left\{ \frac{1}{2m} \left(\boldsymbol{p}_{st}(t,t'') - \frac{e}{c}\boldsymbol{A}(t'') \right)^2 + E_B \right\} dt''. \tag{2.52}$$

Then by using expression of probe-electronic interaction in length gauge $V_{e-L_2}\left(t'\right) = -\hat{\boldsymbol{d}}_e.\boldsymbol{F}\left(t'\right)$ (Eq. (2.22)) and using saddle point method for integration over $\boldsymbol{p}$ [100, 56], we obtain

$$\begin{aligned} D_e\left(t;t_d\right) &= \frac{i}{\hbar} \int_{t_d}^{t_d+t} dt' \left(\frac{\pi}{\epsilon + \frac{i}{2\hbar}(t-t')} \right)^{3/2} \left\langle \phi_e^{(0)} \middle| \hat{\boldsymbol{d}}_e \middle| \boldsymbol{p}\left(t\right) \right\rangle \\ &\quad \times e^{-\frac{i}{\hbar} S_{st}(t,t')} \left\langle \boldsymbol{p}\left(t'\right) \middle| \hat{\boldsymbol{d}}_e.\boldsymbol{F}(t') \middle| \phi_e^{(0)} \right\rangle + c.c. \end{aligned} \tag{2.53}$$

where, $\boldsymbol{p}(t) = \boldsymbol{p}_{st}(t,t') - \frac{e}{c}\boldsymbol{A}(t)$ and $\boldsymbol{p}(t') = \boldsymbol{p}_{st}(t,t') - \frac{e}{c}\boldsymbol{A}(t')$ has been obtained from minimum coupling prescription (Eq. (2.31)). $\boldsymbol{A}(t)$ and $\boldsymbol{F}(t)$ are the instantaneous vector potential and the electric field of the probe pulse. It is also interesting to interpret the last equation in the frame of three-step model of atom. The first factor in Eq. (2.53) (reading from right to left) corresponds to a virtual ionization transition that occurs at time t', $d_{ion} \equiv \left\langle \boldsymbol{p}\left(t'\right) \middle| \hat{\boldsymbol{d}}_e . \boldsymbol{F}(t') \middle| \phi_e^{(0)} \right\rangle$, whereas the last factor corresponds to the virtual recombination of the electron with the initial bound state at a time t, $d_{rec} \equiv \left\langle \phi_e^{(0)} \middle| \hat{\boldsymbol{d}}_e \middle| \boldsymbol{p}\left(t\right) \right\rangle$. The interval $\tau = t - t'$ corresponds to the intermediate time that the electron spends in the virtual continuum Volkov states, between the absorption of n photons in the first step and the emission of the harmonic frequency $\Omega = n\omega$ in the last step. We may further assume that there is no significant depletion of the ground state population during the process. (However, if needed, this could be accounted for without difficulty by introducing in the amplitude the exponential decay factor: $e^{-(\gamma/2)(t+t')}$, where γ is the total ionization rate). To be specific, we choose for a linearly polarized $\boldsymbol{F}(t) = \hat{\boldsymbol{\epsilon}}\, F_0(t)\cos(\omega t)$, and

$$\boldsymbol{A}(t) = -\hat{\boldsymbol{\epsilon}} \left(\frac{cF_0\left(t\right)}{\omega} \right) \sin(\omega t) \tag{2.54}$$

To evaluate dipole of virtual ionization and recombination in Eq. (2.53), we need an initial electronic wave function $\phi_e^{(0)}$. The wave function of the active electron (usually in the highest occupied molecular orbital or HOMO) can be written either in the multi-center LCAO-MO (linear combination of atomic orbitals - molecular orbitals) form, or, by converting it into an equivalent single-center MO by appropriate transformations (e.g. [101, 102]). It is useful to note here that in the later form, it often suffices (e.g. for problems of interaction of molecules with long-wavelength electromagnetic fields, and in conjunction with the 'length gauge', used here) to retain only the asymptotic limit of the orbitals at distances away from the molecular center, without significant loss of accuracy. Thus, quite generally, let the unperturbed MO of the active electron at a given internuclear separation R to be given in the body fixed frame, by a single-center expansion:

$$\phi_e^{(bf)}(\boldsymbol{r}) = \sum_l C_l^{(m)} R_l(r) Y_{lm}(\hat{\boldsymbol{r}}) \tag{2.55}$$

where $C_l^{(m)}$ are the expansion coefficients, $R_l(r)$ are the radial waves of angular momentum l, $Y_{lm}(\hat{\boldsymbol{r}})$ are the spherical harmonics, and m is the *conserved* projection of the angular momentum of the electron along the molecular axis, that characterizes the MO.

Further, the molecular orbitals Eq. (2.55) is transformed to the space fixed system by using the Wigner transformation,

$$\begin{aligned} \phi_e^{(0)}(\boldsymbol{r}) &= \hat{\boldsymbol{D}} \phi_e^{(bf)}(\boldsymbol{r}) \\ &= \sum_l C_l^{(m)} R_l(r) \sum_\mu D^l_{\mu m}(\phi, \theta, \chi) Y_{l\mu}(\hat{\boldsymbol{r}}) \end{aligned} \tag{2.56}$$

In above $D^l_{\mu m}(\phi, \theta, \chi) = e^{-i\mu\phi} d^l_{\mu m}(\theta) e^{-im\chi}$ is the Wigner rotation matrix where (ϕ, θ, χ) are the Euler's angles which define the orientation of the molecular axis to the space fixed coordinate frame [103]. θ is the relative angle between new (space fixed) coordinate and

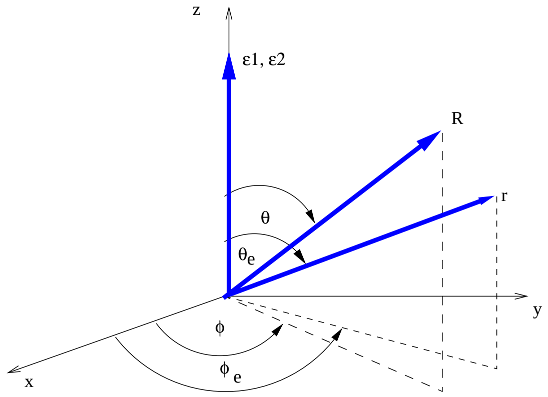

Figure 2.1: Schematic diagram defining the directions of the molecular axis, $\boldsymbol{R}$, electron position vector $\boldsymbol{r}$, and the pump and probe polarization ($\boldsymbol{\epsilon}_1$, $\boldsymbol{\epsilon}_2 \parallel z-$ axis). The fields are assumed to propagate along the y-axis.

the old (body fixed) coordinate, ϕ is the azimuthal angle with respect to new coordinate, whereas χ is the azimuthal angle with respect to old coordinate. The middle term of the Wigner matrix, $d^l_{\mu m}(\theta)$, is given by

$$\begin{aligned} d^l_{\mu m}(\theta) &= \sum_k \left[(-1)^{k-m+\mu} \frac{\sqrt{(l+m)!(l-m)!(l+\mu)!(l-\mu)!}}{(l+m-k)!(l-k-\mu)!k!(k-m+\mu)!} \right. \\ & \left. \times \left(\cos\frac{\theta}{2}\right)^{2l-2k+m-\mu} \left(\sin\frac{\theta}{2}\right)^{2k-m+\mu} \right] \end{aligned} \tag{2.57}$$

and their values for some low l have been tabulated e.g. in references [103, 104].

By using the electronic wavefunction in Eq. (2.56), the matrix element of (ionization) dipole along probe polarization direction appearing in Eq. (2.53), by taking $F(t')$ outside the integration, reads:

$$d_{ion}(t') = F(t') \sum_l C_l^{(m)} \sum_\mu D^l_{\mu m}(\phi, \theta, \chi) \left\langle e^{\frac{i}{\hbar}\boldsymbol{p}_{t'}.\mathbf{r}} \middle| \epsilon_\omega.\mathbf{r} \middle| R_l^m(r) Y_{l\mu}(\widehat{\boldsymbol{r}}) \right\rangle \tag{2.58}$$

Further, we expand $e^{\frac{i}{\hbar}\boldsymbol{p}_{t'}.\boldsymbol{r}}$ in spherical harmonics,

$$e^{\frac{i}{\hbar}\boldsymbol{p}_{t'}.\boldsymbol{r}} = \frac{(2\pi)^{3/2}}{\sqrt{p_{t'}r/\hbar}} \sum_{l'm'} (i)^{l'} J_{l'+1/2}\left(\frac{p_{t'}r}{\hbar}\right) Y_{l'm'}\left(\widehat{\boldsymbol{p}}_{t'}\right) Y_{l'm'}\left(\widehat{\boldsymbol{r}}\right) \tag{2.59}$$

and note that in this system of axes we have,

$$\epsilon_\omega.\boldsymbol{r} = r\sqrt{\frac{4\pi}{3}}\, Y_{10}(\widehat{\boldsymbol{r}}) \tag{2.60}$$

Note also that the instantaneous momentum $\boldsymbol{p}_{t'}$ can be either parallel or anti-parallel with respect to the direction of the field so that $\theta_{p_{t'}} = 0, \pi$ and $\phi_{p_{t'}} = 0$. Therefore, the spherical harmonics with the argument $\hat{\boldsymbol{p}}_{t'}$ can be simplified to $Y_{l'm'}(\hat{\boldsymbol{p}}_{t'}) = (\sigma)^{l'}\sqrt{\frac{2l'+1}{4\pi}}\delta_{m',0}$, with $\sigma = 1$ for $\theta_{p_{t'}} = 0$ and $\sigma = (-1)^{l'}$ for $\theta_{p_{t'}} = \pi$. Then, by substituting Eqs. (2.59) and (2.60) in Eq. (2.58), the ionization dipole reads

$$d_{ion}(t') = F(t')\frac{(2\pi)^{3/2}}{\sqrt{3p_{t'}/\hbar}}\sum_{l,l',\mu} C_l^{(m)} D^l_{\mu m}(\phi,\theta,\chi)(i\sigma)^{l'}\sqrt{(2l'+1)}\left\langle l'0\left|10\right|l\mu\right\rangle I_{l,l'}(t') \tag{2.61}$$

where, the radial integrals (m fixed) is defined by

$$I_{l,l'}(t') = \int_0^\infty J_{l'+\frac{1}{2}}(\frac{p_{t'}r}{\hbar})\, R_l(r) r^{-1/2}\, r\, r^2 dr \tag{2.62}$$

The Clebsch-Gordon coefficient in Eq. (2.61) implies that only the terms with $\mu = 0$ and $l' = l \pm 1$ survive in the sums (e.g. [103, 104])

$$\left\langle l'0\left|10\right|l\mu\right\rangle = \begin{cases} \left(\frac{3}{4\pi}\right)^{1/2}\left(\frac{l+1}{\sqrt{(2l+3)(2l+1)}}\right)\delta_{l'l+1}\delta_{0\mu} \\ \\ \left(\frac{3}{4\pi}\right)^{1/2}\left(\frac{l}{\sqrt{(2l+1)(2l-1)}}\right)\delta_{l'l-1}\delta_{0\mu} \end{cases}. \tag{2.63}$$

The ionization dipole can be simply written as

$$d_{ion}(t') = F(t')\sum_{l_i}\delta_{ion}\left(l_i, m; t'\right) \tag{2.64}$$

with

$$\begin{aligned} \delta_{ion}(l_i, m; t') &= \frac{2\pi}{\sqrt{2p_{t'}/\hbar}}\frac{C_{l_i}^{(m)} D^{l_i}_{0m}(\phi,\theta,\chi)}{\sqrt{(2l_i+1)}} \\ &\times\Big((i\sigma)^{l_i+1}(l_i+1)\, I_{l_i,l_i+1}(t') + (i\sigma)^{l_i-1} l_i\, I_{l_i,l_i-1}(t')\Big) \end{aligned} \tag{2.65}$$

In the two last equations, we replace the notation l with l_i, refers to initial momentum in ionization step, to distinguish it from that of recombination step.

Here we assume that the emitted harmonic is observed with its polarization along the same direction as the probe pulse polarization. (There is no difficulty, except lengthier algebra, to obtain the expression for the polarization direction orthogonal to it, but the former would give the dominant contribution (c.f. [2, §4.7]). Then, following an analogous calculation as above we get the recombination dipole as:

$$d_{rec}(t) = \sum_{l_r}\delta_{rec}\left(l_r, m; t\right) \tag{2.66}$$

with

$$\begin{aligned}\delta_{rec}(l_r,m;t) &= \frac{2\pi}{\sqrt{2p_t/\hbar}}\frac{C_{l_r}^{(m)}D_{0m}^{l_r*}(\phi,\theta,\chi)}{\sqrt{(2l_r+1)}}\\ &\times\Big((-i\sigma)^{l_r+1}(l_r+1)\,I_{l_r,l_r+1}(t)+(-i\sigma)^{l_r-1}l_r\,I_{l_r,l_r-1}(t)\Big) \quad (2.67)\end{aligned}$$

Above we introduce notation l_r for final momentum in recombination step. Substituting Eqs. (2.64) and (2.66) in Eq. (2.53) we obtain

$$D_e\left(t;t_d\right)=\frac{i}{\hbar}\sum_{l_i,l_r}\int_{t_d}^{t_d+t}dt'\left(\frac{\pi}{\epsilon+\frac{i}{2\hbar}\left(t-t'\right)}\right)^{3/2}\delta_{rec}(l_r,m;t)e^{-\frac{i}{\hbar}S_{st}(t,t')}F(t')\delta_{ion}(l_i,m;t')+c.c. \quad (2.68)$$

Further, by integrating over t' and Fourier transforming with respect to t by using Eq. (2.48), we obtain the HHG operator $T_e^{(n)}(\theta)$ at the frequency $\Omega=n\omega$,

$$T_e^{(n)}(\theta)=\sum_{l_i,l_r}d_{0,m}^{l_r}(\theta)\tilde{a}_{zz}^{(n)}(l_r,l_i;m)d_{0,m}^{l_i}(\theta) \quad (2.69)$$

with $\tilde{a}_{zz}^{(n)}(l_r,l_i;m)$ is the dynamic part of electronic dipole and given by

$$\begin{aligned}\tilde{a}_{zz}^{(n)}(l_r,l_i;m) &= F.T.\left[\frac{i}{\hbar}\int_{t_d}^{t_d+t}dt'\left(\frac{\pi}{\epsilon+\frac{i}{2\hbar}\left(t-t'\right)}\right)^{3/2}\frac{\delta_{rec}(l_r,m;t)}{D_{0m}^{l_r*}(\phi,\theta,\chi)}e^{-\frac{i}{\hbar}S_{st}(t,t')}\right.\\ &\left.\times F(t')\frac{\delta_{ion}(l_i,m;t')}{D_{0m}^{l_i}(\phi,\theta,\chi)}+c.c.\right] \quad (2.70)\end{aligned}$$

In Eq. (2.69), $d_{0m}^{l_r}(\theta)d_{0m}^{l_i}(\theta)=D_{0m}^{l_r*}(\phi,\theta,\chi)D_{0m}^{l_i}(\phi,\theta,\chi)$ arises from the geometric part of the operator. In this case, the exponential part of Wigner matrix in ionization part is canceled out by its conjugate in recombination part and therefore $D_{0m}^{l}(\phi,\theta,\chi)$ in both ionization and recombination part reduces to its middle term $d_{0,m}^{l}(\theta)$. The coefficients $\tilde{a}_{zz}^{(n)}(l_r,l_{ri};m)$ are evaluated by fast Fourier transforming [....] and taking the value at nth peak.

2.7 Evaluation the Radial Integration

Throughout this work, the radial part of electronic wave function is given by [105, 106]

$$R_l(r)=r^{\eta-1}e^{-p_Br} \quad (2.71)$$

with $\eta\equiv Z_c/p_B$ with Z_c is the core charge, and $p_B=\sqrt{2m_e\left|E_B\right|}/\hbar$ with E_B is binding energy.

The radial integrals (I's) appearing in the ionization dipole d_{ion} (Eq. (2.65)) and recombination dipole d_{rec} (Eq. (2.67)) can now be evaluated explicitly by using the integral formula [107]

$$
\begin{aligned}
\int_0^\infty e^{-\alpha x} J_\nu(\beta x)\, x^{\mu-1} dx \quad &= \quad \frac{\left(\frac{\beta}{2}\right)^\nu \Gamma(\nu+\mu)}{\sqrt{(\alpha^2+\beta^2)^{\nu+\mu}}\Gamma(\nu+1)} \\
&\quad \times F\left(\frac{\nu+\mu}{2}, \frac{1-\mu+\nu}{2}, \nu+1; \frac{\beta^2}{\alpha^2+\beta^2}\right) \qquad (2.72)
\end{aligned}
$$

where $F(a,b,c;x)$ is a hypergeometric function. To be noted that since the argument $x \equiv \frac{\beta^2}{\alpha^2+\beta^2} < 1$, the hypergeometric function is guaranteed to converge for all values of a, b, and c [108]. For ionization step, the radial integrations read

$$
\begin{aligned}
I_{l_i,l_i+1}(t') \quad &= \quad \frac{\left(\frac{p_{t'}}{2\hbar}\right)^{l+3/2} \Gamma(l_i + Z_c/p_B + 4)}{\sqrt{(P_B^2 + \left(\frac{p_{t'}}{\hbar}\right)^2)^{l_i+Z_c/p_B+4}}\Gamma(l_i+\frac{5}{2})} \\
&\quad \times F\left(\frac{l_i+Z_c/p_B+4}{2}, \frac{l_i-Z_c/p_B}{2}, l_i+\frac{5}{2}; \frac{\left(\frac{p_{t'}}{\hbar}\right)^2}{p_B^2+\left(\frac{p_{t'}}{\hbar}\right)^2}\right) \\
I_{l_i,l_i-1}(t') \quad &= \quad \frac{\left(\frac{p_{t'}}{2\hbar}\right)^{l_i-1/2} \Gamma(l_i + Z_c/p_B + 2)}{\sqrt{(p_B^2 + \left(\frac{p_{t'}}{\hbar}\right)^2)^{l_i+Z_c/p_B+2}}\Gamma(l_i+\frac{1}{2})} \\
&\quad \times F\left(\frac{l_i+Z_c/p_B+2}{2}, \frac{l_i-Z_c/p_B-2}{2}, l_i+\frac{1}{2}; \frac{\left(\frac{p_{t'}}{\hbar}\right)^2}{p_B^2+\left(\frac{p_{t'}}{\hbar}\right)^2}\right) \qquad (2.73)
\end{aligned}
$$

Exactly the same expressions hold for the radial integrals appearing in the recombination dipole $d_{rec}(l_r, m; t)$ throughout (except that l_i is replaced by l_r, and t' by t, in Eq. (2.73)).

2.8 Comparison with Other Mathematical Models: Adiabatic Versus Frozen Nuclei Approximations

To illustrate the distinct character of the present theory, we compare it with the ad hoc mathematical models. First we notice that in our adiabatic model, the nth order HHG signal at time t_d after pump pulse is given by

$$
S_A^{(n)}(t_d) = \sum_{J_0 M_0} \rho(J_0) \left| \left\langle \Phi_{J_0 M_0}(t_d,\theta) \left| T_e^{(n)}(\theta) \right| \Phi_{J_0 M_0}(t_d,\theta) \right\rangle \right|^2 \qquad (2.74)
$$

where A stands for adiabatic. In our derivation, the nuclei are assumed to rotate adiabatically during the probe interaction. The expectation value of the total dipole is therefore obtained from the total wavefunction, including nuclear wavefunction of the system. The signal for pure initial state $\Phi_{J_0 M_0}$ is given by the norm square of Fourier transform of the total dipole expectation value. The total signal is obtained by averaging the signal from all single initial wavepacket states with the Boltzmann weight corresponding to the initial temperature T.

Another model on HHG of aligned molecules was proposed by C.D. Lin and his colleagues [87, 88]. In their model, the molecule axis is restricted to lie fixed along the z-axis, whereas the laser's polarization makes a fixed angle θ with respect to it. The dipole expectation value was then calculated along and perpendicular to the molecular axis and then projected on to the laser polarization direction. The initial electronic wavefunction was given in Gaussian basis which is obtained from GAMESS (General Atomic and Molecular Electronic Structure System) code [109]. In contrast to the present model, the model of Lin *et al.* assumed that the total dipole expectation value did not take the whole molecular wavefunction into account, but was simply given by the electronic dipole $D_e\left(t_d\right)$, independent of the rotational wavepacket states. The HHG yield signal at time t_d after pump pulse for nth order was then obtained from [88, 110]

$$g_n\left(t_d\right) = \int \rho\left(\theta, t_d\right) \bar{g}_n(\theta) d\Omega \tag{2.75}$$

with $\rho\left(\theta, t_d\right)$ was the molecular axis distribution, and $\bar{g}_n(\theta)$ was the average intensity obtained by integrating the calculated intensity between $(n-1)$th and $(n+1)$th order of the aligned molecules. Mathematically, $\overline{g}_n(\theta)$ is given by the norm square of the Fourier transform of $D_e\left(t_d\right)$. In our notation (Eq. (2.49)), the frozen nuclei (FN) signals of their model therefore can be expressed as:

$$S_{FN}^{(n)}\left(t_d\right) = \sum_{J_0 M_0} \rho(J_0) \left\langle \Phi_{J_0 M_0}\left(t_d, \theta\right) \middle| \left| T_e^{(n)}(\theta) \right|^2 \middle| \Phi_{J_0 M_0}\left(t_d, \theta\right) \right\rangle \tag{2.76}$$

which differs significantly from the present results (Eq. (2.74)). The same model (Eq. (2.76)) was used by J.P. Marangos and colleagues [111], except they used atom-like wavefunctions as the initial electronic wavefunction and did not fix the molecular axis along a given z-axis [61, 111].

Using completeness relation of Eq. (2.28), the signal from frozen nuclei model can be written as:

$$\begin{aligned} S_{FN}^{(n)}\left(t_d\right) &= \sum_{J_0 M_0} \sum_{J_0' M_0'} \rho(J_0) \left\langle \Phi_{J_0 M_0}\left(t_d, \theta\right) \middle| T_e^{(n)}(\theta) \middle| \Phi_{J_0' M_0'}\left(t_d, \theta\right) \right\rangle \\ & \quad \times \left\langle \Phi_{J_0' M_0'}\left(t_d, \theta\right) \middle| T_e^{*(n)}(\theta) \middle| \Phi_{J_0 M_0}\left(t_d, \theta\right) \right\rangle \\ &= \sum_{J_0 M_0} \rho(J_0) \left| \left\langle \Phi_{J_0 M_0}\left(t_d, \theta\right) \middle| T_e^{(n)}(\theta) \middle| \Phi_{J_0 M_0}\left(t_d, \theta\right) \right\rangle \right|^2 + \\ & \quad \sum_{J_0 M_0} \sum_{J_0' \neq J_0, M_0' \neq M_0} \rho(J_0) \left| \left\langle \Phi_{J_0 M_0}\left(t_d, \theta\right) \middle| T_e^{(n)}(\theta) \middle| \Phi_{J_0' M_0'}\left(t_d, \theta\right) \right\rangle \right|^2 \end{aligned} \tag{2.77}$$

The first term of Eq. (2.77) is the diagonal terms showing the coherent HHG signal arising from the electron ionized from the initial state $\Phi_{J_0M_0}(t_d,\theta)$ recombines into the same final states. The second term of the last expression is the off-diagonal terms showing the HHG signal arising from the inelastic transitions where the electron ionized from the initial state $\Phi_{J_0M_0}(t_d,\theta)$ recombines into different final states $\Phi_{J_0'M_0'}(t_d,\theta)$. Such transitions lead to incoherent emission of frequencies differing from Ω by $\Delta J_0J_0'$ and should not contribute to the fully coherent high harmonic generation at the frequency Ω.

Still another model was proposed by C.B. Madsen and L.B. Madsen [89, 112]. They took laser polarization to lay along z-axis, whereas molecular axis made angle θ with respect to it. The initial electronic wavefunction was obtained from GAMESS code [109] and then projected on spherical harmonics to get the asymptotic form. As in the model of Lin *et al.*, the molecular rotation was assumed to be negligible under the probe pulse, and hence the total dipole expectation was given by the electronic dipole $D_e(t_d)$. The amplitude of nth harmonic at time t_d after the pump pulse was defined by

$$\bar{d}_n(t_d)=\int_0^\pi \rho(t_d,\theta)\,d_n(\theta)\sin\theta d\theta \tag{2.78}$$

with $d_n(\theta)$ was Fourier transform of the electronic dipole $D_e(t_d)$. They, however, went on to take the thermal average not at the level of probabilities, but at the level of the Fourier transform of the dipole expectation value (proportional to the emission 'amplitude') and defined the signal of nth harmonic (in the present notation) as the modulo square of the thermally averaged amplitude

$$S^{(n)}_{MM}(t_d)=\left|\sum_{J_0M_0}\rho(J_0)\left\langle\Phi_{J_0M_0}(t_d,\theta)\left|T^{(n)}_e(\theta)\right|\Phi_{J_0M_0}(t_d,\theta)\right\rangle\right|^2, \tag{2.79}$$

where MM stands for Madsen and Madsen. This mathematical expression can be expanded as

$$\begin{aligned}
S^{(n)}_{MM}(t_d) &= \left(\sum_{J_0M_0}\rho(J_0)\left\langle\Phi_{J_0M_0}(t_d,\theta)\left|T^{(n)}_e(\theta)\right|\Phi_{J_0M_0}(t_d,\theta)\right\rangle\right)\\
&\quad\times\left(\sum_{J_0'M_0'}\rho(J_0')\left\langle\Phi_{J_0'M_0'}(t_d,\theta)\left|T^{*(n)}_e(\theta)\right|\Phi_{J_0'M_0'}(t_d,\theta)\right\rangle\right)\\
&= \sum_{J_0M_0}(\rho(J_0))^2\left|\left\langle\Phi_{J_0M_0}(t_d,\theta)\left|T^{(n)}_e(\theta)\right|\Phi_{J_0M_0}(t_d,\theta)\right\rangle\right|^2\\
&\quad+\sum_{J_0M_0}\sum_{J_0'\neq J_0,M_0'\neq M_0}\rho(J_0)\rho(J_0')\left\langle\Phi_{J_0M_0}(t_d,\theta)\left|T^{(n)}_e(\theta)\right|\Phi_{J_0M_0}(t_d,\theta)\right\rangle\\
&\quad\times\left\langle\Phi_{J_0'M_0'}(t_d,\theta)\left|T^{*(n)}_e(\theta)\right|\Phi_{J_0'M_0'}(t_d,\theta)\right\rangle
\end{aligned} \tag{2.80}$$

There are some conceptual difficulties which arise in this model. First, as mentioned above the standard thermal averaging is done at the probability level, whereas the quantity $\left\langle \Phi_{J_0M_0}\left(t_d,\theta\right)\left|T_e^{(n)}(\theta)\right|\Phi_{J_0M_0}\left(t_d,\theta\right)\right\rangle$ which is thermally averaged in Eq. (2.79) is a transition amplitude and not a transition probability. Second, $T_e^{(n)}(\theta)$ is not a real quantity and therefore $\left\langle \Phi_{J_0M_0}\left(t_d,\theta\right)\left|T_e^{(n)}(\theta)\right|\Phi_{J_0M_0}\left(t_d,\theta\right)\right\rangle$ is also not a real quantity. Therefore, thermal averaging the last quantity defies the standard requirement of thermal averaging of real signals only. Third, a well defined thermally averaged signal invariably contains the weight linearly. On the other hand, Eq. (2.80) contains not only quadratic term of the weight but also non-vanishing interference between the thermal weights.

Note that the present theory (Eq. (2.74)) gives a coherent signal for the emission of the high harmonics with the usual thermal averaging taken at the probability level, where the two models, do not.

Chapter 3

Dynamic Alignment

The previous chapter derives the general expression of HHG signal. This chapter gives briefly the theory of dynamic alignment of linear molecules of a gas interacting with a linearly polarized short laser pulse and their detection by observing the harmonic signal due to the probe-pulse. Thus, it is required to obtain the nuclear rotational wavepackets and evaluate the HHG transition operator. We start with the Schrödinger equation of the system, the alignment degree and its thermal average, the type of alignment, and the related expectation values. The discussion then shifts to the short pulse alignment where the investigation is focused on some properties of the dynamic alignment, those are required for understanding the dynamic HHG signals. They include high order transition, Fourier transform, period, beat frequencies, and the contribution of each beat to the whole alignment signal. This chapter ends with the investigation on the effect of the probe pulse on the alignment degree.

3.1 Solving Schrödinger Equation of the System

The Schrödinger equation governing a molecule subject to an intense laser field can be written as (Eq. (2.25)):

$$i\hbar\frac{\partial}{\partial t}\Phi_{JM}(t) = \left(H_N^{(0)} + V_{N-L_1}(t)\right)\Phi_{JM}(t) \tag{3.1}$$

where $H_N^{(0)}$ is the field-free nuclear Hamiltonian of the molecule. Consider the molecule as a rigid rotor whose energy operator is $B\widehat{J}^2$ with B and $\widehat{J}$ are rotational constant and angular momentum operator, respectively. $V_{N-L_1}(t)$ is laser-molecule interaction (Eq. (2.21):

$$V_{N-L_1}(t) = -\boldsymbol{\mu}\cdot\boldsymbol{F}_1(t) - \frac{1}{2}\boldsymbol{F}_1(t) : \boldsymbol{\alpha} : \boldsymbol{F}_1(t) \tag{3.2}$$

For a linear symmetric top molecule subject to linearly polarized laser field, it can be expressed as [113, 10]:

$$\begin{aligned} V_{N-L_1}(t) &= -\frac{1}{2}\left(\alpha_{\parallel}\cos^2\theta+\alpha_{\perp}\sin^2\theta\right)\left\langle\varepsilon^2(t)\right\rangle \\ &= -\frac{1}{2}\left(\Delta\alpha\cos^2\theta+\alpha_{\perp}\right)\left\langle\varepsilon^2(t)\right\rangle \end{aligned} \tag{3.3}$$

In the last equation, $\Delta\alpha$ is the difference between parallel and perpendicular polarizability components with respect to the molecular axis. For a field with its oscillating frequency to be far removed from any molecular resonance and much bigger than either τ^{-1} or T^{-1} (with τ and T are pulse width and rotational period, respectively) we can write [114]:

$$\left\langle\varepsilon^2(t)\right\rangle = \frac{8\pi}{c}Ig(t)\left\langle\cos^2\omega t\right\rangle = \frac{4\pi}{c}Ig(t) \tag{3.4}$$

with I and $g(t)$ are peak intensity and pulse time profile, respectively.

By using Eqs. (3.3) and (3.4), the Hamiltonian (Eq. (3.1)) can be cast in the form [21, 38]:

$$\begin{aligned} H(t) &= B\hat{J}^2-\frac{4\pi}{c}Ig(t)\left(\Delta\alpha\cos^2\theta+\alpha_{\perp}\right) \\ &= B\left[\hat{J}^2-\left(\Delta\omega(t)\cos^2\theta+\omega_{\perp}(t)\right)\right] \\ &= B\left[\left(\hat{J}^2-\omega_{\perp}(t)\right)-\Delta\omega(t)\cos^2\theta\right] \end{aligned} \tag{3.5}$$

with $\Delta\omega(t)=(4\pi/c)Ig(t)\Delta\alpha=\Delta\omega\, g(t)$ and $\omega_{\perp}(t)=(4\pi/c)Ig(t)\alpha_{\perp}=\omega_{\perp}g(t)$ are dimensionless interaction parameters. The value of $\Delta\omega$ and $\omega_{\perp}$ are given by the simple recipe [39]:

$$\begin{aligned} \Delta\omega &= \frac{10^{-11}\Delta\alpha\left(\text{Å}^3\right)I\left(\text{W/cm}^2\right)}{B\left(\text{cm}^{-1}\right)} \\ \omega_{\perp} &= \frac{10^{-11}\alpha_{\perp}\left(\text{Å}^3\right)I\left(\text{W/cm}^2\right)}{B\left(\text{cm}^{-1}\right)}. \end{aligned} \tag{3.6}$$

θ is the angle between the molecular axis and the laser field polarization. In the following, we take $\mathbf{E}$ along z-axis so that θ is the polar angle.

The time dependent Schrödinger equation now can be cast in dimensionless form as

$$i\frac{\hbar}{B}\frac{\partial\Phi(t)}{\partial t} = \frac{H(t)}{B}\Phi(t) \tag{3.7}$$

It indicates that $\hbar/B$ plays a role of reduced time. The nuclear wavefunction $\Phi(t)$ can be expanded in term of a series in field-free rotor function $|JM\rangle$ with eigen energy $E_J =$

$\sum_i B_i[J(J+1)]^i$ [115]. For a given single initial state $|\Phi_{J_0M_0}(t)\rangle$, it reads

$$|\Phi_{J_0M_0}(t)\rangle = \sum_{JM} a_{JM}^{J_0M_0}(t)\; |JM\rangle\, exp\left(-i\frac{E_J t}{\hbar}\right). \tag{3.8}$$

The evolution of the expansion coefficient $a_{JM}^{J_0M_0}(t)$ can be found from differential equation [95]:

$$\begin{aligned} i\frac{\hbar}{B}\dot{a}_{JM}^{J_0M_0}(t) &= a_{JM}^{J_0M_0}(t)\left\langle JM\left|\left(\hat{J}^2-\omega_\perp(t)\right)\right|JM\right\rangle \\ &- \sum_{J'M'} a_{J'M'}^{J_0M_0}(t)\left\langle JM\left|\Delta\omega(t)\cos^2\theta\right|J'M'\right\rangle exp\left(-\frac{i\left(E_{J'}-E_J\right)t}{\hbar}\right) \end{aligned} \tag{3.9}$$

The Hamiltonian contains a constant term and angular-dependent term. The constant term, however, is just a coordinate-independent shift which does not introduce any torque and can be dropped for convenience. The $\cos^2\theta$ potential hybridizes rotational states $|JM\rangle$ of molecule, by mixing J's that differ by 0 and ±2 with fixed M.

$$\begin{aligned} i\frac{\hbar}{B}\dot{a}_{J,M}^{J_0M_0}(t) &= -a_{J-2,M_0}^{J_0M_0}(t)\Delta\omega(t)\,C_{J,J-2,M_0}\,exp\left(-i\left(E_{J-2}-E_J\right)t/\hbar\right) \\ &\quad -a_{J,M_0}^{J_0M_0}(t)\Delta\omega(t)\,C_{J,J,M_0} + a_{JM_0}^{J_0M_0}(t)\left(J(J+1)-\omega_\perp(t)\right) \\ &\quad -a_{J+2,M_0}^{J_0M_0}(t)\Delta\omega(t)\,C_{J,J+2,M_0}\,exp\left(-i\left(E_{J+2}-E_J\right)t/\hbar\right) \end{aligned} \tag{3.10}$$

The C_{J,J',M_0} coefficients are the matrix elements whose values are [103, 104]:

$$\begin{aligned} C_{J,J-2,M_0} &= \left\langle J,M_0\left|\cos^2\theta\right|J-2,M_0\right\rangle = \frac{1}{2J-1}\sqrt{\frac{\left((J-1)^2-M_0^2\right)\left(J^2-M_0^2\right)}{(2J-3)(2J+1)}} \\ C_{J,J,M_0} &= \left\langle JM_0\left|\cos^2\theta\right|JM_0\right\rangle = \frac{1}{3}+\frac{2}{3}\left[\frac{J(J+1)-3M_0^2}{(2J-1)(2J+3)}\right] \\ C_{J,J+2,M_0} &= \left\langle J,M_0\left|\cos^2\theta\right|J+2,M_0\right\rangle = \frac{1}{2J+3}\sqrt{\frac{\left((J+1)^2-M_0^2\right)\left((J+2)^2-M_0^2\right)}{(2J+1)(2J+5)}} \end{aligned} \tag{3.11}$$

By increasing J in $C_{J,J-2,M_0}$ by two, one obtains $C_{J+2,J,M_0} = C_{J,J+2,M_0}$, means that C_{J,J',M_0} is a real number. Eq. (3.10) can be simply written as

$$i\frac{\hbar}{B}\dot{\mathbf{a}}_{JM}^{J_0M_0}(t) = -\mathbf{M}\,\mathbf{a}_{JM}^{J_0M_0}(t) \tag{3.12}$$

with $\mathbf{M}$ is a three-diagonal matrix element. Eq. (3.12) is a time dependent differential equation system that in our case is solved by using sixth order Runge-Kutta method [116]. Once $a_{JM}^{J_0M_0}(t)$ is known, the wave function expression at any time can be found. Fig. 3.1 shows that $\left|a_{JM}^{J_0M_0}(t)\right|^2$ is almost constant after the pulse turn off and implies that all properties are conducted essentially by phase of the wave function.

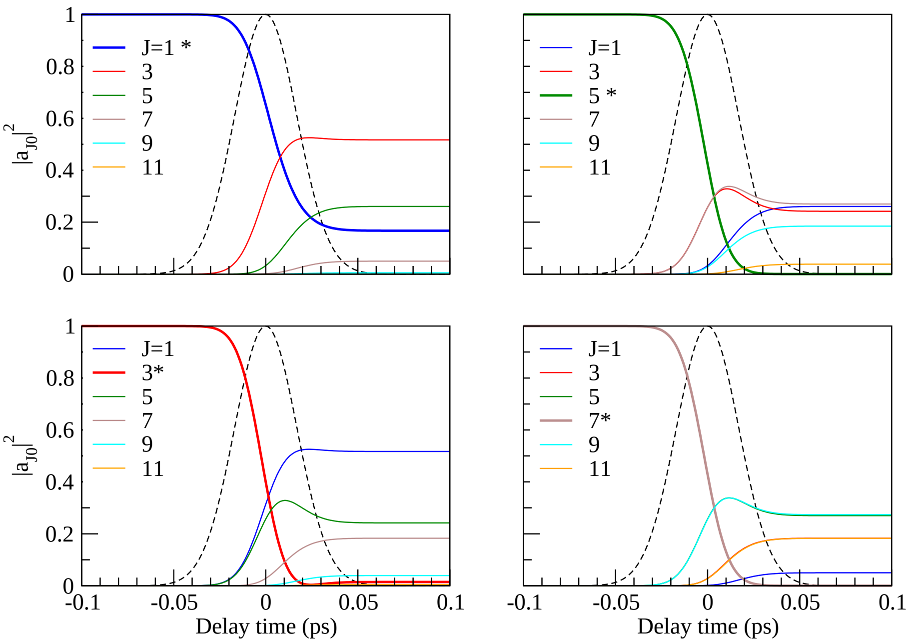

Figure 3.1: $|a_{J0}(t)|^2$ plotted as a function of time delay after peak of laser pulse, for various initial state, i.e. $\Phi(t=0) = |10\rangle$ (panel a), $\Phi(t=0) = |30\rangle$ (panel b), $\Phi(t=0) = |50\rangle$ (panel c), and $\Phi(t=0) = |70\rangle$ (panel d). The initial states are identified by thick line and *. We use here the laser field (dashed line) of intensity 0.5 $\times 10^{14}$ W/cm^2 with FWHM 40 fs subjected to molecule O_2.

3.2 Alignment Degree

It is convenience to express the degree of alignment in term of $\langle\langle\cos^2\theta\rangle\rangle$ [21]. For a linear molecule, with $E_J = BJ(J+1)$, the alignment degree for a given initial state $|J_0M_0\rangle$ reads:

$$\begin{aligned} \langle\cos^2\theta\rangle_{J_0M_0}(t) &= \left\langle\Phi_{J_0M_0}(t)\left|\cos^2\theta\right|\Phi_{J_0M_0}(t)\right\rangle \\ &= \sum_J a^{J_0M_0*}_{J-2,M_0}(t)\, a^{J_0M_0}_{JM_0}(t)\, C_{J,J-2,M_0}\, exp\left(-iB(4J-2)t/\hbar\right) \\ &\quad + \sum_J \left|a^{J_0M_0}_{JM_0}(t)\right|^2 C_{J,J,M_0} \\ &\quad + \sum_J a^{J_0M_0*}_{J+2,J_0}(t)\, a^{J_0M_0}_{JM_0}(t)\, C_{J,J+2,M_0}\, exp\left(-iB(4J+6)t/\hbar\right) \end{aligned} \tag{3.13}$$

By shifting $J \rightarrow J+2$ in the first term, Eq. (3.13) can be written in a symmetric form as:

$$\begin{aligned} \langle\cos^2\theta\rangle_{J_0M_0}(t) &= \sum_{J=2}^{J_{max}} a^{J_0M_0*}_{J-2,M_0}(t)\, a^{J_0M_0}_{JM_0}(t)\, C_{J,J-2,M_0}\, exp\left(-iB(4J+6)t/\hbar\right) \\ &\quad + \sum_J^{J_{max}} \left|a^{J_0M_0}_{JM_0}(t)\right|^2 C_{J,J,M_0} \end{aligned} \tag{3.14}$$

Table 3.1: Molecular properties of N_2, O_2, and CO_2 [117, 118, 119, 120, 121]

Molecule	$B\ (\mathrm{cm}^{-1})$	$D\ (\mathrm{cm}^{-1})$	$\alpha_{\parallel}\ (\mathrm{\AA}^3)$	$\alpha_{\perp}\ (\mathrm{\AA}^3)$	g_{even}	g_{odd}
N_2	1.989581	$5.67\,10^{-6}$	2.38	1.45	2	1
O_2	1.4297	$4.839\,10^{-6}$	2.35	1.21	0	1
CO_2	0.3902	$0.135\,10^{-6}$	4.01 - 4.11	1.97 - 1.93	1	0

$$+\sum_{J=0}^{J_{max}} a_{J+2,M_0}^{J_0M_0*}(t)\, a_{JM_0}^{J_0M_0}(t)\, C_{J,J+2,M_0}\, exp\left(iB(4J+6)t/\hbar\right)$$

with J_{max} is the maximum value of the excited states. The measurement of a value $\langle\cos^2\theta\rangle = 1$ gives an angular distribution perfectly peaked along $\theta = 0$ or $\theta = \pi$, $\langle\cos^2\theta\rangle = 0$ for a distribution peaked along $\theta = \pi/2$, and $\langle\cos^2\theta\rangle = 1/3$ for an isotropic distribution at all θ.

The system of interest is a molecular gas interacting with a linearly polarized laser pulse. Before interaction, the gas ensemble is assumed to be in thermal equilibrium, characterized by Boltzmann temperature T. In quantum picture, an ensemble is described by a statistical mixture of angular momentum state $|J_0M_0\rangle$ with $J_0 = 0, 1, 2, ...$ and $M = -J_0, -(J_0 - 1), ..., 0, ...(J_0 - 1), J_0$ whose distribution follows Boltzmann distribution

$$P_{J_0} \sim (2J_0+1)\, exp(-\frac{E_{J_0}}{kT}) \tag{3.15}$$

where E_{J_0} is the rotational energy of $|J_0M_0\rangle$ state. The $(2J_0+1)$ term accounts for the degeneracy within a given J_0 levels.

In the case of a molecule containing two identical nuclei, there is an additional factor g_{J_0} arising from nuclear spin statistics [93, 122]. This factor controls the relative weight between odd and even J states. Eq (3.15) now can be written as

$$P_{J_0} \sim g_{J_0}(2J_0+1)\, exp(-\frac{E_{J_0}}{kT}) \tag{3.16}$$

The properties of the linear molecules considered in this work, as well as the value of g_{J_0}, are listed in Tab. 3.1.

The alignment degree of the ensemble, at temperature T, can be found by averaging the alignment degree of a single initial state (3.14) over the Boltzmann distribution, including spin nuclear statistics (Eq. (3.16)), as

$$\langle\langle\cos^2\theta\rangle\rangle(t) = \frac{\sum_{J_0}\sum_{M_0=-J_0}^{J_0} g_{J_0}\,\langle\cos^2\theta\rangle_{J_0M_0}(t)\, exp\left(-BJ_0(J_0+1)/kT\right)}{\sum_{J_0}\sum_{M_0=-J_0}^{J_0} g_{J_0}\, exp\left(-BJ_0(J_0+1)/kT\right)} \tag{3.17}$$

where $\langle\cos^2\theta\rangle_{J_0M_0}(t)$ is the alignment degree for a single individual state and given by Eq. (3.14). The summation over J_0 is done over all $|J_0M_0\rangle$ populated at an initial temperature

T. Computationally, this summation is done until the result converges. The double brackets in $\left\langle\left\langle\cos^2\theta\right\rangle\right\rangle(t)$ stands for the expectation value with respect to the rotational wavepackets (inner brackets) and that with respect to the Boltzmann distribution (outer brackets). In what follows, Eq. (3.17) can be written as:

$$\left\langle\left\langle\cos^2\theta\right\rangle\right\rangle = \Sigma_{J_0M_0}\left[\rho\left(J_0\right)\left\langle cos^2\theta\right\rangle\right] \tag{3.18}$$

with $\rho(J_0) = \frac{1}{Z_P}e^{-E_{J_0}/kT}$ where k is the Boltzmann constant, T is the temperature, E_{J_0} is the rotational energy of the eigen state $|J_0M_0\rangle$, and $Z_p = \sum_{J_0}(2J_0+1)e^{-E_{J_0}/kT}$ is the rotational partition function. For the sake of simplicity, the indices J_0M_0 are dropped from $\left\langle\cos^2\theta\right\rangle$. For the same reason, we omit the argument t from $\left\langle\cos^2\theta\right\rangle$ and other expectation values.

It is important to note that the alignment degree is sensitive to molecular properties (i.e. rotational constant B and nuclear statistics g), pulse parameter (peak intensity I and pulse duration τ), and initial ensemble temperature (T).

3.3 Type of Alignment

Depending on the duration of applied laser pulse, there are three kinds of alignments, known as adiabatic alignment, dynamic alignment, and switched-off alignment [9]. In the first case, a laser field is slowly turned on and turned off such that the molecules can adiabatically adjust to the changing potential and rotate. The criterion 'slowly' can be satisfied by using a pulse longer than the rotational period, from which this alignment is also known as long pulse alignment. With a 'long' pulse, each eigenstate of the field-free Hamiltonian is guaranteed to evolve adiabatically during the interaction [21], from which this methods gets its name, adiabatic alignment. Adiabatic alignment can reach high alignment degree but it is lost once the pulse is turned off. The second schema is the alignment by using a 'short' pulse that is rapidly turned on and turned off. This alignment shows recurrence even after the pulse was turned off [23]. Unfortunately, this method can not reach an alignment degree as high as in adiabatic alignment. This alignment is also known as short pulse alignment (referring to the type of the applied pulse), non-adiabatic alignment (referring to the non-adiabatic interaction), or kick alignment (referring to the impulse interaction by the laser pulse). The third case is a 'mixture' between the long pulse and the short pulse method: an applied pulse is slowly turned on but rapidly turned off [24]. This is similar to a long pulse that is suddenly switched off at its peak. The last case takes all the benefits of the two previous cases and provides a dynamic alignment with high alignment degree. The recurring alignment of this case has been first seen experimentally for CO_2 molecule by observing the optical Kerr effect (OKE) signal [32].

For a Gaussian pulse $g(t) = exp\left(-(t/\tau)^2\right)$ with pulse duration $\tau \approx (3/5)\,FWHM$, the limit of 'short' and 'long' pulse depends on the ratio τ and $\hbar/B$. The earliest study was done by Ortigoso *et al.* [95] where they found an adiabatic alignment for $\tau \geq 10(\hbar/B)$ and a dynamic alignment for $\tau \ll (\hbar/B)$. Here we follow a simple description given by Spanner [123]. $\cos^2\theta$ hybridizes the rotational states that are characterized by $\Delta J = 0, \pm 2$. For a transition with lowest initial state $|0M\rangle \rightarrow |2M\rangle$, the energy difference is $\Delta E = 6B$. The time scale related to that transition is $\Delta t \approx \frac{2\pi\hbar}{6B} = \frac{\pi}{3}\left(\frac{\hbar}{B}\right)$. A more formal derivation using the phase difference [124, 9] gives $\tau_{long\,pulse} > \pi(\hbar/B)$, where the quantity $\pi(\hbar/B)$ is also known as the rotational period. For N_2 with $B = 1.989581\,\mathrm{cm}^{-1}$ we have $\hbar/B = 2.65474$ ps. Fig. 3.2 shows the expectation value $\langle\langle\cos^2\theta\rangle\rangle$ of N_2 of three different alignments. We use $\tau = \hbar/B$ for a long pulse and $\tau = 24$ fs for a short pulse.

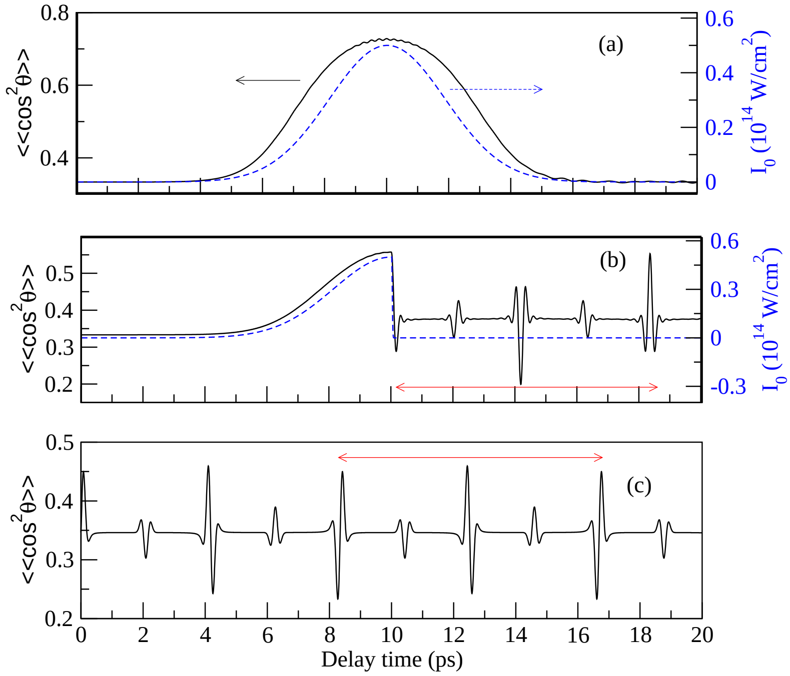

Figure 3.2: Alignment of N_2 with pulse intensity of $0.8\times10^{14}\mathrm{W/cm}^2$ and initial temperature 300 K. We use pulse duration $\tau = 2.6547$ ps (panel a), $\tau = 24$ fs (panel c), and a combination of $\tau = 2.6547$ ps for left side and $\tau = 24$ fs for right (panel b). Solid (black) line is $\langle\langle\cos^2\theta\rangle\rangle$ (left scale), whereas dashed (blue) line for pulse profile (right scale). Pulse profile for panel c is not shown. The red line shows a period .

3.4 Dynamics Alignment: Some Expectation Values

The common expression for alignment degree is $\langle\langle\cos^2\theta\rangle\rangle$. Fig. 3.5 shows dynamic alignment for three linear molecules with different nuclear statistics. The dynamics returns to its initial value after a ‘period’. Among the three molecules, N_2 is the lightest, whereas CO_2 is the heaviest. For heavier molecule we have the longer rotational period, T_{rev}, since it is proportional to the molecular mass or $T_{rev} \sim (1/B)$.

The revival signals for the three molecules generally mimic each other, but differ at

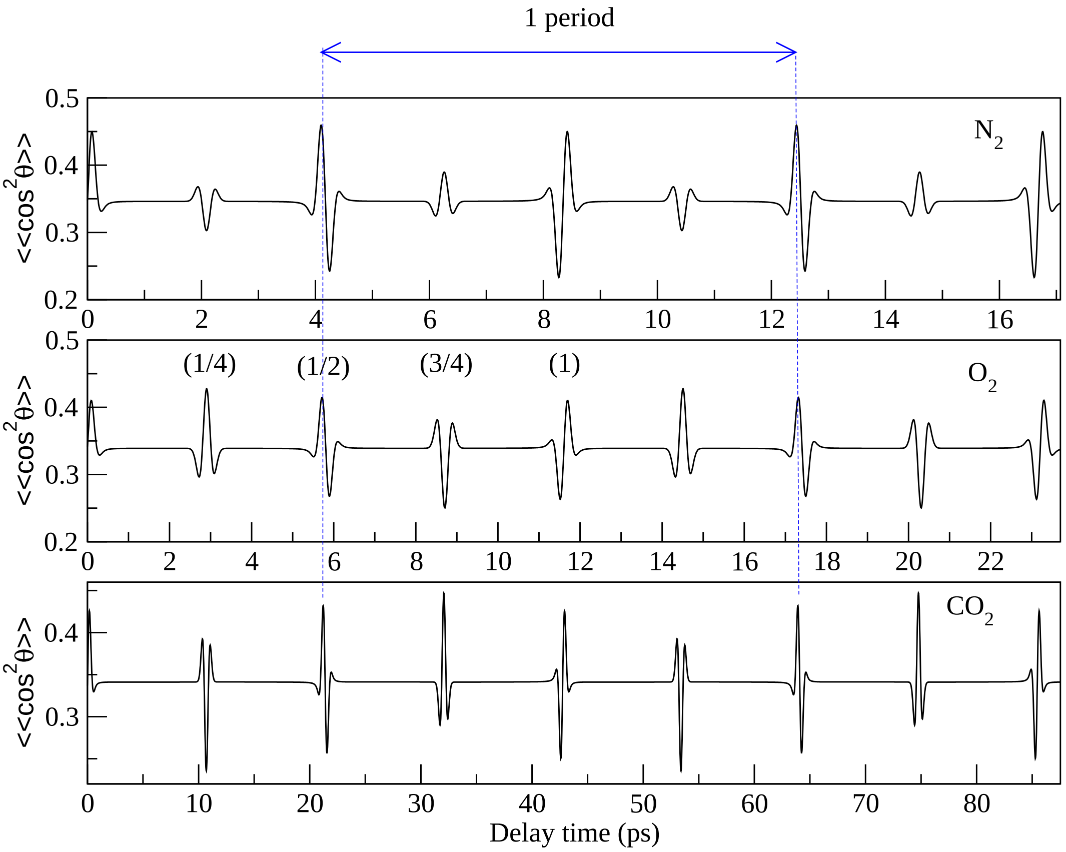

Figure 3.3: Dynamics alignment of N_2, O_2, and CO_2 with initial temperature 300 K. We use laser pulse with peak intensity of 0.5×10^{14} W/cm^2 for O_2 and 0.8×10^{14} W/cm^2 for N_2 and CO_2 with FWHM 40 fs.

$t = (2n-1)\frac{T_{rev}}{4}$ with n an integer. The signal at $t = (1/4)\,T_{rev}$ is peaked up for O_2 but peaked down for CO_2. The reverse situation occurs at $t = (3/4)\,T_{rev}$. The other fact is the alignment signal of N_2 at these times mimics that of CO_2 but with half the strength. This phenomenon is related to the initial ensemble population where O_2 has J_{odd} only, CO_2 has J_{even} only, and N_2 has both J with ratio $J_{even} = 2J_{odd}$.

To understand the above phenomena, we plot the molecular axis distribution (Fig. 3.4) which is given by

$$P\left(t_d, \theta\right) = \sum_{J_0 M_0} \rho\left(J_0\right) \left|\Phi_{J_0 M_0}\left(t_d, \theta\right)\right|^2 . \tag{3.19}$$

For calculating $\left|\Phi_{J_0 M_0}\left(t_d, \theta\right)\right|^2$, we use the series form of spherical harmonics [103]

$$\begin{aligned} Y_{lm}\left(\theta, \phi\right) &= \xi_{m0} e^{im\phi} \sqrt{\frac{2l+1}{4\pi} \frac{\left(l+|m|\right)!}{\left(l-|m|\right)!}} \frac{\sin^m \theta}{|m|!2^{|m|}} \\ &\quad \times F\left(-l+|m|, l+|m|+1, |m|+1; \sin^2 \frac{\theta}{2}\right) \end{aligned} \tag{3.20}$$

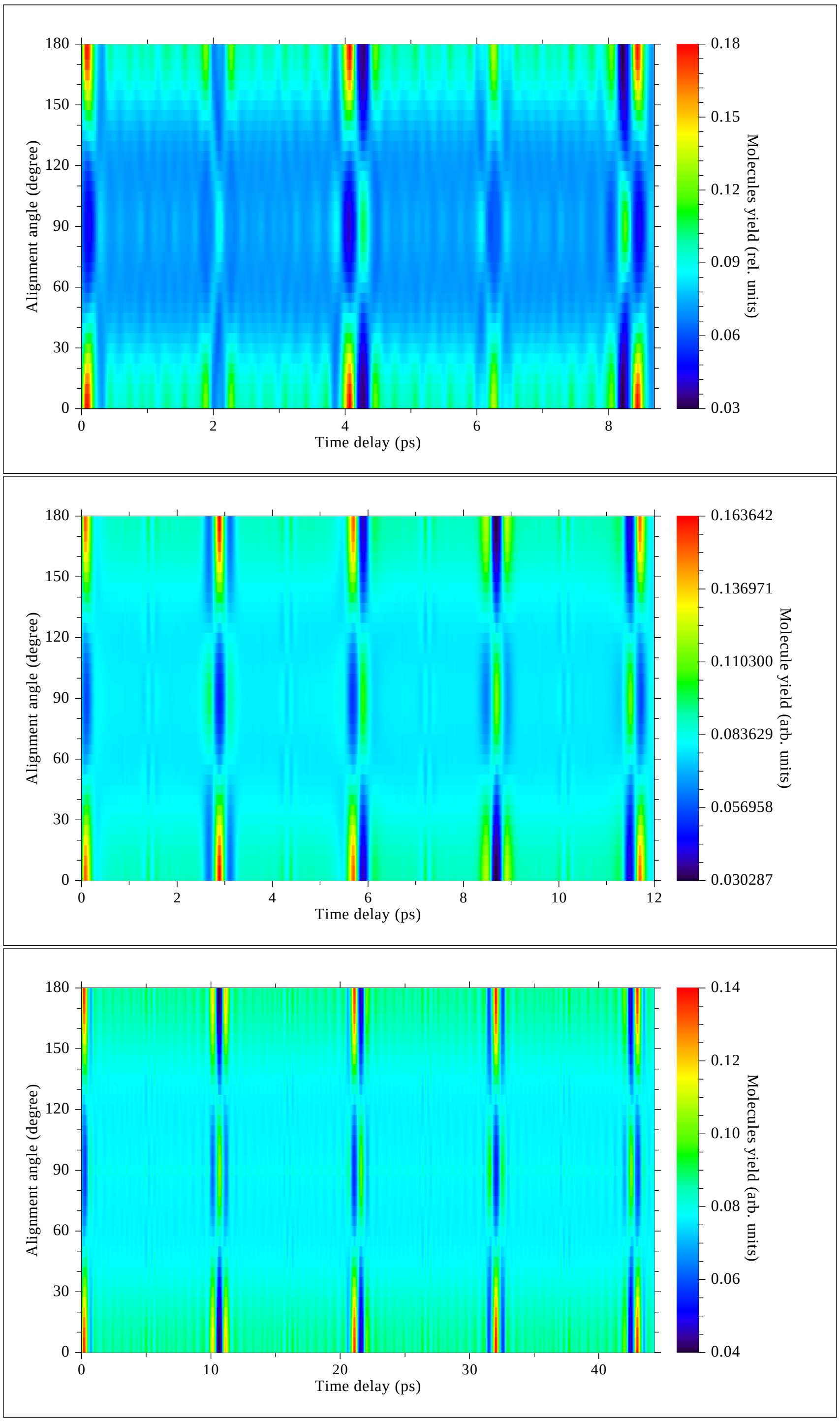

Figure 3.4: Molecular axis distribution of N_2 (upper panel), O_2 (middle panel), and CO_2 (lower panel). The laser parameters are similar with ones of Fig. 3.3.

where $F(a, b, c; x)$ is a hypergeometric function and

$$\xi_{m0} = \begin{cases} (-1)^m & \text{if } m > 0 \\ 1 & \text{if } m \leq 0 \end{cases} \tag{3.21}$$

By comparing three figures in Fig. 3.4, we can see that

- Molecular axis distribution revives with a period which is specific for the molecule and is related to the rotational constant of the molecule. This recurrence is the origin of alignment-revival shown in Fig. 3.3.
- The distribution pattern at $n\,(T_{rev}/2)$ are similar for all molecules, since the corresponding alignment degrees at these time delay have similar phase.
- The distribution pattern at $(2n-1)\frac{T_{rev}}{4}$ is specific for a molecule since the corresponding alignment degrees at these time delay have different phase. It will be shown later that these two last phenomena are related to the nuclear spin statistics.
- From three distributions, the distribution of N_2 has less yield at $\theta = 90^o$, due to the stronger peak intensity of the pump pulse.
- For O_2 and CO_2, there is a weak revival at $(2n-1)\frac{T_{rev}}{8}$, whereas it is absent for N_2.

Once the wave function is known, one can calculate any other expectation values. Here the calculation is done for $\langle\langle \sin^2\theta \rangle\rangle$ and $\langle\langle \sin^2 2\theta \rangle\rangle$. The expectation value of $\langle \sin^2\theta \rangle$ for single initial state $|J_0M_0\rangle$ can be expressed as:

$$\begin{aligned} \left\langle \sin^2\theta \right\rangle_{J_0M_0}(t) &= \left\langle \Phi_{J_0M_0}(t) \left| \sin^2\theta \right| \Phi_{J_0M_0}(t) \right\rangle \\ &= \sum_{J=2}^{J_{max}} a_{J-2,M_0}^{J_0M_0*}(t)\, a_{JM_0}^{J_0M_0}(t)\, D_{J,J-2,M_0}\, exp\left(-iB(4J+6)t/\hbar\right) \\ &\quad + \sum_{J}^{J_{max}} \left| a_{JM_0}^{J_0M_0}(t) \right|^2 D_{J,J,M_0} \\ &\quad + \sum_{J=0}^{J_{max}} a_{J+2,M_0}^{J_0M_0*}(t)\, a_{JM_0}^{J_0M_0}(t)\, D_{J,J+2,M_0}\, exp\left(+iB(4J+6)t/\hbar\right) \end{aligned} \tag{3.22}$$

Where D_{J,J',M_0} is given by [103]

$$\begin{aligned} D_{J,J-2,M_0} &= \left\langle JM_0 \left| \sin^2\theta \right| J-2, M_0 \right\rangle = -\frac{1}{2J-1}\sqrt{\frac{\left((J-1)^2 - M_0^2\right)\left(J^2 - M_0^2\right)}{(2J-3)(2J+1)}} \\ D_{J,J,M_0} &= \left\langle JM_0 \left| \sin^2\theta \right| JM_0 \right\rangle \\ &= \frac{\sqrt{(J-M_0-1)(J-M_0)(J-M_0+1)(J-M_0+2)}}{(2J-1)(2J+1)} \end{aligned} \tag{3.23}$$

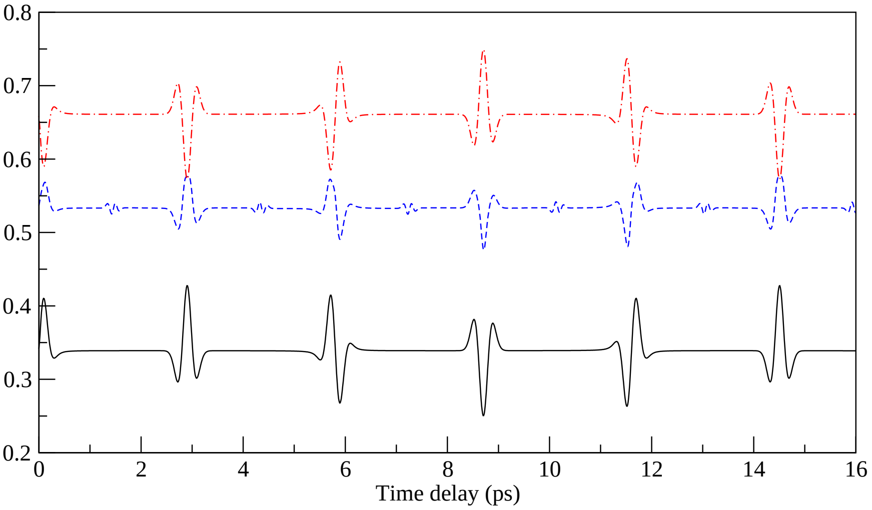

Figure 3.5: Some expectation value of O_2 at 300 K subject to laser field of intensity $0.5 \times 10^{14}\,\mathrm{W/cm^2}$ with FWHM 40 fs. Solid (black) line for $\langle\langle\cos^2\theta\rangle\rangle$, dashed dotted (red) line for $\langle\langle\sin^2\theta\rangle\rangle$, and dashed (blue) line for $\langle\langle\sin^2 2\theta\rangle\rangle$.

$$+\frac{\sqrt{(J+M_0-1)(J+M_0)(J+M_0+1)(J+M_0+2)}}{(2J+1)(2J+3)}$$

$$D_{J,J+2,M_0} = \left\langle JM_0 \left|\sin^2\theta\right| J+2, M_0\right\rangle = -\frac{1}{2J+1}\sqrt{\frac{\left((J+1)^2-M_0^2\right)\left((J+2)^2-M_0^2\right)}{(2J+1)(2J+5)}}$$

Unlike $\cos^2\theta$ and $\sin^2\theta$ that mix J's that differ by $0, \pm 2$ with fixed M, $\sin^2 2\theta$ hybridizes J's that differ by 0, $\pm 2 \pm 4$ with fixed M_0. The expectation value of $\langle\sin^2 2\theta\rangle$ is given by

$$\begin{aligned}
\left\langle\sin^2 2\theta\right\rangle_{J_0M_0}(t) &= \left\langle \Phi_{J_0M_0}(t) \left|\sin^2 2\theta\right| \Phi_{J_0M_0}(t)\right\rangle \\
&= \sum_{J=4}^{J_{max}} a^{J_0M_0*}_{J-4,M_0}(t)\, a^{J_0M_0}_{JM_0}(t)\, F_{J,J-4,M_0}\, exp\left(-iB(8J+20)t/\hbar\right) \\
&\quad + \sum_{J=2}^{J_{max}} a^{J_0M_0*}_{J-2,M_0}(t)\, a^{J_0M_0}_{JM_0}(t)\, F_{J,J-2,M_0}\, exp\left(-iB(4J+6)t/\hbar\right) \\
&\quad + \sum_{J}^{J_{max}} \left|a^{J_0M_0}_{JM_0}(t)\right|^2 F_{J,J,M_0} \qquad (3.24) \\
&\quad + \sum_{J=0}^{J_{max}} a^{J_0M_0*}_{J+2,M_0}(t)\, a^{J_0M_0}_{JM_0}(t)\, F_{J,J+2,M_0}\, exp\left(iB(4J+6)t/\hbar\right) \\
&\quad + \sum_{J=0}^{J_{max}} a^{J_0M_0*}_{J+4,M_0}(t)\, a^{J_0M_0}_{JM_0}(t)\, F_{J,J+4,M_0}\, exp\left(iB(8J+20)t/\hbar\right)
\end{aligned}$$

Where the matrix elements are given by

$$F_{J,J-4,M_0} = \left\langle JM_0 \left|\sin^2 2\theta\right| J-4, M_0\right\rangle$$

$$
\begin{aligned}
&= \frac{-4}{(2J-5)(2J-3)(2J-1)} \\
&\quad \times\sqrt{\frac{((J-1)^2-M_0^2)\left((J-2)^2-(M_0+1)^2\right)(J^2-M_0^2)(J-M_0-1)(J+M_0-3)}{(2J-7)(2J+1)}} \\
F_{J,J-2,M_0} &= \left\langle JM_0\left|\sin^2 2\theta\right| J-2,M_0\right\rangle \\
&= \frac{-4(2M_0+1)}{(2J-5)(2J-1)^2}\sqrt{\frac{((J-2)(J-1)-M_0(M_0+1))(J^2-M_0^2)(J-M_0-2)(J-M_0-1)}{(2J-3)(2J+1)}} \\
&\quad +\frac{4(2M_0+1)}{(2J-1)^2(2J+3)}\sqrt{\frac{\left(J^2-(M_0+1)^2\right)(J(J+1)-M_0(M_0+1))(J+M_0-1)(J+M_0)}{(2J-3)(2J+1)}} \\
F_{J,J,M_0} &= \left\langle JM_0\left|\sin^2 2\theta\right| JM_0\right\rangle \\
&= 4\frac{\sqrt{((J+1)^2-M_0^2)\left((J+2)^2-(M_0+1)^2\right)(J+M_0+1)(J+M_0+2)^2(J+M_0+3)}}{(2J+1)(2J+3)^2(2J+5)} \\
&\quad +4\frac{(2M_0+1)^2(J(J+1)-M_0(M_0+1))}{((2J-1)^2(2J+3))^3} \qquad (3.25) \\
&\quad +4\frac{\sqrt{\left((J-1)^2-(M_0+1)^2\right)(J^2-M_0^2)(J-M_0-2)(J-M_0-1)^2(J-M_0)}}{(2J-3)(2J-1)^2(2J+1)} \\
F_{J,J+2,M_0} &= \left\langle JM_0\left|\sin^2 2\theta\right| J+2,M_0\right\rangle \\
&= \frac{4(2M_0+1)}{(2J+3)^2(2J+7)}\sqrt{\frac{((J+1)^2-M_0^2)((J+2)(J+3)-M_0(M_0+1))(J+M_0+2)(J+M_0+3)}{(2J+1)(2J+5)}} \\
&\quad -\frac{4(2M_0+1)}{(2J-1)(2J+3)^2}\sqrt{\frac{(J(J+1)-M_0(M_0+1))\left((J+1)^2-(M_0+1)^2\right)(J-M_0+1)(J-M_0+2)}{(2J+1)(2J+5)}} \\
F_{J,J+4,M_0} &= \left\langle JM_0\left|\sin^2 2\theta\right| J+4,M_0\right\rangle \\
&= \frac{-4}{(2J+3)(2J+5)(2J+7)} \\
&\quad \times\sqrt{\frac{((J+1)^2-M_0^2)((J+3)^2-M_0^2)\left((J+3)^2-(M_0+1)^2\right)(J-M_0+4)(J+M_0+2)}{(2J+1)(2J+9)}}
\end{aligned}
$$

Figure 3.5 shows some expectation values of O_2. Like any linear operator, these expectation values also follow the summation rules, such as $\left\langle\sin^2\theta\right\rangle+\left\langle\cos^2\theta\right\rangle=1$ and $\left\langle\sin^2 2\theta\right\rangle = 4\left(\left\langle\cos^2\theta\right\rangle-\left\langle\cos^4\theta\right\rangle\right)=4\left\langle\sin^2\theta\cos^2\theta\right\rangle$.

3.5 Periods and Phase of Revival Structures

We consider a Gaussian pulse centered at $t_0=0$ with time profile $g(t)=exp\left(-t^2/\tau^2\right)$. For a short pulse with $\tau\rightarrow 0$, the time evolution of the initial wave function $|J_0M_0\rangle$ under Hamiltonian (Eq. (3.5)), can be approximated, up to order τ, by a propagator $S(t)=exp\left(-(i/\hbar)\int H(t')dt'\right)$ as [40, 114]

$$
\begin{aligned}
|\Phi_{J_0M_0}(t)\rangle &= exp\left(-(i/\hbar)\int H(t')dt'\right)|\Phi_{J_0M_0}(0)\rangle \\
&= \sum_{JM}|JM\rangle\langle JM|
\end{aligned}
$$

$$
\begin{aligned}
& \times exp\left(-(i/\hbar)\left(E_J t - \Delta\omega\cos^2\theta\int g(t')dt' - \omega_\perp\int g(t')dt'\right)\right)|J_0M_0\rangle \\
= & \sum_{JM}|JM\rangle\langle JM| \\
& \times exp\left(-(i/\hbar)\left(E_J t - B\Delta\omega\cos^2\theta G(t) - B\omega_\perp G(t)\right)\right)|J_0M_0\rangle \qquad (3.26)
\end{aligned}
$$

with $G(t)$ is given by

$$
\begin{aligned}
G(t) &= \int_{-\propto}^{t} exp(-t'^2/\tau^2)dt' \\
&= \sigma\frac{\sqrt{\pi}}{2}\left(1 + erf\left(\frac{t}{\tau}\right)\right) \qquad (3.27)
\end{aligned}
$$

Because $erf(12) \simeq 1$, so that for $t \geq 12\tau$ we obtain

$$
G(t \geq 12\tau) = \tau\sqrt{\pi} \qquad (3.28)
$$

and Eq. (3.26) can be written as

$$
\begin{aligned}
\Phi_{J_0M_0}(t \geq 12\tau) &= \sum_{JM}|JM\rangle\langle JM|\, exp\left(-(i/\hbar)(E_J - B\omega_\perp\tau\sqrt{\pi})t\right) \\
&\quad \times exp\left((i/\hbar)B\Delta\omega\tau\sqrt{\pi}\,\cos^2\theta\right)|J_0M_0\rangle \\
&= exp\left(-(i/\hbar)\tau V_0 t\right)\sum_{JM}|JM\rangle\langle JM|\, exp\left(-(i/\hbar)E_J t\right) \\
&\quad \times exp\left((i/\hbar)\tau V_1\cos^2\theta\right)|J_0M_0\rangle \qquad (3.29)
\end{aligned}
$$

where $V_0 = B\omega_\perp\sqrt{\pi}$ and $V_1 = B\Delta\omega\tau\sqrt{\pi}$. The wave function now consists of three component factors. The first component is just a phase shift component that is coordinate independent and is removed by the product with its conjugate. The second factor is phase dependent. The interaction is governed by the last one that can be expanded in a series, and we get

$$
\begin{aligned}
|\Phi_{J_0M_0}(t \geq 12\tau)\rangle &= exp\left(-(i/\hbar)\tau V_0 t\right)\sum_{JM}|JM\rangle\langle JM|\, exp\left(-(i/\hbar)E_J t\right) \\
&\quad \times\left[1 + \frac{i\tau V_1}{\hbar}\cos^2\theta - \frac{(\tau V_1)^2}{2!\hbar^2}\cos^4\theta - \frac{(\tau V_1)^3}{3!\hbar^3}\cos^6\theta + ...\right]|J_0M_0\rangle \\
&= exp\left(-(i/\hbar)\tau V_0 t\right) \\
&\quad \times\sum_{j=0,\pm1,\pm2,...} exp\left(-(i/\hbar)E_{J_0\pm2j}t\right)\, b^{J_0M_0}_{J_0+2j,M_0}\,|J_0+2j, M_0\rangle \qquad (3.30)
\end{aligned}
$$

Above, $|J_0M_0\rangle$ hybridizes to $|J_0+2j, M_0\rangle$ with $j = 0, \pm1, \pm2, ...$ as a results of interaction with $\cos^2\theta$ (cf. Hamiltonian of Eq. (3.3)). The expectation value of $\cos^N\theta$ can be expressed as

$$\begin{aligned}\left\langle \cos^N \theta \right\rangle_{J_0 M_0}(t) &= \left\langle \Phi_{J_0 M_0}(t) \left| \cos^N \theta \right| \Phi_{J_0 M_0}(t) \right\rangle \\ &= \sum_{N=0,\pm 2,\ldots,\pm N} \sum_{j} \Big[b^{J_0 M_0 *}_{J_0+2j,\, M_0} b^{J_0 M_0}_{J_0+2j+N,\, M_0} \\ &\quad \times exp\left(-i\left(E_{J_0+2j+N} - E_{J_0+2j}\right)\right) \Big] \qquad (3.31)\end{aligned}$$

The phase operator of the expectation of $\left\langle \cos^N \theta \right\rangle$ for any single initial state $|J_0 M_0\rangle$, of a system whose Hamiltonian is proportional to $\cos^2 \theta$, reads

$$\Delta\phi^{J_0}_{2,N} = 2\pi Bct \left(2NJ_0 + N^2 + N + 4Nj\right) \qquad (3.32)$$

For the system whose Hamiltonian is proportional to $\cos^n \theta$, the above equation reads:

$$\Delta\phi^{J_0}_{n,N} = 2\pi Bct \left(2NJ_0 + N^2 + N + 2nNj\right) \qquad (3.33)$$

Above $N = |\Delta J|_{max}$ and for $\left\langle \cos^2 \theta \right\rangle$ it is equal to 2. The quantity in the bracket is always even for any combination (N, J_0, j), therefore the full revival occurs whenever $2\pi Bct = \pi$ giving the well known revival period [25, 44, 45]

$$T_{rev} = \frac{1}{2Bc} \qquad (3.34)$$

where B and c are in cm^{-1} and cm/second, respectively.[1] For higher transition with $N > 2$, the quantities in the bracket is $(N/2)$ multiple of an even number. As a consequence, one should find also the shorter revival periods $T^N_{rev} = \frac{1}{(N/2)2Bc} = \frac{1}{NBc} = \frac{T_{rev}}{(N/2)}$, which is more general than Eq. (3.34). In Fig. 3.7, we show the dynamic expectation value of $\left\langle\left\langle \sin^2 2\theta \right\rangle\right\rangle$ of O_2, corresponding to $N = |\Delta J| = 0, 2, 4$. For $N = 0$, we obtain a constant signal (panel b). For $N = 2$, we obtain $T^{N=2}_{rev} = \frac{T_{rev}}{2/2} = T_{rev} = 11.6\,\mathrm{ps}$ (panel c). For $N = 4$, we obtain $T^{N=4}_{rev} = \frac{T_{rev}}{4/2} = \frac{T_{rev}}{2} = 5.8\,\mathrm{ps}$ (panel d). However, since transition with $N = 4$ also includes the lower one with $N = 2$, the observed period is $T_{rev} = 11.6\,\mathrm{ps}$ (panel a). These phenomena have been observed experimentally [71].

For phase matching that is independent of j and J_0, the condition $2\pi Bct2Nnj = 2\pi jk$ must be fulfilled, from which we get the lowest fractional revival

$$t_{fr} = \frac{k}{2BcNn} = \frac{k}{Nn} T_{rev} \qquad (3.35)$$

where k is an integer fulfills $k \leq Nn$. Eq. (3.35) shows that the fractional revival t_{fr} depends on the interaction Hamiltonian via n, molecular properties via $T_{rev} = 1/2Bc$, and the order of measured expectation value $\left\langle \cos^N \theta \right\rangle$ via N. As seen in Fig. 3.5, we find that

---

[1] In atomic units, Eq. (3.34) reads $T_{rev} = \frac{\pi}{2B}$. Another popular expression is $T_{rev} = \frac{1}{2B}$ with B is given in MHz.

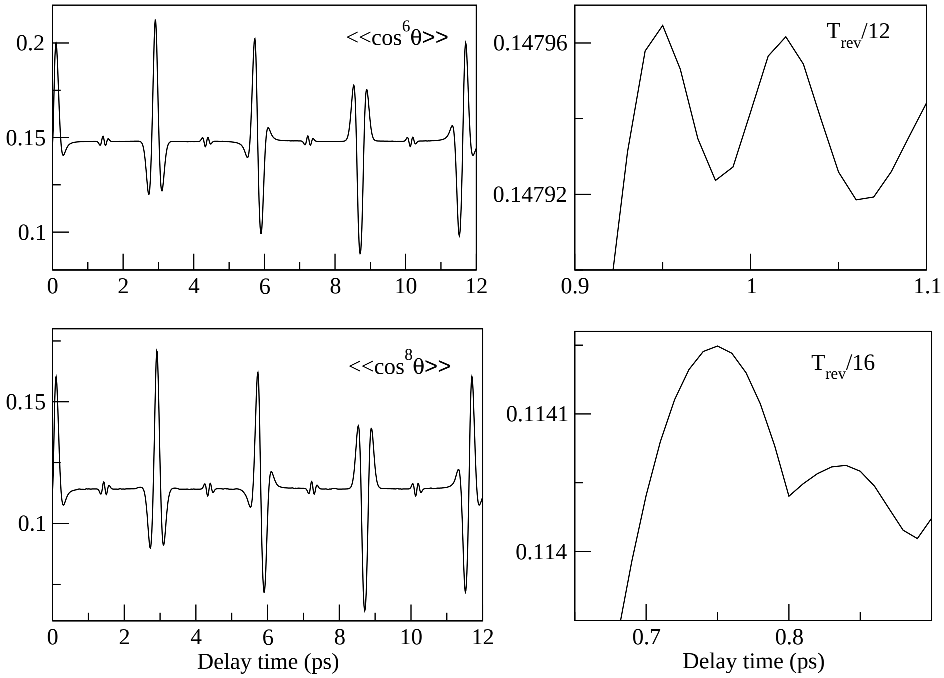

Figure 3.6: The lowest fractional revival of dynamics alignment of O_2 for $\langle\langle\cos^4\theta\rangle\rangle$ at $T_{rev}/12$ (upper panel) and $\langle\langle\cos^6\theta\rangle\rangle$ at $T_{rev}/16$ (lower panel). Note hat these fractional revivals are so small that does not appear in full figure. We use here the pulse of intensity 0.5×10^{14} W/cm^2 and FWHM 40 fs with initial temperature 300 K.

for interaction Hamiltonian $\cos^2\theta$ or $n = 2$, the lowest revival periods are $\frac{1}{4}T_{rev}$ for $\langle\cos^2\theta\rangle$ ($N = 2$) and $\frac{1}{8}T_{rev}$ for $\langle\sin^2 2\theta\rangle$ ($N = 4$), respectively. An interaction Hamiltonian with $\cos\theta$ or $n = 1$ shows that its dynamic orientation $\langle\cos\theta\rangle$ or $N = 1$ has the lowest revival at T_{rev} [125, 126]. Our result is more general and more complete than the previous results with models obeying the interaction Hamiltonian [45, 127, 128, 129].

In general, Eq. (3.35) always hold for any combination (N, n). The only restriction is coming from the fact that for large N the matrix element is so small that the fractional revival can not be observed. Fig. 3.6 shows a lowest fractional revival for $\langle\cos^6\theta\rangle$ ($N = 6$) and $\langle\cos^8\theta\rangle$ ($N = 8$).

We now consider the alignment degree $\langle\cos^2\theta\rangle$ ($N = 2$) generated by Hamiltonian $\cos^2\theta$ ($n = 2$). For this case, the relative phases of the revival structures (Eq. (3.32)) can be written as

$$\Delta\phi_{2,2}^{J_0}(t) = 2\pi\frac{t}{T_{rev}}\,(2J_0 + 3 + 2j) \tag{3.36}$$

It follows that $\Delta\phi_{2,2}^{J_0}(T_{rev}) - \Delta\phi_{2,2}^{J_0}(T_{rev}/2) = \pi\,(2J_0 + 3 + 2j)$. As a result, the wave packet at $t = T_{rev}/2$ is π out phase with respect to that at $t = T_{rev}$. Therefore the half-revival is nearly an exact mirror image of the full revival (that is independent of J_0 and j). It is also possible to compare the revival properties between J_{even} and J_{odd} at such time as

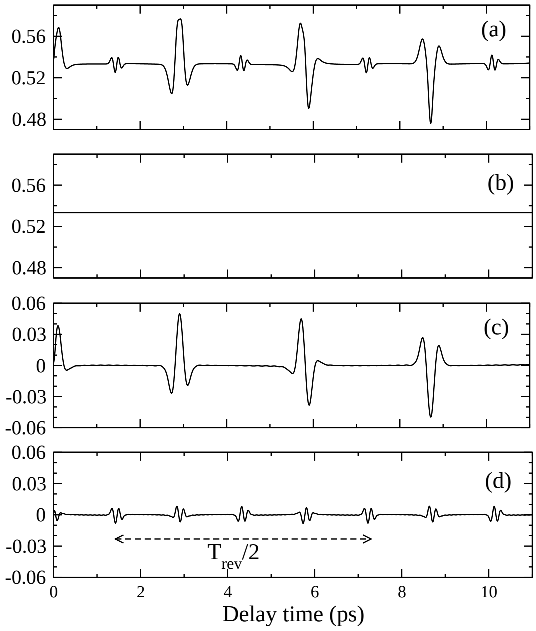

Figure 3.7: Revival structure of $\langle\langle \sin^2 2\theta \rangle\rangle$ of O_2, for the total frequency (panel a), with $\Delta J = 0$ only (panel b), with $\Delta J = \pm 2$ only (panel c), and with $\Delta J = \pm 4$ only (panel d). It is clear that the transition with $\Delta J = \pm 4$ has lowest fractional revival at $\frac{1}{8}T_{rev}$. Panel (d) also tells us that the transition with $\Delta J = \pm 4$ has rotational period $\frac{1}{2}T_{rev}$.

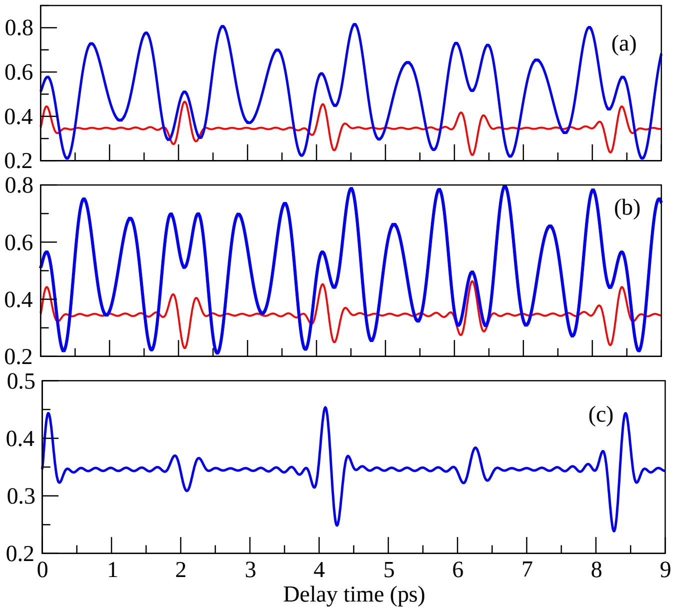

Figure 3.8: Dynamics alignment $\langle\langle \cos^2 \theta \rangle\rangle$ of N_2 with same parameter of Fig. 3.3. Panel (a): dynamics for single initial state $|50\rangle$ only (blue) and for all odd J with $J_{max} = 19$ (black). Panel (b): for $|60\rangle$ only (blue) and all even J with $J_{max} = 20$ (black). Panel (c): for all J with $J_{max} = 20$. We use here pulse of intensity 0.8×10^{14} W/cm^2 and FWHM 40 fs with initial temperature 300 K.

$$\begin{aligned}\Delta\phi_{2,2}^{J_0+1}(T_{rev}) \; - \; \Delta\phi_{2,2}^{J_0}(T_{rev}) \; &= \; 4\pi \\ \Delta\phi_{2,2}^{J_0+1}(T_{rev}/2) \; - \; \Delta\phi_{2,2}^{J_0}(T_{rev}/2) \; &= \; 2\pi \\ \Delta\phi_{2,2}^{J_0+1}(T_{rev}/4) \; - \; \Delta\phi_{2,2}^{J_0}(T_{rev}/4) \; &= \; \pi\end{aligned} \tag{3.37}$$

Eq. (3.37) tells us that at $\frac{1}{4}T_{rev}$ the phase of J_{even} is an exact mirror image of the phase of J_{odd}, as shown at Fig. 3.8. Thus, we predict that O_2 with J_{odd} only has a peak at $T_{rev}/4$, whereas CO_2 with J_{even} only has a valley at $T_{rev}/4$. For N_2 with $J_{even} = 2J_{odd}$, the revival at $T_{rev}/4$ is similar with one of J_{even} only but with half the intensity. Vice verse, we can predict the nuclear statistics of such a molecule by comparing the revival shape at $T_{rev}/2$ and $T_{rev}/4$. Let's define a modulation amplitude at half revival to be equal to the difference between peak and the average signal ($A_{1/2} = S_{1/2}^{top} - S_{1/2}^{ave}$). Similarly, a modulation amplitude at quarter revival is equal to the difference between peak and the average signal ($A_{1/4} = S_{1/4}^{top} - S_{1/4}^{ave}$). The amplitude at half revival is a sum of even and odd J contribution, and therefore $A_{1/2}$ is always positive. In contrast, the amplitude at quarter arises from their difference, and therefore $A_{1/4}$ can be positive (if it makes a top) or negative (if it makes an anti-top). Therefore, the existence of a top (an anti-top) at quarter revival is a sign that even (odd) J is dominant. We can deduce the nuclear ratio between the even and the odd J by using

$$\frac{J_{even}}{J_{odd}} = \frac{A_{1/2} - A_{1/4}}{A_{1/2} + A_{1/4}} \tag{3.38}$$

The dynamic signal of O_2 satisfies $A_{1/2} = A_{1/4}$ indicating absence of the even J. In contrast, $A_{1/2} = -A_{1/4}$ for CO_2, indicating absence odd J. For N_2, we have $A_{1/4} = -\frac{1}{3}A_{1/2}$, and hence we have $J_{even} : J_{odd} = 2 : 1$. This property can be used for detecting the existence of isotope in a molecular sample, as suggested recently [12].

3.6 Beat Frequencies

From Eq. (3.22), it is seen that the phase difference associated with $\langle\langle\cos^2\theta\rangle\rangle$ is $(B/\hbar)(4J+6)$. For B in cm^{-1}, the phase difference reads

$$\Delta\phi\,(J \to J \pm 2) = \; 2\pi Bc(4J+6) \tag{3.39}$$

with c in cm/second. According to Eq. (3.39), one can make a Fourier transform of $\langle\cos^2\theta\rangle$ using Bc as basis frequency and find a series of peaks at $(4J+6)$. Fig. 3.9 shows the Fourier transform of $\langle\langle\cos^2\theta\rangle\rangle$ of N_2, O_2, and CO_2. The spectrum of O_2 has peak series at $(10, 18, 26, ..)Bc = (4J_{odd}+6)Bc$, showing that O_2 has odd J only. In contrast, the peak series of CO_2 are located at $(6, 14, 22, 30, ...)Bc = (4J_{even}+6)$, showing that CO_2 has even J only. For N_2, we obtain a peak series $(6, 14, 22, 30, ...)Bc = (4J_{even}+6)$ is twice greater than that of $(10, 18, 26, ..)Bc = (4J_{odd}+6)Bc$. It means that both J present in N_2, where

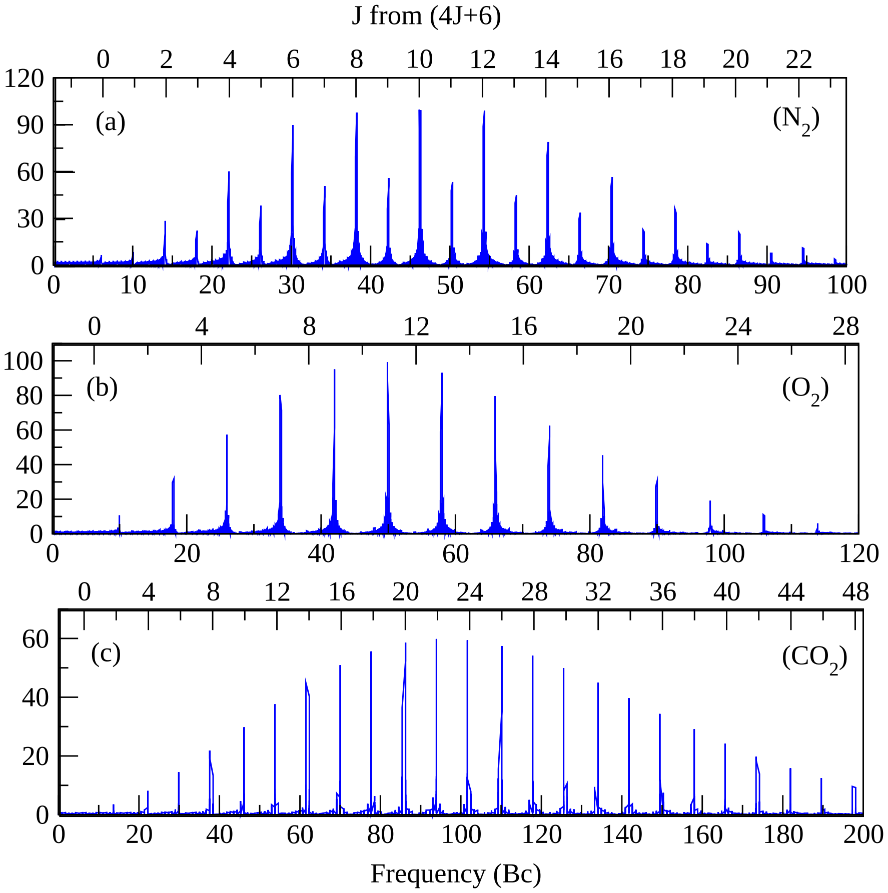

Figure 3.9: Fourier transform of dynamics alignment of Fig. 3.3, plotted using Bc as basis frequency (lower scale). Following $4J+6$ rule for $\langle\langle\cos^2\theta\rangle\rangle$, it is clear that the peak frequencies occur for J odd only for O_2, even only (CO_2), and both even and odd (N_2). The corresponding J values are shown in upper scale.

$J_{even} : J_{odd} = 2 : 1$. These conclusion are in agreement with that obtaining by investigating the dynamic signal.

For $\langle\langle\sin^2 2\theta\rangle\rangle$, there are two kinds of phase differences (Eq. (3.24)). The first one is related to the transition with $\Delta J = \pm 2$ and is expressed by Eq. (3.39). The second one is related to transition with $\Delta J = \pm 4$ and can be expressed as

$$\Delta\phi(J \to J \pm 4) = 2\pi Bc(8J + 20) \tag{3.40}$$

As a results, in addition to the series of $(4J + 6)$, the Fourier transform of $\langle\langle\sin^2 2\theta\rangle\rangle$ also has another series peaked at $(8J + 20)$, with beats at $\Delta J = 4$. Fig. 3.10 shows the Fourier transform of $\langle\langle\sin^2 2\theta\rangle\rangle$ of O_2.

It is seen from Fig. 3.10, that the first transition ($\Delta J = \pm 2$) reaches its maximum at $J_{max} = 11$, while the second one ($\Delta J = \pm 4$) at $J_{max} = 13$. This difference comes from the fact that the $\Delta J = 4$ transition requires $\Delta J = 2$ as an intermediate transition. As a

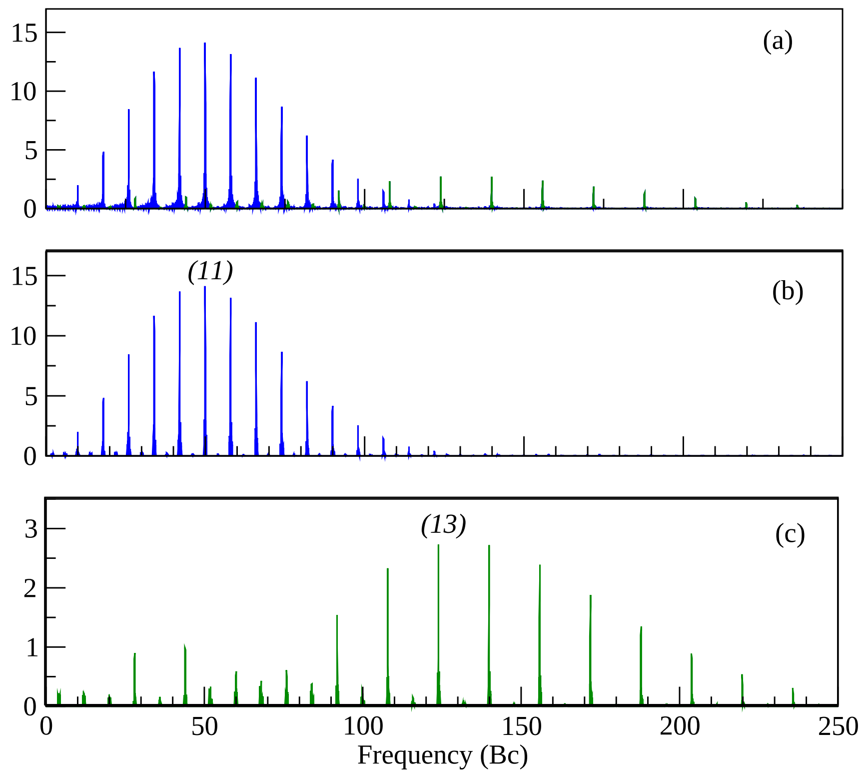

Figure 3.10: Fourier transform of $\langle\langle \sin^2 2\theta \rangle\rangle$ of O_2 : whole frequencies (panel a), beat frequencies coming from transition with $\Delta J = \pm 2$ only (panel b), and beats frequencies coming from transition with $\Delta J = \pm 4$ (panel c). We use here pulse of intensity 0.5×10^{14} W/cm^2 and FWHM 40 fs with initial temperature 300 K.

result, $\Delta J = 4$ comes one step after $\Delta J = 2$ transition. For O_2 containing J_{odd} only, one step means shifting J by 2 (see Eq. (3.24)).

From Fig. 3.10 one can also find that the intensity of the second transition is smaller than the first one. This fact is qualitatively related to the matrix element (Eq. (3.25)) where the element for the second transition is weaker than that of the first transition.

3.7 Temperature Effect

Consider that initially the molecule is in a state $|J_0 M_0\rangle$. The laser interaction will change the rotational state as $|J_0 M_0\rangle \rightarrow |J_0', M_0\rangle$. Unlike an up transition where the molecule can find any J_0' state, there is a restriction for a down transition so that $J_0' \geq M_0$. As a result, the new wave packet would consist of states with higher $J_0' \geq M_0$ (meaning that the vector of rotational angular momentum tends to lie in plane perpendicular to laser polarization direction). Since the rotational angular momentum is perpendicular to the internuclear axis in diatomic molecules, the condition $J_0' \geq M_0$ means that the molecular axis would tend to align in the direction of the laser polarization. This is the reason why the alignment angle after the laser interaction is always smaller than one before the interaction. In other words,

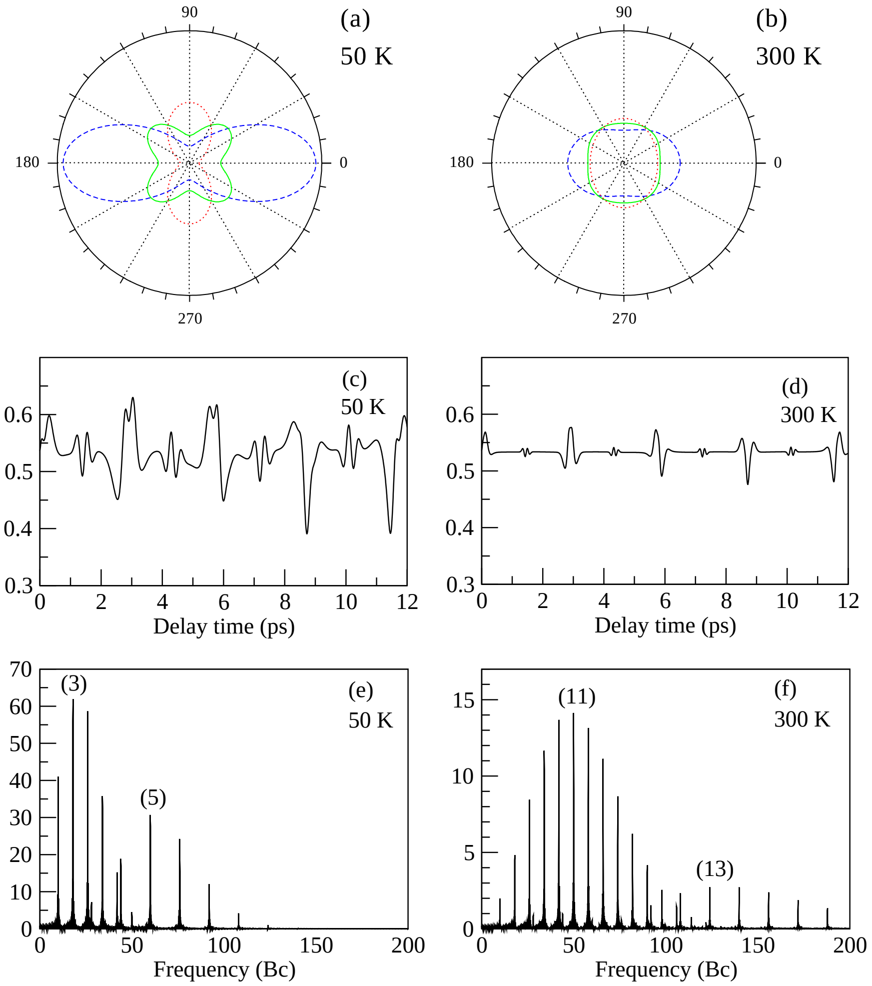

Figure 3.11: Signature of initial temperature of jet gas O_2, on the molecular axis distribution (panel a-b) of O_2, on the expectation value of $\langle\langle \sin^2 2\theta \rangle\rangle$ (panel c-d), and the Fourier spectrum (panel e-f). The molecular distribution on panel a-b are given at various time delay, i.e. at top alignment $t = 5.649\,\text{ps}$ (blue, dashed line), at average alignment $t = 5.812\,\text{ps}$ (green, solid line), and at anti-top alignment $t = 5.975\,\text{ps}$ (red, dotted line). The radii are in same scale. The peak intensity of laser field is $0.5 \times 10^{14}\,\text{W/cm}^2$ with FWHM 40 fs.

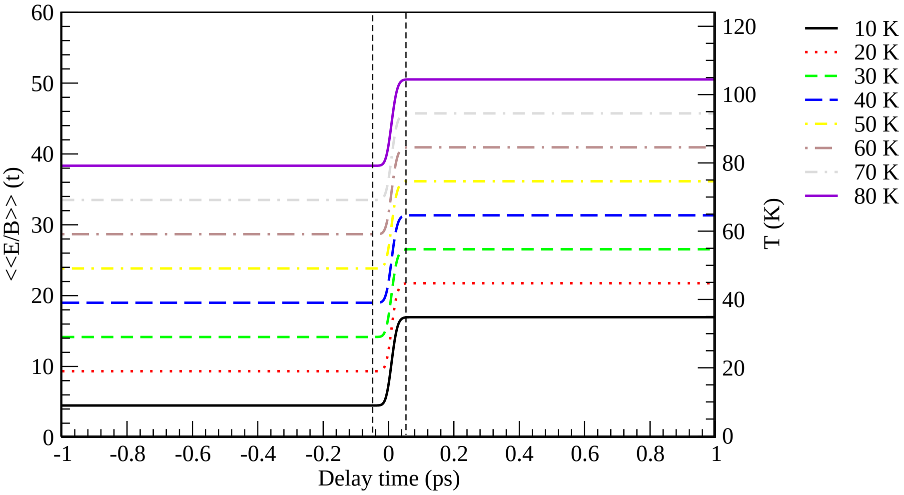

Figure 3.12: Mean energy of O_2 before and after interaction with the laser pulse, for different initial temperature. The peak intensity of laser field is 0.5×10^{14} W/cm^2 with FWHM 40 fs.

the alignment degree after the laser interaction is always higher than the one before the interaction. For a lower initial temperature we have lower initial M_0 so that the ratio J_0' to M_0 is higher. As consequences, for lower initial temperature the $\langle\langle\cos^2\theta\rangle\rangle$ and $\langle\langle\sin^2 2\theta\rangle\rangle$ values are higher. It means that for lower initial temperature, molecule is easier to align. Fig. 3.11(c-d) shows a dynamic plot of $\langle\langle\sin^2 2\theta\rangle\rangle$ for different initial temperatures. The corresponding molecular distributions are shown in Fig. 3.11(a-b).

It is also seen from Fig. 3.11 (e-f) that for a higher initial temperature, the Fourier transform has a higher J_{max}. The J_{max} value should reflect both the initial temperature and the 'rotational heating' due to laser interaction. A previous calculation [125] in fact showed that the J population depended on the laser intensity chosen.

Fig. 3.12 shows the mean energy before and after the interaction with the laser pulse. As expected, the figure shows increasing the mean energy of the molecule and therefore also raising up the 'temperature'. However, the final system is not an equilibrium system but a dynamical system that can not be characterized by a temperature rigorously.

3.8 Does Probe Pulse Affect The Dynamic Alignment?

To observe alignments of molecules by a pulse, one needs another pulse either e.g. to ionize molecule, or to dissociative the molecule, or to generate a high harmonic signal. (We call the first and second pulse as the pump and the probe pulse, respectively.)

So far it is assumed that the alignment is due to the pump pulse only, while the second one only gives the observed signal, without rotating it during the short duration of the probe pulse. To check the validity of this assumption, we directly compare here the alignment by the pump pulse only with that obtained by using both the pump and the probe pulses. For the second schema, we allow the possibility that the probe pulse also may rotate the

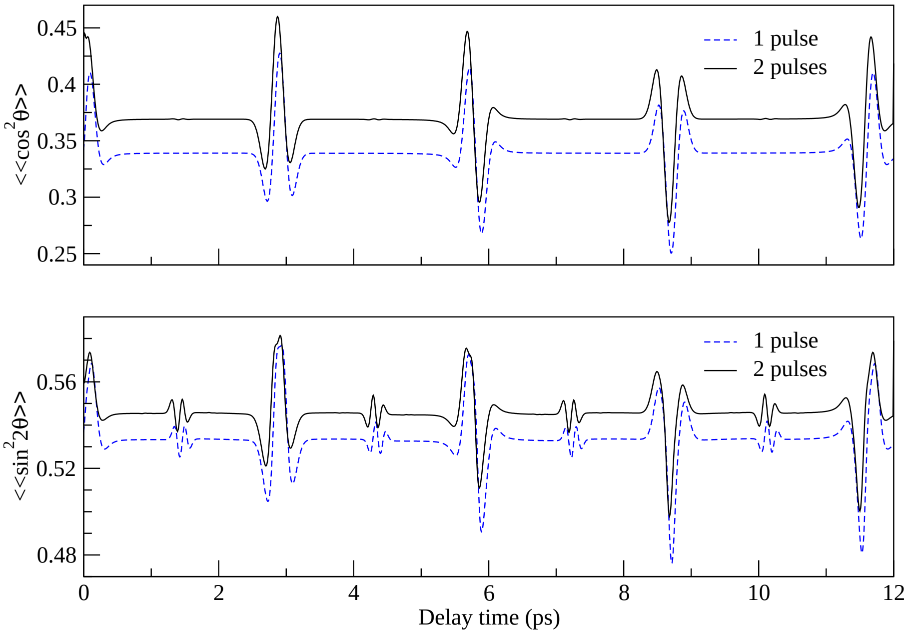

Figure 3.13: Dynamics alignment of $\langle\langle\cos^2\theta\rangle\rangle$ (upper panel) and $\langle\langle\sin^2 2\theta\rangle\rangle$ (lower panel) of O_2 at 300 K subject to laser pulses of $I_{pump} = 0.8 \times 10^{14}\mathrm{W/cm^2}$ and $I_{probe} = 1.7 \times 10^{14}\mathrm{W/cm^2}$ with FWHM 40 fs. We keep second pulse to interact for 40 fs.

molecule before generating the observed signal. The field is assumed to consist of the sum of the two pulses:

$$\begin{aligned} \varepsilon(t) &= \varepsilon_1(t) + \varepsilon_{20}(t-\Delta t) \\ &= \varepsilon_{10}\sqrt{g_1(t)}cos(\omega_1 t) + \varepsilon_{20}\sqrt{g_2(t-\Delta t)}cos(\omega_2(t-\Delta t)) \end{aligned} \tag{3.41}$$

and

$$\begin{aligned} \langle\varepsilon^2(t)\rangle &= \frac{1}{2}\varepsilon_{10}^2 g_1(t) + \frac{1}{2}\varepsilon_{10}^2 g_1(t-\Delta t) \\ &+2\varepsilon_{10}\varepsilon_{20}g_1(t)g_2(t-\Delta t)\,\langle(cos\,(\omega_1 t))\,(cos\,(\omega_2(t-\Delta t)))\rangle \end{aligned} \tag{3.42}$$

In the above indices 1 and 2 stand for pump and probe pulse, respectively. Δt is the delay time between the two pulses. For two pulses, dynamic alignment is characterized by pump and probe intensity, pump and probe time profiles, delay time between them, and interaction time (i.e. delay time between entering probe pulse and observing signal) [2].

The schema for alignment by the pump and the probe pulses is the following. The probe pulse is given Δt after the pump pulse. We let the probe pulse to interact with the molecule at a given time and then take the $\langle\langle\cos^2\theta\rangle\rangle$ value and plot as function of the delay time Δt,

---

[2] It is important to distinguish the present work with the alignment by using multi pulses, as first introduced theoretically by Leibscher *et. al.* [130, 34] and realized in a experiment by Lee *et. al.* [35, 131]. In their works, they aligned molecules with two (or more) sequential pulses but assumed the probe pulse to generate observed signal only and not enhance the alignment.

as shown in Fig. 3.13. We choose here the pulse duration as the interaction time between the probe pulse and the molecule. The results shows that the probe pulse does not change the dynamics of $\langle\langle\cos^2\theta\rangle\rangle$ except in two aspects. First, the probe pulse intensity adds up the intensity of the pump pulse and enhances the alignment process prepared and generated by the pump pulse, so that the expectation value of $\langle\langle\cos^2\theta\rangle\rangle$ with two pulses is higher than the one with pump pulse only. Second, the alignment enhancement by the probe pulse depends on the delay time between the two pulses and reaches a maximum when the slope of alignment degree is positive. This means that the degree of alignment is enhanced before its maximum and as a consequence reaches the maximum earlier than the alignment with one pulse only, as seen in Fig. 3.13.

In general, these aspects do not change the general characteristic of the dynamical signals and their Fourier transforms. Therefore, based on the above understanding, one can neglect the probe effect on the dynamics of alignment.

3.9 Comparison with Physical Observable

To compare the calculated alignment degree with the experimental results, one must take in to account the following factors. (1) The probe schema. As mentioned in chapter 1, the dynamic alignment can be probed through many ways such as ionization [26, 27], dissociation [25, 44], HHG [69, 70, 43], or optical Kerr effect (OKE) [28, 32]. (2) The alignment-dependence of interaction which depends on the HOMO of molecule, which will be investigated in chapter 4 and 5. (3) The geometric schema of experiment including the relative angle between the pump and the probe pulse, as will be investigated in chapter 7. (4) The medium properties, where some medium is dissipative [132]. In this work we limit our investigation for alignment in non-dissipative medium only.

Chapter 4

Application to Diatomic Molecules: Case N_2 and O_2

The main features of the dynamic HHG signals in N_2 and O_2 may be summarized as follows. It was observed by several authors [69, 133, 70, 72, 71, 82, 134, 43] that the delay-time HHG signal obtained in pump-probe experiments for N_2 strongly mimicked the usual alignment degree defined by the expectation value $\left\langle\left\langle\cos^2\theta\right\rangle\right\rangle(t_d)$, where t_d was the delay between the probe and the pump pulses. This result exhibited the well-known phenomenon of rotational revival [44, 9] including the full-revival with a period $T_{rev} = \frac{1}{2Bc}$, where B was the rotational constant [117], as well as a $\frac{1}{2}$-revival, and a $\frac{1}{4}$-revival, which were consistent with the behavior of $\left\langle\left\langle\cos^2\theta\right\rangle\right\rangle(t_d)$. In the case of O_2 also the analogous full-revival, $\frac{1}{2}$-revival, and the $\frac{1}{4}$-revival were observed but more interestingly also an unexpected $\frac{1}{8}$-revival appeared in the delay-time dependent signal [70, 43, 71, 134].

To fit the observational data of O_2, Itatani *et al.* [70] proposed empirically to take the expectation value $\left\langle\left\langle\sin^2 2\theta\right\rangle\right\rangle(t_d)$. Subsequently, a theoretical model of the HHG signal [88, 89] obtained a similar result for O_2 and $\left\langle\left\langle\cos^2\theta\right\rangle\right\rangle(t_d)$ for N_2, which appeared to justify the empirical models to fit the data in N_2 and O_2. These results also suggest that the maximum HHG signal of N_2 occurs when laser field polarization and molecular axis are parallel whereas the maximum signal of O_2 occurs when they make an angle 45^o.

Careful examination, however, has revealed surprising discrepancies with the above understanding of the HHG signals from N_2 and O_2. First: The HHG signal of N_2 observed by Itatani *et al.* [70] showed asymmetrically greater 'hill' (the difference between the top and the average signal) than 'valley' (the difference between the anti-top and the average signal). On the other hand, the $\left\langle\left\langle\cos^2\theta\right\rangle\right\rangle(t_d)$ for N_2 has the 'hill' almost equal to the 'valley'. Second: Kanai *et al.* [43] found that their experimental HHG signals for N_2 and O_2 could not be fitted by the expectation values of the operators $\cos^2\theta$ and $\sin^2 2\theta$, alone. They proposed additional operators involving *higher* powers of them, to fit the data empirically. Third: Miyazaki *et al.* [82, 135, 71] measured the dynamical HHG signals of N_2 and

Table 4.1: Explicit form of $d^l_{0m}(\theta)$ required for evaluating Eqs. (4.3) and (4.10) [103, 104]

l	N_2 $(m=0)$	O_2 $(m=1)$
0	1	-
2	$\frac{1}{2}\left(3\cos^2\theta - 1\right)$	$\sqrt{\frac{3}{2}}\,\sin\theta\cos\theta$
4	$\frac{1}{8}(3 - 30\cos^2\theta + 35\cos^4\theta)$	$-\frac{\sqrt{5}}{4}\,\sin\theta\cos\theta\left(3 - 7\cos^2\theta\right)$

O_2 and Fourier transformed their signals and discovered extra series of peaks, for both the N_2 and the O_2 spectra, that could not be associated with the respective Fourier transform of $\left\langle\left\langle\cos^2\theta\right\rangle\right\rangle(t_d)$ for N_2 and of $\left\langle\left\langle\sin^2 2\theta\right\rangle\right\rangle(t_d)$ for O_2.

In this chapter, we apply the present theory to the molecules N_2 and O_2 and obtain explicit analytic expressions for the HHG operators governing their pump-probe HHG signals. The analytic result is then used to analyze the recent experimental data obtained for non-adiabatically aligned molecules, in the usual case of parallel polarizations, and it provides a unified interpretation of the salient experimental features, observed.

4.1 Explicit Expression of HHG Transition Operator for N_2 and O_2

4.1.1 HHG operator $T_e^{(n)}(\theta)$ and dynamic signal for N_2

We start with N_2 whose HHG spectra have been extensively observed [69, 43, 70, 134]. N_2 has molecular symmetry σ_g [136], and we approximate its highest occupied molecular orbital (HOMO) by the asymptotic approximation obtained from single center wavefunction of the molecule [101] in the body-frame as

$$\phi_e^{(bf)}(\boldsymbol{r}) = \sum_{l=0,2,4} C_l^{(0)} R_l(r) Y_{l0}(\hat{\boldsymbol{r}}) \tag{4.1}$$

i.e. with $m = 0$ and $l = 0, 2, 4$ [105, 106].

Evaluating the HHG operator (Eq. (2.69)) for $m = 0$ and $l_i, l_r = 0, 2, 4$ for N_2 we get the results

$$T_e^{(n)}(\theta) = \sum_{l_i,l_r=0,2,4} \left\{ d^{l_r}_{00}(\theta)\tilde{a}^n_{zz}(l_r, l_i; 0)d^{l_i}_{00}(\theta) \right\} \tag{4.2}$$

Where $\tilde{a}^n_{zz}(l_r, l_i; 0)$ is the electronic part of the Fourier transform of the expectation value of the electronic dipole operator, given by Eq. (2.70), with the initial angular momentum l_i, the final angular momentum l_r, and the conserved projection of the angular momentum of the electron along the molecular axis, $m = 0$. Using the expressions for the reduced rotation matrices $d^l_{00}(\theta)$ from Tab. 4.1 and simplifying them, we may rewrite the HHG operator of

N_2 as a sum of powers of $\cos^2\theta$ only,

$$T_e^{(n)}(\theta) = b_0^{(n)} + b_1^{(n)}\cos^2\theta + b_2^{(n)}\cos^4\theta + b_3^{(n)}\cos^6\theta \tag{4.3}$$

where the coefficients $b_j^{(n)}$s read,

$$\begin{aligned}
b_0^{(n)} &= \tilde{a}_{zz}^{(n)}(0,0;0) - \frac{1}{2}\tilde{a}_{zz}^{(n)}(2,2;0) + \frac{3}{8}\tilde{a}_{zz}^{(n)}(4,4;0) - \frac{1}{2}\left(\tilde{a}_{zz}^{(n)}(0,2;0) + \tilde{a}_{zz}^{(n)}(2,0;0)\right) \\
&\quad + \frac{3}{8}\left(\tilde{a}_{zz}^{(n)}(0,4;0) + \tilde{a}_{zz}^{(n)}(4,0;0)\right) - \frac{3}{16}\left(\tilde{a}_{zz}^{(n)}(2,4;0) + \tilde{a}_{zz}^{(n)}(4,2;0)\right) \\
b_1^{(n)} &= \frac{3}{2}\tilde{a}_{zz}^{(n)}(2,2;0) - \frac{15}{4}\tilde{a}_{zz}^{(n)}(0,0;0) + \frac{3}{2}\left(\tilde{a}_{zz}^{(n)}(0,2;0) + \tilde{a}_{zz}^{(n)}(2,0;0)\right) \\
&\quad - \frac{15}{4}\left(\tilde{a}_{zz}^{(n)}(0,4;0) + \tilde{a}_{zz}^{(n)}(4,0;0)\right) - \frac{21}{16}\left(\tilde{a}_{zz}^{(n)}(2,4;0) + \tilde{a}_{zz}^{(n)}(4,2;0)\right) \\
b_2^{(n)} &= \frac{35}{8}\left(\tilde{a}_{zz}^{(n)}(0,4;0) + \tilde{a}_{zz}^{(n)}(4,0;0)\right) - \frac{55}{16}\left(\tilde{a}_{zz}^{(n)}(2,4;0) + \tilde{a}_{zz}^{(n)}(4,2;0)\right) \\
b_3^{(n)} &= \frac{150}{16}\left(\tilde{a}_{zz}^{(n)}(2,4;0) + \tilde{a}_{zz}^{(n)}(4,2;0)\right)
\end{aligned} \tag{4.4}$$

Thus, by using Eq. (2.49), the nth harmonic signal for N_2 becomes

$$\begin{aligned}
S^{(n)}(t_d) &= c_{00}^{(n)} + c_{01}^{(n)}\left\langle\left\langle\cos^2\theta\right\rangle\right\rangle(t_d) + c_{11}^{(n)}\left\langle\left\langle\cos^2\theta\right\rangle^2\right\rangle(t_d) + c_{02}^{(n)}\left\langle\left\langle\cos^4\theta\right\rangle\right\rangle(t_d) \\
&\quad + c_{12}^{(n)}\left\langle\left\langle\cos^2\theta\right\rangle\left\langle\cos^4\theta\right\rangle\right\rangle(t_d) + c_{03}^{(n)}\left\langle\left\langle\cos^6\theta\right\rangle\right\rangle(t_d) + c_{13}^{(n)}\left\langle\left\langle\cos^2\theta\right\rangle\left\langle\cos^6\theta\right\rangle\right\rangle(t_d) \\
&\quad + c_{22}^{(n)}\left\langle\left\langle\cos^4\theta\right\rangle^2\right\rangle(t_d) + c_{23}^{(n)}\left\langle\left\langle\cos^4\theta\right\rangle\left\langle\cos^6\theta\right\rangle\right\rangle(t_d) + c_{33}^{(n)}\left\langle\left\langle\cos^6\theta\right\rangle^2\right\rangle(t_d)
\end{aligned} \tag{4.5}$$

Or it is simply written as

$$S^{(n)}(t_d) = \sum_{j=0}^{3}\sum_{j'\geq j}^{3} c_{jj'}^{(n)}\left\langle\left\langle\cos^{2j}\theta\right\rangle\left\langle\cos^{2j'}\theta\right\rangle\right\rangle(t_d) \tag{4.6}$$

where the coefficients $c_{j,j'}^{(n)}$ are related to $b_j^{(n)}$ as follow

$$c_{j,j'}^{(n)} = \begin{cases} \left|b_j^{(n)}\right|^2 & \text{for } j = j' \\ 2Re\left(b_j^{(n)}b_{j'}^{(n)*}\right) & \text{for } j \neq j' \end{cases} \tag{4.7}$$

4.1.2 HHG operator $T_e^{(n)}(\theta)$ and dynamic signal for O_2

O_2 has the symmetry π_g [136], and thus we approximate its HOMO by the asymptotic approximation from single center molecule with $m = 1$ and $l = 2, 4$ [105, 106] in the body-frame

$$\phi_e^{(bf)}(\boldsymbol{r}) = \sum_{l=2,4} C_l^{(1)} R_l(r) Y_{l1}(\hat{\boldsymbol{r}}). \tag{4.8}$$

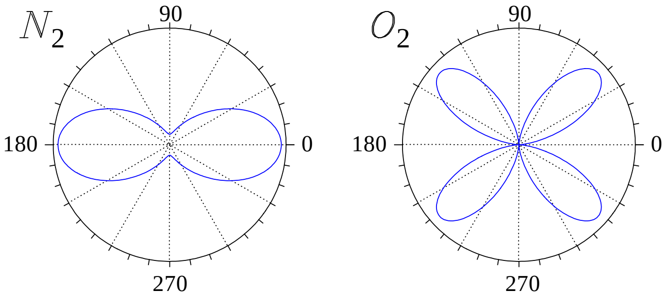

Figure 4.1: The calculated squared asymptotic wavefunction for N_2 (left panel) and O_2 (right panel).

The HHG operator (Eq. (2.69)) for O_2 therefore reduces to

$$T_e^{(n)}(\theta) \quad = \sum_{l_i, l_r = 2,4} \left\{ d_{01}^{l_r}(\theta) \tilde{a}_{zz}^{(n)}(l_r, l_i; 1) d_{01}^{l_i}(\theta) \right\} \tag{4.9}$$

By using the expressions for the reduced rotation matrices $d_{01}^{l}(\theta)$ from Tab. 4.1 and simplifying them, we may rewrite the HHG operator of O_2 as a sum of powers of $\sin^2\theta\cos^{2n}\theta$ only [1]

$$T_e^{(n)}(\theta) = b_1^{(n)} \sin^2\theta\cos^2\theta + b_2^{(n)} \sin^2\theta\cos^4\theta + b_3^{(n)} \sin^2\theta\cos^6\theta \tag{4.10}$$

where $b_j^{(n)}$ -coefficients are given by

$$\begin{aligned} b_1^{(n)} &= \frac{3}{2}\tilde{a}_{zz}^{(n)}(2,2;1) + \frac{45}{16}\tilde{a}_{zz}^{(n)}(4,4;1) - \frac{3}{4}\sqrt{\frac{15}{2}}\left(\tilde{a}_{zz}^{(n)}(2,4;1) + \tilde{a}^{(n)}(4,2;1)\right) \\ b_2^{(n)} &= -\frac{105}{8}\tilde{a}_{zz}^{(n)}(4,4;1) + \frac{7}{4}\sqrt{\frac{15}{2}}\left(\tilde{a}_{zz}^{(n)}(2,4;1) + \tilde{a}_{zz}^{(n)}(4,2;1)\right) \\ b_3^{(n)} &= \frac{245}{16}\tilde{a}_{zz}^{(n)}(4,4;1) \end{aligned} \tag{4.11}$$

Finally, by substituting operator expression (Eq. (4.10)) in Eq. (2.49), we obtain the nth harmonic signal of O_2

$$\begin{aligned} S^{(n)}(t_d) \quad = \quad & c_{11}^{(n)} \left\langle \left\langle \sin^2\theta\cos^2\theta \right\rangle^2 \right\rangle (t_d) + c_{12}^{(n)} \left\langle \left\langle \sin^2\theta\cos^2\theta \right\rangle \left\langle \sin^2\theta\cos^4\theta \right\rangle \right\rangle (t_d) \\ & + c_{13}^{(n)} \left\langle \left\langle \sin^2\theta\cos^2\theta \right\rangle \left\langle \sin^2\theta\cos^6\theta \right\rangle \right\rangle (t_d) + c_{22}^{(n)} \left\langle \left\langle \sin^2\theta\cos^4\theta \right\rangle^2 \right\rangle (t_d) \end{aligned}$$

---

[1] It is also possible to express the HHG operator of O_2 as

$$T_e^{(n)}(\theta) = b_I^{(n)} \cos^2\theta + b_{II}^{(n)} \cos^4\theta + b_{III}^{(n)} \cos^6\theta + b_{IV}^{(n)} \cos^6\theta$$

where $b_I^{(n)} = b_1^{(n)}$, $b_{II}^{(n)} = b_2^{(n)} - b_1^{(n)}$, $b_{III}^{(n)} = b_3^{(n)} - b_2^{(n)}$, and $b_{IV}^{(n)} = -b_3^{(n)}$. Expressing HHG operator of O_2 (and other molecules) in $\cos\theta$ powers gives a unified representation for HHG operators of aligned molecules. However, expressing HHG operator of O_2 in $\sin\theta\cos\theta$ power gives somewhat more physical insight [70]. We use the last expression in this work.

Table 4.2: The molecular properties of N_2 and O_2 used in this work. I_p is ionization potential, B is rotational constant of molecule, $\alpha_\parallel$ and $\alpha_\perp$ are parallel and perpendicular polarizability, and $C_l^{(m)}$'s are angular coefficient of electronic wave function.

	N_2	O_2	Ref.
HOMO	σ_g, $m=0$	π_g, $m=1$	[136, 117]
I_p (eV)	15.58	12.03	[105]
B (cm^{-1})	2.0	1.4377	[121]
$\alpha_\parallel\left(\text{Å}^3\right)$	2.38	2.35	[118]
$\alpha_\perp\left(\text{Å}^3\right)$	1.45	1.21	[118]
$C_0^{(m)}$	2.02	-	[105]
$C_2^{(m)}$	0.78	0.62	[105]
$C_4^{(m)}$	0.04	0.03	[105]

$$+c_{23}^{(n)}\left\langle\left\langle\sin^2\theta\cos^4\theta\right\rangle\left\langle\sin^2\theta\cos^6\theta\right\rangle\right\rangle(t_d)+c_{33}^{(n)}\left\langle\left\langle\sin^2\theta\cos^6\theta\right\rangle^2\right\rangle(t_d) \quad (4.12)$$

Or it is simply written as

$$S^{(n)}(t_d)=\sum_{j=1}^{3}\sum_{j'\geq j}^{3}c_{j,j'}^{(n)}\left\langle\left\langle\sin^2\theta\cos^{2j}\theta\right\rangle\left\langle\sin^2\theta\cos^{2j'}\theta\right\rangle\right\rangle(t_d) \quad (4.13)$$

Above, coefficients $c_{j,j'}^{(n)}$ are related to $b_j^{(n)}$ coefficients of Eq. (4.11) through Eq. (4.7).

Eq. (4.6) [Eq. (4.13)] is an exact expression of dynamic HHG signal of N_2 [O_2] at time t_d after the pump pulse. The value of $\langle\langle f(\theta)\rangle\rangle$ depends on the pump parameters, the initial temperature, and the molecular properties such as polarizability, nuclear spin statistics, and molecular rotational constant. We note that, in general, the value of $\langle\langle f(\theta)\rangle\rangle$ decreases with increasing orders of $f(\theta)$. On the other hand, $c_{j,j'}^{(n)}$ coefficient depends on the probe parameters and the molecular properties such as ionization potential and HOMO symmetry. As mentioned above, $c_{j,j'}^{(n)}$ depends on $\tilde{a}_{zz}^{(n)}(l_r,l_i;m)$ through $b_j^{(n)}$. It will be shown later that $\tilde{a}_{zz}(l_r,l_i;m)$ depends on (l_r,l_i) such that a higher (l_r,l_i) gives a weaker signal. Therefore the value of $c_{j,j'}^{(n)}$ is reduced by increasing j and/or j'. Since both$\langle\langle f(\theta)\rangle\rangle$ and $c_{j,j'}^{(n)}$ decrease with increasing term's order, therefore only the lowest order terms of Eqs. (4.6) and (4.13) are significant for the calculated HHG signal.

4.2 HHG Spectra

We first performed the calculation of HHG spectrum, i.e. harmonic signals as a function of their order. The recent experiment by Itatani *et al.* [70] showed that, among other steps, the recombination step played a greater role in the alignment dependence of HHG signal of N_2 and O_2. In other experiment by Miyazaki and his colleagues [69], it was seen that the

HHG spectrum of N_2 had a minimum at $n = 9$.[2] In addition, Miyazaki and his colleagues also saw that the signal of aligned N_2 was greater than the one of non-aligned N_2. This sub chapter is addressed to understand the three above phenomena.

To investigate the results of Itatani *et al.*, we first calculate $\tilde{a}_{zz}(l_r, l_i; m)$ which is the electronic part of the Fourier transform of the expectation value of the electronic dipole operator (see Eq. (2.70)). In real computation, we use the molecular properties which are shown in Tab. 4.2. The calculated spectra are shown in Figs. 4.2 and 4.3 for N_2 and O_2, respectively. For the given parameters, it is found that $\gamma < 1$ for both N_2 and O_2, allows us to describe the HHG process in the frame of three-step model. It can be seen from the figures that the shape of the spectrum and the position of its minima depend on the initial and the final angular momentum, implying that the whole spectrum strongly depends on nature of the HOMO molecular. A more careful examination of the figures shows that the final angular momentum has a stronger effects than the initial momentum. For N_2 (Fig. 4.2), $l_r = 0$ gives a minimum at $n = 27$ (whatever the value of l_i is). On the other hand, $l_r = 2$ gives a minimum at $n = 19$ and $l_r = 4$ gives a minimum at $n = 9$. For O_2 (Fig. 4.3), the minima occur at $n = 19$ for $l_r = 2$ and $n = 9$ for $l_r = 4$. This means that the recombination step plays a greater role in the alignment dependence of HHG signal. In contrast, the ionization step plays a lesser role or its role is diminished by the intermediate acceleration step. These behaviors are in agreement with the experiment by Itatani *et al.* [70]. In fact, Figs. 4.2 and 4.3 also show that the value $\tilde{a}_{zz}(l_r, l_i; m)$ depends on (l_r, l_i) such that a lower (l_r, l_i) gives a stronger spectrum. It can be easily understood because $\tilde{a}_{zz}(l_r, l_i; m)$ depends on $C_{l_r}^{(m)} C_{l_i}^{(m)}$, and $C_l^{(m)}$ of N_2 and O_2 decrease with increasing l.

---

[2] The term 'minimum' refers to the harmonic order its signal is weaker than that of neighboring order.

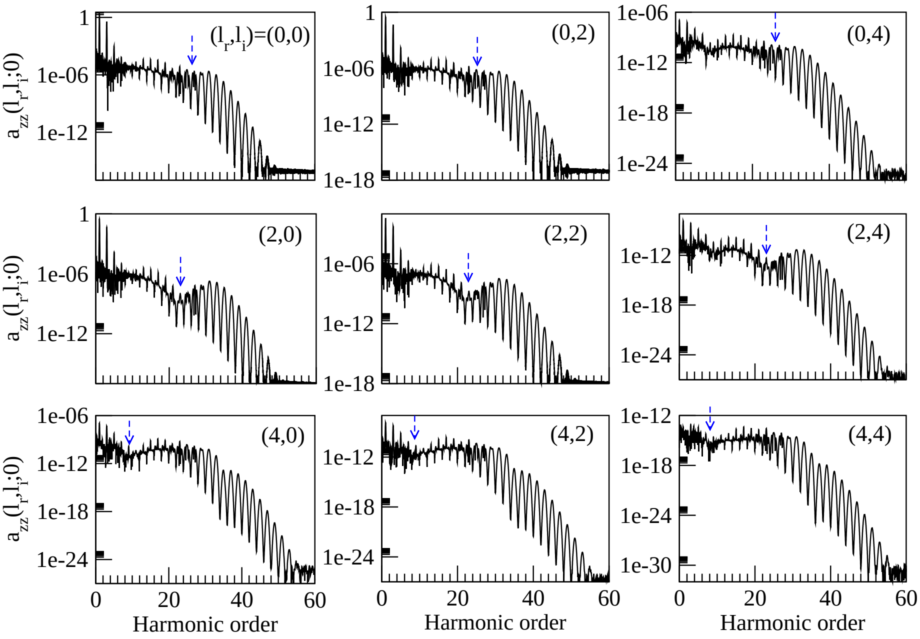

Figure 4.2: The contribution of different angular momentum (l_r, l_i) to the whole HHG spectrum of N_2. The quantities in y-axis are $\tilde{a}_{zz}(l_r, l_i; m)$, which is the electronic part of Fourier transform of electronic dipole. We use (probe) pulse of intensity $I_{probe} = 1.7 \times 10^{14}$ W/cm^2, wavelength $\lambda = 800$ nm, and 36 cycles, corresponding to $\gamma = 0.876$

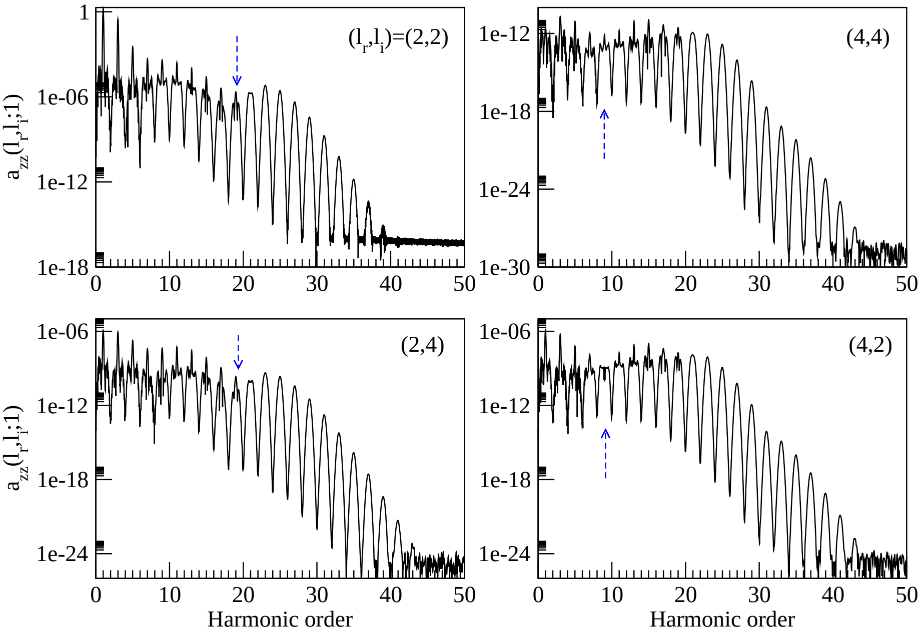

Figure 4.3: The contribution of different angular momentum (l_r, l_i) to the whole HHG spectrum of O_2. The quantities in y-axis are $\tilde{a}_{zz}(l_r, l_i; m)$, which is the electronic part of Fourier transform of electronic dipole. We use (probe) pulse of intensity $I_{probe} = 1.2 \times 10^{14}$ W/cm^2, wavelength $\lambda = 800$ nm, and 36 cycles, , corresponding to $\gamma = 0.917$

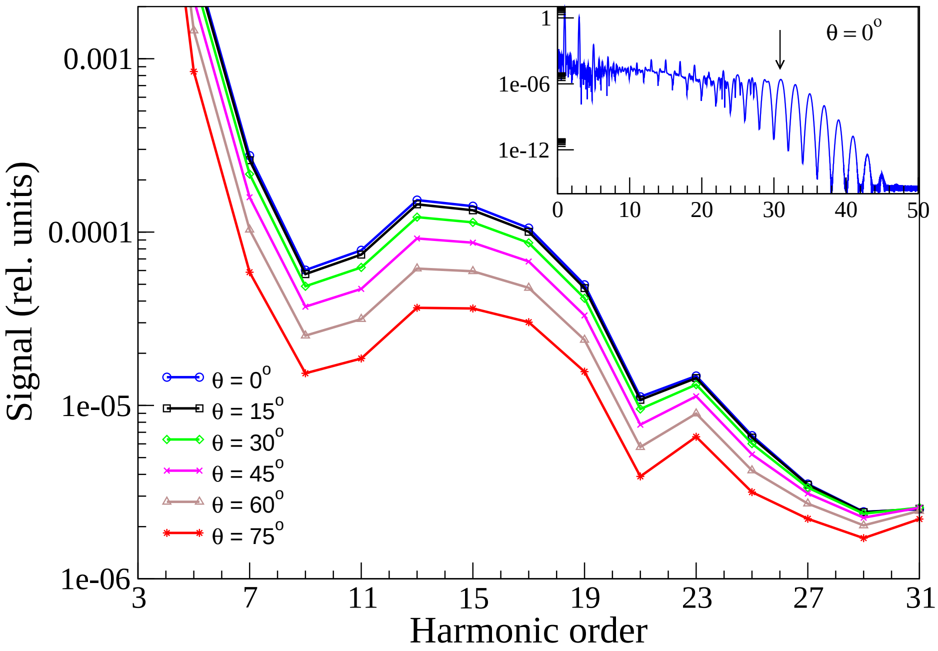

Figure 4.4: HHG spectrum of N_2 for various alignment angle. The pulse parameters are equal to those of Fig. 4.2. The arrow shows the cut off position according to the three-step model.

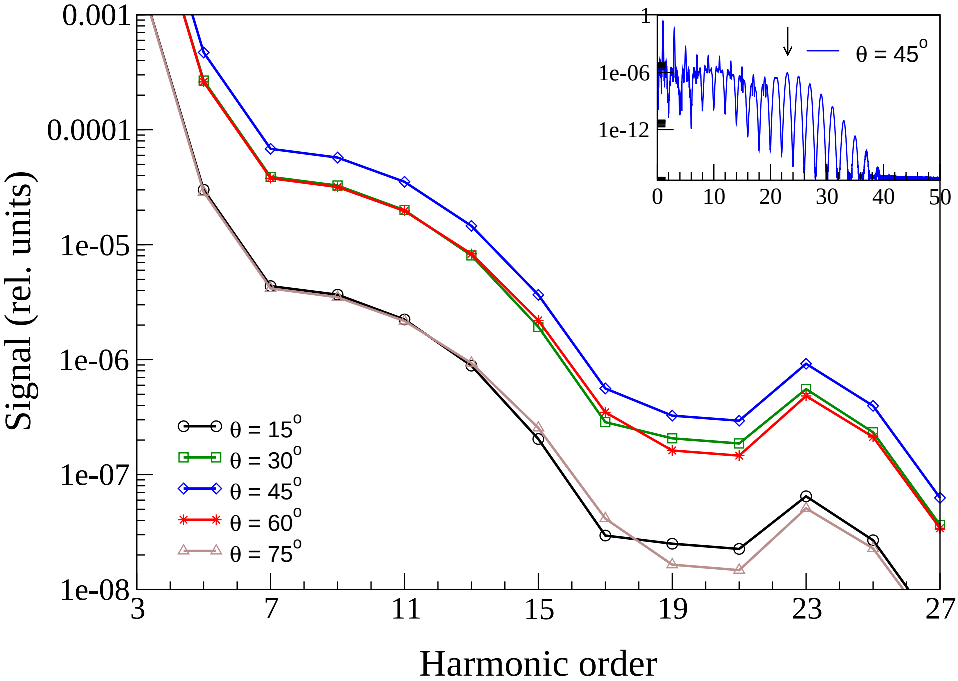

Figure 4.5: HHG spectrum of O_2 for various alignment angle. The pulse parameters are equal to those of Fig. 4.3. The arrow shows the cut off position according to the three-step model.

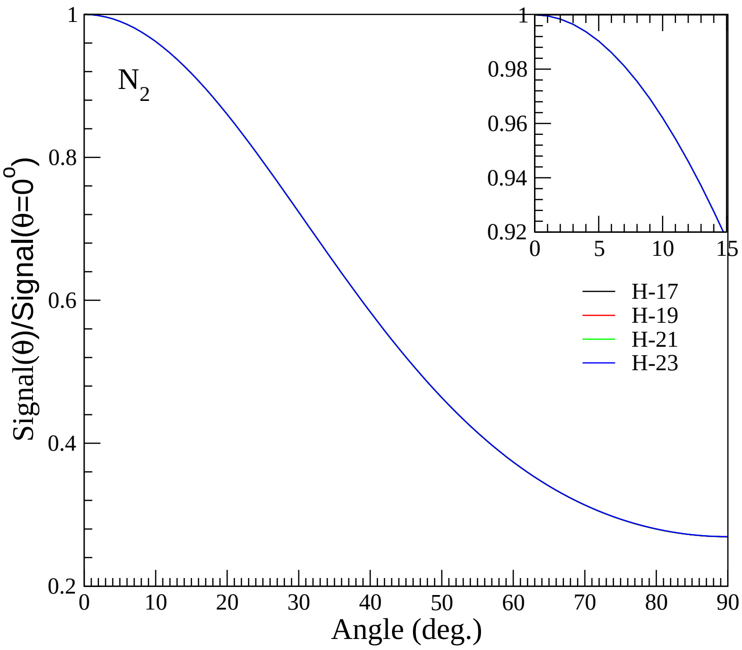

Figure 4.6: Alignment-dependent HHG signal of N_2 for various order. The pulse parameters are equal to those of Fig. 4.2.

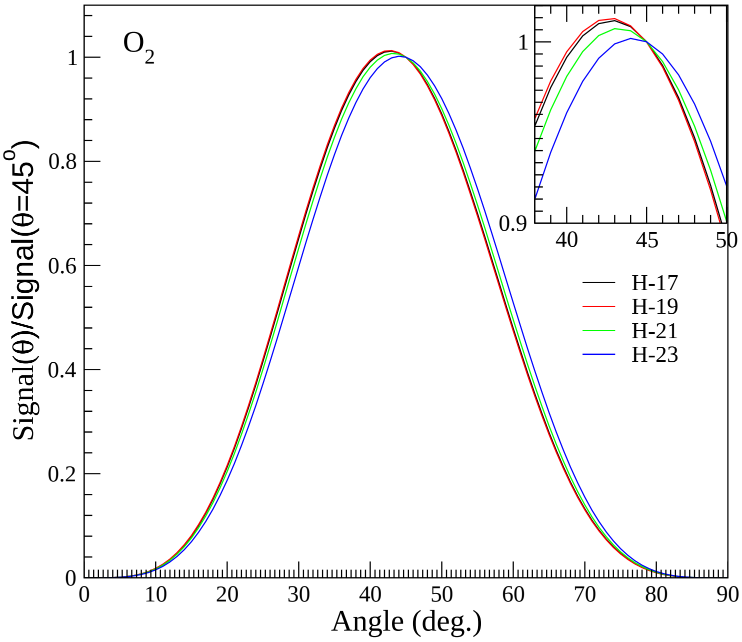

Figure 4.7: Alignment-dependent HHG signal of O_2 for various order. The pulse parameters are equal to those of Fig. 4.3.

The total calculated spectra, i.e. including the whole contributions of all initial and final angular momenta, for various alignment angles θ are shown in Figs. 4.4 and 4.5, for N_2 and O_2, respectively. It can be seen from the Fig. 4.4, that the HHG spectrum of

N_2 reaches its minimum at $n = 9$ and $n = 21$. As mentioned above, the first minimum is due to the recombination process with $l_r = 4$, while the second minima is related to the recombination process with $l_r = 2$. The recombination with final angular momentum $l_r = 0$ has a minimum at $n = 27$, but it is so weak that it does not appear in the harmonic spectrum. We note here that the previous theoretical analysis did not predict the existence of quantum interference for N_2 [137]. However, the experimental data of Miyazaki and his colleagues showed a strong minima at $n = 9$ and a weaker minima $n = 23$, quite close to the present calculated spectra. It means that, the most recombined electrons has greater angular momentum than the ionized electrons. For O_2, the spectrum reaches its minimum at $n = 17 - 23$, which is due to the recombination with $l_r = 2$. It means that the most returned electron for O_2 has a lowest angular momentum.

It can be seen in the figures, that the HHG signals reach the maximum at $\theta = 0^o$ for N_2 and $\theta \simeq 45^o$ for O_2. These phenomena can be attributed to the HOMO symmetry. The HOMO of N_2 is σ_g and hence its electron density is maximized along the nuclear axis direction. Since HHG mechanism starts with the ionization process, which is maximum (in the low frequency tunnel limit) along $\theta = 0^o$, it yields a maximum signal when the laser polarization is parallel with the nuclear axis, and it decreases with increasing alignment angle. This results well agree with the observation by Miyazaki and his colleagues [69]. Their spectrum of aligned N_2 was always greater that of non-aligned N_2. It could be understood, since the aligned molecules have smaller alignment angle than the non-aligned molecules. For O_2 with HOMO π_g, its electron density is maximum at $\theta = 45^o$. Therefore the HHG maximum signal occurs at intermediate angle $\theta \simeq 45^o$. It will be discuss more detail in § 4.5.

In Fig. 4.4, we also present the results for the calculated HHG spectrum of N_2 for $\theta = 0^o$ showing that its 'cut-off' harmonic is in agreement with the one obtained from the so called simple-man's model [53, 54]

$$n_{cut-off} = (I_p + 3.17U_p)/\hbar\omega \tag{4.14}$$

with $U_p = \frac{e^2E^2}{4m\omega^2}$ is a ponderomotive energy (see § 1.2). For O_2, the calculated spectrum for $\theta = 45^o$ is shown in Fig. 4.5 whose cut-off harmonic also agrees with the above predicted cut-off. More specifically, the peak signal of O_2 depends on its order, as shown in Fig. 4.7. In contrast, the signal of N_2 always reaches a maximum at $\theta = 0^o$ for all orders, as shown in Fig. 4.6.

4.3 Dynamic Signal

The central issue of HHG of aligned molecule is the dynamic HHG signal as a function of the delay time between the pump and the probe pulses. We start with a short pump-pulse and wait for the molecules to be aligned at a later time (a few picoseconds) when they

Table 4.3: The $c_{j,j'}^{(n)}$ and the related expectation values of N_2 for different harmonic order. The coefficients for 19th harmonic order are calculated by using Miyazaki's parameters [71] and *normalized* so that $c_{0,1}^{(19)} = 1$. The coefficients for 23th and 35th harmonic orders are obtained by using Itatani's parameters [70] and *normalized* so that $c_{0,1}^{(23)} = 1$.

(i,j)	Expectation value	19th harmonic	23th harmonic	35th harmonic
(0,0)	1	0.3327	0.5168	0.0329
(0,1)	$\langle\langle\cos^2\theta\rangle\rangle$	1	1	0.2067
(1,1)	$\left\langle\langle\cos^2\theta\rangle^2\right\rangle$	0.7513	0.4837	0.3251
(0,2)	$\langle\langle\cos^4\theta\rangle\rangle$	0.0064	0.0733	0.0027
(1,2)	$\langle\langle\cos^2\theta\rangle\langle\cos^4\theta\rangle\rangle$	0.0097	0.0710	0.0085
(0,3)	$\langle\langle\cos^6\theta\rangle\rangle$	0.0022	0.0543	0.0034
(1,3)	$\langle\langle cos^2\theta\rangle\langle cos^6\theta\rangle\rangle$	0.0034	0.0525	0.0106
(2,2)	$\left\langle\langle\cos^4\theta\rangle^2\right\rangle$	3.1140×10^{-5}	0.0026	0.0001
(2,3)	$\langle\langle\cos^4\theta\rangle\langle\cos^6\theta\rangle\rangle$	2.1864×10^{-5}	0.0039	0.0001
(3,3)	$\left\langle\langle\cos^6\theta\rangle^2\right\rangle$	3.8372×10^{-6}	0.0014	0.0001

undergo 'rotational revival'. A second short probe-pulse is then used to generate the HHG signal from these aligned molecules. The HHG yield is then measured against the delay time between the two pulses.

Here, we test the present calculation against the experiment of Miyazaki *et al.* [71, 138] providing a complete data set in both time- and spectral-domain for any arbitrary pump-probe polarization's angle α. In their experiment, an ensemble of N_2 molecules was aligned by using a pump-pulse of peak intensity $0.8\times10^{14}\,\mathrm{W/cm^2}$ and pulse duration 40 fs. The HHG signal was then generated by using a probe-pulse of peak intensity $1.7\times10^{14}\,\mathrm{W/cm^2}$, mean wavelength $\lambda = 800\,\mathrm{nm}$, and pulse duration 40 fs. For O_2, they used a pump- and probe-pulse of peak intensity $0.5\times10^{14}\,\mathrm{W/cm^2}$ and $1.2\times10^{14}\,\mathrm{W/cm^2}$, respectively. In the experiment, the initial gas temperature was not known. We choose the initial temperature to be 200 K (which gives the best agreement of calculated frequency spectral results with respect to the experimental data, as will be shown in chapter 6).

The dynamic signal of N_2 can be obtained by using Eq. (4.5) whose $c_{j,j'}^{(n)}$ coefficients are obtained by evaluating $\tilde{a}_{zz}(l_r, l_i; 0)$ from Fig. 4.2. The $c_{j,j'}^{(n)}$ coefficients for $n = 19$ are listed in Tab. 4.3. The comparison between theoretical calculations and experimental data for the 19th harmonic order is given in Fig. 4.8. Both signals show revivals at a quarter, half, and full period with $T_{rev} = 8.4\,\mathrm{ps}$, which are consistent with $T_{rev} = 1/(2Bc)$ given in Eq. (3.34) and also consistent with the other experimental data [70, 43, 134]. Examining the $c_{jj'}^{(n)}$ coefficients from Tab. 4.3, the dynamic HHG signal for $n = 19$ can be approximated as:

$$S^{(n)}(t_d) \simeq c_{00}^{(n)} + c_{01}^{(n)}\langle\langle\cos^2\theta\rangle\rangle(t_d) + c_{11}^{(n)}\left\langle\langle\cos^2\theta\rangle^2\right\rangle(t_d) \tag{4.15}$$

The properties of the dynamic HHG signal of N_2 are therefore determined mainly by the

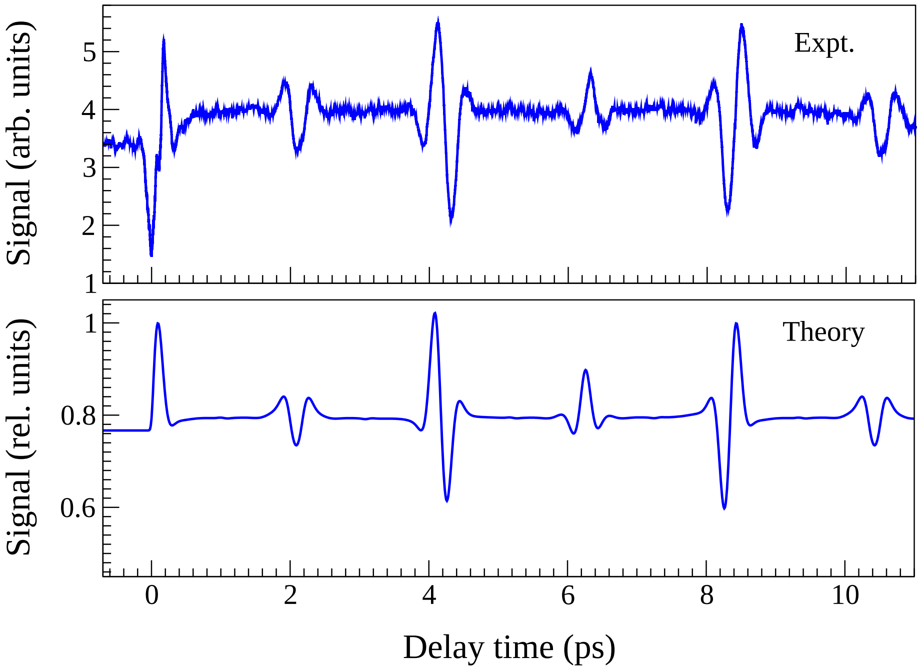

Figure 4.8: Comparison of the experimental (from [69, 71]) and the theoretical dynamic 19th harmonic signal for N_2; pump intensity $I_{pump} = 0.8 \times 10^{14}$ W/cm^2, probe intensity $I_{probe} = 1.7 \times 10^{14}$ W/cm^2; duration 40 fs, wavelength 800 nm, temperature 200 K.

expectation values $\left\langle\left\langle\cos^2\theta\right\rangle\right\rangle(t_d)$ and $\left\langle\left\langle\cos^2\theta\right\rangle^2\right\rangle(t_d)$. The term $\left\langle\left\langle\cos^2\theta\right\rangle\right\rangle(t_d)$ is the dominant term and makes the dynamic signal mimic the dynamics of the alignment degree $\left\langle\left\langle\cos^2\theta\right\rangle\right\rangle(t_d)$. However, the next term $\left\langle\left\langle\cos^2\theta\right\rangle^2\right\rangle(t_d)$ has also a significant contribution. We note that for different orders or different probe parameters, some times the $c^{(n)}_{j,j'}$ coefficients can change to make terms like $\left\langle\left\langle\cos^2\theta\right\rangle^2\right\rangle(t_d)$ and $\left\langle\left\langle\cos^4\theta\right\rangle\right\rangle(t_d)$ more dominant in the signal.

Another experimental data set was reported by Itatani *et al.* [70]. A laser pulse with intensity $I_{pump} = 0.4 \times 10^{14}$ W/cm^2 and duration 60 fs was used to generate coherent rotation of molecules in a gas jet at 30 K. The HHG signal was then generated by using a probe-pulse with $I_{probe} = 2 \times 10^{14}$ W/cm^2, duration 30 fs, and mean wavelength 800 nm. In Fig. 4.9 we show the calculated result by using the same parameters and directly compare it with the experimental data. Compare to the signal of Miyazaki, the signal of Itatani *et al.* have different coefficients, in which the higher terms have more significant strengths, as shown in Tab. 4.3. As a consequence, the HHG signals have some distinct properties, in which their ‘hill’ is greater than their ‘valley’. In addition, the revival at $t = \frac{1}{4}T_{rev}$ is not a mirror symmetric image of revival at $t = \frac{1}{3}T_{rev}$. These properties are due mainly to the terms $\left\langle\left\langle\cos^2\theta\right\rangle^2\right\rangle(t_d)$ and $\left\langle\left\langle\cos^4\theta\right\rangle\right\rangle(t_d)$. Fig. 4.9 also directly shows a comparison between the 23th order harmonic which is in the plateau region and the 35th order near the cut-off region.

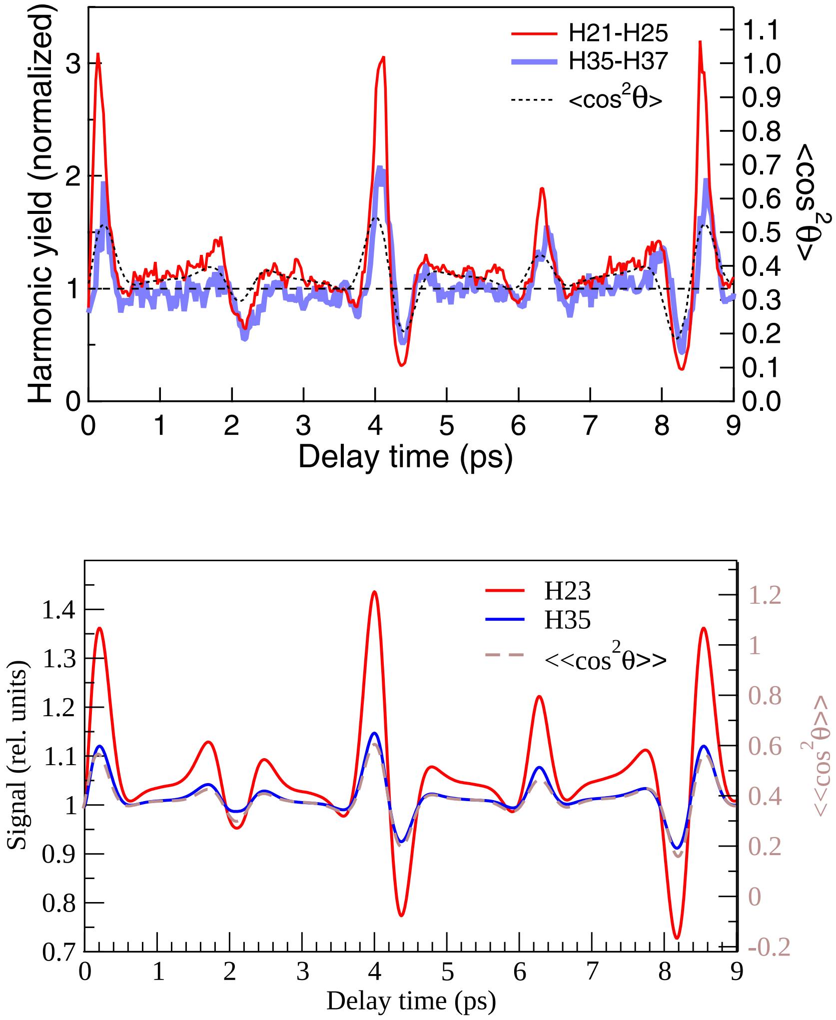

Figure 4.9: Comparison of the experimental (upper panel) (from [70]) and the theoretical (lower panel) dynamic HHG signal for N_2; pump pulse: $I_{pump} = 0.4 \times 10^{14}$ W/cm^2 and 60 fs; probe pulse: $I_{probe} = 2 \times 10^{14}$ W/cm^2 and 30 fs, wavelength 800 nm, temperature 30 K.

We now turn to the harmonic signal of O_2. The dynamic signal of O_2 is obtained by using Eq. (4.12) whose $c^{(n)}_{j,j'}$ coefficients are obtained from $\tilde{a}_{zz}(l_r, l_i; 1)$ in Fig. 4.3. The $c^{(n)}_{j,j'}$ coefficients for $n = 19$ are given in Tab. 4.4. The comparison between the theoretical calculations and the experimental data for the 19th harmonic order are given in Fig. 4.10. Like N_2, the signal of O_2 shows revivals at half, fourth, and the full revival with period $T_{rev} = 11.6\,\mathrm{ps}$. In addition to the above revival, the signal of O_2 shows a revival at $\frac{1}{8}T_{rev}$. These phenomena are also consistent with the experimental data [70, 43, 134]. For O_2, one of the puzzles regarding its dynamic signal (as observed by Itatani *et al.* [70]), was the failure of the expectation value of the alignment measure $\langle\langle\cos^2\theta\rangle\rangle(t_d)$ to account for the dynamic HHG signal. In fact, Itatani *et al.* found empirically that their data behaved more closely to the expectation value $\langle\langle\sin^2 2\theta\rangle\rangle(t_d)$. Examining the $c^{(n)}_{j,j'}$ coefficients from Tab. 4.3, the dynamic HHG signal for $n = 19$ can be approximated as:

$$\begin{aligned} S^{(n)}(t_d) \;\simeq\;& c^{(n)}_{11}\left\langle\left\langle\sin^2\theta\cos^2\theta\right\rangle^2\right\rangle(t_d) + c^{(n)}_{12}\left\langle\left\langle\sin^2\theta\cos^2\theta\right\rangle\left\langle\sin^2\theta\cos^4\theta\right\rangle\right\rangle(t_d) \\ &+ c^{(n)}_{22}\left\langle\left\langle\sin^2\theta\cos^4\theta\right\rangle^2\right\rangle(t_d) \end{aligned} \tag{4.16}$$

From equation above, it can be seen that indeed the *leading* term of the signal for O_2 is given by $\left\langle\left\langle\sin^2\theta\cos^2\theta\right\rangle^2\right\rangle(t_d) = \frac{1}{16}\left\langle\left\langle\sin^2 2\theta\right\rangle^2\right\rangle(t_d)$, which is directly proportional to the proposed empirical fit by Itatani *et al.* [70]. Moreover, the present theory also predicts that there ought to be modifications to this result due to the higher order terms in Eq. (4.16). Moreover, in contrast to N_2, there is no difference between the heights of ‘hill’ and ‘valley’ for O_2, since all terms in Eq. (4.16) have their ‘hill’ almost equal to their ‘valley’.

In fact, as mentioned earlier, Kanai *et al.* [43] found empirically that their experimental HHG signals for N_2 and O_2 demanded heuristic introduction of operators involving *higher* order functions, implying that their dynamic signal could not be expressed in term of $\langle\langle\cos^2\theta\rangle\rangle(t_d)$ only for N_2 and $\langle\langle\sin^2 2\theta\rangle\rangle(t_d)$ only for O_2. A related phenomenon of interest first, observed by Miyazaki *et al.* [138], is the appearance of extra series of lines in the Fourier spectrum of the dynamic HHG signal for *both* N_2 and O_2. These extra lines can not be attributed to $\langle\langle\cos^2\theta\rangle\rangle(t_d)$ for N_2 and $\langle\langle\sin^2 2\theta\rangle\rangle(t_d)$ for O_2. It can be seen now from Eq. (4.15) for N_2 and from Eq. (4.16) for O_2, that respective higher order contributions with decreasing strengths are predicted by the present theory. Directly comparing the signals for N_2 and O_2 also show that the signal for N_2 is much stronger than the one of O_2, as observed experimentally [138].

The existence of $\frac{1}{8}$th revival in O_2 and its absence in N_2 is also due to the different leading terms of the signal. The leading term of N_2 is $\langle\langle\cos^2\theta\rangle\rangle$ $(N = 2)$ that gives the lowest fractional revival at $t_{fr} = \frac{1}{4}T_{rev}$ (see Eq. (3.35)). On the other hand, the leading term of O_2 is $\left\langle\left\langle\sin^2\theta\cos^2\theta\right\rangle^2\right\rangle(N = 4)$ that implies $t_{fr} = \frac{1}{8}T_{rev}$. Classically, an average alignment ($\langle\langle\cos^2\theta\rangle\rangle = 0.34$) corresponds to $\theta_{ave} \simeq 54^o$. The $\frac{1}{8}$th revival corresponds to a molecular motion with a small angle around θ_{ave}. For O_2, with $\theta_{max} \simeq 40^o - 45^o$, this

Table 4.4: The $c^{(n)}_{j,j'}$ and related expectation values of O_2 for 19th harmonic order. The coefficients are *normalized* so that $c_{1,1} = 1$.

(i,j)	Expectation value	19th harmonic
(1,1)	$\left\langle \left\langle \sin^2\theta \cos^2\theta \right\rangle^2 \right\rangle$	1
(1,2)	$\left\langle \left\langle \sin^2\theta \cos^2\theta \right\rangle \left\langle \sin^2\theta \cos^4\theta \right\rangle \right\rangle$	0.4829
(1,3)	$\left\langle \left\langle \sin^2\theta \cos^2\theta \right\rangle \left\langle \sin^2\theta \cos^6\theta \right\rangle \right\rangle$	0.0188
(2,2)	$\left\langle \left\langle \sin^2\theta \cos^4\theta \right\rangle^2 \right\rangle$	0.1045
(2,3)	$\left\langle \left\langle \sin^2\theta \cos^4\theta \right\rangle \left\langle \sin^2\theta \cos^{26}\theta \right\rangle \right\rangle$	0.0082
(3,3)	$\left\langle \left\langle \sin^2\theta \cos^6\theta \right\rangle^2 \right\rangle$	0.0002

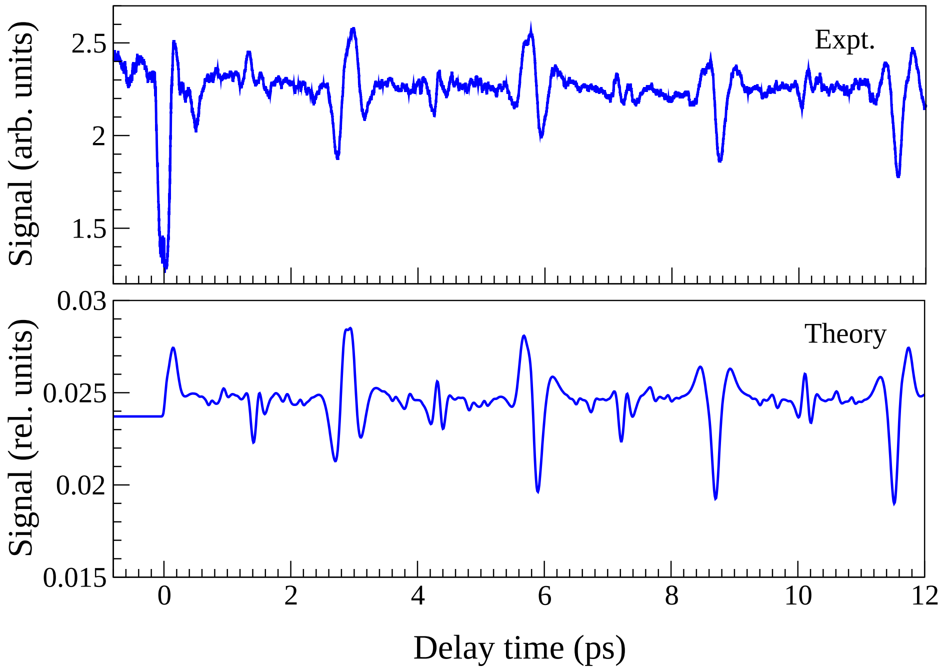

Figure 4.10: Comparison of the experimental (from [71]) and the theoretical dynamic 19th HHG signal for O_2; pump intensity $I_{pump} = 0.5 \times 10^{14}$ W/cm^2, probe intensity $I_{probe} = 1.2 \times 10^{14}$ W/cm^2; duration 40 fs, wavelength 800 nm, temperature 200 K.

motion shows a revival. However, this revival is not as large as when the molecules rotate with a greater angle, as in the case of the half period. For N_2, this motion does not cause a revival (or causes a negligible revival), because the electron's cloud is centered at $\theta_{max} = 0^o$.

In general, both the calculated and the experimental HHG signals contain four distinct regions, as a function of the delay-time between the pump and the probe pulses:

- $\Delta t < 0$, when the probe pulse precedes the pump pulse. In this region, no alignment is present. The HHG signal is therefore generated by the homogeneously distributed molecules, which is time independent. Therefore the signal is flat during this time domain.

- $\Delta t \simeq 0$ when the pump and probe pulses overlap in time. Experimentally, it is difficult to adjust precisely the overlap of the first pulse (pump pulse) and the second one (probe pulse). The experimental spectrum in this time domain, for any molecules and any pump-probe polarization angles, is quiet weak [138]. It means the absence of any observed harmonic signals. The combined pump and probe pulse therefore creates something else, for example a strong ionization signal that prevents efficient HHG.[3]

- $\Delta t > 0$ when the pump pulse proceeds significantly from the probe pulse. In this region the probe pulse generates clear harmonic signals from the aligned molecules. The average signal in this time domain is stronger than the one for $\Delta t < 0$ due to molecular alignment by the pump pulse.

- $\Delta t \simeq n\frac{1}{4}T_{rev}$ for N_2 and $\Delta t \simeq n\frac{1}{8}T_{rev}$ for O_2, with n integer. As mentioned above, there is a clear revival structure with rapid change of molecular alignment.

4.4 Effect of Initial Temperature

The dependency of HHG signal on some expectation values implies its dependency on the initial temperature of gas jet, as shown in Figs. 4.11 and 4.12. It can be seen from the figures that the lower initial temperature produces the HHG signal with a greater revival amplitude, as seen experimentally for both adiabatic [139] and non-adiabatic alignment [44, 140]. These phenomena have been discussed at § 3.7.

Comparing the dynamic HHG signal of O_2 for different initial temperature, one obtains that the peaks at quarter and half revival split to make a double-peaks at a lower initial temperature, a phenomena does not occur in case of N_2. For O_2, the *most effective angle* (i.e. the angle gives a maximum HHG signal) is an intermediate angle ($\theta_{peak} \simeq 40^o - 45^o$). For any alignment angle which is greater than the most effective angle, the HHG signal

---

[3] It was also seen in experiment that the ionization signal [43] and dissociation signal [44] increase in this time domain.

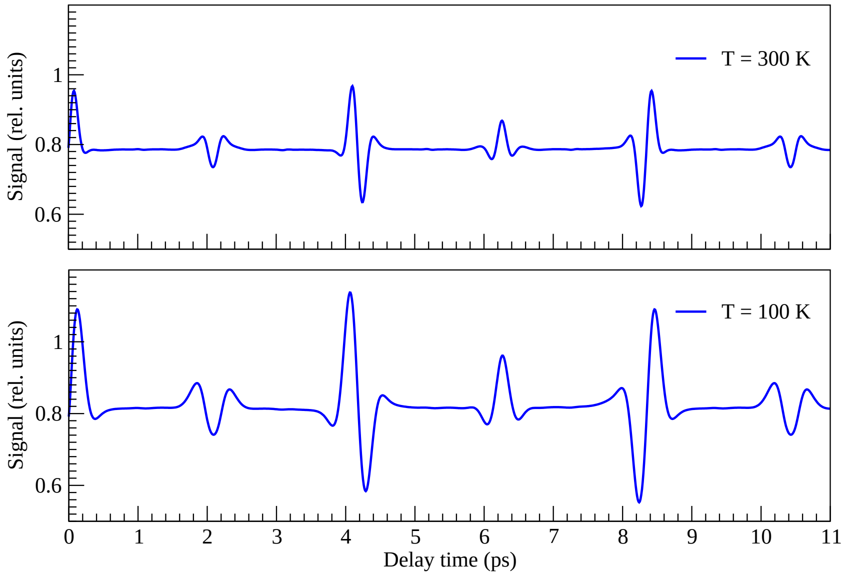

Figure 4.11: Dynamic 19th harmonic signal of N_2 for various initial temperature . The laser parameters and the initial temperature are similar with Fig. 4.8.

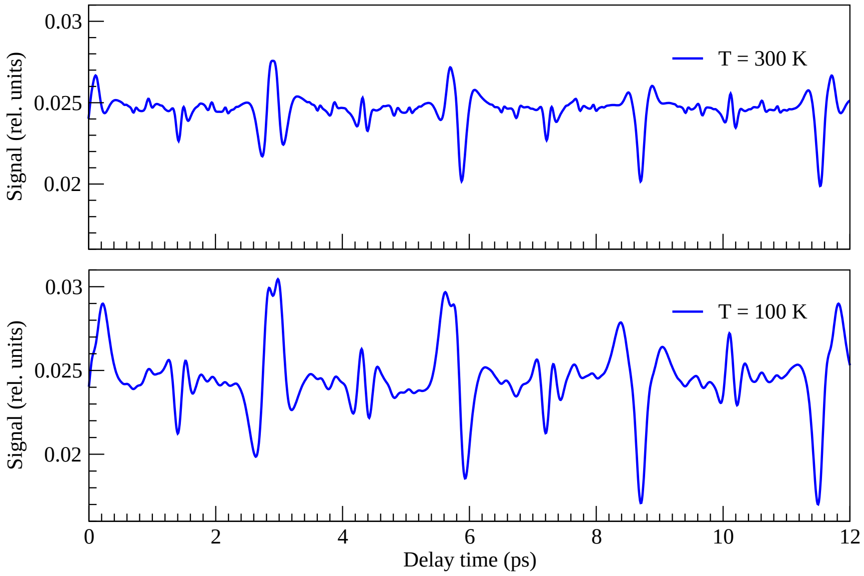

Figure 4.12: Dynamic 19th harmonic signal of O_2 for various initial temperature. The laser parameters and the initial temperature are similar with Fig. 4.10.

increases with increasing alignment angle. In contrast, for alignment angle which is less than the most effective angle, the HHG signal decreases by increasing the alignment angle. Therefore the 'valley' at the top signal is due to the alignment angle exceeds the maximum angle. For a higher initial temperature, the molecules never reach alignment angle which is less than the maximum angle, therefore the splitting top signal is not observed. For N_2, the maximum angle is $\theta = 0^o$, therefore the splitting top signal is never observed, because molecular is never perfectly aligned, whatever the initial temperature is.

4.5 Molecular Axis Distribution, Alignment Dependent Signal, and Differential Signal

One interesting issue in HHG of aligned molecule is how the signal depends on the angle between the nuclear axis and the probe polarization. In the present model, the dependence of HHG signal on the alignment angle is governed by the HHG operator $T_e^{(n)}(\theta)$ whose square represents the alignment dependence of HHG signal for a 'single' molecule. The quantity $\left|T_e^{(n)}(\theta)\right|^2$ is shown in Fig. 4.13 as a dashed curve. It can be seen from the figure that the most effective angle, θ_{peak}, is 0^o for N_2 and 40^o for O_2, due to the different HOMO symmetry of each molecules. The HOMO of N_2 is σ_g and hence its electron density is maximized along the nuclear axis direction. For O_2 with HOMO π_g, its electron density is maximum at $\theta = 45^o$. The discrepancy between maximum electron density before interaction ($\theta = 45^o$) and the alignment dependence of HHG signal ($\theta = 40^o$) shows a dynamics of the electron due to the pump pulse interaction.

For molecular ensemble, the HHG signal also depends on the molecular-axis distribution, $P\left(t_d, \theta\right) = \left|\Phi_{J_0M_0}(t_d, \theta_0)\right|^2$, whose value can be obtained by using Eq. (3.19). The molecular distribution is shown as dash-dotted curve in Fig. 4.13. From the figures, it was shown that $P\left(t_d, \theta\right)$ is peaked at $\theta = 0^o$ for top alignment, at $\theta = 90^o$ for anti top alignment, and almost homogeneously distributed for average alignment. For a lower initial temperature, the molecules are easily aligned, and therefore the distribution is sharply peaked at $\theta = 0^o$ for top alignment and at $\theta = 90^o$ for anti top alignment.

The relative observed signal as a contribution of molecule with specific alignment angle $\theta = \theta_0$ and $\phi = \phi_0$ can be obtained from Eq. (2.49) as

$$dS^{(n)}(t_d, \theta_0, \phi_0) \propto \sum_{J_0M_0} \rho(J_0) \left|\Phi^*_{J_0M_0}(t_d, \theta_0) T_e^{(n)}(\theta_0) \Phi_{J_0M_0}(t_d, \theta_0)\right|^2 \tag{4.17}$$

The differential signal $dS^{(n)}(t_d, \theta_0, \phi_0)$ near the first revival as a function of alignment angle θ_0 for a fixed $\phi_0 = 0^o$ is drawn (as a solid line) in Fig. 4.13. For N_2 whose effective alignment angle is 0°, the signal reaches its maximum at the top alignment, as molecular distribution also peaks at $\theta = 0°$ as seen in Fig. 4.13(a). In contrast, at the anti-top alignment, the molecular distribution is peaked at $\theta = 90°$, as shown in Fig. 4.13(c). For O_2, the most

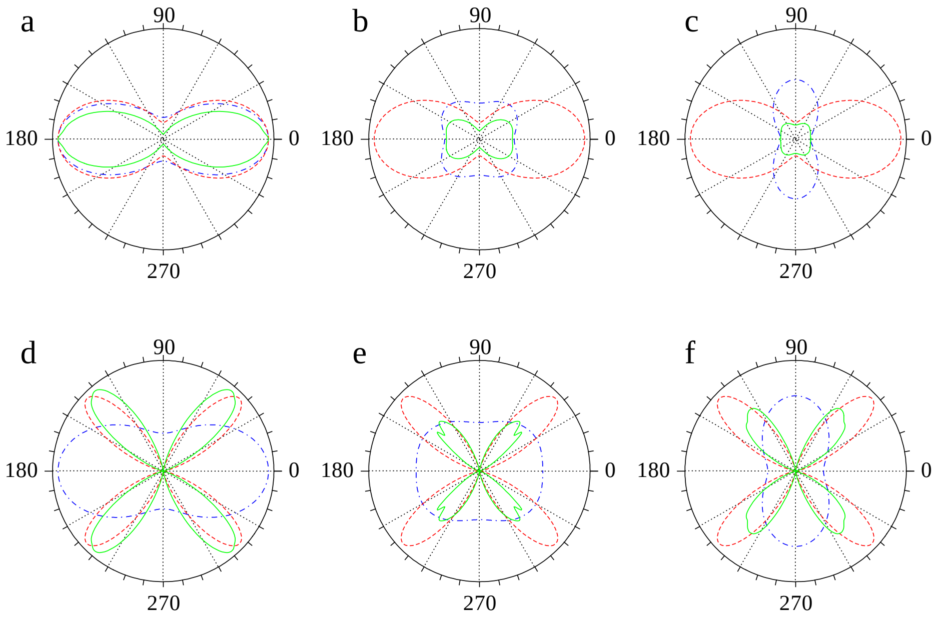

Figure 4.13: Alignment-dependent HHG signal for single molecule (red, dashed line), molecular distribution (blue, dash-dotted line), and $dS^{(n)}(t_d, \theta_0, \phi = 0^o)$ (green, solid line) calculated at first half revival. (a) N_2 at top signal $t_d = 4.09\,\mathrm{ps}$, (b) N_2 at average signal $t_d = 4.18\,\mathrm{ps}$, (c) N_2 at anti-top signal $t_d = 4.27\,\mathrm{ps}$, (d) O_2 at top signal $t_d = 5.68\,\mathrm{ps}$, (e) O_2 at average signal $t_d = 5.79\,\mathrm{ps}$, and (f) O_2 at anti-top signal $t_d = 5.90\,\mathrm{ps}$. The laser parameters are similar with Figs. 4.8 and 4.10 for N_2 and O_2, respectively. The initial temperature is 200 K.

effective angle for harmonic generation from the electron cloud is $\theta = 45°$. Therefore the peak of the HHG signal should be shifted by $\Delta\theta \approx 45°$ from the maximum molecular-axis distribution. In fact, the signal reaches maximum at $\theta = 40^o$ at the top alignment and $\theta = 55^o$ at anti-top alignment, as shown in Figs. 4.13(d-f).

It is clear from Eq. (4.17) that $dS^{(n)}(t_d, \theta_0, \phi_0)$ depends on both alignment-dependent signal $\left|T_e^{(n)}(\theta)\right|^2$ which is specific for the molecule but time-independent, and molecular-axis distribution $P(t_d, \theta)$ which is time-dependent but qualitatively does not depend on the specific molecule. As a consequence, the differential signal depends on both the delay time and the alignment angle. However, there is no experimental data available for HHG signal as function of the alignment angle of the molecular axis with respect to the pump polarization axis[4]. Here, we compare our results with the other theoretical results. In fact, the most efficient HHG signal has been calculated by extending the atomic Lewenstein model for

---

[4] Some experimentalist [67, 141, 142] tried to obtain the differential HHG signal by keeping the delay time between the pump and the probe pulses to be equal to the top signal, and rotating the relative polarization angle between them. In this delay time, most of molecules are assumed to align parallel to the pump polarization. Therefore, they assumed, the relative polarization angle to be equal to the molecular axis alignment angle. However, this method is not really true, because, not the whole molecules are aligned along the pump's polarization, as shown in Fig. 4.13. We will discuss it later in chapter 7.

the molecule [87, 88], by the quantum calculation including nuclear motion [89, 66], and by directly solving Schrödinger equation within time dependent density functional theory [143]. In contrast to our results, they found that the HHG signal, for any delay time between the pump and the probe pulse, reached maximum at $\theta = 0^o$ for N_2 and at $\theta \simeq 45^o$ for O_2, which is *time-independent*. This is because they toke the electronic dipole only and neglected the molecular distribution. Therefore, their results can be interpreted as alignment-dependent signal $\left|T_e^{(n)}(\theta)\right|^2$ of the present theory.

The distinction result of the present theory is shown in Fig. 4.14: a calculated $dS^{(n)}(t_d, \theta_0, \phi_0)$ as a function of both the delay time and the alignment angle. The calculation is done for initial temperature $T = 200\,\mathrm{K}$. The distribution rapidly changes both in time and angle, and have a complex structure with several nodes. For N_2, in general, the signal decreases with increasing alignment angle. However, at some delay times correspond to the anti top alignment, the differential signal is maximized at $\theta = 90^o$. For O_2, the signal is peaked at $\theta \simeq 45^o$, due mainly to its alignment dependency $\left|T_e^{(n)}(\theta)\right|^2$ which is maximized at this intermediate angle. However, the differential signal at $\theta \simeq 45^o$ also changes with delay time due to the time dependence of the molecular distribution $P\left(t_d, \theta\right)$.

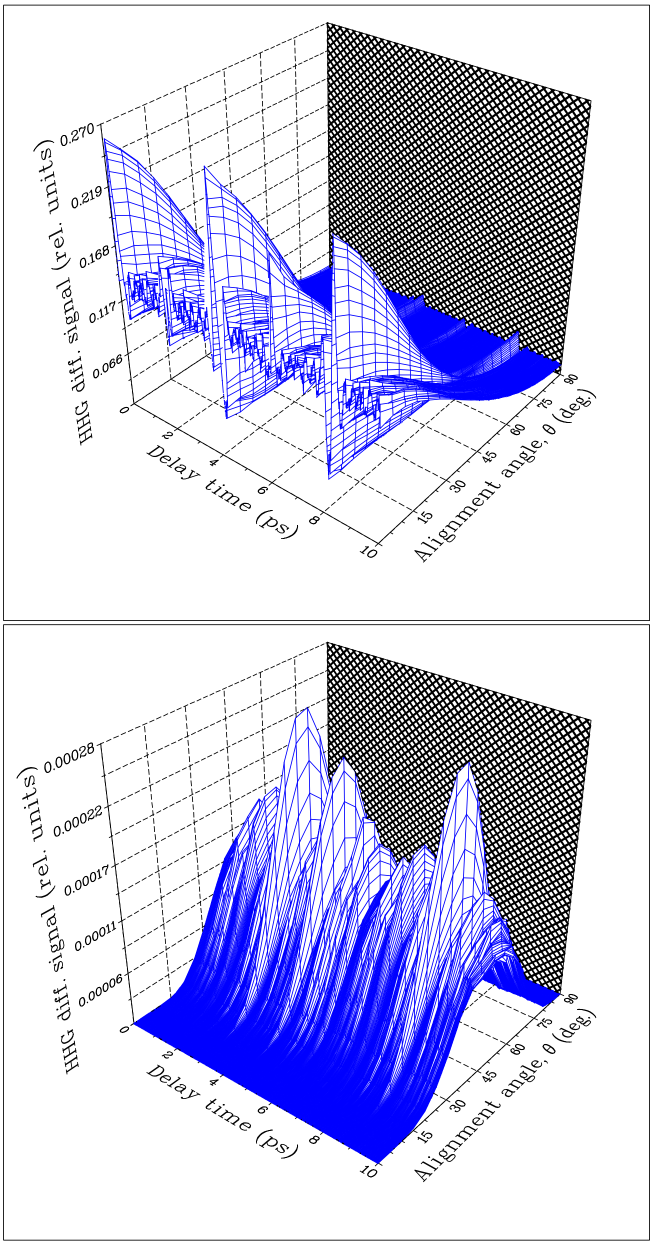

Figure 4.14: Differential signal of 19th harmonic as function of both time delay and alignment angle for N_2 (upper panel) and O_2 (lower panel). The laser parameters are similar with Figs. 4.8 and 4.10 for N_2 and O_2, respectively. The initial temperature is 200 K.

Chapter 5

Application to the Three-atomic Molecule: CO_2

In this chapter, we discuss the HHG of CO_2 whose experimental spectrum shows a richer dynamics [43, 144, 138]. In contrast to N_2 and O_2, the phase modulation of dynamic HHG signal of aligned CO_2 molecules can be in the same or in the inverted phase with respect to its dynamic ionization signal, and it depends also on its order [43, 144, 73, 138]. In addition, the harmonic cut-off position for CO_2 can be more extended or compressed compared to that observed for its companion atom Kr, depending on the peak laser intensity [61, 111].[1]

The first experimental data on dynamic HHG signal of CO_2 was reported by Kanai *et al.* [43]. They observed the dynamic HHG signal in the plateau region as a function of the pump-probe delay and compared the spectrum with its dynamic ionization signal. The HHG signal showed an inverted modulation phase with respect to the ionization signal, i.e. the HHG yield is maximum (minimum) when the ionization signal is minimum (maximum). More recently, the inverted modulation phase in the plateau region was also reported by Vozzi *et al.* [144, 73], Miyazaki *et al.* [72], Lee *et al.* [134], and Merdji *et al.* [145].

In addition, Kanai *et al.* [43] and Vozzi *et al.* [73] measured the top signal (the HHG signal when its alignment degree is maximum) and directly compared it with the anti-top signal (the HHG signal when its alignment degree is minimum) for various harmonic orders in the plateau region. They obtained that for several harmonic orders, the top signal was always smaller than the anti-top signal meaning that the HHG signal has inverted modulation compare with its ionization signal. For smaller and greater harmonic orders, the top signal increases whereas the anti-top signal decreases and they tend to become close to each other, suggesting a possibility to obtain a non-inverted modulation-phase of HHG signal in the lower and the higher orders. Recently, the non-inverted HHG signal was reported by Miyazaki *et al.* [138] in the lower perturbative order region and by Vozzi *et al.* [144, 73] near the cut-off region.

---

[1] We note here that a ‘companion atom’ of a molecule is defined as an atom with an equal or comparable ionization potential, as that of the molecule.

What is the origin of the phase difference between the HHG and the ionization signal in CO_2? Kanai *et al.* [43], Marangos [146], and Vozzi *et al.* [144, 73] attributed the inverted phase of HHG signal of CO_2 as a manifestation of the destructive interference in the recombination process. The idea of the interference of two-center molecules was originally proposed by Faisal and his colleagues[2] for ionization and was adopted by Lein *et al.* for HHG [85, 86]. Lein *et al.* investigated the HHG spectrum (harmonic signal as a function of its order) of aligned H_2^+ model by directly solving the time-dependent Schrödinger equation (TDSE) for an arbitrary alignment angle between the molecular axis and the laser polarization. The harmonic spectra exhibited minima whose positions shift to the higher orders on increasing the alignment angle. The further investigations also have shown that the positions of minima shift to higher order on reducing the internuclear distance [86], but they did not depend on the laser intensity [142]. Similar interference effect has been also found later in H_2^+ using more realistic 3D simulation [150] and in other molecules such as H_3^{2+} [130] and H_2 [151] for both 2D and 3D simulations. The similar minima was clearly seen in the calculated spectra of N_2 and O_2 presented in chapter 4.

The correlation between minima and phase inversion in HHG of CO_2 has been confirmed experimentally by Vozzi *et al.* [144]. They measured HHG spectrum of both aligned and non-aligned CO_2 at a fixed pump-probe delay $t_d = 21.1\,\mathrm{ps}$, when the alignment degree reached its maximum. The minima were found in the spectra of the aligned molecules but were absent in that of non-aligned molecules. They also obtained that the dynamic signal in the minima region has inverted phase with respect to the ionization signal, while in the other region both HHG and ionization signals have the same phase.[3]

The theoretical investigation by Le *et al.* [110, 152] gave another possible interpretation for the origin of the inverted modulation. By using the atomic Lewenstein model [56] extended for molecules [87, 88], it was shown that the inverted modulation was strongly related to its alignment dependence. The HHG signal was peaked at $\theta_{peak} \simeq 45^o$ for non-inverted modulation and at $\theta_{peak} > 45^o$ for inverted modulation. The dependence of the HHG peaks from adiabatically aligned CO_2 on the harmonic order also has been investigated recently both theoretically and experimentally by Nalda *et al.* [68, 151]. However, both Le *et al.* and Nalda *et al.* did not give explanation why HHG peak of CO_2 changed with its order.

To fit their inverted CO_2 spectrum, Kanai *et al.* [43] needed to postulate empirically the higher power of $-\cos^{2n}\theta$, which implied that the phase of their dynamic signal was not simply the opposite of the phase of $\langle\langle\cos^2\theta\rangle\rangle(t_d)$. A careful examination of the Fourier

---

[2] The interference idea was initially proposed by Faisal and his colleagues for describing suppressed ionization of molecules anti-bonding symmetry [147, 148]. It also successfully described the existence of minima in above threshold ionization spectra of those molecules [149].

[3] In their experiment, Vozzi *et al.* used the signal from non-aligned molecules as a reference or as a substitute of signal of the average alignment. When the signal of the top-alignment was found to be weaker than the reference, they concluded that the signal to have an inverted phase. Unfortunately, they did not measure the signal of anti-top alignment to know if they were stronger than the top and reference signals (or not).

spectrum of the dynamic signal for a given harmonics by Miyazaki *et al.* [138] showed the existence not only of a series of peaks spaced by $8Bc$, but also a peak-series spaced by $16Bc$ as well as another extra series. For CO_2 with only even allowed J values, the peak series spaced by $16Bc$ in frequency domain corresponds to $\frac{1}{8}$ revival in time domain signal.

In this chapter, we (i) apply the present theory to CO_2 and derive a general operator governing the dynamic HHG from the molecule, (ii) observe how the operator governs the signal phase, and (iii) observe the origin of the inverted modulation. Finally, we (iv) consider the possibility to invert the modulation in O_2.

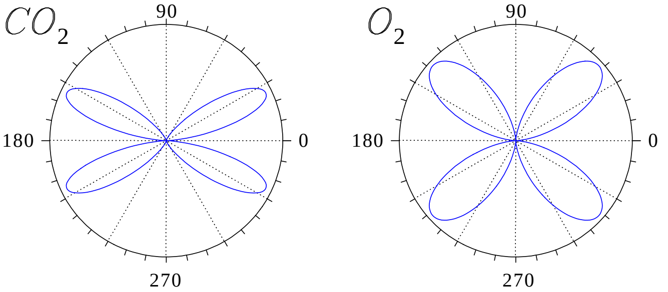

Figure 5.1: The calculated squared asymptotic wavefunction. The left column for CO_2 whereas the right one for O_2, as a comparison.

5.1 HHG Operator $T_e^{(n)}(\theta)$ for CO_2

CO_2 has the symmetry π_g [136], and we approximate its HOMO by the asymptotic approximation from single center molecule in body frame (bf) with $m = 1$ and $l = 2, 4, 6$ [152] as follows

$$\phi_e^{(bf)}(\boldsymbol{r}) = \sum_{l=2,4,6} C_l^{(1)} R_l(r) Y_{l1}(\hat{\boldsymbol{r}}) \tag{5.1}$$

where $R_l(r)$ is given by Eq. (2.71), whereas $C_l^{(1)}$ is the asymptotic coefficients, their value are listed in Tab. 5.2. The HOMO of CO_2 is shown in Fig. 5.1, together with that of O_2, as a comparison. However, the electronic density of CO_2 reaches its maximum at a smaller angle than those of O_2, because the first has a longer internuclear distance $O - O$. Therefore, the angular momentum $l = 4$ of CO_2 has more significant contribution on the asymptotic form of the electronic wavefunction than the one in O_2. In addition, $C_6^{(1)}$ is not zero for CO_2, in contrast to that of O_2.

Evaluating the HHG operator (Eq. (2.69)) for $m = 1$ and $l_i, l_r = 2, 4, 6$ for CO_2 we get

$$T_e^{(n)}(\theta) \quad = \sum_{l_i, l_r = 2,4,6} \left\{ d_{01}^{l_r}(\theta) \tilde{a}_{zz}^{(n)}(l_r, l_i; 1) d_{01}^{l_i}(\theta) \right\} \tag{5.2}$$

Where $\tilde{a}_{zz}^{n}(l_r, l_i; 1)$ is the electronic part of the Fourier transform of the expectation value

Table 5.1: Explicit form of $d^l_{0m}(\theta)$ required for evaluating Eq. (5.2) [103, 104, 153]

l	$d^l_{01}(\theta)$
2	$\sqrt{\frac{3}{2}}\,\sin\theta\cos\theta$
4	$-\frac{\sqrt{5}}{4}\,\sin\theta\cos\theta\left(3-7\cos^2\theta\right)$
6	$\frac{1}{112}\sqrt{\frac{6}{7}}\sin\theta\cos\theta\left(5-30\cos^2\theta+33\cos^4\theta\right)$

of the electronic dipole operator, given by Eq. (2.70), with the initial angular momentum l_i, the final angular momentum l_r, and the conserved projection of the angular momentum of the electron along the molecular axis, $m = 1$. By using the expressions for the reduced rotation matrices $d^l_{01}(\theta)$ from Tab. 5.1 and simplifying them, we may rewrite the HHG operator of CO_2 as a sum of powers of $\sin^2\theta\cos^{2n}\theta$ only

$$\begin{aligned} T_e^{(n)}(\theta) &= b_1^{(n)}\sin^2\theta\cos^2\theta + b_2^{(n)}\sin^2\theta\cos^4\theta + b_3^{(n)}\sin^2\theta\cos^6\theta \\ &\quad + b_4^{(n)}\sin^2\theta\cos^8\theta + b_5^{(n)}\sin^2\theta\cos^{10}\theta \end{aligned} \tag{5.3}$$

where $b_j^{(n)}$ -coefficients are given by

$$\begin{aligned} b_1^{(n)} &= \frac{3}{2}\tilde{a}_{zz}^{(n)}(2,2;1) + \frac{45}{16}\tilde{a}_{zz}^{(n)}(4,4;1) + \frac{75}{43904}\tilde{a}_{zz}^{(n)}(6,6;1) \\ &\quad - \frac{3}{4}\sqrt{\frac{15}{2}}\left(\tilde{a}_{zz}^{(n)}(2,4;1) + \tilde{a}^{(n)}(4,2;1)\right) + \frac{15}{112}\sqrt{\frac{1}{7}}\left(\tilde{a}_{zz}^{(n)}(2,6;1) + \tilde{a}^{(n)}(6,2;1)\right) \\ &\quad - \frac{15}{448}\sqrt{\frac{30}{7}}\left(\tilde{a}_{zz}^{(n)}(4,6;1) + \tilde{a}^{(n)}(6,4;1)\right) \\ b_2^{(n)} &= -\frac{105}{8}\tilde{a}_{zz}^{(n)}(4,4;1) - \frac{90}{43904}\tilde{a}_{zz}^{(n)}(6,6;1) + \frac{7}{4}\sqrt{\frac{15}{2}}\left(\tilde{a}_{zz}^{(n)}(2,4;1) + \tilde{a}_{zz}^{(n)}(4,2;1)\right) \\ &\quad - \frac{45}{56}\sqrt{\frac{1}{7}}\left(\tilde{a}_{zz}^{(n)}(2,6;1) + \tilde{a}_{zz}^{(n)}(6,2;1)\right) + \frac{125}{448}\sqrt{\frac{30}{7}}\left(\tilde{a}_{zz}^{(n)}(4,6;1) + \tilde{a}_{zz}^{(n)}(6,4;1)\right) \\ b_3^{(n)} &= \frac{245}{16}\tilde{a}_{zz}^{(n)}(4,4;1) + \frac{1845}{21952}\tilde{a}_{zz}^{(n)}(6,6;1) + \frac{99}{112}\sqrt{\frac{1}{7}}\left(\tilde{a}_{zz}^{(n)}(42,6;1) + \tilde{a}_{zz}^{(n)}(6,2;1)\right) \\ &\quad - \frac{309}{448}\sqrt{\frac{30}{7}}\left(\tilde{a}_{zz}^{(n)}(4,6;1) + \tilde{a}_{zz}^{(n)}(6,4;1)\right) \\ b_4^{(n)} &= -\frac{85}{686}\tilde{a}_{zz}^{(n)}(6,6;1) + \frac{231}{448}\sqrt{\frac{30}{7}}\left(\tilde{a}_{zz}^{(n)}(4,6;1) + \tilde{a}_{zz}^{(n)}(6,4;1)\right) \\ b_5^{(n)} &= \frac{6534}{87808}\tilde{a}_{zz}^{(n)}(6,6;1) \end{aligned} \tag{5.4}$$

The corresponding harmonic signal for nth harmonic order is then given by

$$\begin{aligned} S^{(n)}(t_d) &= c_{11}^{(n)}\left\langle\left\langle\sin^2\theta\cos^2\theta\right\rangle^2\right\rangle(t_d) + c_{12}^{(n)}\left\langle\left\langle\sin^2\theta\cos^2\theta\right\rangle\left\langle\sin^2\theta\cos^4\theta\right\rangle\right\rangle(t_d) \\ &+ c_{13}^{(n)}\left\langle\left\langle\sin^2\theta\cos^2\theta\right\rangle\left\langle\sin^2\theta\cos^6\theta\right\rangle\right\rangle(t_d) + c_{14}^{(n)}\left\langle\left\langle\sin^2\theta\cos^2\theta\right\rangle\left\langle\sin^2\theta\cos^8\theta\right\rangle\right\rangle(t_d) \end{aligned}$$

Table 5.2: The molecular properties of CO_2 and O_2 (as a comparison) used in this work. I_p is ionization potential, B is rotational constant of molecule, $\alpha_\parallel$ and $\alpha_\perp$ are parallel and perpendicular polarizability, R_0 is the internuclear distance, and $C_l^{(m)}$'s are angular coefficient of electronic wave function. The $C_l^{(m)}$ for CO_2 are *normalized* so that $C_2^{(1)}$ has the same value for both O_2 and CO_2.

	CO_2	O_2	Ref.
HOMO	π_g, $m=1$	π_g, $m=1$	[136, 117]
I_p (eV)	13.77	12.03	[105]
B (cm^{-1})	0.3902	1.4377	[121]
R_0 (Å)	2.352	1.208	[154]
$\alpha_\parallel$ $\left(\text{Å}^3\right)$	4.01-4.11	2.35	[118]
$\alpha_\perp$ $\left(\text{Å}^3\right)$	1.97-1.93	1.21	[118]
$C_2^{(m)}$	0.62	0.62	[105, 152]
$C_4^{(m)}$	0.27	0.03	[105, 152]
$C_6^{(m)}$	0.08		[152]

$$
\begin{aligned}
&+\ c_{15}^{(n)}\left\langle\left\langle\sin^2\theta\cos^2\theta\right\rangle\left\langle\sin^2\theta\cos^{10}\theta\right\rangle\right\rangle(t_d)+c_{22}^{(n)}\left\langle\left\langle\sin^2\theta\cos^4\theta\right\rangle^2\right\rangle(t_d)\\
&+\ c_{23}^{(n)}\left\langle\left\langle\sin^2\theta\cos^4\theta\right\rangle\left\langle\sin^2\theta\cos^6\theta\right\rangle\right\rangle(t_d)+c_{24}^{(n)}\left\langle\left\langle\sin^2\theta\cos^4\theta\right\rangle\left\langle\sin^2\theta\cos^8\theta\right\rangle\right\rangle(t_d)\\
&+\ c_{25}^{(n)}\left\langle\left\langle\sin^2\theta\cos^4\theta\right\rangle\left\langle\sin^2\theta\cos^{10}\theta\right\rangle\right\rangle(t_d)+c_{33}^{(n)}\left\langle\left\langle\sin^2\theta\cos^6\theta\right\rangle^2\right\rangle(t_d)\\
&+\ c_{34}^{(n)}\left\langle\left\langle\sin^2\theta\cos^6\theta\right\rangle\left\langle\sin^2\theta\cos^8\theta\right\rangle\right\rangle(t_d)+c_{35}^{(n)}\left\langle\left\langle\sin^2\theta\cos^6\theta\right\rangle\left\langle\sin^2\theta\cos^{10}\theta\right\rangle\right\rangle(t_d)\\
&+\ c_{45}^{(n)}\left\langle\left\langle\sin^2\theta\cos^8\theta\right\rangle\left\langle\sin^2\theta\cos^{10}\theta\right\rangle\right\rangle(t_d)+c_{55}^{(n)}\left\langle\left\langle\sin^2\theta\cos^{10}\theta\right\rangle^2\right\rangle(t_d) \qquad (5.5)
\end{aligned}
$$

Or it is simply written as

$$
S^{(n)}(t_d)=\sum_{j=1}^{5}\sum_{j'\geq j}^{5}c_{jj'}^{(n)}\left\langle\left\langle\sin^2\theta\cos^{2j}\theta\right\rangle\left\langle\sin^2\theta\cos^{2j'}\theta\right\rangle\right\rangle(t_d) \qquad (5.6)
$$

Above, coefficients $c_{jj'}^{(n)}$ are related to $b_j^{(n)}$ coefficients of Eq. (5.4) through

$$
c_{j,j'}^{(n)}=\begin{cases}\left|b_j^{(n)}\right|^2 & \text{for } j=j'\\ 2Re\left(b_j^{(n)}b_{j'}^{(n)*}\right) & \text{for } j\neq j'\end{cases} \qquad (5.7)
$$

Eq. (5.6) is an exact expression for the dynamic HHG signal of CO_2 at a delay time t_d after the pump pulse. The value of $\langle\langle f(\theta)\rangle\rangle$ depends on the pump parameters, the initial temperature, and the molecular properties such as the polarizability, the nuclear statistics, the molecular rotational constant, and the HOMO symmetry. In contrast, $c_{jj'}^{(n)}$ coefficients depend on the probe parameters and the molecular properties such as the ionization potential, the binding energy, and the HOMO symmetry.

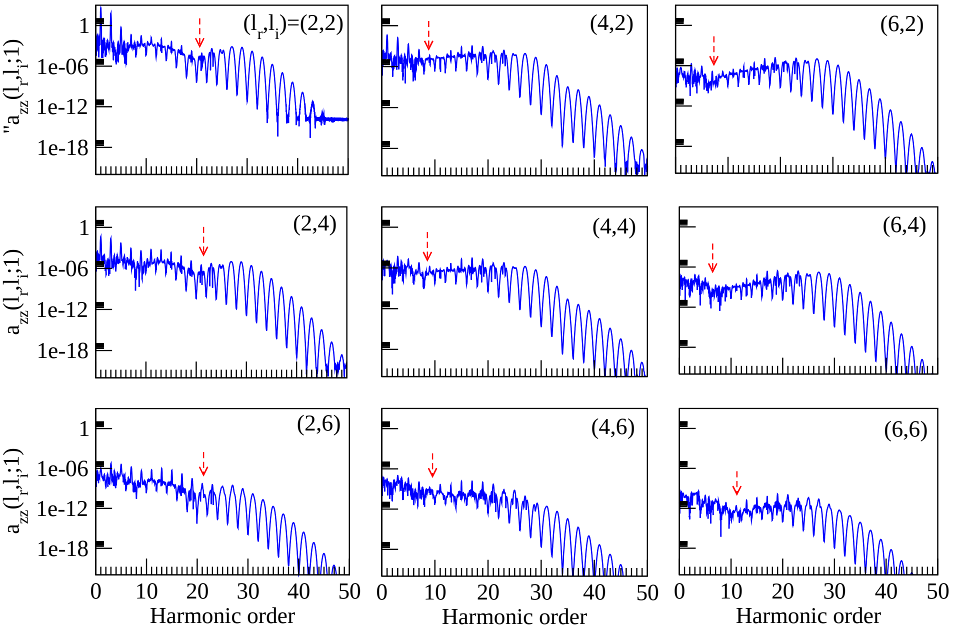

Figure 5.2: The contribution of different angular momentum (l_r, l_i) to the whole HHG spectrum of CO_2. The quantities in y-axis are $\tilde{a}_{zz}(l_r, l_i; m = 1)$, which is the electronic part of Fourier transform of electronic dipole. We use (probe) pulse of intensity $I_{probe} = 1.5 \times 10^{14}\,\mathrm{W/cm^2}$, wavelength $\lambda = 800\,\mathrm{nm}$, and 36 cycles, corresponding to $\gamma = 0.876$. The arrows show the position of minima.

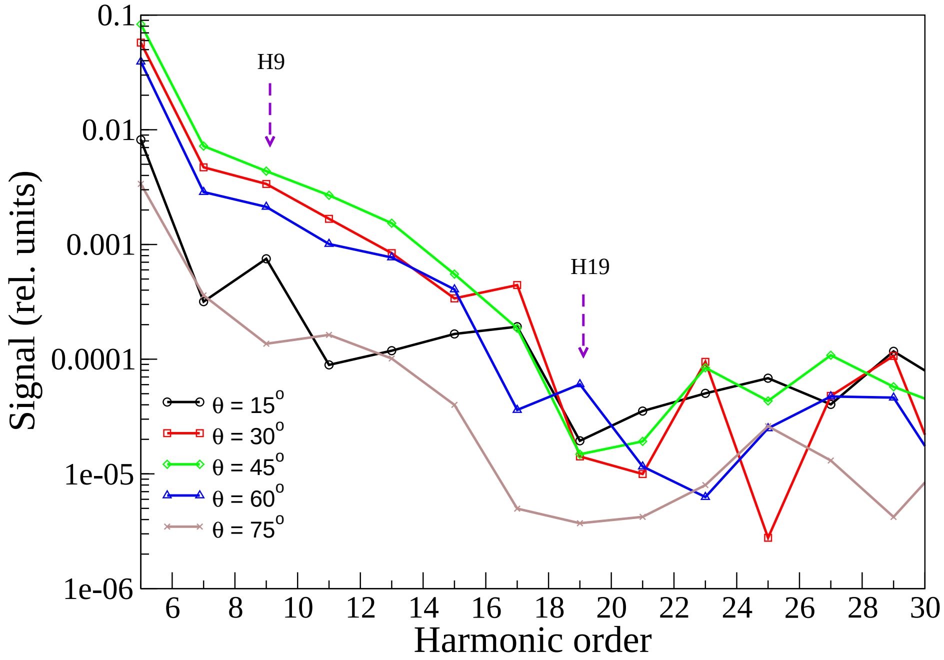

Figure 5.3: HHG spectrum of CO_2 for various alignment angle. The pulse parameters are similar to those of Fig. 5.2

5.2 HHG Spectrum

To obtain the $c_{jj'}^{(n)}$ coefficients, we first calculate $\tilde{a}_{zz}(l_r, l_i; m)$ which is the electronic part of the Fourier transform of the expectation value of the electronic dipole operator (see Eq. (2.70)). In real computations, we use the molecular properties which are shown in Tab. 5.2. The calculated spectra of CO_2 for individual angular momentum are shown in Fig. 5.2. It can be seen from the figures that the shape of spectrum and its minima positions change with the initial and final angular momenta, implying that the whole spectrum strongly depends on its HOMO. The minima occurs at $n = 21$ for the final momentum $l_r = 2$ and $n = 9$ for $l_r = 4$, regardless of the initial momentum l_i. For $l_f = 6$, the position of minima depends on the l_i, where $n = 9$ for $(l_r, l_i) = (6, 2)$, $n = 7$ for $(6, 4)$, and $n = 11$ for $(6, 6)$. From the shifting of the minima positions, one can see that the recombination plays a greater role on the harmonic signal. This conclusion well agree with the experimental observation by Itatani *et al.* [70]. Fig. 5.2 also shows that the value $\tilde{a}_{zz}(l_r, l_i; m)$ depends on (l_r, l_i) such that the lower (l_r, l_i) gives stronger contribution to the spectrum. The later fact can be easily understood because $\tilde{a}_{zz}(l_r, l_i; m)$ depends on $C_{l_r}^{(m)} C_{l_i}^{(m)}$, whereas $C_l^{(m)}$ decreases with increasing l.

The total spectrum calculated by including the contributions of all the initial and the final angular momenta, for various alignment angles θ, is shown in Fig. 5.3. It is seen in the figures, the maximum alignment angle, i.e. the angle that gives a maximum HHG signal, changes with the order of the harmonic. For low harmonic orders, the maximum angle is $\theta_{peak} = 45^o$, whereas for $n \geq 17$, the peak of harmonic is quite sensitive to the harmonic order. Comparing 9th and 19th harmonic orders, we obtain that $S(\theta = 45°) > S(\theta = 30°) > S(\theta = 60°) > S(\theta = 15°) > S(\theta = 75°)$ for the 9th harmonic order whereas $S(\theta = 60°) > S(\theta = 15°) > S(\theta = 45°) > S(\theta = 30°) > S(\theta = 75°)$ for the 19th harmonic order. These phenomena will be discussed further later.

5.3 Dynamic Signal

We tested the present theory against the experiment by Miyazaki *et al.* [138, 72]. They presented the dynamic HHG signal as a function of the delay time between the pump and the probe pulse, for the 19th and the 9th harmonic orders, for the following laser parameters: $I_{pump} = 0.56 \times 10^{14}\,\mathrm{W/cm^2}$ and $I_{probe} = 1.3 \times 10^{14}\,\mathrm{W/cm^2}$ for the 9th harmonic while $I_{pump} = 0.53 \times 10^{14}\,\mathrm{W/cm^2}$ and $I_{probe} = 1.5 \times 10^{14}\,\mathrm{W/cm^2}$ for 19th harmonic. The initial temperature is assumed to be 300 K. The calculated Fourier spectra are found to well agree with the experimental data (cf. discussion in § 6.4). For calculating the dynamic signal, we first evaluate $\tilde{a}_{zz}(l_r, l_i; m)$ from Fig. 5.2, and then we obtain the $c_{j,j'}^{(n)}$ coefficients, whose value for $n = 9$ and $n = 19$ are given in Tab. 5.3.

The calculated dynamic HHG signals for the 9th harmonic order is shown in Fig. 5.4. As a comparison, also shown is the expectation value of its dynamic alignment degree

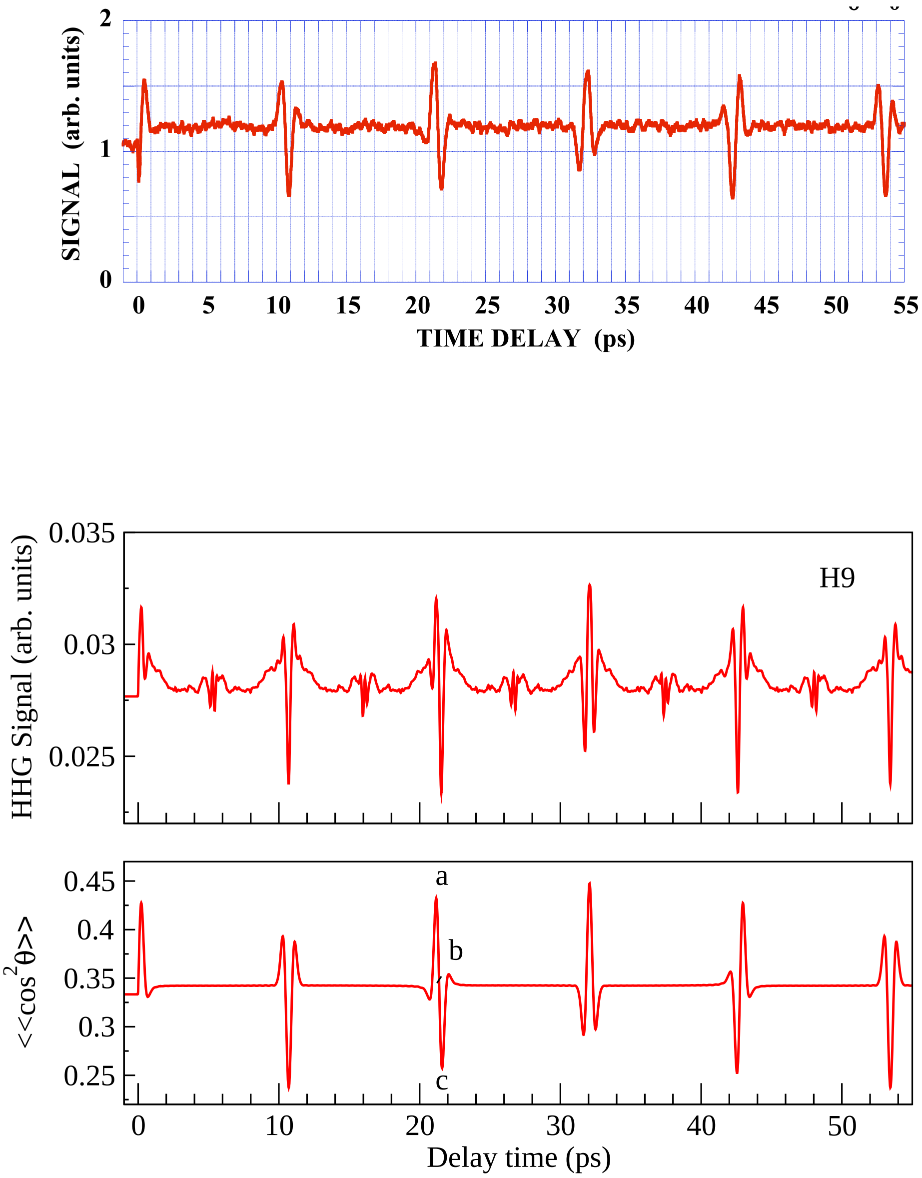

Figure 5.4: Comparison of the experimental (upper panel) (from [138]) and the theoretical dynamic (middle panel) of 9th HHG signal for CO_2; pump intensity $I = 0.56 \times 10^{14}$ W/cm^2, probe intensity $I = 1.3 \times 10^{14}$ W/cm^2; duration 40 fs, wavelength 800 nm, temperature 300 K. The corresponding alignment degree $\langle\langle \cos^2\theta \rangle\rangle$ is presented in lower panel.

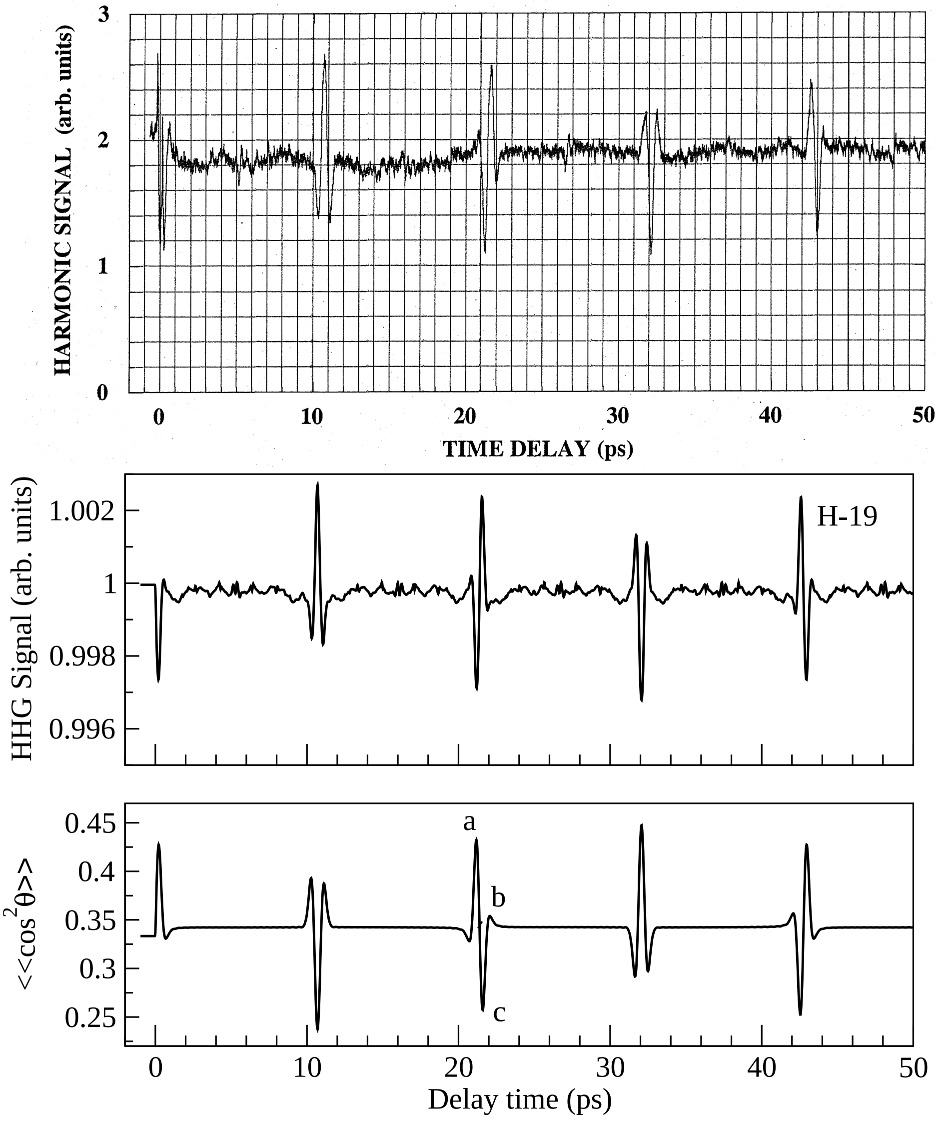

Figure 5.5: Comparison of the experimental (upper panel) (from [138, 72]) and the theoretical dynamic (middle panel) of 19th HHG signal for CO_2; pump intensity $I = 0.53 \times 10^{14}$ W/cm^2, probe intensity $I = 1.5 \times 10^{14}$ W/cm^2; duration 40 fs, wavelength 800 nm, temperature 300 K. The corresponding alignment degree $\langle\langle \cos^2\theta \rangle\rangle$ is presented in lower panel.

Table 5.3: The $c_{j,j'}^{(n)}$ and related expectation values of CO_2 for different harmonic order. The coefficients are *normalized* so that $c_{1,1} = 1$.

(i,j)	Expectation value	9th harmonic	19th harmonic
(1,1)	$\left\langle \left\langle \sin^2\theta \cos^2\theta \right\rangle^2 \right\rangle$	1	1
(1,2)	$\left\langle \left\langle \sin^2\theta \cos^2\theta \right\rangle \left\langle \sin^2\theta \cos^4\theta \right\rangle \right\rangle$	0.9017	-2.4287
(1,3)	$\left\langle \left\langle \sin^2\theta \cos^2\theta \right\rangle \left\langle \sin^2\theta \cos^6\theta \right\rangle \right\rangle$	-3.6058×10^{-2}	-2.07249
(1.4)	$\left\langle \left\langle \sin^2\theta \cos^2\theta \right\rangle \left\langle \sin^2\theta \cos^8\theta \right\rangle \right\rangle$	-8.6300×10^{-4}	1.7335×10^{-2}
(1,5)	$\left\langle \left\langle \sin^2\theta \cos^2\theta \right\rangle \left\langle \sin^2\theta \cos^{10}\theta \right\rangle \right\rangle$	-4.5539×10^{-7}	$-1.7726 \times 10^{\cdot 5}$
(2,2)	$\left\langle \left\langle \sin^2\theta \cos^4\theta \right\rangle^2 \right\rangle$	0.2891	1.4999
(2,3)	$\left\langle \left\langle \sin^2\theta \cos^4\theta \right\rangle \left\langle \sin^2\theta \cos^6\theta \right\rangle \right\rangle$	3.6113×10^{-2}	2.6921
(2,4)	$\left\langle \left\langle \sin^2\theta \cos^4\theta \right\rangle \left\langle \sin^2\theta \cos^8\theta \right\rangle \right\rangle$	-3.6735×10^{-4}	-2.2063×10^{-2}
(2,5)	$\left\langle \left\langle \sin^2\theta \cos^4\theta \right\rangle \left\langle \sin^2\theta \cos^{10}\theta \right\rangle \right\rangle$	-7.3397 $\times 10^{-7}$	1.7583×10^{-5}
(3,3)	$\left\langle \left\langle \sin^2\theta \cos^6\theta \right\rangle^2 \right\rangle$	8.3103×10^{-3}	1.3783
(3,4)	$\left\langle \left\langle \sin^2\theta \cos^6\theta \right\rangle \left\langle \sin^2\theta \cos^8\theta \right\rangle \right\rangle$	2.2193×10^{-5}	-2.1479×10^{-2}
(3,5)	$\left\langle \left\langle \sin^2\theta \cos^6\theta \right\rangle \left\langle \sin^2\theta \cos^{10}\theta \right\rangle \right\rangle$	-1.5300×10^{-7}	4.6776×10^{-6}
(4,4)	$\left\langle \left\langle \sin^2\theta \cos^8\theta \right\rangle^2 \right\rangle$	14004×10^{-7}	8.5274×10^{-5}
(4,5)	$\left\langle \left\langle \sin^2\theta \cos^8\theta \right\rangle \left\langle \sin^2\theta \cos^{10}\theta \right\rangle \right\rangle$	1.2954×10^{-10}	-7.4602×10^{-8}
(5,5)	$\left\langle \left\langle \sin^2\theta \cos^{10}\theta \right\rangle^2 \right\rangle$	8.6550×10^{-13}	2.3247×10^{-10}

$\langle\langle \cos^2\theta \rangle\rangle$.[4] As can be seen from figure, both the 9th harmonic signal and its alignment degree $\langle\langle cos^2\theta \rangle\rangle$ have the same phase, by means that the harmonic signal is maximum (minimum) when its alignment degree is maximum (minimum). In contrast, the 19th harmonic signal (Fig. 5.5) has inverted phase compare with its dynamic alignment. Both signal have revival period $T_{rev} = 42.7\,\mathrm{ps}$, which satisfies $T_{rev} = 1/(2Bc)$ (Eq. (3.34)), which B is rotational constant whose value for CO_2 is listed in Tab. 5.2. Compare with N_2 and O_2, the dynamic signal of CO_2 has longer period due to its heavier molecular mass. The signal of CO_2 also shows a revival at $\frac{1}{8}T_{rev}$, even though with a weaker strength compare with one of O_2. These phenomena are also consistent with other experimental data [43, 138].

We note here that both inverted and non inverted signal are generated by the same HHG operator of CO_2 (Eq. (5.6)). The only differences are the strength and the sign of the coefficients, implies the different phase. The whole combination also affects on the ratio of $\frac{1}{8}$- and $\frac{1}{4}$-revival. By examining the $c_{jj'}^{(n)}$ coefficients from Tab. 5.3, it is shown that some terms do not have significant contribution. On the other hand, the expectation value reduces with increasing its order, so that the dynamic HHG signal for $n = 9$ and $n = 19$

---

[4] We note that the alignment degree and the ionization signal always have the same modulation phase. Therefore comparison of the phase of the dynamic HHG signal with that of the dynamic ionization signal can be simply done by comparing the phase of dynamic HHG signal with that of the alignment degree.

can be approximated as:

$$S^{(n)}(t_d) = \sum_{j=1}^{3} \sum_{j' \geq j}^{3} c_{jj'}^{(n)} \left\langle \left\langle \sin^2\theta \cos^{2j}\theta \right\rangle \left\langle \sin^2\theta \cos^{2j'}\theta \right\rangle \right\rangle (t_d) \tag{5.8}$$

In fact, as mentioned earlier, Kanai *et al.* [43] found empirically that their experimental HHG signals for CO_2 demanded heuristic introduction of operators involving *higher* order functions, meaning that the dynamic signal can not be expressed in term of $\left\langle \left\langle \sin^2 2\theta \right\rangle \right\rangle (t_d)$ only. A related phenomenon of interest first observed by Miyazaki *et al.* [138] is the appearance of extra series of lines in the Fourier spectrum of the dynamic HHG signal for CO_2, that can not be attributed to $\left\langle \left\langle \sin^2 2\theta \right\rangle \right\rangle (t_d)$. It can be seen now from Eq. (5.8), that the correspondingly higher order contributions with decreasing strengths are predicted by the present theory.

5.4 Origin of Inverted Modulation Phase

As mentioned above, the first interpretation on the origin of the inverted modulation on the dynamic HHG signal of CO_2 was proposed by Kanai *et al.* [43]. They attributed the inverted modulation phase as a manifestation of the destructive interference of recombination process from the two oxygen centers in CO_2. The idea was then adopted by other groups [146, 144].

However, there are some difficulties to understand the inverted modulation in the frame of Kanai *et al.*'s model. First, according to them, the destructive interference occurs when the recombined electron satisfies condition $R_0 \cos\theta = m\lambda$, where R_0 is internuclear distance, θ is alignment angle of molecule, m is integer, and λ is the wavelength of recombined electron. This destructive interference reduces the harmonic signal of the corresponding harmonic order and appears as a minimum in the harmonic spectra and as an inverted modulation in the dynamic signal. It implies that the minimum and inverted modulation occur in the same order, but without explanation how the minimum causes an inverted phase modulation. In addition, the model needs a quantity alignment angle θ to be constant. In fact, θ is a time-dependent quantity and should be averaged over the ensemble. Second, the bare quantum-interference model of Kanai *et al.* is not a complete interpretation because it does not take the probe parameters, tunneling ionization step, and electron acceleration step in to account. As a consequence, the order of inverted modulation should not change with the changing of the probe parameters. In fact, by using the same wavelength but different probe parameters, Miyazaki *et al.* [72], Vozzi *et al.* [144], and Lee *et al.* [134] have observed inverted phase at different harmonic order.

Concerning to the first point, we directly compare the calculated harmonic spectra at the top alignment and the spectra at the anti-top alignment (points a and c in Fig. 5.5(c), respectively), and draw the results in Fig. 5.6. The top spectrum reaches its minimum at $n = 21$, whereas the anti-top spectrum has minimum at $n = 23$. According, to Kanai *et*

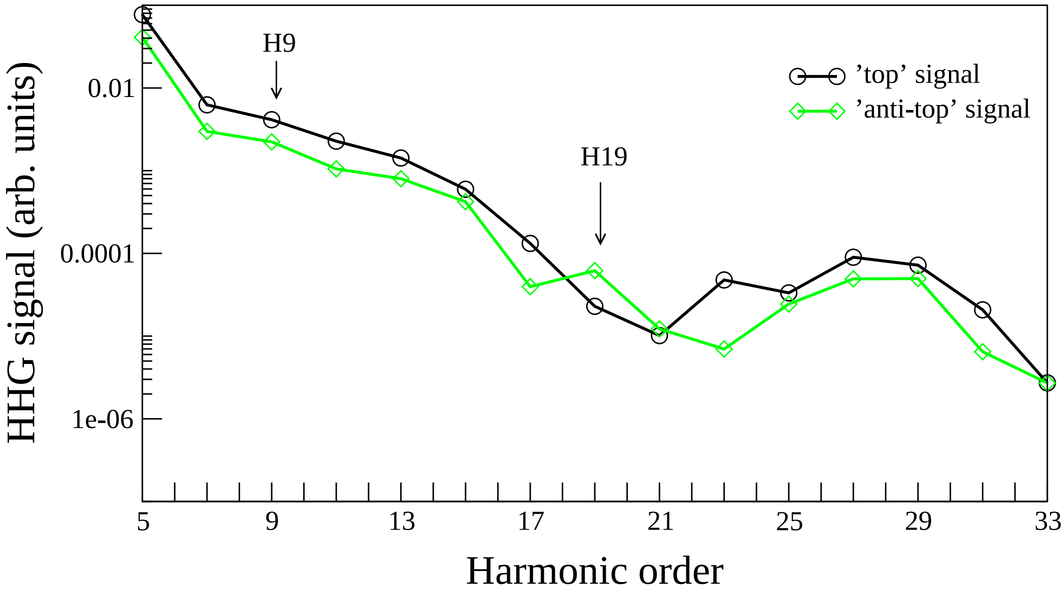

Figure 5.6: A direct comparison between the spectrum of the top alignment and the one of the anti-top alignment. The term top and anti-top alignment refer to the points a and c in Fig. 5.4. The pulse parameters are similar to those of Fig. 5.5.

al.'s model, the inverted modulation should occur at the same orders, either at $n = 21$ or $n = 23$. In fact, the dynamic signal of those both orders are not inverted, and we obtain the inverted modulation at $n = 19$, as shown in Fig. 5.5. We note that the dynamic signal of 19th harmonic order has a smaller top signal than the anti-top signal. On the other hand, for $n = 9$, whose dynamic signal is non inverted (Fig. 5.4), the top alignment signal is greater than that of the anti-top alignment. By using the same parameters, it was experimentally observed that the 19th harmonic signal has indeed inverted modulation as well as the 9th harmonic signal has the non-inverted signal compare to its ionization signal [138]. We remark that the inverted modulation is due mainly to the different minima's position of the top and the anti-top signal, and is not due to the minima itself, as claimed by Kanai *et al.*. In this regard, the inverted modulation can take place on the different order with respect to the order of minima, even tough they should close to each other.

Concerning to the second point, we recalculate the same HHG spectrum as in Fig. 5.6, but for a higher probe intensity. The results are shown in Fig. 5.7(a). In contrast to the prediction of Kanai *et al.*'s model, the present model shows that the inverted modulation shifts to higher order with increasing the probe intensity. The corresponding dynamic HHG signal with inverted modulation is shown in Fig. 5.7(b).

Another theoretical interpretation by Le *et al.* [110] stated that the inverted modulation was related to the squared HHG operator $\left|T_e^{(n)}(\theta)\right|^2$ of the interest harmonic order. The inverted modulation take places when $\left|T_e^{(n)}(\theta)\right|^2$ is peaked at $\theta_{peak} > 45^o$, whereas the non-inverted modulation occurs when $\theta_{peak} \leq 45^o$. To check the model, we draw the θ_{peak} for

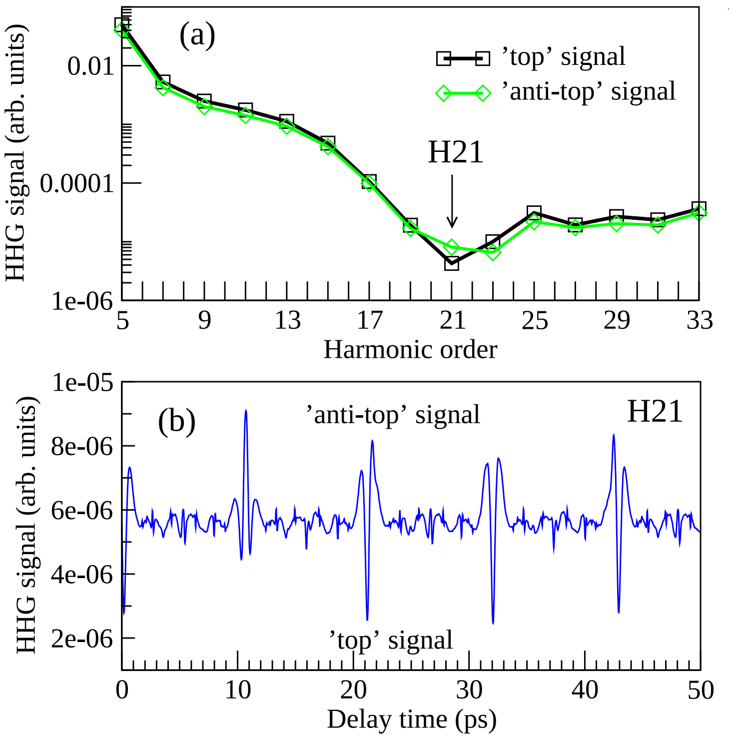

Figure 5.7: (a) A direct comparison between the spectrum of the top alignment and that of the anti-top alignment. (b) The dynamic signal of 21th harmonic order. The laser parameters are equal to the ones in Fig. 5.6, except the probe intensity which is $I = 2 \times 10^{14}\,\mathrm{W/cm^2}$.

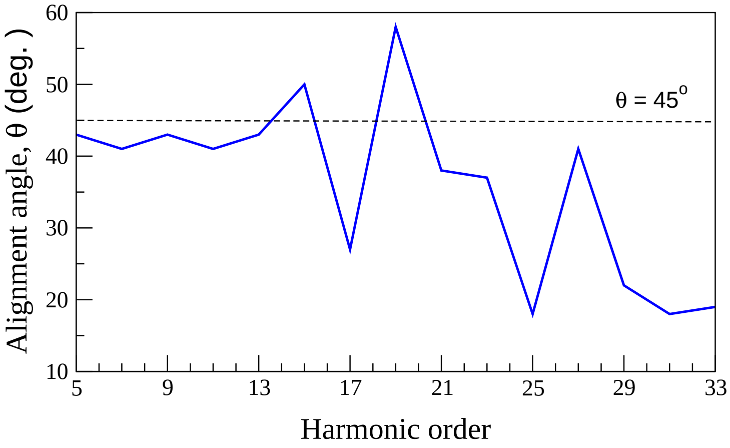

Figure 5.8: Peak of alignment dependence of HHG signal θ_{peak} as a function of harmonic order. The laser parameters are equal to those in Fig. 5.6.

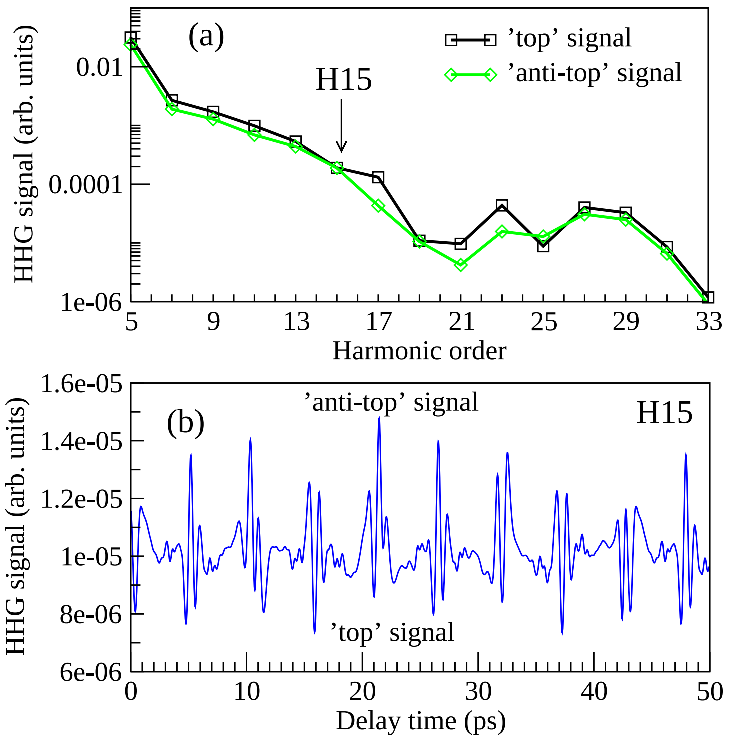

Figure 5.9: (a) A direct comparison between the spectrum of the top alignment and the one of the anti-top alignment. (b) The dynamic signal of 21th harmonic order. The laser parameters are equal to the one in Fig. 5.6, except the initial temperature, T = 25 K.

$5 \leq n \leq 33$, in Fig. 5.8. It was shown that the squared operator reaches its maximum at angle greater than 45^o for $n = 15$ and $n = 19$. According to Le *et al.*'s model, both harmonic orders should have an inverted modulation. However, our calculation shows that the dynamic signal of 15th harmonic order has non-inverted modulation. We will discuss it further later.

The Le *et al.*'s model has shown the dependence of the order of inverted modulation on the probe pulse. But, on the other hand, it did not take into account the changing of molecular distribution due to different pump parameters. Our calculation however, shows that the different initial temperature gives different position of minima. For initial temperature T = 25 K, we get inverted modulation for 19th and 15th harmonic orders, as shown in Fig. 5.9.

We now come to the interpretation of inverted modulation according to the present theory. Based on the previous discussion, one can say that the signal modulation is due to the different strength between the top signal and the anti-top signal, as a result of different spectrum and position of minima between them. If top signal is stronger [weaker] than the anti-top signal, then we get non-inverted [inverted] modulation. Therefore, the best way to predict the phase modulation is by drawing the spectrum of the top and anti-top signal, and directly comparing them, to each ther, as done in Figs. 5.6,

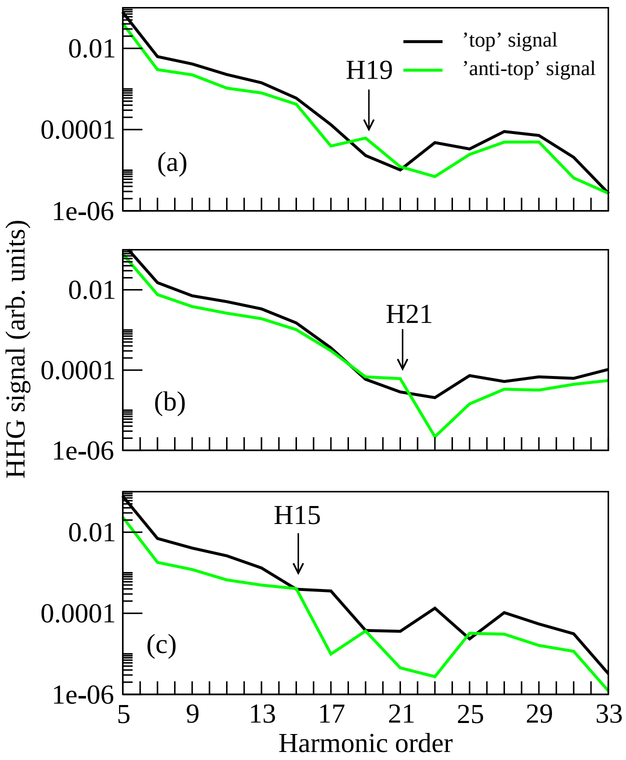

Figure 5.10: Semi-classical HHG spectrum of Fig 5.6 (panel a), Fig 5.7 (panel b), and Fig. 5.9 (panel c).

5.7(a), and 5.9(a). Instead of quantum mechanical calculation which is very time consuming, it can be done quickly by semi classical interpretation that molecules have a classical angle $\theta_{top} = \arccos\left(\sqrt{\langle\langle\cos^2\theta\rangle\rangle\,(t_d = t_{top})}\right)$ at top signal and have $\theta_{anti\,top} = \arccos\left(\sqrt{\langle\langle\cos^2\theta\rangle\rangle\,(t_d = t_{anti\,top})}\right)$ at anti-top signal. Fig. 5.10 shows the HHG spectra of the previous three cases, which are recalculated by using semi classical way. In general, the semiclassical spectrum are similar to the that calculated by using quantum mechanics. They predict the same position of minima, inverted phase, and harmonic cut-off.

Another signature of inverted modulation is related to θ_{peak}, θ_{top}, and $\theta_{anti\,top}$. Let first define $\Delta\theta_{top} \equiv |\theta_{top} - \theta_{peak}|$ and $\Delta\theta_{anti\,top} \equiv |\theta_{anti\,top} - \theta_{peak}|$. If $\Delta\theta_{top} \leq \Delta\theta_{anti\,top}$, it means that θ_{top} is closer to θ_{peak}, than $\theta_{anti\,top}$. Therefore the top signal is stronger than the anti-top signal, provides a non-inverted modulation dynamic signal. In contrast, if $\Delta\theta_{top} > \Delta\theta_{anti\,top}$, we obtain an inverted modulation signal. In Fig. 5.11(a) we draw the peak alignment of the HHG spectrum from Fig. 5.6, for $n = 15 - 23$. From the figure, one can see that θ_{peak} for 15th and 19th harmonic orders are greater than 45^o, and according to the Le *et al.*'s model, their dynamic signal should be inverted. From the view of the present theory, we get that $\Delta\theta_{top} > \Delta\theta_{anti\,top}$ for 19th harmonic order and therefore its dynamic signal has an inverted modulation. In contrast, for 15th harmonic order, we get $\Delta\theta_{top} < \Delta\theta_{anti\,top}$, so that its dynamic signal is non-inverted. Fig. 5.11(b) shows the the

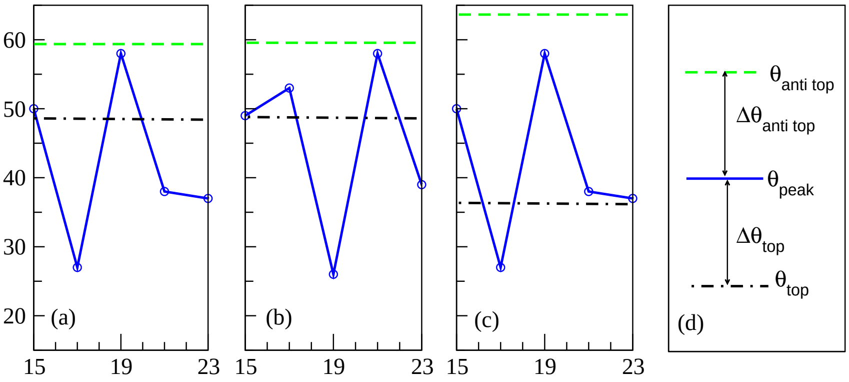

Figure 5.11: Peak of alignment dependence of HHG signal θ_{peak} as a function of harmonic order, obtained from Fig. 5.6 (panel a), Fig 5.7 (panel b), and Fig. 5.9 (panel c).

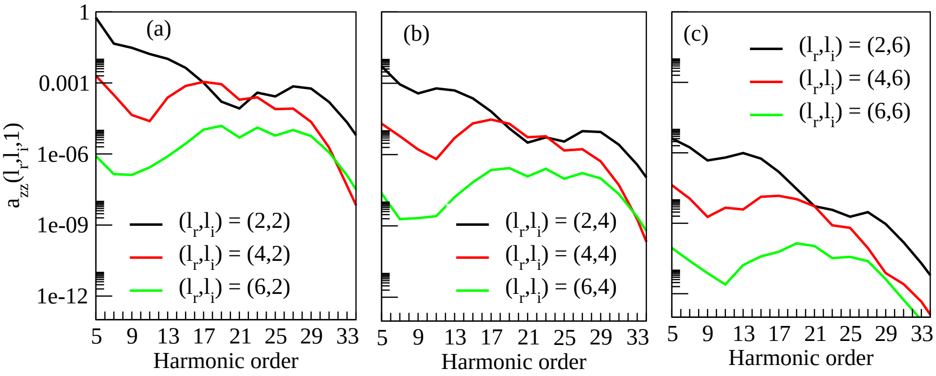

Figure 5.12: Contribution of individual $\tilde{a}_{zz}(l_r, l_i; m)$ on the whole spectrum.

peak alignment of HHG spectrum from Fig. 5.7. From the spectrum, we predict the 17th harmonic order to have non-inverted modulation, even tough it satisfies $\theta_{peak} > 45^o$. On the other hand, the 21th harmonic order has an inverted modulation, as it has been calculated. Fig. 5.11(c) shows the peak alignment of the HHG spectrum from Fig. 5.9. From the spectrum, we obtain an inverted modulation for $n = 19$ and $n = 15$ harmonic orders.

We note here that the present model has covered all parameters used in experiments. θ_{peak} depends on the probe parameters, whereas θ_{top} and $\theta_{anti\,top}$ depend on the pump parameters. Figs. 5.11(a) and 5.11(b) have a similar pump parameters, but different probe parameters. As a results, they have the same θ_{top} and $\theta_{anti\,top}$, but different θ_{peak}. The other case, Figs. 5.11(a) and 5.11(c) have a similar probe parameters, but different pump parameters. Therefore they have the same θ_{peak} but different θ_{top} and $\theta_{anti\,top}$.

To further understand the origin of the inverted phase, we calculate the individual contribution of $\tilde{a}_{zz}(l_r, l_i; m)$ for various (l_r, l_i), where l_r and l_i stand for the final and the initial angular momentum, respectively. The results are drawn in Fig. 5.12. In general, the value of $\tilde{a}_{zz}(l_r, l_i; m)$ depends on their asymptotic coefficients $C_{l_r}^{(m)}$ and $C_{l_i}^{(m)}$. In fact, $C_{l_r}^{(m)}$ ($C_{l_i}^{(m)}$) reduces with increasing l_r (l_i), and therefore the contribution of $\tilde{a}_{zz}(l_r, l_i; m)$ reduces

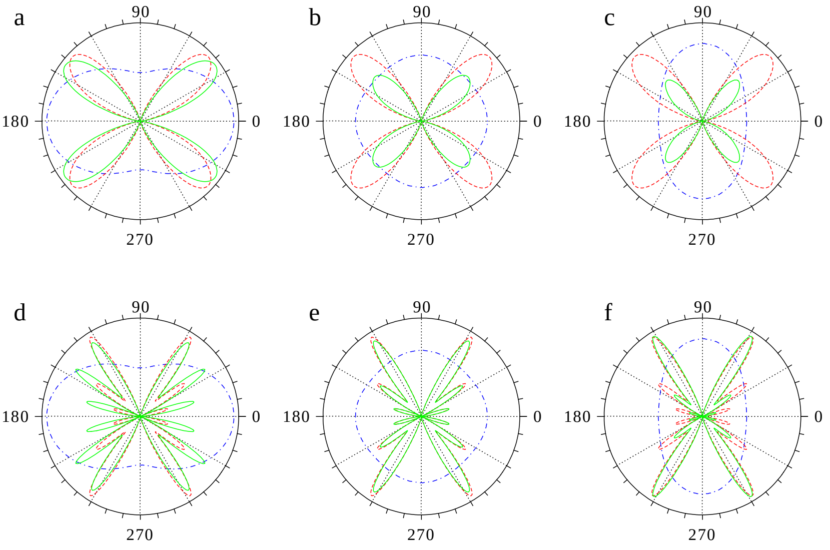

Figure 5.13: Molecular-axis distribution (blue, dash-dotted line), alignment-dependent signal (red, dashed line), and differential signal (green, solid line) at first half revival of CO_2. (a) H9 at top signal $t_d = 21.06\,\mathrm{ps}$, (b) H9 at average signal $t_d = 20.80\,\mathrm{ps}$, (c) H9 at anti-top signal $t_d = 21.60\,\mathrm{ps}$, (d) H-19 at top signal $t_d = 21.06\,\mathrm{ps}$, (e) H19 at average signal $t_d = 20.80\,\mathrm{ps}$, and (f) H19 at anti-top signal $t_d = 21.60\,\mathrm{ps}$. The laser parameters are similar with Fig. 5.4. The initial temperature is 300 K.

with increasing l_r and/or l_i. This situation takes places in the lower and higher harmonic orders, where the the greatest contribution comes from $\tilde{a}_{zz}(2,2;1)$ whose geometric factor $\left|d^2_{01}(\theta)\right|^2$ is peaked at $\theta \approx 45^o$, and therefore the dynamic signal in this harmonic region has non-inverted modulation. However, for CO_2 with a long internuclear distance, the ratio of asymptotic coefficients $C^{(1)}_{l+1}/C^{(1)}_l$ is significant, and therefore it is possible to obtain $\tilde{a}_{zz}(l_r+1,l_i;1)$ to be greater than $\tilde{a}_{zz}(l_r,l_i;1)$. For $n = 15-25$, some transitions with $l_r = 4$ grow rapidly and for some orders become more dominant than that with $l_r = 2$ (see Fig. 5.12(a)). The signals in this harmonic region are mainly generated by $\tilde{a}_{zz}(4,2;1)$ whose geometric factor $\left|d^2_{01}(\theta)d^4_{01}(\theta)\right|^2$ has two peaks: $\theta \approx 29^o$ and $\theta \approx 64^o$. The second peak contributes on the shifting of the peak alignment θ_{peak} to a higher θ, and enhances the possibility of inverted modulation on its dynamic signal. We remark that the inverted modulation takes place if most of the recombined electron have higher final momentum, than their initial momentum.

In Fig. 5.13 we plot the squared operator $\left|T^{(n)}_e(\theta)\right|^2$ (red, dashed line) that can be interpreted as alignment-dependence of HHG signal of a 'single' molecule. It can be seen that the HHG operator is peaked at $\theta \simeq 42^o$ for the 9th harmonic order, whereas for the 19th harmonic order it is peaked at three angles: $\theta \simeq 58^o$, $\theta \simeq 37^o$, and $\theta \simeq 15^o$. We also plot molecular-axis distribution, $P\left(t_d,\theta\right) = \Sigma_{J_0}\rho_{J_0}|\Phi_{J_0M_0}\left(t_d,\theta\right)|^2$, (blue, dash-dotted curve). The differential signal $dS^{(n)}\left(t_d,\theta_0,\phi_0\right)$ (green, solid line) is obtained by averaging the alignment angle dependent signal over the molecular distribution (c.f. Eq. (4.17)). Therefore $dS^{(n)}(t_d, \theta_0, \phi_0)$ tends to mimic $\left|T_e^{(n)}(\theta)\right|^2$. As $\left|T_e^{(n)}(\theta)\right|^2$, the differential signal has stronger peaks at $\theta \simeq 60^o$ and $\theta \simeq 30^o$, for $n = 19$. The existence of two peaks on θ-dependent signal is also found experimentally and theoretically by directly solving a model of Schrödinger equation [68].

Fig. 5.14 shows the time-dependent HHG differential signal for the 9th (upper panel) and the 19th (lower panel) of CO_2 calculated for $T = 300\,\mathrm{K}$. The distributions rapidly change both in time and axis angle and have a complex structure with several nodes. Even though the signals change with changing of delay time due to its dynamic electronic and molecular distribution, but they peak at the same alignment angle for all revival periods. This is the signature of $\left|T_e^{(n)}(\theta)\right|^2$ which is time-independent.

We summarize the origin of the inverted phase in HHG signal in CO_2 as follow. (i) The interaction between electron clouds and a laser probe creates different contributions from the angular momenta quantum states, and gives different HHG transition operator $\left|T_e^{(n)}(\theta)\right|^2$ which is specific for different harmonic order. (ii) Plotting $\left|T_e^{(n)}(\theta)\right|^2$ as a function of harmonic order n, gives us the minima, where their positions depend on a given alignment angle θ. Due to different alignment angle θ between the top and the anti-top signals, they have different position of minimum n. As a consequence, the top signal can be stronger [weaker] than the anti-top signal and give the non-inverted [inverted] phases modulation. (iii) For each harmonic order, $\left|T_e^{(n)}(\theta)\right|^2$ reaches its maximum at specific angle θ_{peak}. The inverted [non-inverted] modulation takes place if θ_{peak} close to $\theta_{anti\,top}$ [θ_{top}]. In general, we remark: (i) The *quantum interference* effect of a two-center molecule, appears in the one-center expansion of the molecular wavefunction as different contributions from the angular momenta components. (ii) The inverted phase is an effect of different strength between the top and the anti-top signal (as a consequence of different position of their minima), due to the recombined electrons mostly occupied a high momentum state l_r. Therefore, the inverted modulation is not due to the destructive interference itself. (iii) The inverted modulation is indicated by one of the following: (a) a greater spectrum from $\theta_{anti\,top}$ than that of θ_{top} or (b) θ_{peak} is closer to $\theta_{anti\,top}$, than to θ_{top}. The inverted phase, therefore, depends on all the three steps of HHG and all pump and probe parameters, taken together.

5.5 Inverted Modulation in Other Molecules

From the above discussion, it was concluded that the inverted modulation in CO_2 is due mainly to its π_g symmetry ($m = 1$). For the molecules with π_g symmetry, the electron clouds are peaked at an intermediate angle. In this situation, the most effective angle for HHG, θ_{peak}, can shift to be closer to classical top angle, θ_{top}, or classical anti-top angle, $\theta_{anti\,top}$. Therefore, it is also reasonable to expect the inverted modulation to occur in other π_g symmetry molecules. We will use two above indicators to investigate the possibility of

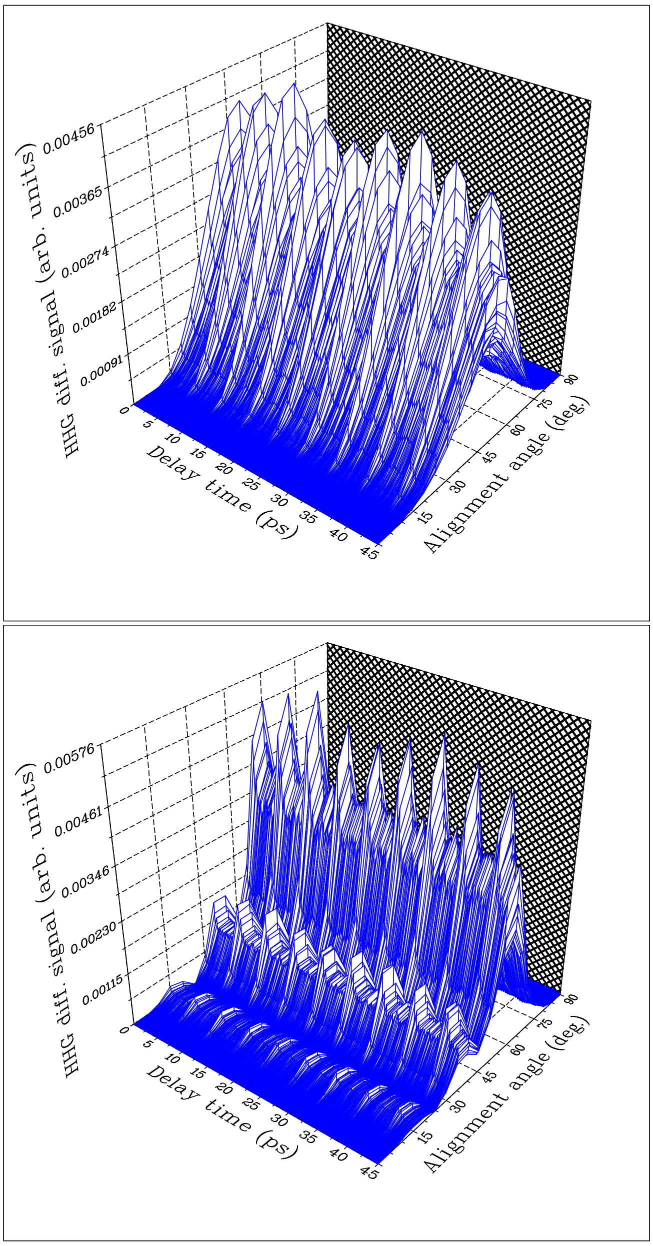

Figure 5.14: HHG differential signal for 9th (upper panel) and 19th (lower panel) of CO_2. The laser parameters are similar with Fig. 5.4 and 5.5, for 9th and 19th harmonic, respectively. The initial temperature is 300 K.

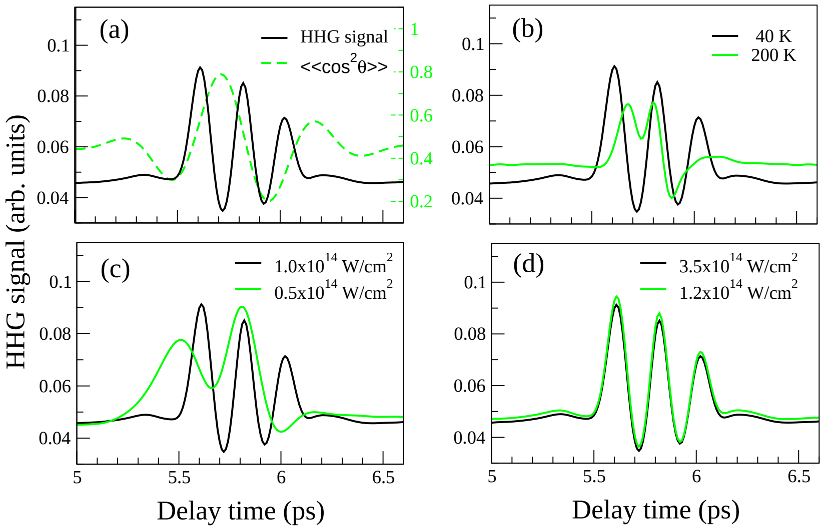

Figure 5.15: (a) Comparison between the dynamic signal of 47th harmonic signal for O_2 and its alignment degree at their first revival, for initial temperature 40 K. Pump intensity $I_{pump} = 1.0 \times 10^{14}\,\mathrm{W/cm^2}$, duration 60 fs; probe intensity $I_{probe} = 3.5 \times 10^{14}\,\mathrm{W/cm^2}$, duration 30 fs, mean wavelength 800 nm. (b) Harmonic signal in (a) for various initial temperature. (c) Harmonic signal in (a) for various pump intensities. (d) Harmonic signal in (a) for various probe intensities.

inverted modulation in other molecules, in connecting with the recent experiments.

Recently, by using 30 fs and $3.5 \times 10^{14}\,\mathrm{W/cm^2}$ probe pulse (corresponding to theoretical cut-off $n = 51$), Vozzi *et al.* [73] have indeed observed a double peak structure of the 47th HHG signal of O_2, at its first half revival.[5] They claimed the double structure as an inverted modulation due to the destructive interference. In Fig. 5.15(a) we draw the theoretical dynamic signal of 47th harmonic of O_2 around its first half revival, by using the same pulse parameters as those in experiment. In contrast to the alignment degree, the peak of harmonic signal has a double structure, and it reaches its minimum when the alignment degree $\langle\langle\cos^2\theta\rangle\rangle$ reaches maximum. As discussed in § 4.4, the double structure occurs when $\theta_{peak} \leq \theta \leq \theta_{top}$ for $\theta_{peak} < \theta_{top}$: a condition when the alignment degree still grows due to its angle has not reached θ_{top}, whereas the harmonic signal reduces as the alignment angle exceeds θ_{peak}. The same situation occurs when $\theta_{peak} \geq \theta \geq \theta_{top}$ for $\theta_{peak} > \theta_{top}$. In this delay time, harmonic signal has the opposite phase with respect to the alignment degree. For a higher initial temperature, the top angle θ_{top} become closer to the peak alignment θ_{peak}, gives a shallower 'valley' in a double peak structure, as shown in Fig. 5.15(b). A possible explanation is that the 'inverted-like' modulation observed by Vozzi *et al.* is not due to the destructive interference, but due to the double structure at a lower initial temperature gas jet. In contrast to the inverted modulation, the double peak is sensitive to the pump parameters (Fig. 5.15(c)), but not sensitive to the probe parameters

---

[5] Unfortunately, they did not present the full period dynamic signal, except around its first revival. Therefore we do not know the phase of HHG signal at the other fractional revivals.

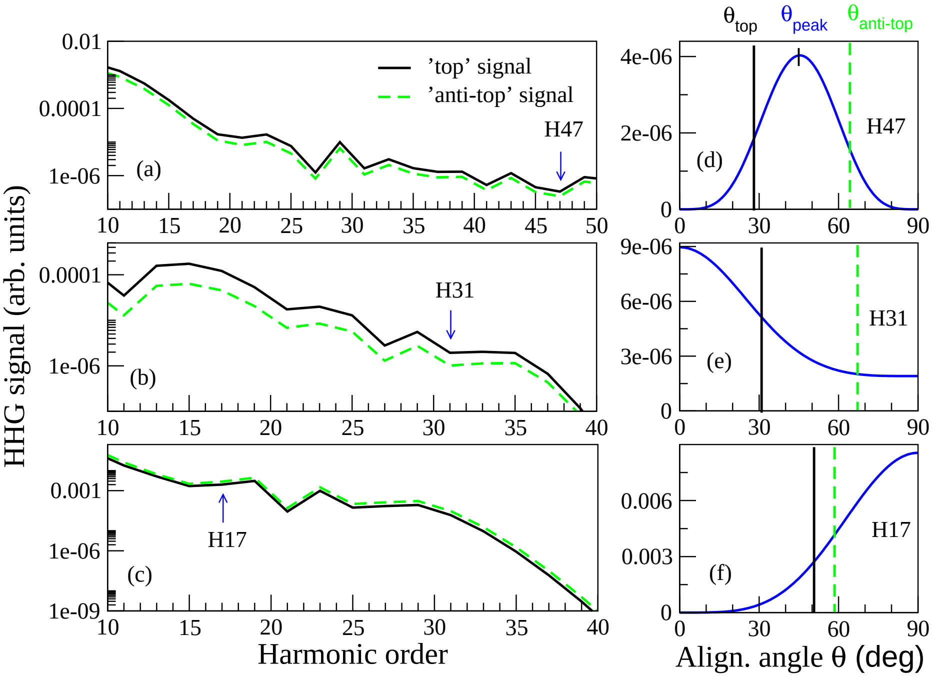

Figure 5.16: Left column: harmonic spectra of O_2 (panel a), N_2 (panel b), and ethylene (panel c). Right column: the corresponding alignment dependent signal for interest orders, i.e for O_2 (panel d), N_2 (panel e), and ethylene (panel f). The pulse parameters are given in text.

(Fig. 5.15(d)).

In Fig. 5.16(a), we directly compare the harmonic spectra for the top and anti-top classical angles. It can be seen in the figure that even-tough there is a local minimum at $n = 47$, but the top signal is always stronger that of the anti-top signal: a characteristic of a non-inverted modulation (see also Fig. 5.15(a)). The conclusion is supported by Fig. 5.16(d) confirms that $\Delta\theta_{top} < \Delta\theta_{anti-top}$.

It is also interesting to know if inverted modulation occurs in σ_g molecules, like N_2. Recently, by using $I_{pump} = 6 \times 10^{13}\,\mathrm{W/cm^2}$, 50 fs pump pulse and $I_{probe} = 2 \times 10^{14}\,\mathrm{W/cm^2}$, 50 fs, and 800 nm, Kanai *et al.* have measured the ellipticity dependence of HHG signal of aligned molecules [74]. They found that for N_2 at top signal, the 31st harmonic signal was suppressed in a small range around zero ellipticity, in contrast to the HHG from its companion atom, Ar. They argued that the suppression was a signature of inverted modulation.[6] In Fig. 5.16(b), we draw theoretical HHG spectrum with the same parameters and $T = 25\,\mathrm{K}$. However, the present theory does not predict the inverted modulation to

---

[6] Another experiment by Flettner *et al.* [155, 156] has shown a discrepancy between the ellipticity dependence HHG signal of non-aligned N_2 and the one of Ar . They measured that the HHG signal of N_2 is enhanced for $\epsilon \geq 0.2$, in contrast to the HHG signal of Ar. On the other words, one can say that the HHG signal of N_2 is suppressed at $\epsilon < 0.2$, in contrast to that of Ar. Our remark, if both top-aligned signal (as observed by Kanai *et al.*) and non-aligned signal (as observed by Flettner *et al.*) are suppressed, then it is a signature of minima, not a signature of inverted modulation.

occur in N_2, even though there is a minimum at $n = 31$. For N_2, the signal is peaked at $\theta = 0^o$. Therefore $\Delta\theta_{top}$ is always smaller than $\Delta\theta_{anti-top}$, as shown in Fig. 5.16(e). In this case, the top alignment always has stronger signal than the anti-top alignment. It gives us a non-inverted modulation.

More recently, the inverted modulation phase was seen in plateau region (17th - 27th harmonic orders) for some organic molecules, such as acetylene ($\mathrm{HC} \equiv \mathrm{CH}$, linear), allene ($\mathrm{H_2C} = \mathrm{C} = \mathrm{CH_2}$, symmetric top), and ethylene ($\mathrm{H_2C} = \mathrm{CH_2}$, asymmetric top), all of which have bonding π orbitals between the carbon atoms [157, 158]. Among three molecules, the dynamic alignment of ethylene is most well investigated from the point of view that its one dimensional alignment has been observed experimentally [159, 160] and its three dimensional alignment has been explored theoretically [161]. In Fig. 5.16(c), we draw a theoretical spectrum for ethylene. We use the same parameters as those in experiment: a probe pulse of intensity $I_{probe} = 1.8 \times 10^{14}\,\mathrm{W/cm^2}$ and duration 14 fs. The pump pulse reaches a classical top angle $\theta_{top} \approx 50^o$ and an classical anti-top angle $\theta_{anti\,top} \approx 58^o$. The wavefunction is approximated by $l = 1, 3$ and $m = \pm 1$, with $C_1^{(\pm 1)} = \pm 1.10$ and $C_3^{(\pm 1)} = \pm 0.22$ [162]. The electron clouds is therefore peaked at $\theta \approx 37^o$. From the figure, one sees that for the whole orders, the top signal is weaker than the anti-top signal, gives us an inverted modulation. Fig. 5.16(f) shows that the alignment signal of 17th harmonic order is peaked at $\theta_{peak} = 90^o$: a guarantee that the inverted modulation for this order is kept for any initial temperature.

Chapter 6

Signal in Frequency Domain: Fourier Analysis of Dynamic HHG Signal

The previous discussion on the dynamic signal of N_2, O_2 (chapter 4), and CO_2 (chapter 5) provides that the dynamic signal is generated by transitions which differ in their rotational quantum numbers by ΔJ related to the frequency $\{(J+\Delta J)(J+\Delta J+1)-J(J+1)\}Bc$. A better understanding of the above transition can be obtained by investigating the HHG spectrum in the frequency domain, that can be obtained by Fourier transforming the dynamic signal (t_d-dependence) and plotting the Fourier amplitude as a function of its frequency in units of Bc.

The first experimental data of the spectral frequency of dynamic alignment was the spectrum of aligned I_2 observed by using its dissociation signal [140, 44]. The spectrum showed a ladder of beat frequencies with a spacing equal to $4Bc$. Dooley *et al.* then reported the frequency spectrum of dynamic alignment of N_2 and O_2 observed by using dissociation by Coulomb explosion [27]. They also reported that the signal ratio between the even and the odd J could be understood as due to the nuclear statistics of the corresponding molecule. Later on, the frequency spectrum of the dynamic alignment of CO_2, observed by monitoring its optical Kerr effect, was also reported [32]. The Kerr signal was proportional to the square of measured alignment ($I(t_d) = \left[\left\langle\left\langle \cos^2\theta \right\rangle\right\rangle(t_d) - \frac{1}{3}\right]^2$) and, therefore, the frequency spectrum not only consisted of its original frequency but also the sum and the difference frequencies, as indicated by the presence of an extra series at low frequencies. A similar frequency-spectra was also produced from the aligned O_2 molecules observed by time-dependent degenerate four-wave mixing (TD-DFWM) [163].

The first frequency spectrum of dynamic HHG signal was reported by Miyazaki *et al.* [135, 82, 71, 138]. They measured the dynamical HHG signals of N_2, O_2, and CO_2 and Fourier transformed them to obtain the signals in the frequency domain. For all the three molecules, the signals showed initially unexpected extra series of peaks, that could not be associated with the respective Fourier transform ($F.T.$) of $\left\langle\left\langle\cos^2\theta\right\rangle\right\rangle$ for N_2 and $\left\langle\left\langle\sin^2 2\theta\right\rangle\right\rangle$ for O_2 and CO_2. As mentioned above, these extra series were also present in the frequency spectrum observed by optical Kerr signal [32] but absent in its ionization signal [44, 140, 27]. These facts suggest that the HHG signal is proportional to the square of the measured alignment as shown in Eq. (2.49). For HHG, the signal is proportional to the square of the expectation value of the $F.T.$ of the total dipole. It implies the dependence of HHG signal on higher order alignment moments.

Unlike the dynamic signal, the frequency spectrum provides more succinct and clearer information of the beats involved in the signal and provides a better way for distinguishing the role of the order of the alignment operator. Based on Eq. (4.5) for N_2, Eq. (4.12) for O_2, and Eq. (5.5) for CO_2, the dynamic HHG signal is also related to the sum and difference frequencies

$$\begin{aligned} &= \left[\{(J+\Delta J)(J+\Delta J+1)-J(J+1)\} \pm \{(J'+\Delta J')(J'+\Delta J'+1)-J'(J'+1)\}\right] Bc \\ &= \left[\Delta J\,(2J+\Delta J+1) \pm \Delta J'\left(2J'+\Delta J'+1\right)\right] Bc \end{aligned} \tag{6.1}$$

For $\left\langle\left\langle\cos^2\theta\right\rangle\right\rangle$, we have $\Delta J = 0, \pm 2$ and $\Delta J' = 0$. For $\left\langle\left\langle\sin^2\theta\cos^2\theta\right\rangle^2\right\rangle$, we have $\Delta J = 0, \pm 2, \pm 4$ and $\Delta J' = 0, \pm 2, \pm 4$. Moreover, the frequency spectrum also confirms the existence not only Raman transition with $|\Delta J| = 2$ and $|\Delta J'| = 2$ but also higher order transitions with $|\Delta J| \geq 4$ ($|\Delta J'| \geq 4$). In this chapter, we present the frequency spectrum of the dynamic alignment of N_2, O_2, and CO_2, directly compare them with experimental spectrum, and give a unified interpretation of their origin. We use the leading term of HHG operator to explain the salient features of the series observed by Miyazaki *et al.* [71, 138].

6.1 Frequency Spectrum of N_2

First, we Fourier transform the calculated dynamic signals of N_2 (c.f. Eq. (4.5)) to get their spectrum in frequency domain and directly compare the results with the experimental data, as shown in Fig. 6.1. The calculated data was obtained by assuming an initial temperature 200 K. We will discuss the initial temperature later. It can be seen from the figure that the experimental spectrum (panel a) exhibits two prominent series I: $(6, 14, 22, 30, ..)\,Bc$ and II: $(\mathit{10}, \mathit{18}, \mathit{26}, \mathit{34}, ..)\,Bc$, which are also present in the theoretical spectrum (panel b). They are easily understood to arise from the $F.T.$ of the $\left\langle\left\langle\cos^2\theta\right\rangle\right\rangle(t_d)$ term in Eq. (4.5) which vanishes unless $\Delta J = 0, \pm 2$, produces a sequence of lines $(E_{J+2} - E_J)/2\pi = (4J+6)\,Bc$, and gives series I and II for even and odd J, respectively. The relative prominence of the series I over the series II, in both the panels in Fig. 6.1, could be understood as the 2 : 1 ratio of even J over odd J value of the nuclear spin statistics of N_2 (e.g. [27, 117]). The weakly resolved series III: $(\mathbf{20}, \mathbf{28}, \mathbf{36}, \mathbf{44}, ..)Bc$ and series IV: $(\boldsymbol{4}, \boldsymbol{8}, \boldsymbol{12}, \boldsymbol{16}, \boldsymbol{..})Bc$ in Fig. 6.1(a) is the unexpected series and can not be produced by the $F.T.$ of the leading term $\left\langle\left\langle\cos^2\theta\right\rangle\right\rangle(t_d)$

Table 6.1: All possible frequency arising from $\langle\langle\cos^2\theta\rangle\rangle$, $\left\langle\langle\cos^2\theta\rangle^2\right\rangle$, and $\langle\langle\cos^4\theta\rangle\rangle$ for N_2 whose both odd and even J 's are allowed

No.	Group freq.	Weighting factor	Formula	Peak series (in Bc)	Expt. series
$\langle\langle\cos^2\theta\rangle\rangle$					
1	-	a	-	0	-
2	ω_1	b	$4J+6$	$10, 18, 26, \ldots$ for odd J $6, 14, 22, \ldots$ for even J	II I
$\left\langle\langle\cos^2\theta\rangle^2\right\rangle$					
3	-	aa'	-	0	-
4	ω_1 and ω_1'	$a'b$ and ab'	$4J+6$	$10, 18, 26, \ldots$ for odd J $6, 14, 22, \ldots.$ for even J	II I
5	$\omega_1+\omega_1'$	$\frac{bb'}{2}$	$4(J+J')+12$	$20, 28, 36, ..$	III
6	$\omega_1-\omega_1'$	$\frac{bb'}{2}$	$4(J-J')>0$	$4, 8, 12, ..$	IV
$\langle\langle\cos^4\theta\rangle\rangle$					
7	-	a	-	0	-
8	ω_1	b	$4J+6$	$10, 18, 26, \ldots$ for odd J $6, 14, 22, \ldots.$ for even J	II I
9	ω_2	c	$8J+20$	$28, 44, 60..$	III

(see Fig. 3.9(a)). We note that the series III and IV, although relatively weak, are certainly also present in the calculated spectrum (Fig. 6.1(b)). To interpret their origin, we therefore consider the two higher order terms involving $\left\langle\langle\cos^2\theta\rangle^2\right\rangle(t_d)$ and $\langle\langle\cos^4\theta\rangle\rangle(t_d)$ in Eq. (4.5). Because of squaring, the expected frequency from $\left\langle\langle\cos^2\theta\rangle^2\right\rangle(t_d)$ not only included the $(4J+6)Bc$ series but also its sum and its difference, as follow

$$\begin{aligned}(a+b\cos\omega_1 t)\left(a'+b'\cos\omega_1' t\right) &= aa'+a'b\cos\omega_1 t+ab'\cos\omega_1' t+bb'\cos\omega_1 t\cos\omega_1' t\\ &= aa'+a'b\cos\omega_1 t+ab'\cos\omega_1' t\\ &\quad+\frac{bb'}{2}\cos\left(\omega_1+\omega_1'\right)t+\frac{bb'}{2}\cos\left(\omega_1-\omega_1'\right)t \qquad (6.2)\end{aligned}$$

Above, the term a (a') is a weighting for the transition of $\Delta J=0$ ($\Delta J'=0$) with frequency $\omega_0=0$, whereas b (b') is the weighting factor for the transition of $\Delta J=\pm 2$ ($\Delta J'=\pm 2$) with frequency ω (ω'). The sum frequency $(\omega_1+\omega_1')$ is corresponding to the transition with $\Delta J=2$ and $\Delta J'=2$, and according to Eq. (6.1), it produces $(4(J+J')+12)\,Bc$ series. On the other hand, the difference frequency $(\omega_1-\omega_1')$ produces $(4(J-J')Bc)>0$ series. For integer J and J' they yield series IV: $(\boldsymbol{4, 8, 12, 16, ..})Bc$. The next term $\langle\langle\cos^4\theta\rangle\rangle(t_d)$ vanishes unless $\Delta J=0,\pm 2$, and ± 4 produces not only $(E_{J+2}-E_J)/2\pi=(4J+6)\,Bc$ sequences lines but also $(E_{J+4}-E_J)/2\pi=(8J+20)Bc$ gives series III $(\mathbf{20}, \mathbf{28}, \mathbf{36}, \mathbf{44}, ..)Bc$. The whole possible series arising from these three leading terms and their grouping according to experimental series are shown in Tab. 6.1. Note that series III is identical and hence

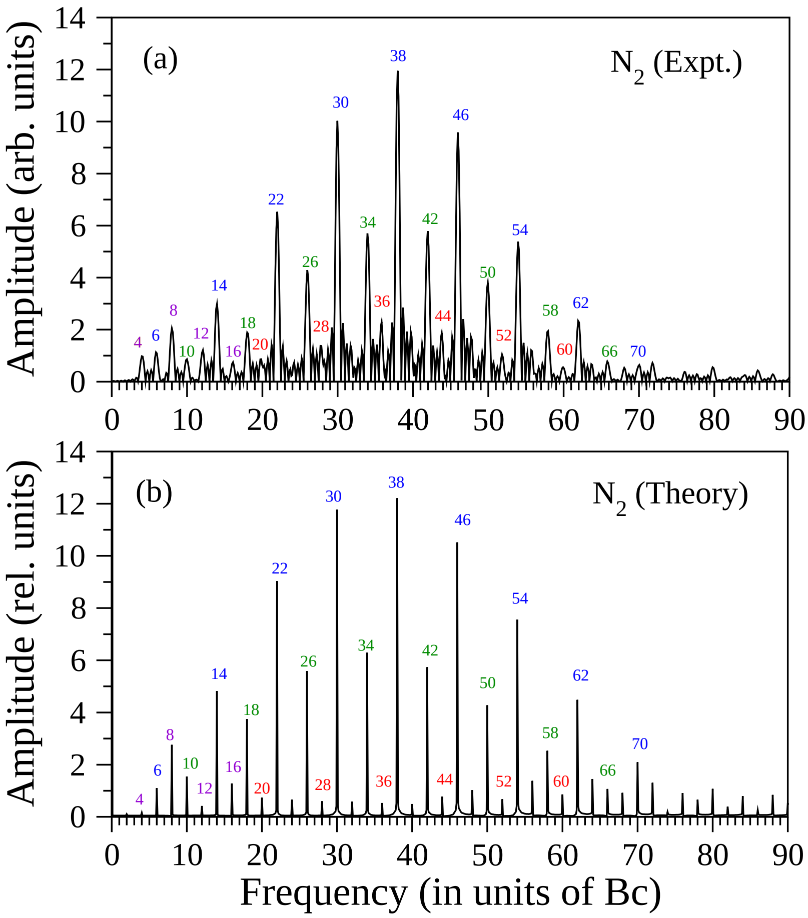

Figure 6.1: Comparison of the experimental (from [71]) and theoretical Fourier spectrum of the dynamic 19th harmonic signal for N_2. The spectrum shows series I: $(6, 14, 22, 30, 38, ..)\, Bc$ (blue mark), series II: $(\mathit{10}, \mathit{18}, \mathit{26}, \mathit{34}, \mathit{42}, ..)\, Bc$ (green mark), series III: $(\mathbf{20}, \mathbf{28}, \mathbf{36}, \mathbf{44}, \mathbf{52}, \mathbf{60}, ..)Bc$ (red mark), and series IV: $(\boldsymbol{4}, \boldsymbol{8}, \boldsymbol{12}, \boldsymbol{16}, \boldsymbol{..})Bc$ (violet mark). We use pump pulse of intensity $I_{pump} = 0.8 \times 10^{14}\,\mathrm{W/cm^2}$ and pulse width $FWHM = 40\,\mathrm{fs}$, and probe pulse of intensity $I_{probe} = 1.7 \times 10^{14}\,\mathrm{W/cm^2}$, wavelength $\lambda = 800\,\mathrm{nm}$, and 36 cycles. The initial temperature is 200 K.

overlap with the series IV: $(\boldsymbol{4}, \boldsymbol{8}, \boldsymbol{12}, \boldsymbol{16}, \boldsymbol{..})Bc$ and strengthen it. Moreover, the remaining lines at $(\boldsymbol{4}, \boldsymbol{8}, \boldsymbol{12}, \boldsymbol{16}, \mathbf{24}, \boldsymbol{32}, \boldsymbol{40}, \boldsymbol{48}, \boldsymbol{...})Bc$ found in the experimental spectrum in Fig. 6.1(a) as well as in the theoretical spectrum in Fig. 6.1(b), confirms the existence of series IV and distinguishes itself from series III. The existence of series III and IV is a prove that the dynamic signal of N_2 can not be described in term of $\langle\langle \cos^2\theta \rangle\rangle\,(t_d)$ only.

6.2 Frequency Spectrum of O_2

In Fig. 6.2 we compare the experimental spectrum (panel a) for O_2 [71] with the theoretical spectrum (panel b) calculated from Eq. (4.12). Both the experimental and the theoretical spectra in Fig. 6.2 show the Raman-allowed series II: $(\mathit{10}, \mathit{18}, \mathit{26}, \mathit{34}, \mathit{42}, ..)\, Bc$, but not the

Table 6.2: All possible frequency arising from $\left\langle\left\langle\sin^2\cos^2\theta\right\rangle^2\right\rangle$ for O_2 whose only odd J 's are allowed. The group of frequencies with a weak intensity are noticed with (*).

No.	Group freq.	Weighting factor	Formula	Peak series (in Bc)	Expt. series
1	-	aa'	-	0	
2	ω_1 and ω_1'	$a'b$ and ab'	$4J+6$	$10, 18, 26, ...$	II
3	ω_2 and ω_2'	$a'c$ and ac'	$8J+20$	$28, 44, 60, ...$	III
4	$\omega_1+\omega_1'$	$\frac{bb'}{2}$	$4(J+J')+12$	$20, 28, 36, ..$	III
5	$\omega_1-\omega_1'$	$\frac{bb'}{2}$	$4(J-J')>0$	$8, 16, 24, ..$	V
6	$\omega_2+\omega_2'$	$\frac{cc'}{2}$	$8(J+J')+40$	$56, 72, 88, ..$	I*
7	$\omega_2-\omega_2'$	$\frac{cc'}{2}$	$8(J-J')>0$	$16, 32, 48, ..$	V*
8	$\omega_1+\omega_2'$ and $\omega_2+\omega_1'$	$\frac{bc'}{2}$ and $\frac{b'c}{2}$	$4(J+2J')+26$	$38, 46, 54, ..$	VI*
9	$\omega_1-\omega_2'$	$\frac{bc'}{2}$	$4(J-2J')-14>0$	$6, 14, 22, ...$	VI*
10	$\omega_2-\omega_1'$	$\frac{b'c}{2}$	$4(-J+2J')+14>0$	$2, 10, 18, ...$	II*

series I: $(6, 14, 22, 30, 38, ..)\,Bc$. The anomalous series III: $(\mathbf{20}, \mathbf{28}, \mathbf{36}, \mathbf{44}, ..)\,Bc$, discussed in the case of N_2 above, also appears for O_2 as well. Finally, another anomalous sequence V: $(\boldsymbol{8}, \boldsymbol{16}, \boldsymbol{24}, ..)\,Bc$ can be seen to be present in the data for O_2 in Fig. 6.3(a), but can not be generated by *F.T.* of $\langle\langle\sin^2 2\theta\rangle\rangle$ term (see Fig. 3.10).

To interpret the origin of the observed series in O_2 we first consider the first term given by Eq. (4.12), $\left\langle\left\langle\sin^2\theta\cos^2\theta\right\rangle^2\right\rangle$. The matrix element of $\left\langle\sin^2\theta\cos^2\theta\right\rangle$ vanishes unless for $\Delta J = 0, \pm 2, \pm 4$ corresponds to frequency ω_0, ω_1, and ω_2. For $\left\langle\left\langle\sin^2\theta\cos^2\theta\right\rangle^2\right\rangle$, there will be sum and difference frequencies that arise from the squaring, as follows

$$\begin{aligned}
&(a + b\cos\omega_1 t + c\cos\omega_2 t)\left(a' + b'\cos\omega_1' t + c'\cos\omega_2' t\right)\\
&\quad= aa' + ab'\cos\omega_1' t + a'b\cos\omega_1 t + ac'\cos\omega_2' t + a'c\cos\omega_2 t\\
&\qquad+\frac{bb'}{2}\cos\left(\omega_1+\omega_1'\right)t + \frac{bb'}{2}\cos\left(\omega_1-\omega_1'\right)t + \frac{cc'}{2}\cos\left(\omega_2+\omega_2'\right)t\\
&\qquad+\frac{cc'}{2}\cos\left(\omega_2-\omega_2'\right)t + \frac{bc'}{2}\cos\left(\omega_1+\omega_2'\right)t + \frac{bc'}{2}\cos\left(\omega_1-\omega_2'\right)t\\
&\qquad+\frac{b'c}{2}\cos\left(\omega_2+\omega_1'\right)t + \frac{b'c}{2}\cos\left(\omega_2-\omega_1'\right)t
\end{aligned}\tag{6.3}$$

with $a > b > c$. As discussed before, the frequency ω_1 generates the series $(4J+6)$ that for odd J will give us series II: $(10, 18, 26, ..)Bc$. The series I: $(6, 14, 22, ..)\,Bc$ that originates from even J, is absent from the spectrum. The latter fact is easily understood as due to the nuclear spin of O atoms, which is 0, that strictly forbids any even J rotational state for O_2, as required by the overall symmetry of the total wavefunction for O_2 (e.g. [27, 117]). With odd J, the frequency ω_2 produces series $(8J+20)Bc = (28, 44, 60, ...)Bc$, whereas $(\omega_1+\omega_1')$ produces $(4(J+J')+12)\,Bc = (20, 28, 36, ...)Bc$, together generates series III: $(\mathbf{20}, \mathbf{28}, \mathbf{36}, \mathbf{44}, ..)Bc$. The remain series, $\omega_1-\omega_1'$, $\omega_2+\omega_2'$, and $\omega_2-\omega_2'$, together generate

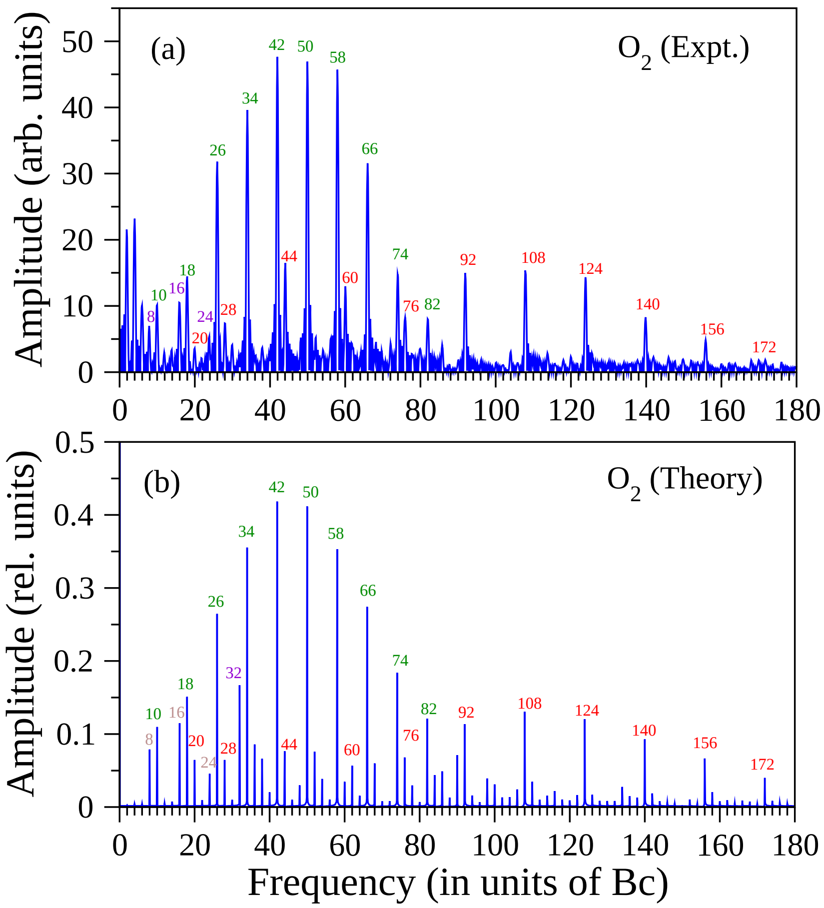

Figure 6.2: Comparison of the experimental (from [71]) and theoretical Fourier spectrum of the dynamic 19th harmonic signal for O_2. The spectrum shows series II: $(\mathit{10}, \mathit{18}, \mathit{26}, \mathit{34}, \mathit{42}, ..)\,Bc$ (green mark), series III: $(\mathbf{20}, \mathbf{28}, \mathbf{36}, \mathbf{44}, \mathbf{52}, \mathbf{60}, ..)\,Bc$ (red mark), and series V: $(\boldsymbol{8, 16, 24, ..})\,Bc$ (brown mark). We use pump pulse of intensity $I_{pump} = 0.5 \times 10^{14}\,\mathrm{W/cm^2}$ and pulse width $FWHM = 40\,\mathrm{fs}$, and probe pulse of intensity $I_{probe} = 1.2 \times 10^{14}\,\mathrm{W/cm^2}$, wavelength $\lambda = 800\,\mathrm{nm}$, and 36 cycles. The initial temperature is 200 K.

series V: $(\boldsymbol{8, 16, 24, ..})Bc$, as shown in Tab. 6.2. It is also shown in Tab. 6.2 that frequency $\omega_1 + \omega_2'$, $\omega_2 + \omega_1'$, and $\omega_1 - \omega_2'$ produce a peak series of $(4(J + 2J') + 26)Bc = (6, 14, 22, ..., 38, 46, 54, ...)Bc$ overlaps with series I, even though with a weak intensity. These series were also observed experimentally as a peak at interval 38 Bc. (These additional series can not be generated from $\langle\langle \sin^2 2\theta \rangle\rangle$). The remaining higher order terms in Eq. (4.12) contribute, generally weakly, to the same series as above or to some additional lines that can be seen in Fig. 6.2(b), but hardly resolved in experimental Fig. 6.2(a). Finally, we may point out that the observed heights of the few lowest frequency lines in the data in Fig. 6.2(a) for O_2 are due mostly to the fluctuation of the laser outputs (foot-note [20] of [71]).

Table 6.3: All possible frequency arising from $\left\langle \left\langle \sin^2 \cos^2 \theta \right\rangle^2 \right\rangle$ for CO_2 whose only even J 's are allowed. The group of frequencies with a weak intensity are noticed with (*).

No.	Group freq.	Weighting factor	Formula	Peak series (in Bc)	Expt. series
1	-	aa'	-	0	-
2	$\omega_1$and $\omega_1^{'}$	$a'b$ and ab'	$4J + 6$	$6, 14, 22, ...$	I
3	ω_2 and $\omega_2^{'}$	$a'c$ and ac'	$8J + 20$	$20, 36, 52, ...$	III
4	$\omega_1 + \omega_1'$	$\frac{bb'}{2}$	$4(J + J') + 12$	$12, 20, 28, ..$	III
5	$\omega_1 - \omega_1'$	$\frac{bb'}{2}$	$4(J - J') > 0$	$8, 16, 24, ..$	V
6	$\omega_2 + \omega_2'$	$\frac{cc'}{2}$	$8(J + J') + 40$	$40, 56, 72, ..$	V*
7	$\omega_2 - \omega_2'$	$\frac{cc'}{2}$	$8(J - J') > 0$	$16, 32, 48, ..$	V*
8	$\omega_1 + \omega_2'$ and $\omega_1' + \omega_2$	$\frac{bc'}{2}$ and $\frac{b'c}{2}$	$4(J + 2J') + 26$	$26, 34, 42, ..$	II*
9	$\omega_1 - \omega_2'$	$\frac{bc'}{2}$	$4(J - 2J') - 14 > 0$	$2, 10, 18, ...$	II*
10	$\omega_2 - \omega_1'$	$\frac{b'c}{2}$	$4(-J + 2J') + 14 > 0$	$6, 14, 22, ...$	I*

6.3 Frequency Spectrum of CO_2

In Fig. 6.3 we compare the experimental spectrum (panel a) for 19th harmonic of CO_2 [72] with the theoretical spectrum (panel b) calculated from Eq. (5.5) (assuming an initial temperature 300 K). Both the experimental and the theoretical spectra in Fig. 6.3 (panel a, and panel b, respectively) show three main series, i.e. Raman-allowed series I: $(6, 14, 22, 30, ..)\,Bc$, series III: $(\mathbf{20}, \mathbf{28}, \mathbf{36}, \mathbf{44},..)\,Bc$, and series V: $(\boldsymbol{8}, \boldsymbol{16}, \boldsymbol{24}, \boldsymbol{..})Bc$. The series II arises from $4J + 6$ with even J only, a nuclear characteristic of CO_2. Series III arises from two series, i.e. $(8J + 20)Bc = (\mathbf{20}, \mathbf{36}, \mathbf{52},..)Bc$ and $(4(J + J') + 12)Bc = (\mathbf{12}, \mathbf{20}, \mathbf{28},..)Bc$. The contribution of the series $(\mathbf{12}, \mathbf{20}, \mathbf{28},..)Bc$ appear in the experimental spectrum at $(\mathbf{90}, \mathbf{98}, \mathbf{104}, ...)Bc$ that can not be associated with the series $(\mathbf{20}, \mathbf{36}, \mathbf{52},..)Bc$. The series $(\mathbf{12}, \mathbf{20}, \mathbf{28},..)Bc$ also makes spectrum at $20\,Bc$ stronger than the following peaks. In general, the existence of two different series $(\mathbf{20}, \mathbf{36}, \mathbf{52},..)Bc$ and $(\mathbf{12}, \mathbf{20}, \mathbf{28},..)Bc$, and their overlapping, makes the series III has more than one peak. The series V and the series $(\mathbf{12}, \mathbf{20}, \mathbf{28},..)Bc$ can not be associated with $\langle\langle \sin^2 2\theta \rangle\rangle$, but can be generated by $\left\langle \left\langle \sin^2 \theta \cos^2 \theta \right\rangle^2 \right\rangle$, providing strong evidence of the validity of the present model. In addition to these three series, there are also some additional weaker series, as listed in Tab. 6.3.

In Fig. 6.4, we present the calculated HHG spectrum for 9th harmonic for CO_2. Like the 19th harmonic spectrum, the 9th harmonic spectrum also shows a similar behavior with a dominant series, i.e. series II: $(\mathit{10}, \mathit{18}, \mathit{26}, \mathit{34}, \mathit{42}, ..)\,Bc$, III: $(\mathbf{20}, \mathbf{28}, \mathbf{36}, \mathbf{44},..)\,Bc$, V: $(\boldsymbol{8}, \boldsymbol{16}, \boldsymbol{24}, \boldsymbol{..})Bc$, and additional weak series. Please note that the series III is more prominent in 9th harmonic spectrum, than in the 19th harmonic spectrum. In time domain, the 9th harmonic spectrum has greater $\frac{1}{8}$revival than the one for the 19th harmonic.

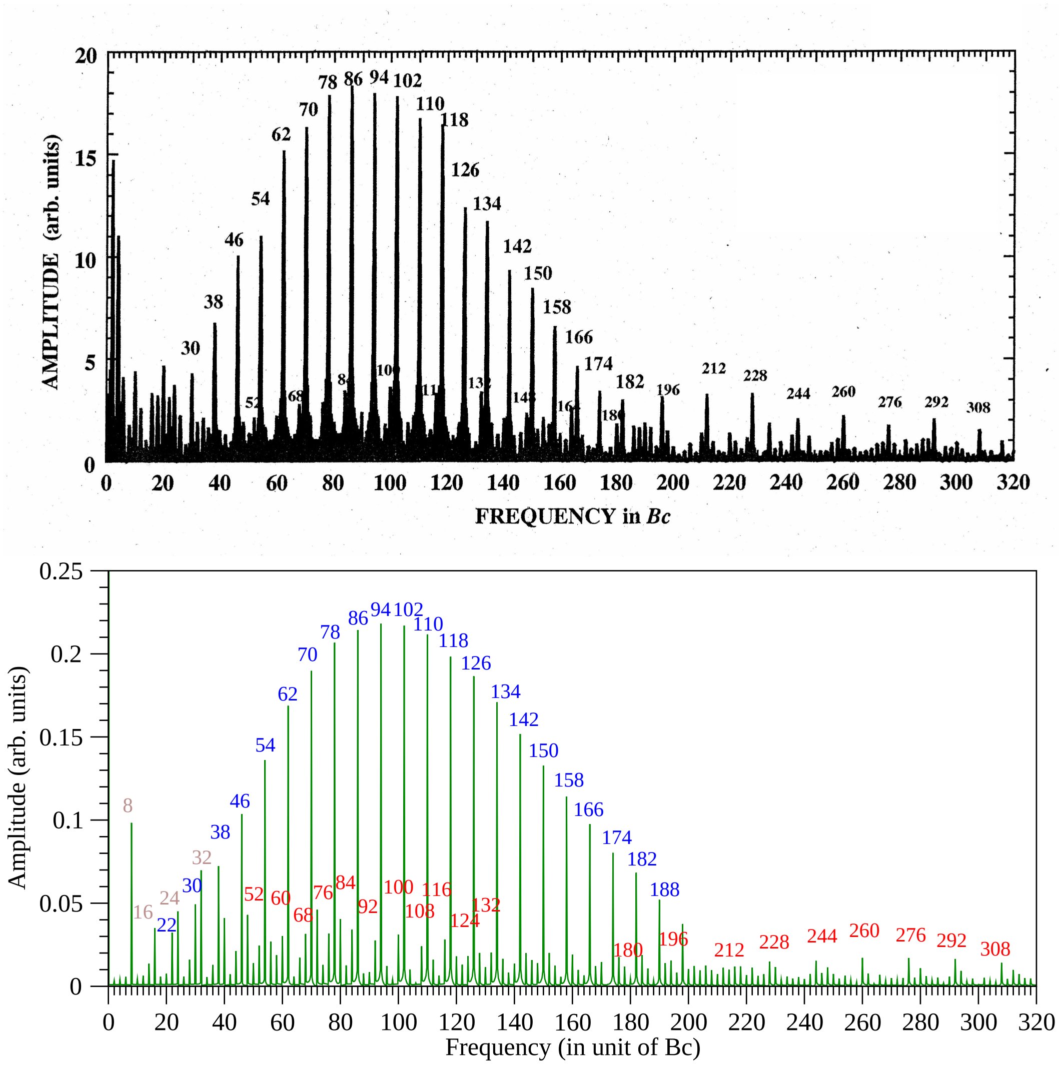

Figure 6.3: Comparison of the experimental (from [138]) and theoretical Fourier spectrum of the dynamic 19th harmonic signal for CO_2. The spectrum is dominated by three main series, i.e. series I: $(6, 14, 22, ..)\,Bc$, series III: $(\mathbf{20, 28, 36, 44}, ..)Bc$, and series V: $(\boldsymbol{8, 16, 24, ..})Bc$. We use pump pulse of intensity $I_{pump} = 0.53\times10^{14}\,\mathrm{W/cm^2}$ and pulse width $FWHM = 40\,\mathrm{fs}$, and probe pulse of intensity $I_{probe} = 1.5\times10^{14}\,\mathrm{W/cm^2}$, wavelength $\lambda = 800\,\mathrm{nm}$, and 36 cycles. The initial temperature is 300 K.

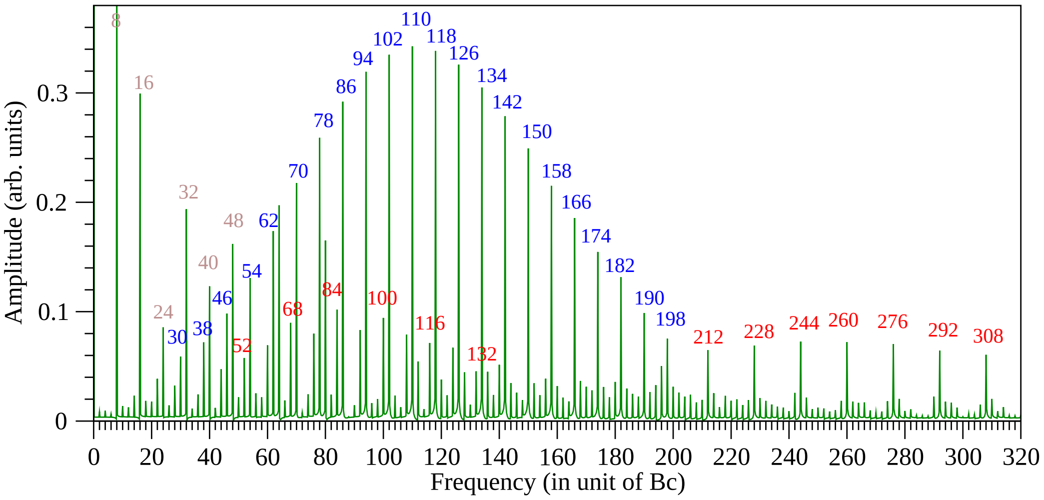

Figure 6.4: Theoretical Fourier spectrum of the dynamic 9th harmonic signal for CO_2. The spectrum is dominated by three main series, i.e. series I: $(6, 14, 22, ..)\,Bc$, series III: $(\mathbf{20, 28, 36, 44}, ..)Bc$, and series V: $(\boldsymbol{8, 16, 24, ..})Bc$. We use pump pulse of intensity $I_{pump} = 0.56 \times 10^{14}\,\mathrm{W/cm^2}$ and pulse width $FWHM = 40\,\mathrm{fs}$, and probe pulse of intensity $I_{probe} = 1.23 \times 10^{14}\,\mathrm{W/cm^2}$, wavelength $\lambda = 800\,\mathrm{nm}$, and 36 cycles. The initial temperature is 300 K. There is no experimental spectrum reported.

6.4 Effect of Initial Temperature

We point out that during the test calculations, the relative strengths of the lines in a calculated spectrum were found to depend significantly on the assumed molecular temperature (which is rather difficult to determine experimentally), provides a way of determine temperature of ensemble. Typically, the signature of initial temperature appear in both its dynamic and Fourier spectrum (see § 4.4). The gas jet with a lower initial temperature will produce a stronger signal with a greater modulation depth, as observed both in adiabatic (for example, aligned I_2 observed with its dissociation signal [164] and a class of asymmetric top molecule observed by using Coulomb explosion [139]) and non-adiabatic case (for example, aligned I_2 observed with its dissociation signal [44, 140]). In Fourier spectrum, the lower initial temperature produces spectrum with lower J_{max}.

From the previous figures, one sees that the experimental spectra give a main series reaching their maximum at 38 Bc (correspondent to $J_{max} = 8$) for N_2, 42 Bc ($J_{max} = 9$) for O_2, 94 Bc ($J_{max} = 22$) for 19th harmonic order of CO_2, and 110 Bc ($J_{max} = 26$) for 9th harmonic order. These similar spectra with same position J_{max} can be obtained theoretically by an initial temperature 200 K for N_2 and O_2 and 300 K for CO_2, that are somewhat higher than the expected temperature of the gas, which is estimated to be some what less than 100 K [71]. In contrast, the calculated data for initial temperature 100 K gives smaller J_{max} of the main series, those are 6 for N_2, 7 for O_2, and for 14 CO_2. (Figs.

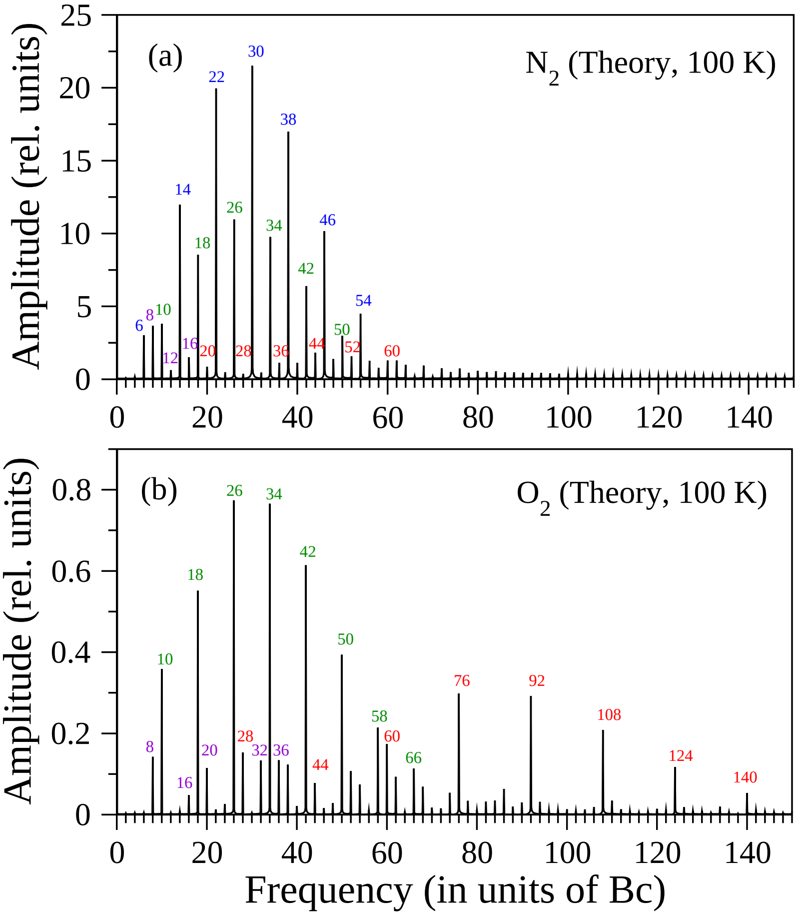

Figure 6.5: Calculated spectra for19th harmonic signal of N_2 (panel a) and O_2 (panel b) at Boltzmann temperature 100 K; laser parameters as in Fig. 6.1, for N_2 and, as in Fig. 6.2 for O_2.

6.5 and 6.6).[1]

The difference between theoretical temperature obtained from the spectral signal and that estimated from the experiment could be caused by the following. (1) There is a delay time between the moment of measuring temperature and the moment of entering the pump pulse. To be interact with laser beam, the valve should be opened, a little bit earlier before entering pulse. During the delay time (between opening valve and entering the pulse), the gas jet interacts with the environment with higher temperature, and therefore it makes the nozzle's temperature to be higher. Rosca-Pruna and Vrakking has observed the effect of the delay time on the dynamic alignment of I_2 by observing its dissociation signal [140, 44]. They found that the modulation signal obtained by applying the laser pulse 440 μs after opening the valve is a half of the one obtained from an opening time 420 μs. The smaller

---

[1] The fact that the initial temperature estimated from Fourier spectra is higher than the measured initial temperature in experiment is not only observed in this case -i.e. aligned N_2, O_2, and CO_2 observed with HHG- but also occurs in aligned N_2 and O_2 observed with Coulomb explosion [27] and aligned CO_2 observed by its Kerr effect [32].

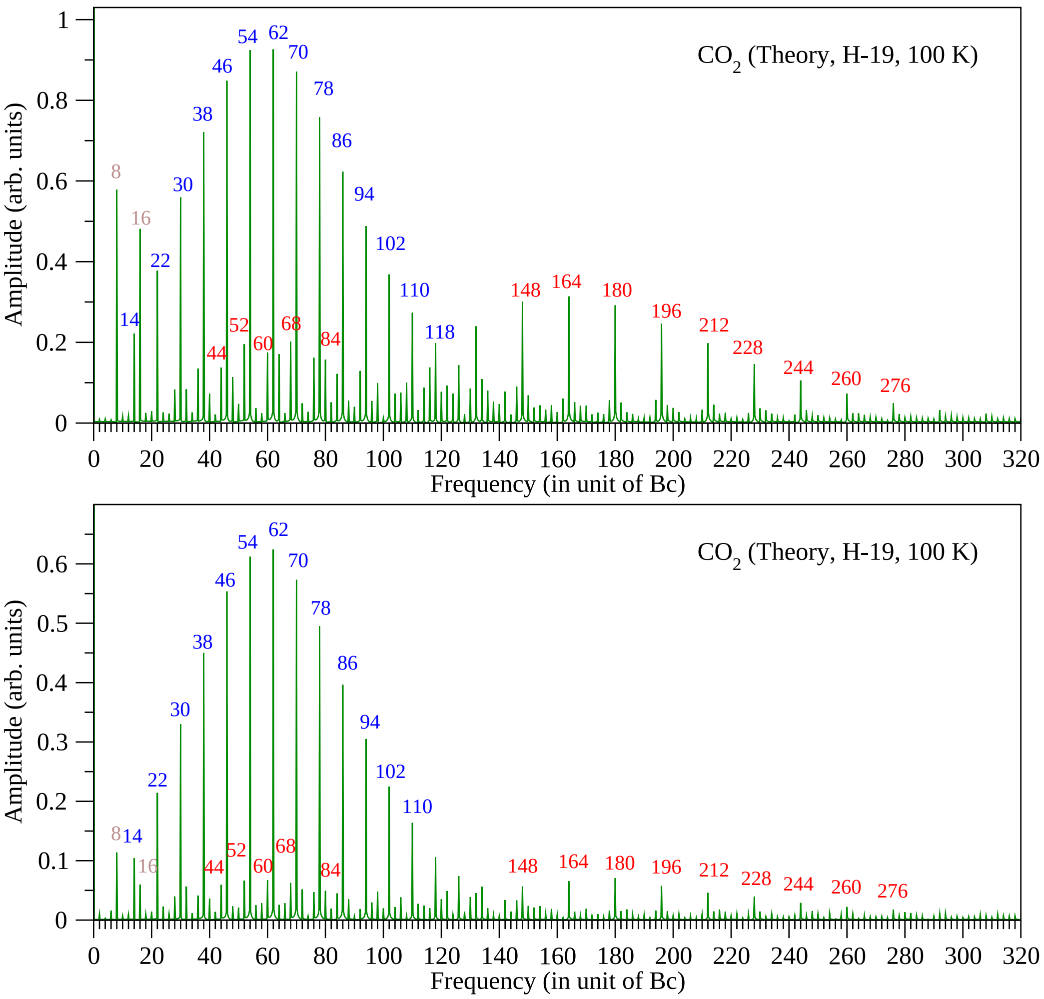

Figure 6.6: Calculated spectra for CO_2 of 9th harmonic (upper panel) and 19th harmonic (lower panel) at Boltzmann temperature 100 K; laser parameters as in Fig. 6.4, for 9th harmonic order and, as in Fig. 6.3 for 19th harmonic order.

modulation signal is a sign of higher initial temperature. It means that a longer opening time corresponds to a higher initial temperature. We note here that Miyazaki *et al.* enter the pulse 200 μs after measuring the temperature [138]. (2) So far, it was generally assumed that the second pulse just acts as a probe only (it generates HHG signal only). However, if we assume the second pulse also induces the molecule to rotate, the situation is similar with the case of alignment by two pulses. The calculation in § 3.8 (Fig. 3.13) and some experimental data (for example [35]), implies that the HHG signal from molecular ensemble aligned with a combination the pump and the probe pulses should have a smaller modulation depth, than the HHG signal of ensemble aligned with the pump pulse only. The reduction of modulation depth is a characteristic of dynamic alignment with higher initial temperature. Finally, it is important to note that the dynamic signal of O_2 and CO_2 have no double peak at their half and fourth revivals. The absence of double peak is another characteristic of alignment with high initial temperature.

6.5 Comparison with Other Theoretical Model: Case O_2

So far, the frequency spectra are calculated with assuming the adiabatic nuclear approximation of the present theory (Eq. (2.74)). First, we calculate the individual dipole expectation value from each reference wave packet state produced by the pump pulse (Eq. (2.42)). Second, we calculate the individual probability of HHG emission from each reference wave packet, which is given by the modulus square of the *F.T.* of individual dipole expectation value. Third, we obtain the HHG emission signal by taking thermal average from the individual probabilities, as shown in Eq. (2.46)

The model of Lin and his colleagues [88] uses instead a more drastic a 'frozen' nuclei model, in which the nuclei are assumed to be totally at rest during the interaction and hence the total dipole expectation value is just the electronic dipole expectation value. The HHG signal was obtained by averaging the electronic transition probability with the molecular-axis distribution, as shown by Eq. (2.76). Compared to the present theory, where the nuclear position is allowed to vary, the model of Lin *et al.* makes too strong assumption, where the probability is obtained at a fix nuclear position.

Another model was proposed by Madsen and Madsen [89, 112]. First, they calculate the electronic dipole expectation value. Second, the corresponding transition matrix element is obtained by taking *F.T.* of the electronic dipole . Third, they thermal average the complex matrix element. And finally, they squared the last thermal average quantity to obtain HHG signal (see Eq. (2.79)). This is a very unorthodox thermal average and does not appear to be justified by quantum statistical mechanics.

We show in Fig. 6.7 the calculated signals based on the three definitions of the signal, for O_2, together with the experimental spectrum, as a comparison. There are two distinctions appear between three definitions. First, the existence of an extra series. We can see from the figure that the 'frozen' nuclei model (Lin *et al.*'s model) does not produce the extra series (series V : $(\boldsymbol{8}, \boldsymbol{16}, \boldsymbol{24}, ..)Bc$) which was well produced by the present adiabatic nuclei theory and is also observed experimentally. Model of Madsen and Madsen produces the series V, but with much weaker intensity compared to the experimental spectrum. To understand the origin, we turn to the leading term of HHG signal which is

$$S_A^{(n)}(t_d) = c_{11}^{(n)} \left\langle \left\langle \sin^2\theta \cos^2\theta \right\rangle^2 \right\rangle + c_{12}^{(n)} \left\langle \left\langle \sin^2\theta \cos^2\theta \right\rangle \left\langle \sin^2\theta \cos^4\theta \right\rangle \right\rangle + ... \tag{6.4}$$

$$S_{FN}^{(n)}(t_d) = c_{11}^{(n)} \left\langle \left\langle \sin^4\theta \cos^4\theta \right\rangle \right\rangle + c_{12}^{(n)} \left\langle \left\langle \sin^4\theta \cos^6\theta \right\rangle \right\rangle + ... \tag{6.5}$$

$$\begin{aligned} S_{MM}^{(n)}(t_d) \quad = \quad & c_{11}^{(n)} \left\langle \left\langle \sin^2\theta \cos^2\theta \right\rangle \right\rangle \left\langle \left\langle \sin^2\theta \cos^2\theta \right\rangle \right\rangle \\ & + c_{12}^{(n)} \left\langle \left\langle \sin^2\theta \cos^2\theta \right\rangle \right\rangle \left\langle \left\langle \sin^2\theta \cos^4\theta \right\rangle \right\rangle + ... \end{aligned} \tag{6.6}$$

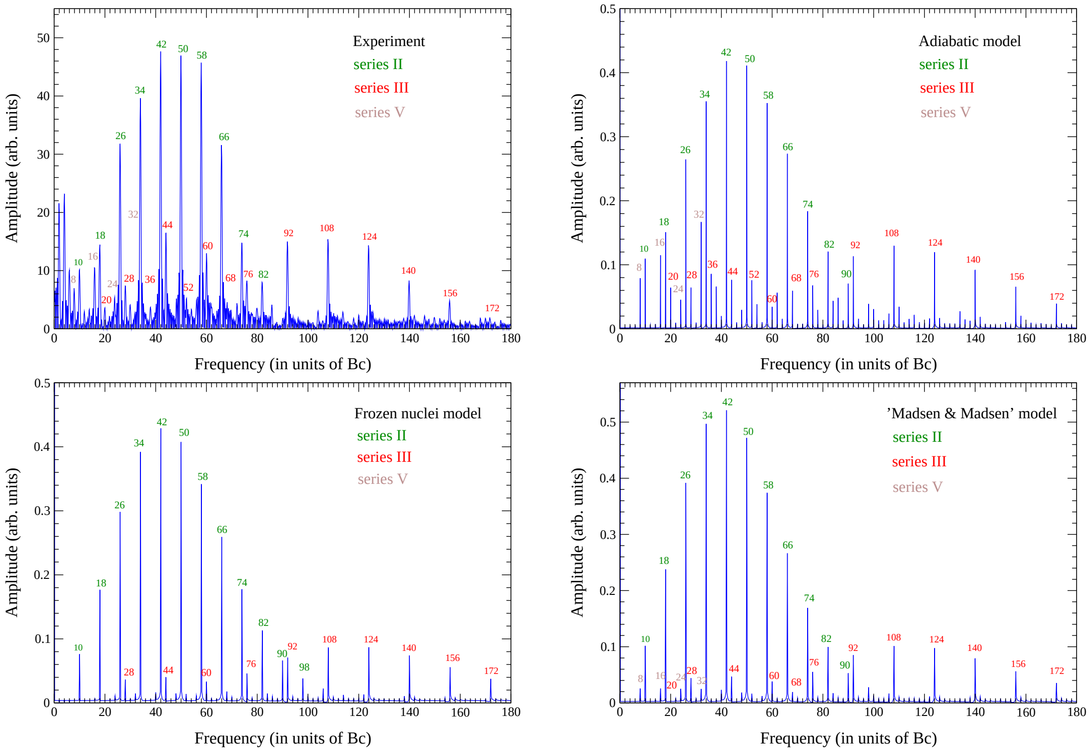

Figure 6.7: Theoretical Fourier spectrum of the dynamic 19th harmonic signal for O_2; pump intensity $I = 0.5\times10^{14}$ W/cm^2, probe intensity $I = 1.2\times10^{14}$ W/cm^{2}W/cm^2, duration 40 fs, wavelength 800 nm, and temperature 200 K. The calculation was done based on the semi adiabatic model (left-lower panel), the frozen nuclei model of Lin (right-upper panel) , the 'mixture model' of Madsen (right-lower panel). As comparison, the experimental spectrum (left-upper panel) is also shown.

where the indices A, FN, and MM stand for adiabatic, frozen nuclei, and Madsen and Madsen, respectively. It is clear that the adiabatic signal as well as the Madsen and Madsen's signal contain mix-term (i.e. the squaring or multiply between different expectation values of operator) which is the origin on the series V. On the other hand, the signal of 'frozen' nuclei does not contain mix-term and therefore does not produce series V. The difference in the strength between the series V in the adiabatic signal, and the one in the Madsen and Madsen's signal is related to the way of multiplying. For the adiabatic theory, the squaring was done before the thermal averaging, and therefore the the mix-term has a weight of $\rho\,(J_0)$. For the Madsen and Madsen theory, on the other hand, the squaring is done after thermal averaging, and therefore the mix-term has a weight of $\rho\,(J_0)\,\rho\,(J_0')$.

Second, the ratio between series the III $((\mathbf{20, 28, 36, 44}, ..)Bc)$ and the series II $((10, 18, 26, ..)Bc)$. Theory of Madsen and Madsen as well as theory of Lin *et al.* produce too weak signal of the series III, relative to the series II. The best ratio is produced by the present adiabatic nuclei approximation. To understand the origin, we back to Tab. 6.2. From the table, one sees that the series III in adiabatic signal is generated not only by a group frequency ω_2 (and $\omega_2^{'}$), with the weighting factor $a'c$ (and ac'), but also by a group frequency $\omega_1 + \omega_1^{'}$ with a weighting factor $\frac{bb'}{2}$. For the signal of Madsen and Madsen, the group of frequency $\omega_1 + \omega_1^{'}$ is present, but with much weaker intensity due to the squaring of thermal weight $\rho\left(J_0\right)\rho\left(J_0'\right)$, instead of $\rho\left(J_0\right)$ in the adiabatic signal. For the signal of 'frozen' nuclei, the group of frequency $\omega_1 + \omega_1^{'}$ is absent.

These above facts speak strong in favor of the present theory and reject the two other models discussed.

Chapter 7

Dependence of the Dynamic Signal on the Relative Angle Between the Pump and the Probe Polarizations α

7.1 Salient Experimental Data

So far we have limited ourselves to the usual experimental geometry in which the pump and the probe polarizations are kept parallel to each other. We now consider the more general case in which the probe and the pump polarizations make an arbitrary angle α between them.

The dependence of dynamic HHG signal on the relative angle, α, between the pump and the probe polarizations was first reported by Marangos and collaborators [67]. They revealed a marked difference of the HHG signals of adiabatically aligned molecules by a long pulse, for the parallel and perpendicular geometries of the pump and the probe polarizations for the fixed 9th order for H_2, N_2, and CS_2 [67, 141, 142]. Moreover, they also obtained the dependence of HHG signal of CO_2 on the angle α, for several other harmonic orders [68, 151].

Following Marangos *et al.*, Itatani *et al.* [13] measured the HHG signal of non-adiabatically aligned N_2 by a short pulse at a fixed delay time $t_d \simeq 4.0\,\mathrm{ps}$ (corresponds to the top signal) for various relative polarization angle α between the pump and the probe polarization. They found that the signal reached its maximum when the pump polarization was parallel to the probe polarization ($\alpha = 0^o$), and was reduced by increasing the angle α, and it reached the minimum at $\alpha = 90^o$. A similar conclusion was obtained by A. Scrinzi, when he normalized HHG signal of N_2 with respect to HHG signal of its companion atom Ar for several angle α [165].

Kanai *et al.* [43] and Miyazaki *et al.* [71, 138] measured the dynamic HHG signal as a function of delay time between the pump and the probe pulse for the diatomic molecules N_2, O_2, and triatomic CO_2 molecules for different relative angles α (= 0°, 45°, and 90°) and observed that the HHG modulation signals were smaller in the perpendicular case, than in the parallel case, and showed an *opposite* phase relation in the two geometries. In fact, the dynamic HHG signal had a similar phase in the parallel case when $\alpha < 60$ and had an opposite phase when $\alpha > 60$ [138, 145][1]. In addition, Miyazaki *et. al.* measured the modulation depth, which is the difference between the maximum and minimum signal observed during one period and plotted the results against the angle α [138]. Moreover, Miyazaki and his colleagues also measured HHG signal by varying the angle α and keeping t_d at the top-signal around its half revival period [72]. The results for the 19th harmonic signal were the following. For N_2, the signal was maximum at $\alpha = 0$ and minimum $\alpha = 90^o$. In contrast, due to the inverted phase, the signal of CO_2 was maximum at $\alpha = 90$ and minimum $\alpha = 0^o$. For O_2, an interesting phenomenon was reported: the signal reached a maximum at $\alpha \simeq 20^o$ and a minimum at $\alpha \simeq 80^o$.

The first heuristic explanation on the dependence of HHG signal on the angle α was proposed by Kanai *et al.* [43]. They proposed a planar emission model of HHG which predicted an opposite phase relation, as observed, but could not account for the observed unequal modulation of the signals in the two geometries. In addition, the planar model could not explain why the signal amplitude was equal to zero at critical angle $\alpha_c \simeq 54.7^o$ [138]. A more satisfactory model was then proposed by Zhou *et al.* [88]. They predicted that the HHG signal of N_2 should monotonically decrease on increasing the angle α, which was in agreement with the experimental data. For O_2, they predicted that the signal to be maximized at $\alpha \approx 50^o$, which however, differed from the experimental data.

The present theoretical investigation of the α-dependent dynamic HHG signal is therefore motivated by the following. First, the necessity of a consistent theory for explaining the salient experimental data. Second, unlike the dependence on the alignment angle θ, the relative polarization angle α can be controlled in the laboratory and therefore provides a possible way in controlling the HHG signal. In this chapter, we investigate the α-dependent of HHG signals and directly compare the results with the experimental data.

7.2 Generalization of the Expression of Dynamic Signal for Arbitrary Relative Polarization Angle α

To derive the HHG signal in more general case, it is convenient to choose a coordinate system where the pump polarization along the space fixed polar axis (z-axis) is kept fixed as before, but to rotate the probe polarization by an angle α from it and let the pump and

---

[1] Actually, Miyazaki *et al.* reported the HHG yield for different angle $\alpha = 0^o, 10^o, 20^o, ..., 90$, whereas, Merdji *et al.* reported for $\alpha = 0, 30, 60, 90$. Their results imply the existence of angles between 50^o and 60^o, where the signal is flat.

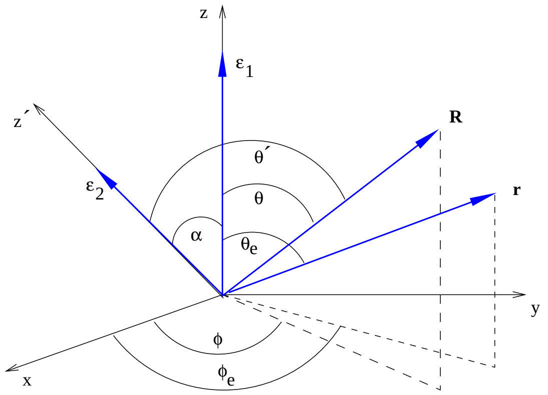

Figure 7.1: Schematic diagram defining the directions of the molecular axis, $\boldsymbol{R}$, electron position vector $\boldsymbol{r}$, the pump polarization ($\boldsymbol{\epsilon}_1 \parallel z-$axis), and the probe polarization ($\boldsymbol{\epsilon}_2 \parallel z'-$axis). The z and z' axes lie on the common x-z plane; the fields are assumed to propagate along the y-axis.

the probe polarization vectors define the common $(x - z' - z)$-plane, as shown in Fig. 7.1. Let the direction of the probe polarization be the polar axis z' of the rotated frame, and the direction of the molecular axis in this frame be denoted by (θ', ϕ'). Then we may carry out the electronic dipole integrals as before with z' as the polar axis, and obtain the same expressions as before for the HHG operators (Eq. (4.3) for N_2, Eq. (4.10) for O_2, and Eq (5.3) for CO_2) *except* that they are now given in terms of the variables (θ', ϕ') in the rotated frame. The HHG signal (Eq. (4.5) for N_2 for an arbitrary angle α now can be written as:

$$\begin{aligned} S^{(n)}(t_d;\alpha) &= c_{00}^{(n)} + c_{01}^{(n)} \left\langle\left\langle \cos^2\theta' \right\rangle\right\rangle (t_d) \\ &\quad + c_{11}^{(n)} \left\langle \left\langle \cos^2\theta' \right\rangle^2 \right\rangle (t_d) + \cdots + c_{33}^{(n)} \left\langle \left\langle \cos^6\theta' \right\rangle^2 \right\rangle (t_d) \,. \end{aligned} \tag{7.1}$$

Similarly, the HHG signal of O_2 (Eq. (4.12)) reads

$$\begin{aligned} S^{(n)}(t_d;\alpha) &= c_{11}^{(n)} \left\langle \left\langle \sin^2\theta' \cos^2\theta' \right\rangle^2 \right\rangle (t_d) + c_{12}^{(n)} \left\langle \left\langle \sin^2\theta' \cos^2\theta' \right\rangle \left\langle \sin^2\theta' \cos^4\theta' \right\rangle \right\rangle (t_d) \\ &\quad + \cdots + c_{33}^{(n)} \left\langle \left\langle \sin^2\theta' \cos^6\theta' \right\rangle^2 \right\rangle (t_d) \end{aligned} \tag{7.2}$$

whereas the HHG of CO_2 (Eq. (5.5)) can be written as

$$\begin{aligned} S^{(n)}(t_d;\alpha) &= c_{11}^{(n)} \left\langle \left\langle \sin^2\theta' \cos^2\theta' \right\rangle^2 \right\rangle (t_d) + c_{12}^{(n)} \left\langle \left\langle \sin^2\theta' \cos^2\theta' \right\rangle \left\langle \sin^2\theta' \cos^4\theta' \right\rangle \right\rangle (t_d) \\ &\quad + \cdots + c_{55}^{(n)} \left\langle \left\langle \sin^2\theta' \cos^{10}\theta' \right\rangle^2 \right\rangle (t_d) \end{aligned} \tag{7.3}$$

In the equations above, a quantity $\langle\langle f(\theta')\rangle\rangle\,(t_d)$ is an expectation value of the function $f(\theta')$, given in probe frame, but evaluated with respect to the rotational wave packet obtained in the pump frame, or $\langle\langle f(\theta')\rangle\rangle\,(t_d) \equiv \sum_{J_0M_0} \rho(J_0) \left\langle \Phi_{J_0M_0}(t_d,\theta) \left| f(\theta') \right| \Phi_{J_0M_0}(t_d,\theta) \right\rangle$. Before evaluating integral, it is convenient, therefore, to transform the HHG operators which is given in the variables (θ', ϕ') of probe frame to the angles (θ, ϕ) of the pump frame (i.e. with the z along the pump polarization). This can be done by the simple transformation

$$\cos\theta' = \cos\theta\cos\alpha + \sin\theta\sin\alpha\cos\phi \tag{7.4}$$

where ϕ is the azimuth angle between plane of the molecular axis and the pump pulse, and plane of the pump and the the probe pulses.

Using the above transformation, for example, the expectation value of $\langle\cos^2\theta'\rangle$ in the case of a non-zero angle α reads

$$\begin{aligned}\langle\cos^2\theta'\rangle &= \left(\cos^2\alpha - \frac{1}{2}\sin^2\alpha\right)\langle\cos^2\theta\rangle + \frac{1}{2}\sin^2\alpha \\ &+\frac{1}{4}\sin^2\alpha\left(\left\langle\sin^2\theta e^{2i\phi}\right\rangle + c.c.\right) + \frac{1}{2}\sin 2\alpha\left(\left\langle\sin\theta\cos\theta e^{i\phi}\right\rangle + c.c.\right)\end{aligned} \tag{7.5}$$

where $\langle\sin\theta\cos\theta e^{\pm i\phi}\rangle$ couples the $J \longrightarrow J'$ states with $\Delta J = 0, \pm 2$ and $M \longrightarrow M'$ states with $\Delta M = \pm 1$ whereas $\langle\sin^2\theta e^{\pm 2i\phi}\rangle$ couples the $J \longrightarrow J'$ states with $\Delta J = 0, \pm 2$ and $M \longrightarrow M'$ states with $\Delta M = \pm 2$.[2] We note that for the linearly polarized pump pulse of the present interest, the interaction Hamiltonian is proportional to $\cos^2\theta$, which is independent of M in the space fixed pump-frame. Thus the M-quantum number of the rotational wave-packet remains constant, or $M = M_0$, throughout the evolution. Hence, the expectation values of $\langle\sin\theta\cos\theta e^{\pm i\phi}\rangle$ and $\langle\sin^2\theta e^{\pm 2i\phi}\rangle$ are zero, and Eq. (7.5) reads

$$\langle\cos^2\theta'\rangle = \frac{1}{2}\left(3\cos^2\alpha - 1\right)\langle\cos^2\theta\rangle + \frac{1}{2}\sin^2\alpha \tag{7.8}$$

In a similar way, we obtain the expectation value for higher terms

$$\begin{aligned}\langle\cos^4\theta'\rangle &= \frac{1}{8}\left(35\cos^4\alpha - 30\cos^2\alpha + 3\right)\langle\cos^4\theta\rangle \\ &+\frac{3}{8}\left(-10\cos^4\alpha + 12\cos^2\alpha - 2\right)\langle\cos^2\theta\rangle + \frac{3}{8}\sin^4\alpha\end{aligned} \tag{7.9}$$

---

[2] The non vanishing element matrix of $\langle\sin\theta\cos\theta e^{\pm i\phi}\rangle$ are [103]

$$\begin{aligned}\left\langle J, M\left|\sin\theta\cos\theta e^{\pm i\phi}\right| J-2, M\pm 1\right\rangle &= \mp\tfrac{1}{(2J+3)}\sqrt{\tfrac{\left((J+1)^2-M^2\right)(J\pm M+2)(J\pm M+3)}{(2J+1)(2J+5)}} \\ \left\langle J, M\left|\sin\theta\cos\theta e^{\pm i\phi}\right| J, M\pm 1\right\rangle &= -\tfrac{(2M\pm 1)}{(2J-1)(2J+3)}\sqrt{J(J+1)-M(M\pm 1)} \\ \left\langle J, M\left|\sin\theta\cos\theta e^{\pm i\phi}\right| J+2, M\pm 1\right\rangle &= \pm\tfrac{1}{(2J-1)}\sqrt{\tfrac{\left(J^2-M^2\right)(J\mp M-1)(J\mp M-2)}{(2J+1)(2J-3)}}\end{aligned}\quad , \tag{7.6}$$

For $\langle\sin^2\theta e^{\pm 2i\phi}\rangle$, the non vanishing matrix are:

$$\begin{aligned}\left\langle J, M\left|\sin^2\theta e^{\pm 2i\phi}\right| J-2, M\pm 2\right\rangle &= \tfrac{1}{(2J-1)\sqrt{(2J+1)(2J-3)}}\sqrt{\tfrac{(J\pm M)!}{(J\pm M-4)!}} \\ \left\langle J, M\left|\sin^2\theta e^{\pm 2i\phi}\right| J, M\pm 2\right\rangle &= \tfrac{1}{(2J-1)(2J+3)}\sqrt{\tfrac{(J\pm M)!}{(J\pm M-4)!}} \\ \left\langle J, M\left|\sin^2\theta e^{\pm 2i\phi}\right| J+2, M\pm 2\right\rangle &= \tfrac{1}{(2J+1)\sqrt{(2J+1)(2J-3)}}\sqrt{\tfrac{(J\pm M+2)!\,(J\mp M)!}{(J\mp M-2)!\,(J\pm M)!}}\end{aligned} \tag{7.7}$$

Notice that for $\alpha = 0$, $\left\langle \cos^2\theta' \right\rangle$ in Eq. (7.8) and $\left\langle \cos^4\theta' \right\rangle$ in Eq. (7.9) reduce to $\left\langle \cos^2\theta \right\rangle$ and $\left\langle \cos^4\theta \right\rangle$, respectively, as they should. Thermal averaging Eqs. (7.8) and (7.9) gives us $\left\langle\left\langle \cos^2\theta' \right\rangle\right\rangle$ and $\left\langle\left\langle \cos^4\theta' \right\rangle\right\rangle$ which are the second and the fourth term of HHG signal of N_2 for an arbitrary angle α (Eq. (7.1)). On the other hand, squaring and thermal averaging Eq. (7.8) gives us $\left\langle\left\langle \cos^2\theta' \right\rangle^2\right\rangle$, the third term of HHG signal of N_2. Further, substracting Eq. (7.9) from Eq. (7.8) gives us

$$\begin{aligned}\left\langle \sin^2\theta' \cos^2\theta' \right\rangle &= \frac{1}{8}\left(-35\cos^4\alpha + 30\cos^2\alpha - 3\right)\left\langle \cos^4\theta \right\rangle \\ &+\frac{1}{8}\left(30\cos^4\alpha - 24\cos^2\alpha + 2\right)\left\langle \cos^2\theta \right\rangle \\ &+\frac{1}{8}\left(-3\sin^4\alpha + 4\sin^2\alpha\right) \qquad (7.10)\end{aligned}$$

In a similar way, squaring and then thermal averaging Eq. (7.10) gives us the first term of HHG signal of O_2 and CO_2 that appear in Eqs. (7.2) and (7.3), respectively. We obtain the higher order terms, analogously.

An alternative way to express the HHG signal for arbitrary relative polarization angle α can be done as follow. Suppose the probe pulse is placed at angle θ' with respect to the molecular axis, as shown in Fig. 7.1. The expectation value of an operator $T_e^{(n)}(\theta')$ at delay time t_d is given by

$$\left\langle T_e^{(n)}(\theta') \right\rangle = \int_0^{\pi}\int_0^{2\pi} \left|\Phi\left(t_d;\theta,\phi\right)\right|^2 T_e^{(n)}(\theta,\phi,\alpha)\,\sin\theta d\phi d\theta \qquad (7.11)$$

In above, θ' is a function of alignment angle θ, azimuth angle ϕ, and relative polarization angle α, as given by Eq. (7.4). We note that our interaction Hamiltonian is proportional to $\cos^2\theta$, which is independent of M in the space fixed pump-frame. Therefore the squared wavefunction $\left|\Phi\left(t_d;\theta,\phi\right)\right|^2$ is M-independent. If we define

$$T_e^{(n)}(\theta,\alpha) = \int_0^{2\pi} T_e^{(n)}(\theta,\phi,\alpha) d\phi, \qquad (7.12)$$

the expectation value of $T_e^{(n)}(\theta,\phi,\alpha)$ reads

$$\left\langle T_e^{(n)}(\theta') \right\rangle = \int_0^{\pi} \left|\Phi\left(t_d;\theta\right)\right|^2 T_e^{(n)}(\theta,\alpha)\,\sin\theta d\theta. \qquad (7.13)$$

We note that Eq. (7.13) satisfies only for linear polarization. For circularly polarized pump pulse, we use the more general form, Eq. (7.11).

For the lowest order HHG signal of N_2, we have $T_e^{(n)}(\theta') = \cos^2\theta'$. The corresponding $T_e^{(n)}(\theta,\alpha)$ is given by

$$T_e^{(n)}(\theta,\alpha) = \int_0^{\pi} \left[\cos^2\theta\cos^2\alpha + \sin^2\theta\sin^2\alpha\cos^2\phi\right.$$

$$
\begin{aligned}
& + 2\sin\theta\cos\theta sin\alpha\cos\alpha\cos\phi\big]\, d\phi \\
= \quad & 2\pi\left(\cos^2\theta\cos^2\alpha + \frac{1}{2}\sin^2\theta\sin^2\alpha\right) \qquad (7.14)
\end{aligned}
$$

Finally, substituting Eq. (7.14) in Eq. (7.13) gives the value of $\langle\cos^2\theta'\rangle$, which is equal to Eq. (7.8).

7.3 Harmonic Spectrum

As mentioned above, the first evidence of the dependence of HHG signal of non-adiabatic aligned molecule, on the relative polarization angle, α, is the experiment of Itatani *et al.* [13]. They aligned N_2 at initial temperature $T = 30\,\mathrm{K}$ by using a pump pulse of intensity $I_{pump} = 0.4 \times 10^{14}$ W/cm^2 and pulse duration 60 fs. The HHG signal was then generated by using a probe pulse of intensity $I_{probe} = 2 \times 10^{14}$ W/cm^2, duration 30 fs, and wavelength 800 nm at fixed delay time $t_d \simeq$ 4.0 ps when the HHG signal reached its maximum. The HHG spectra was then measured for various relative angle α.

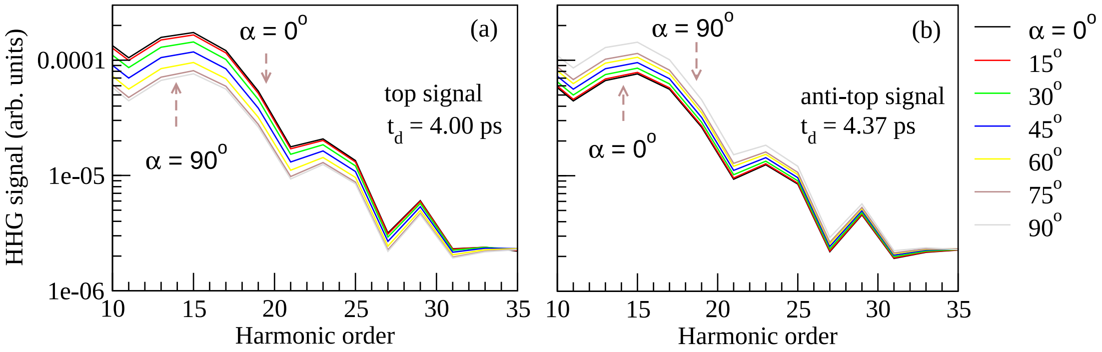

Figure 7.2: Theoretical harmonic spectra of N_2 for various relative polarization angle, α, at top signal (left panel) and anti-top signal (right panel); pump pulse: $I_{pump} = 0.4 \times 10^{14}$ W/cm^2 and 60 fs; probe pulse: $I_{probe} = 2 \times 10^{14}$ W/cm^2 and 30 fs, wavelength 800 nm, temperature 30 K.

Fig. 7.2(a) shows the calculated spectra obtained with the same parameters as those of Itatani *et al.* and observed at the delay time when the dynamic HHG signal reaches its maximum. As experimental data, the theoretical spectrum reaches its maximum for parallel polarization ($\alpha = 0^o$), decreases with increasing α, and reaches its minimum for perpendicular polarization. At this delay time of observation, most of the molecules are aligned along pump polarization ($\theta \simeq 0^o$) and therefore the polarization angle, α, represents the angle between the probe polarization and the molecular axis. Due to the electron cloud of N_2 are peaked along its nuclear axis, therefore the signal reaches its maximum at parallel polarization ($\alpha = 0^o$). For perpendicular polarization ($\alpha = 90^o$), most of molecules are aligned perpendicular to the probe polarization, and therefore the signal becomes minimum. We note that the molecular distribution depends on the initial temperature, where the lower temperature gives the sharper distribution around pump polarization. The present data is calculated with the initial temperature $T = 30\,\mathrm{K}$, where molecule distribution is sharply peaked at pump polarization. Therefore, the α-dependent spectrum is almost similar to the θ-dependent spectrum, as shown in Fig. 4.4. We also present the calculated spectrum measured at delay time $t_d = 4.37\,\mathrm{ps}$ (when the signal reaches its minimum), as shown in Fig. 7.2(b). At this delay time, most of the molecules are aligned perpendicular to the pump polarization's direction. Therefore, the signal reaches its maximum when the probe polarization is perpendicular to the pump polarization.

7.4 Dynamic Signal as Function of Delay Time for Fixed Relative Pump-Probe Polarization Angle α

To further compare with the experimental data, we calculate the HHG signals as a function of the delay time between the two pulses t_d, at three different relative polarization angles α, i.e. $\alpha = 0^o$, 45^o, and 90^o, as shown in Fig. 7.3 for N_2, Fig. 7.4 for O_2, and Figs. 7.5 and 7.6 for CO_2. In general, the signal for $\alpha = 90^o$ changes its phase by π with respect to the signal for $\alpha = 0^o$, a phenomenon that is observed experimentally [43, 138]. The signal for $\alpha = 45^o$ is seem to remain rather flat as a function of α.

We start with N_2. To see qualitatively the α dependence of HHG signal of N_2, we may consider the leading term of Eq. (7.1) which is given by

$$S^{(n)}\left(t_d;\alpha\right) = c_{00}^{(n)} + c_{01}^{(n)}\left[\frac{1}{2}\sin^2\alpha + \frac{1}{2}\left(3\cos^2\alpha - 1\right)\left\langle\left\langle\cos^2\theta\right\rangle\right\rangle\left(t_d\right)\right] \tag{7.15}$$

Thus, for the parallel polarizations we have, $S^{(n)}\left(t_d;0^o\right) \approx c_{00}^{(n)} + c_{01}^{(n)}\left\langle\left\langle\cos^2\theta\right\rangle\right\rangle\left(t_d\right)$ and for the perpendicular polarizations, $S^{(n)}\left(t_d;90^o\right) \approx c_{00}^{(n)} + \frac{c_{01}^{(n)}}{2}\left(1 - \left\langle\left\langle\cos^2\theta\right\rangle\right\rangle\left(t_d\right)\right)$ which are clearly of opposite phase, as a function of t_d. The expressions also show that the modulation depth for $\alpha = 90^o$ is smaller than the one for $\alpha = 0^o$, that can not be obtained by planar model [43], as will be further discussed in § 7.7.

For O_2, the leading term of HHG signal (Eq. (7.2)) reads

$$\begin{aligned} S^{(n)}(t_d;\alpha) \;\approx\; & \frac{c_{11}^{(n)}}{64}\left\langle\left(\left(35\cos^4\alpha - 30\cos^2\alpha + 3\right)\left\langle\sin^2\theta\cos^2\theta\right\rangle\left(t_d\right)\right.\right. \\ & + \left(-5\cos^4\alpha + 6\cos^2\alpha - 1\right)\left\langle\cos^2\theta\right\rangle\left(t_d\right) \\ & \left.\left. + \;\left(-3\sin^4\alpha + 4\sin^2\alpha\right)\right)^2\right\rangle \end{aligned} \tag{7.16}$$

Thus, for the parallel polarizations we have, $S^{(n)}\left(t_d;0^o\right) \approx c_{11}^{(n)}\left\langle\left\langle\sin^2\theta\cos^2\theta\right\rangle^2\right\rangle$, as they should, and for the perpendicular polarizations, $S\left(t_d;90^o\right) \approx \frac{c_{11}^{(n)}}{64}\left\langle\left(3\left\langle\sin^2\theta\cos^2\theta\right\rangle - \left\langle\cos^2\theta\right\rangle + 1\right)^2\right\rangle$. It was clear that the sign of $\left\langle\cos^2\theta\right\rangle$ changes from positive for $\alpha = 0^o$ to negative for $\alpha = 90^o$. It implies that the half and fourth

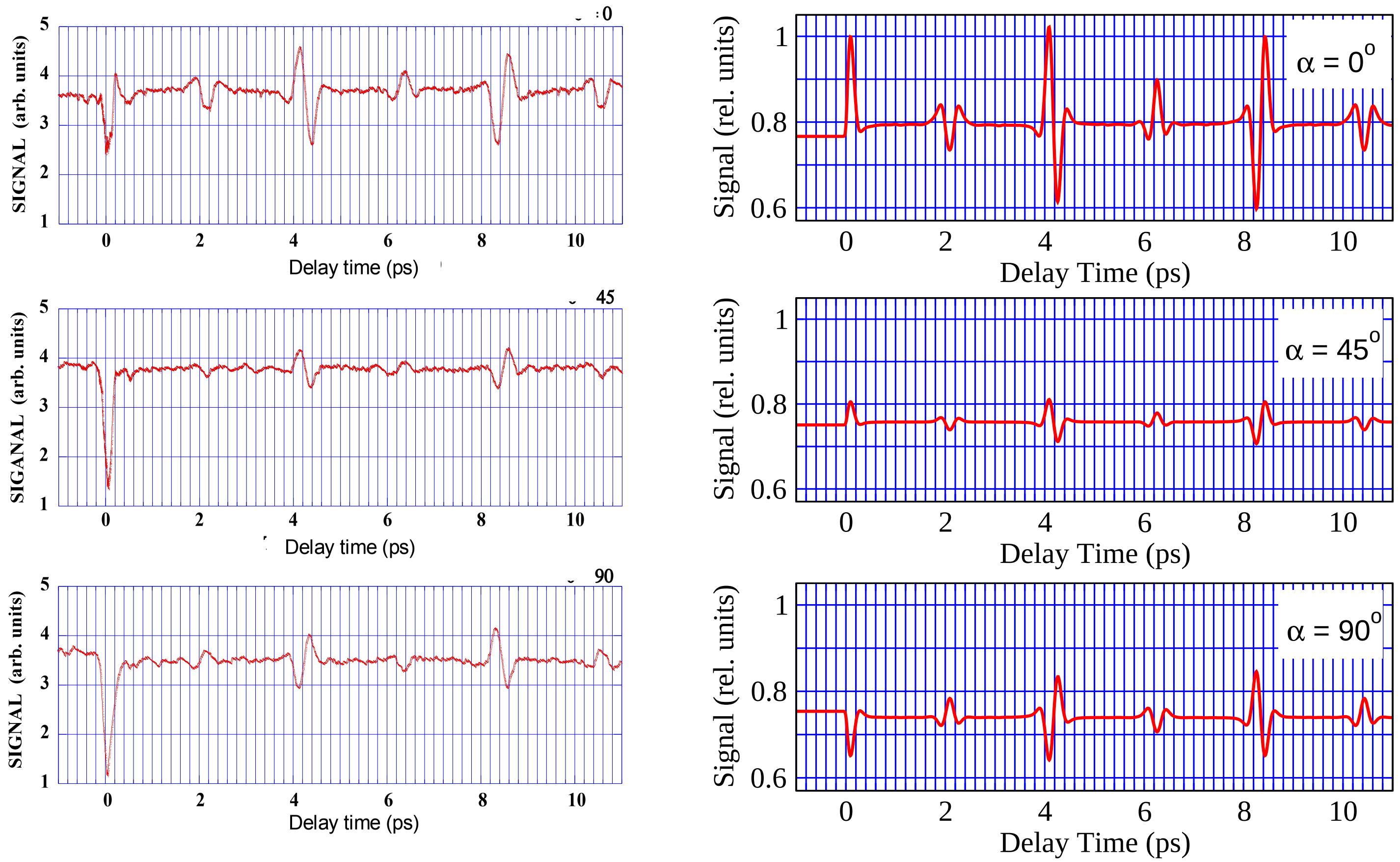

Figure 7.3: Comparison of experimental (left panel) (from [138]) and calculated (right panel) dynamic 19th harmonic order for N_2 for various relative pump-probe polarization angles, i.e. $\alpha = 0^o$, $\alpha = 45^o$, and $\alpha = 90^o$. The laser parameters are $I_{pump} = 0.8 \times 10^{14}\,\mathrm{W/cm^2}$, $I_{probe} = 1.7 \times 10^{14}\,\mathrm{W/cm^2}$, $FWHM = 40\,\mathrm{fs}$, $\lambda = 800\,\mathrm{nm}$, and 36 cycles. The initial temperature is 200 K.

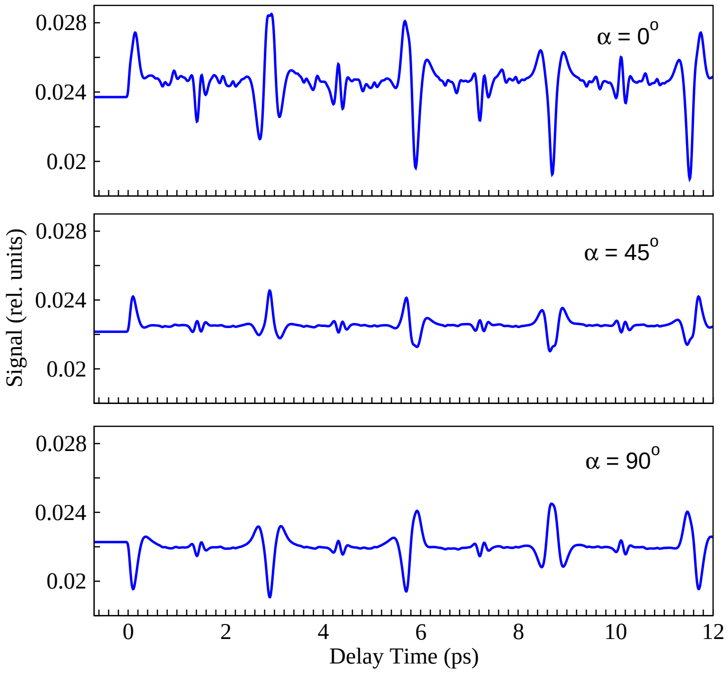

Figure 7.4: Calculated dynamic 19th harmonic order for O_2 for various relative pump-probe polarization angles, i.e. $\alpha = 0^o$, $\alpha = 45^o$, and $\alpha = 90^o$. The laser parameters are $I_{pump} = 0.5 \times 10^{14}\mathrm{W/cm^2}$, $I_{probe} = 1.2 \times 10^{14}\mathrm{W/cm^2}$, $FWHM = 40\,\mathrm{fs}$, $\lambda = 800\,\mathrm{nm}$, and 36 cycles. The initial temperature is 200 K.

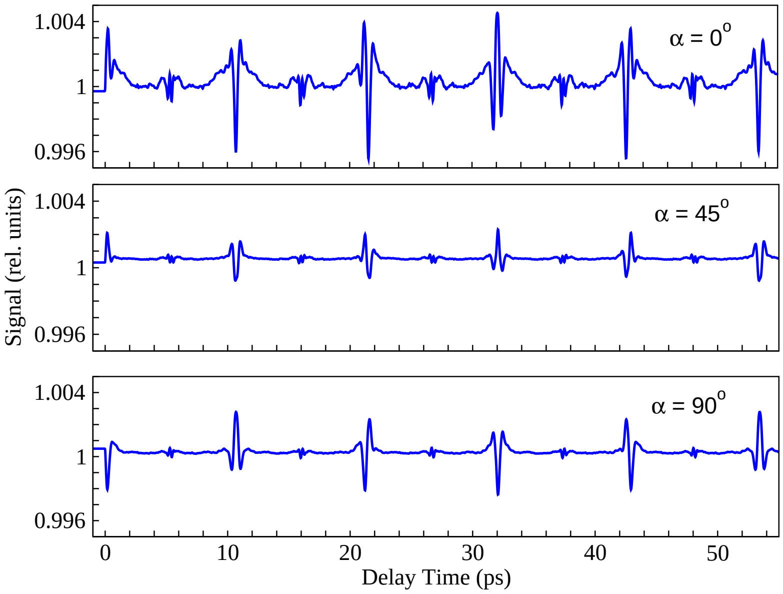

Figure 7.5: Calculated dynamic 9th harmonic order for CO_2 for various relative pump-probe polarization angles, i.e. $\alpha = 0^o$, $\alpha = 45^o$, and $\alpha = 90^o$. The laser parameters are $I_{pump} = 0.56 \times 10^{14}\,\mathrm{W/cm^2}$, $I_{probe} = 1.3 \times 10^{14}\,\mathrm{W/cm^2}$, $FWHM = 40\,\mathrm{fs}$, $\lambda = 800\,\mathrm{nm}$, and 36 cycles. The initial temperature is 300 K.

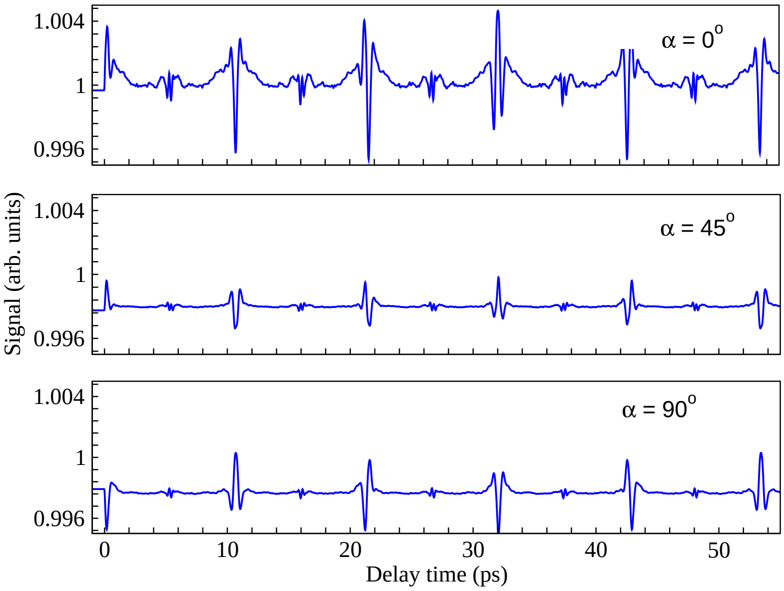

Figure 7.6: Calculated dynamic 19th harmonic order for CO_2 for various relative pump-probe polarization angles. The laser parameters are $I_{pump} = 0.53 \times 10^{14}\,\mathrm{W/cm^2}$, $I_{probe} = 1.5 \times 10^{14}\,\mathrm{W/cm^2}$, $FWHM = 40\,\mathrm{fs}$, $\lambda = 800\,\mathrm{nm}$, and 36 cycles. The initial temperature is 300 K.

revival signals for $\alpha = 90^o$ are in opposite phase, compared with $\alpha = 0^o$. On the other hand, the sign of $\left\langle \sin^2\theta \cos^2\theta \right\rangle$ does not change and hence the phase of the $\frac{1}{8}$-revival also remains constant, as seen in Fig. 7.4 (lower panel) and this is also observed experimentally [43, 138]. The expression $S\left(t_d; 90^o\right) \approx \frac{c_{11}^{(n)}}{64} \left\langle \left(3\left\langle \sin^2\theta\cos^2\theta\right\rangle - \left\langle \cos^2\theta \right\rangle + 1\right)^2 \right\rangle$ also shows that the modulation depth for $\alpha = 90^o$ is smaller than that for $\alpha = 0^o$ (that can not be obtained by the planar model [43]). The α-dependent signal of CO_2 (Figs. 7.5 for the 19th harmonic order and 7.6 for the 9th harmonic order) are qualitatively similar to the one of O_2.

7.5 Harmonic Signal as Function of Relative Polarization Angle α at a Fixed Delay Time

To further compare the present theoretical results with the experimental data, we have calculated the harmonic signal by keeping the time delay to be fixed and equal to the top alignment at first half revival $t_d \approx \frac{1}{2}T_{rev}$ and rotate the relative polarization angle α. In Fig. 7.7, we show the results for the 19th harmonic for N_2, O_2, and CO_2 and compare them with the experimental data. For $0^o \leq \alpha \leq 90$, the signal of N_2 and O_2 reduce with increasing α, whereas the signal of the 19th harmonic for CO_2 increases with increasing α. It can be seen that the calculated results qualitatively agree with the experimental data. We also point out that the calculated α-dependent signal given by Zhou *et. al.* [88] gives

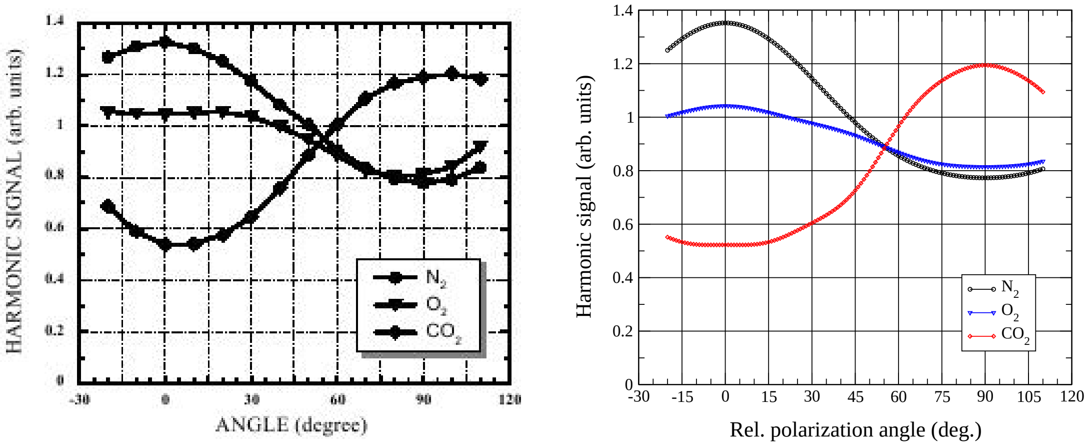

Figure 7.7: Experimental (left panel) (from [72]) and calculated (right panel) 19th harmonic at peak of its first half-revival (when its alignment degree is maximum) plotted as a function of pump-probe angle α, for N_2 ($t_d = 4.09\,\mathrm{ps}$), O_2 ($t_d = 5.68\,\mathrm{ps}$), and CO_2 ($t_d = 21.18\,\mathrm{ps}$) [72]. The laser parameters for both calculation and experiment are similar with Fig. 7.3 for N_2, Fig. 7.4 for O_2, and Fig. 7.6 for CO_2.

the same properties for N_2, but they predict unsatisfactorily that the signal for O_2 to be maximized at $\alpha \approx 50^o$, which defies from the experimental data.

The experimental results also show an extreme angle where the signal reaches a maximum or a minimum. Theoretically, the extreme angles satisfy

$$\frac{\partial S^{(n)}\left(t_d,\alpha\right)}{\partial\alpha} = 0 \tag{7.17}$$

For N_2 (Eq. (7.15)) the above equation gives us $\sin\alpha\cos\alpha\left[1-3\left\langle\left\langle\cos^2\theta\right\rangle\right\rangle(t_d)\right] = 0$. It implies that the extrema of the signal occur for $\sin\alpha\cos\alpha = 0$, corresponding to $\alpha = 0^o$ and $\alpha = 90^o$, as indeed confirmed experimentally. The last results do not depend on the delay time t_d, as will be seen later. The present theory also predicts that for randomly distributed molecules, $\left\langle\left\langle\cos^2\theta\right\rangle\right\rangle(t_d) = \frac{1}{3}$, the signal will be α-independent. Unlike N_2, the dominant contribution for HHG signal of O_2 and CO_2 come from more than one term. Therefore their derivative with respect to α also depend on at least two expectation values and hence depend on the initial temperature, even in relative scale. The extrema experimental values occur at $\alpha \simeq 20^o$ and $\alpha \simeq 80^o$ for O_2 and at $\alpha \simeq 0^o$ and $\alpha \simeq 100^o$ for CO_2. The theoretical results with $T = 200\,\mathrm{K}$ gives $\alpha \simeq 0^o$ and $\alpha \simeq 90$ for both O_2 and CO_2. However, a calculation with a lower initial temperature (T=25 K), gives the extrema signal at 30^o for O_2, as expected.

In Fig. 7.8 we show the results for N_2, O_2, and CO_2, for three points around the first half-revival time, i.e. at the top, the average, and the anti top alignments. For the case of N_2, a coincidence of the three signals is seen to occur at a critical angle $\alpha_c \approx 54.7^o$. This can be understood from its leading term, Eq. (7.15). The dynamic signal essentially remains

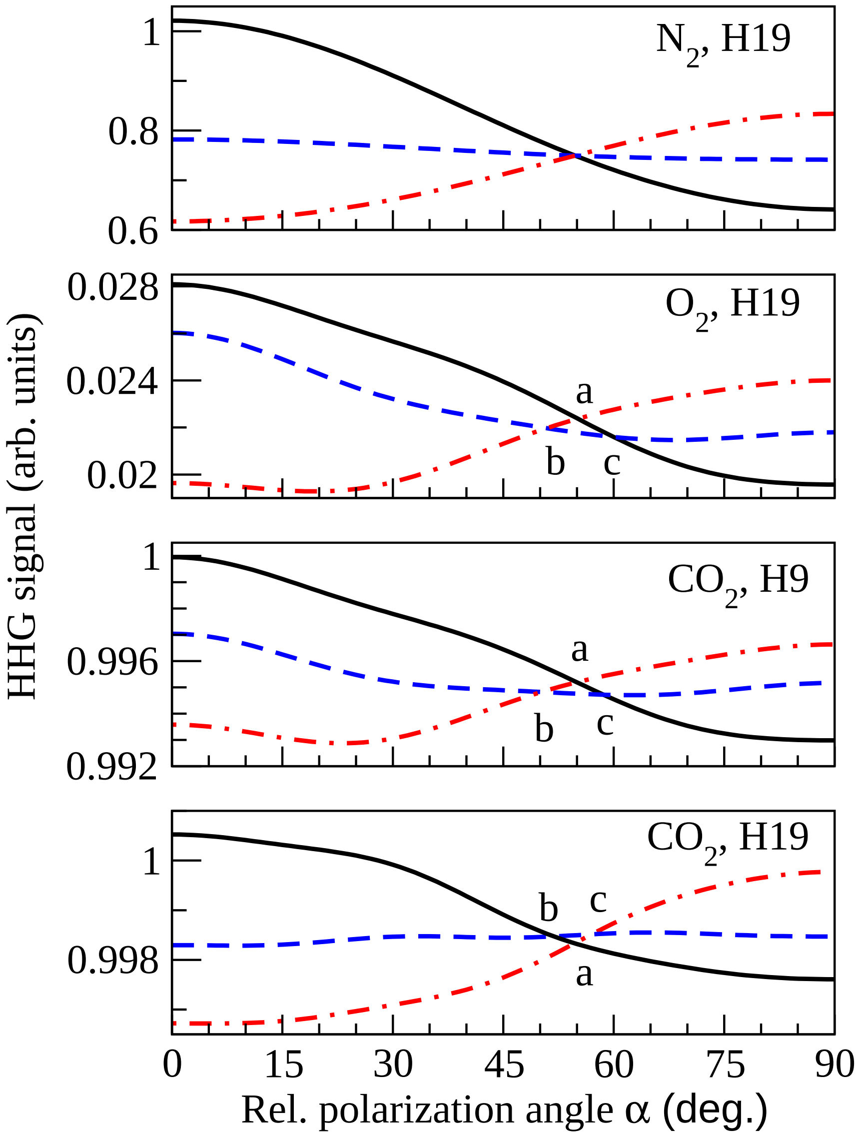

Figure 7.8: HHG signal near the first half-revival plotted as a function of pump-probe angle α, for N_2, O_2, and CO_2. The solid (black) line for 'top signal', i.e. when its alignment degree $\langle\langle\cos^2\theta\rangle\rangle$ is maximized. The dashed (blue) line for 'anti-top signal', i.e. when its alignment degree is minimum. The dash-dotted (red) line for 'average signal', i.e. when its alignment degree is in average. The observation times for top, average, and anti-top are: (4.09 ps, 4.18 ps, and 4.27 ps) for N_2, (5.680 ps, 5.790 ps, and 5.900 ps) for O_2, and (21.18 ps, 21.38 ps, and 21.58 ps) for CO_2. The pulse parameters are the same as in Fig. 7.3 for N_2, Fig. 7.4 for O_2, Fig. 7.5 for 9th harmonic order of CO_2, and Fig. 7.6 for 19th harmonic order of CO_2.

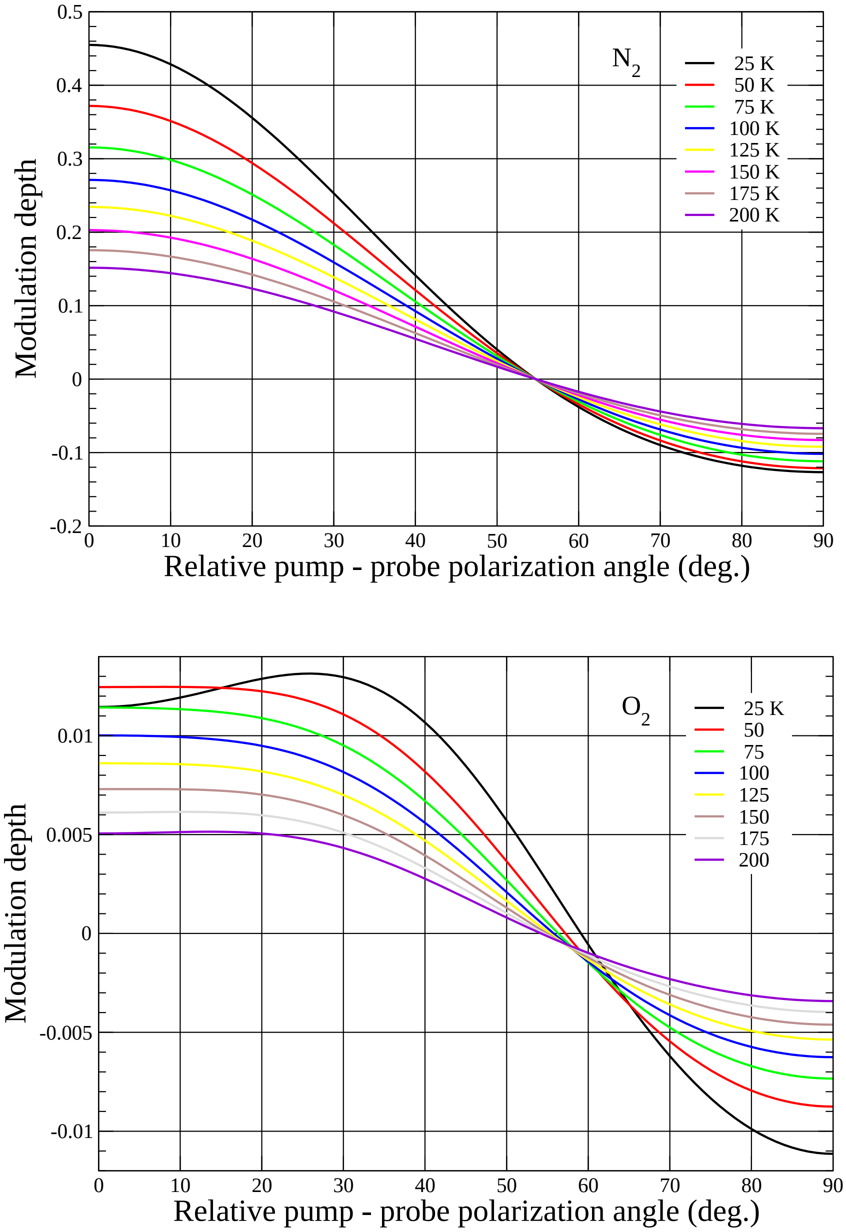

Figure 7.9: The modulation depth around first half revival of HHG signal of N_2 (upper panel) and O_2 (lower panel) for various initial temperature. The pulse parameters are similar with Figs. 7.3 and 7.4 for N_2 and O_2, respectively.

constant and *independent* of the delay t_d between the pulses if contribution of $\langle\langle\cos^2\theta\rangle\rangle(t_d)$ is zero. This condition is satisfied by $\left(3\cos^2\alpha_c - 1\right) = 0$, or $\alpha_c = \arccos\left(\sqrt{\frac{1}{3}}\right) \approx 54.7^o$. In general, the HHG signal at $t_d = 4.090\,\mathrm{ps}$ ('top'-alignment) (solid curve) lies above the signal at $t_d = 4.27\,\mathrm{ps}$ ('anti-top' alignment) (dash-dotted), for all angles α smaller than the critical $\alpha_c \approx 54.7^o$; the opposite relation holds above α_c. This geometry therefore can be used to generate a steady state HHG signal from N_2 with femtosecond pulses. The theoretical predictions on the existence of the critical angle has been seen in experiment by Miyazaki and his coworkers. The typical experimental results for N_2 are shown in Fig. 1(b) appendix G.

The existence of the critical angle α_c can be used to check the validity the other models. For the frozen nuclei model, the HHG signal of N_2 can be approximated as $S^{(n)}(t_d;\alpha) \simeq c_{00}^{(n)} + c_{01}^{(n)}\langle\langle\cos^2\theta'\rangle\rangle(t_d) + c_{11}^{(n)}\langle\langle\cos^4\theta'\rangle\rangle(t_d)$. In contrast to $\langle\cos^2\theta'\rangle$, the $\langle\cos^4\theta'\rangle$ has three crossing points, and therefore the HHG signal of N_2 has no critical angle α_c. This fact strongly supports on rejecting the frozen nuclei model.

For the case of O_2 and CO_2, in contrast, there is no single critical value of α where the signals for all t_d's could coincide. This is due mainly to the leading term $\left\langle\langle\sin^2\theta'\cos^2\theta'\rangle^2\right\rangle$ which has three crossing points. As a result, the HHG signal also has three crossing points, those are point a, when the signal at the top alignment become equal to the signal at the anti-top alignment, point b when the 'top' signal is equal to the 'average' signal, and point c when the 'anti-top' signal is equal to the 'average' signal. Nevertheless, it can be seen that these three points are not far from the critical angle $\alpha_c \approx 54.7^o$. For the 19th harmonic signal of CO_2, these three points are close to each other. The presence of these three points have been observed experimentally [138]. We also note that for the angles α smaller than that at point a the signals have the same phase with the case of parallel polarization ($\alpha = 0^o$) and they reverse their phases above it. During the calculation, we found that the position of the points a, b, and c depend on the choice of the initial temperature. For all molecules, experiment results show that the top signal is equal to anti top signal at relative polarization angle closed to $\alpha_c = 54.7^o$.

Recently, the α-dependent signals have been seen in the experiment for three organic molecules, acetylene ($\mathrm{HC} \equiv \mathrm{CH}$, linear), allene ($\mathrm{H_2C} = \mathrm{C} = \mathrm{CH_2}$, symmetric top), and ethylene ($\mathrm{H_2C} = \mathrm{CH_2}$, asymmetric top) [157, 158], all of which have bonding π orbitals between the carbon atoms. Acetylene and allene exhibit a crossover near the magic angle $\alpha_c \approx 54.7^o$, while ethylene does not. A spherical top molecule has, in addition to a conserved M-projection, also a conserved K projection, but the later has no effect on the rotational spectrum that remains constant. The present theory therefore predicts that the acetylene and allene would show a crossover, like in O_2 and CO_2, near the magic angle. In contrast, the asymmetric-top molecule ethylene has no conserved M, does not follow Eq. (7.13), and therefore does not show the same α-dependence.

In Fig. 7.9, we present the signal modulation depth, i.e. the difference between the

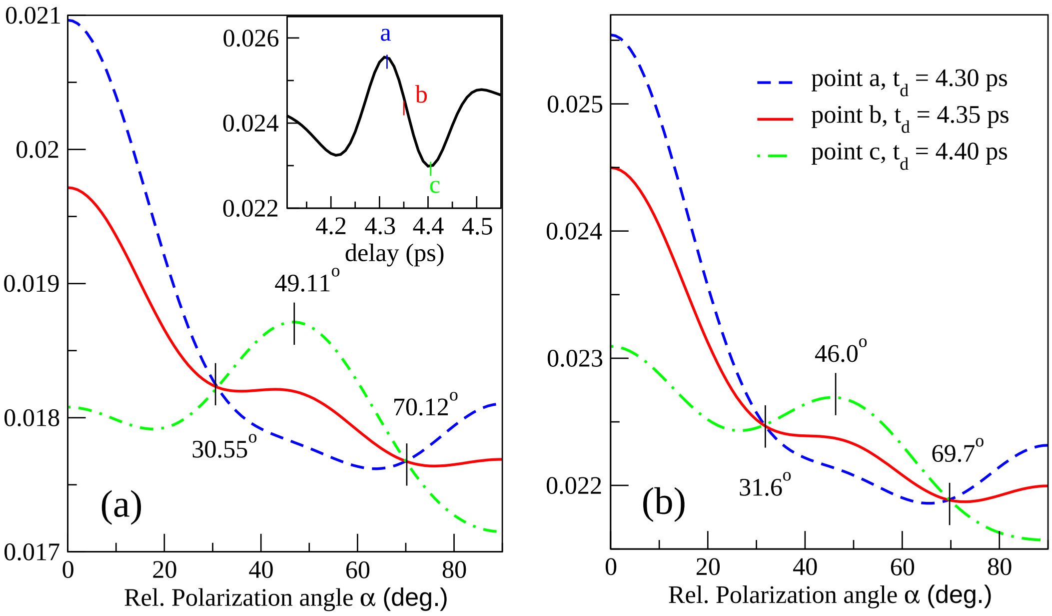

Figure 7.10: The 19th harmonic signal of O_2 near the second eight-revival, plotted as a function of pump-probe angle α. In panel (a), the signal is approximated by its first leading term only (Eq. (7.16)), whereas the true signal is shown in panel (b). The pulse parameters are the same as in Fig. 7.4 .

'top' and the 'anti-top' signals. The zero modulation corresponds to the point a in Fig. 7.8. The figures show that the position of zero modulation depends on the Boltzmann temperature for O_2. This is due to the different temperature dependence of $\langle\langle\cos^2\theta'\rangle\rangle$ and $\langle\langle\cos^4\theta'\rangle\rangle$, both which are dominant in dynamic signal of O_2. For N_2, the dominant terms are $\langle\langle\cos^2\theta'\rangle\rangle$ and $\left\langle\langle\cos^2\theta'\rangle^2\right\rangle$ and hence its zero modulation is temperature-independent.

We now turn to the eighth revivals of dynamic HHG signal of O_2 and CO_2, which are due to the transition with $\Delta J = \pm 4$. For the approximated signal taking the first leading term only (Eq. (7.16)), the transition with $\Delta J = \pm 4$ is generated by the $\langle\sin^2\theta'\cos^2\theta'\rangle$ term. The eighth revivals, therefore, dissapear when the contribution of the $\langle\sin^2\theta'\cos^2\theta'\rangle$ term is zero or $\left(35\cos^4\alpha - 30\cos^2\alpha + 3\right) = 0$, satisfied by $\alpha_c = 30.55^o$ or $\alpha_c = 70.12^o$. It mans that the eighth-revivals have two 'magic angles', in contrast to the only one 'magic angle' of the half-revivals. Moreover, the eighth revivals have extreme modulation depth (the difference between top signal and anti-top signal in eighth revival) when $\partial\left(35\cos^4\alpha - 30\cos^2\alpha + 3\right)/\partial\alpha = 0$, which is satisfied by $\alpha = 0^o$, $\alpha = 49.11^o$, and $\alpha = 90^o$. The modulation depth, therefore, reduces with increasing α for $0 \leq \alpha \leq 30.55^o$, increases again for $30.55^o \leq \alpha \leq 49.11^o$ and reduces again for $49.11^o \leq \alpha \leq 70.12$ with opposite phase, and finally increases again with original phase for $\alpha \geq 70.12$. However, the exact position of the 'magic angles' and the 'extreme angle' can shift from the above values, due to the contribution of the higher term. The dependence of eighth-revivals of dynamic signal of O_2 on the relative polarization angle α is shown in Fig. 7.10.

7.6 Harmonic Signal as Function of Delay Time t_d and Polarization Angle α

Using the above results, it is possible to obtain the HHG signal as a function of both delay time t_d and the relative polarization angle α. The calculated results are shown in Fig. 7.11 for the 19th harmonic of N_2 and O_2 and Fig. 7.12 for the 9th and the 19th harmonic orders of CO_2.

The figures show how the signals change with the delay time and the angle between the pump and the probe pulse. Keeping the angle α equal to zero, we obtain a condition when the pump and the probe polarization are parallel. By increasing α, the revival amplitude reduces and closes to zero at $\alpha \simeq 54.7^o$, and then increases again but with a different phase. For N_2, there is a critical angle $\alpha_c \simeq 54.7^o$ (Fig. 7.8), and therefore its dynamic signal at $\alpha = \alpha_c$ is time-independent. The theoretical dynamic signals of N_2 for various angle including $\alpha = \alpha_c$ are presented in Fig. 7.11 (top-right panel), whereas the corresponding experimental signals are shown in appendix G. However, O_2 and CO_2 do not have critical angle, and they never have a delay time-independent dynamic signal, as shown in Fig. 7.11 (lower panel) and Fig. 7.12. At $\alpha = 90^o$, the signal is in opposite phase but has only half the amplitude compared to the one at $\alpha = 0^o$. Further calculations show that the period of α is 180^o, beyond which the signal returns to its origin, or $S^{(n)}(t_d; \alpha + 180^o) = S^{(n)}(t_d; \alpha)$. Physically, $\alpha = 0^o$ (pump and probe pulses are parallel) and $\alpha = 180^o$ (they are anti-parallel) are indistinguishable, for the linear symmetric top molecules considered.

Finally, it is important to note here that the 'direction' of the probe pulse with respect to the pump pulse is defined by relative polarization angle α only, and it does not depend on the azimuthal angle between them, ϕ, as mentioned in Eq. (7.15) for N_2 as well as Eq. (7.16) for O_2 and CO_2. Suppose the polarization of the pump pulse is along z-axis direction, the equations above for $\alpha = 90^o$ represent the HHG observed signal for the probe pulse lie either at x-axis or y-axis direction. It means that the linear polarization pump pulse aligns molecules in the polar angle only, but leave the molecules to randomly distributed in the azimuthal angle.

7.7 Comparison with the Planar Model : Case N_2

As mentioned at the beginning of this chapter, the first heuristic model on the relative polarization angle between the pump and the probe pulses was the planar model, proposed by Kanai *et al.* [43]. In this section, we shows the distinction between the present 3 dimension (3D) model and the planar model, for case the dynamic signal of N_2.[3]

---

[3] We neglect two other theoretical models for different reason. The model of Madsen and Madsen did not say anything for $\alpha \neq 0^o$. The Lin *et al.*'s model, on the other hand, gave only a prediction on the dependence of the top signal of N_2 and O_2 on the relative polarization angle. But, their prediction for O_2 defies from the experimental data. However, they did not give any theoretical dynamic signal for $\alpha \neq 0^o$.

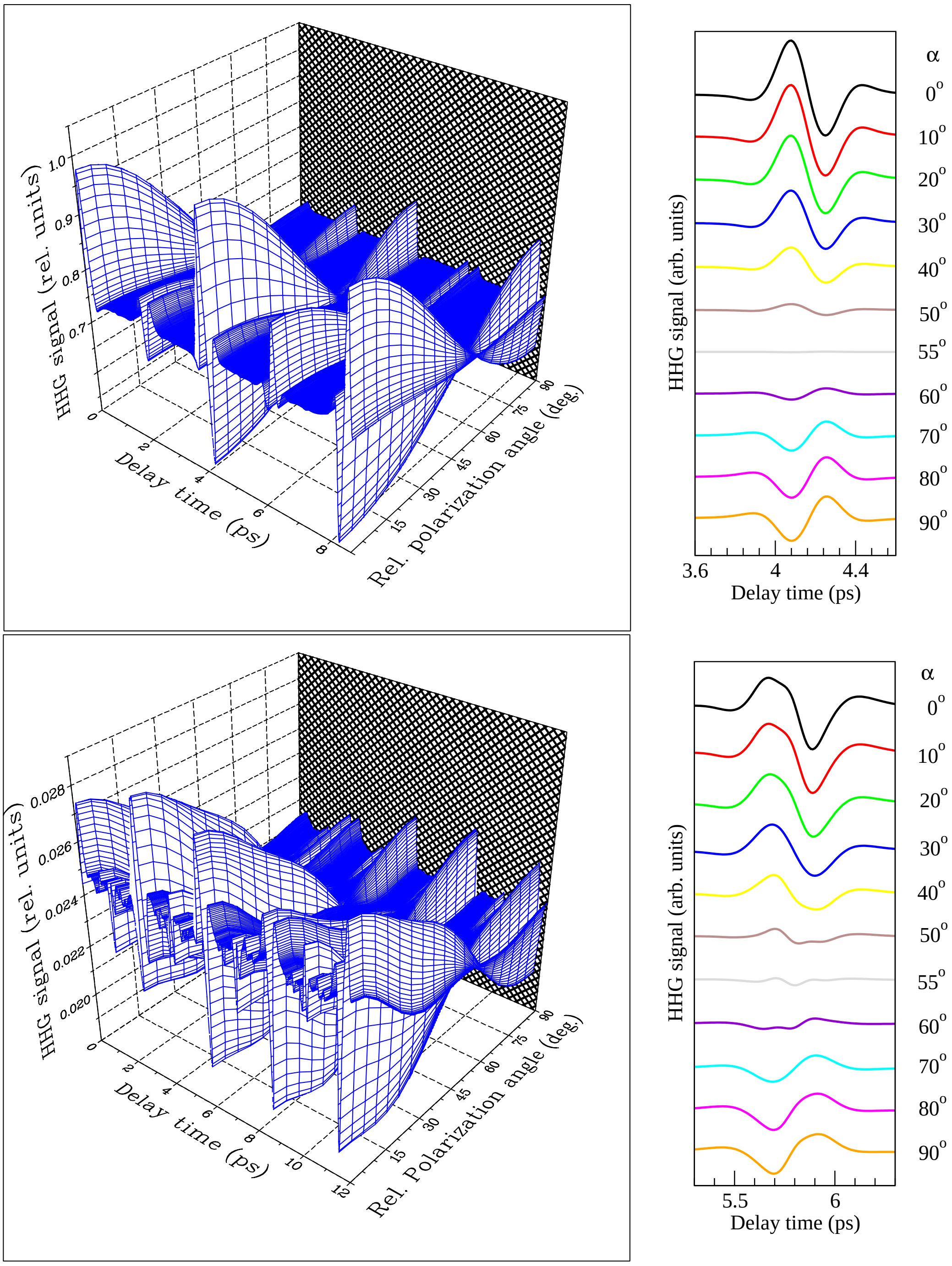

Figure 7.11: The 19th harmonic signal for N_2 (left upper panel) and O_2 (left lower panel) as function of time delay and relative polarization angle between pump and probe pulses. We also show the dynamic signals around their half revival for both N_2 (right upper panel) and O_2 (right lower panel). The pulse parameters are the same as in Figs. 7.3 and 7.4 for N_2 and O_2, respectively. The initial temperature is 200 K.

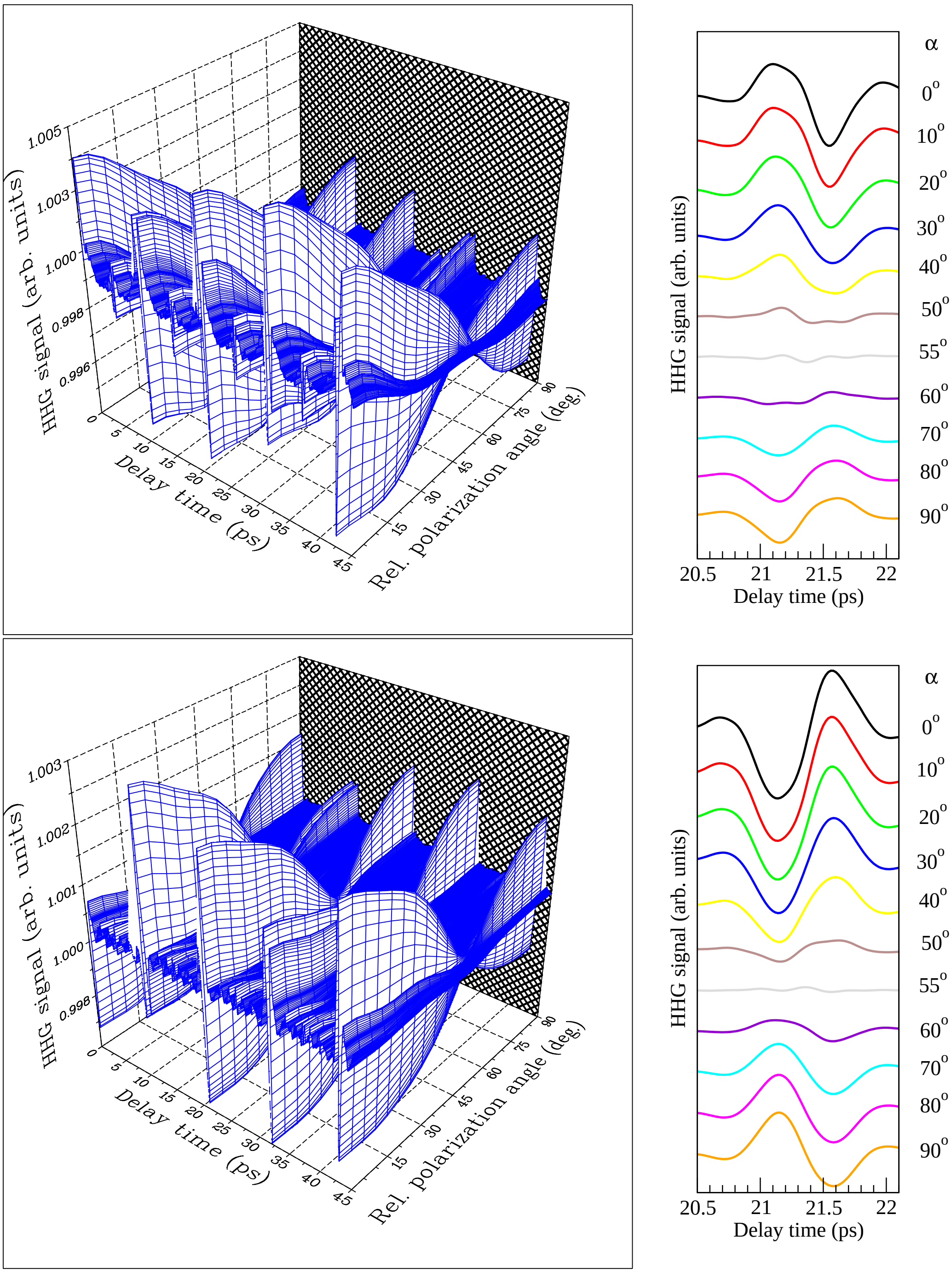

Figure 7.12: The HHG signal for CO_2 for 9th (upper panel) and 19th (lower panel) harmonic orders as function of time delay and relative polarization angle between pump and probe pulses. We also show the dynamic signals around their half revival for both 9th (right upper panel) and 19th (right lower panel). The pulse parameters are the same as in Figs. 7.5 and 7.6 for 9th and 19th, respectively. The initial temperature is 300 K.

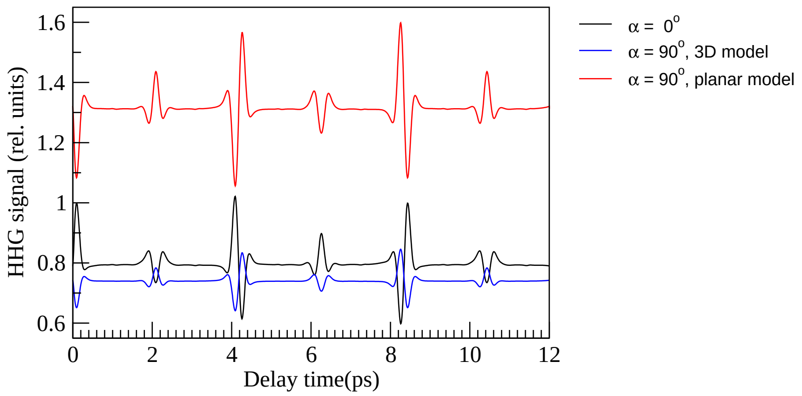

Figure 7.13: Comparison between planar model and 3D model, for 19th harmonic of N_2. The pulse parameters are the same as in Fig. 7.3.

The planar model assumed the molecular axis, the pump polarization, and the probe polarization to lie in the same plane. In this assumption, the angle between the probe polarization and the molecular axis θ' is given by

$$\theta' = \theta \pm \alpha \tag{7.18}$$

with θ is the alignment angle between the molecule and the pump pulse, while α are the relative angle between the two pulses. Following Eq. (7.18), the nth harmonic order signal of N_2 for any arbitrary angle α reads

$$\begin{aligned} S^{(n)}_{planar}\left(t_d;\alpha\right) &= c^{(n)}_{00} + c^{(n)}_{01}\left[\sin^2\alpha + \cos 2\alpha \left\langle\left\langle\cos^2\theta\right\rangle\right\rangle(t_d) \pm \frac{1}{2}\sin 2\alpha \left\langle\left\langle\sin 2\theta\right\rangle\right\rangle(t_d)\right] \\ &+ c^{(n)}_{11}\left\langle\left(\sin^2\alpha + \cos 2\alpha\left\langle\cos^2\theta\right\rangle(t_d) \pm \frac{1}{2}\sin 2\alpha\left\langle\sin 2\theta\right\rangle(t_d)\right)^2\right\rangle + \ldots \end{aligned} \tag{7.19}$$

For $\alpha = 90^o$, Eq. (7.19) reduces to:

$$S^{(n)}_{planar}\left(t_d;90^o\right) = c^{(n)}_{00} + c^{(n)}_{01}\left[1 - \left\langle\left\langle\cos^2\theta\right\rangle\right\rangle(t_d)\right] + c^{(n)}_{11}\left\langle\left(1 - \left\langle\cos^2\theta\right\rangle(t_d)\right)^2\right\rangle + \ldots \tag{7.20}$$

The calculated result for $\alpha = 90^0$ is shown in Fig. 7.13. As the 3D model, the planar model also predicts the opposite phase of the dynamic signal of perpendicular polarization compared to that of parallel polarization. However, the results from planar model defy from the experimental data in the following:

- The experimental data [72, 43], as well as the 3D model, shows that the top signal decreases with increasing the relative polarization angle α. In contrast, the planar

---

Kanai *et al.* did not give any theoretical expression for dynamic HHG signal. Here we use the dynamic HHG signal obtained by using the present adiabatic theory, generalize it for arbitrary relative polarization angle α by using both the present α-recipe and the planar model of Kanai *et al.*, and compare the results to each other.

model predicts the strength of signal, for any delay time, to increase with increasing the relative polarization angle α.

- It was shown from the experimental data [72, 43] and the 3D models, that the depth modulation at $\alpha = 90^o$ ($\Delta S_{\alpha=90^o} = S\left(t_{top}; 90^o\right) - S\left(t_{anti\,top}; 90^o\right)$) is almost a half of one at $\alpha = 0^o$. The planar model, on the other hands, gives a greater depth modulation for $\alpha = 90^o$ than that of $\alpha = 0^o$. It can be understood from Eq. (7.20) that the first and second term give the same depth for both $\alpha = 0^o$ and $\alpha = 90^o$. The difference is, therefore, due to the third term.[4]
- The planar model did not predict the existence of the critical angle $\alpha_c = 54.7°$, which is seen in the experiment.

We note here that, the discrepancy between Kanai *et al.*'s and experimental results is due to their planar assumption, or just taking the case for $\phi = 0^o$. In fact, the results also shows that the azimuthal symmetry of molecular-axis distribution around the probe pulse is broken for $\alpha \neq 0^o$. Therefore the observed signal should be obtain by integrating over ϕ. Due to the some failures mentioned above, we neglect the planar model.

7.8 A Special Case: Application to Adiabatic and Turn-off Alignment

Finally, we apply the present theory to HHG spectrum of adiabatically aligned ensemble. An experiment has been reported long time ago by Marangos and collaborator [67, 141, 142], however it remained without any theoretical explanation. In their experiment, an ensemble of N_2 molecule was aligned by a long (300 ps) pump pulse. The HHG signal was then generated by a short (70 fs) probe pulse. The HHG signal was observed for parallel and perpendicular polarizations. The calculated results for the same laser parameters and geometries are shown in Fig. 7.14, and directly compared with experimental data. For the sake of comparison we also show the intensity profile (dash-curve) of the pump pulse (right scale). As can be seen immediately from the figure, the HHG signal closely follows the evolution of the long pump pulse itself (which might be expected for an adiabatic process) and the maximum of the signal occurs at the maximum of the pulse profile, for $\alpha = 0^o$. On the other hand, a minimum is predicted for the signal at the maximum intensity, for $\alpha = 90^o$. These characteristics of the theoretical adiabatic signals for N_2 are consistent with the observed data.

---

[4] Kanai *et al.* fitted their experimental data for parallel polarization as $S\left(t_d; \alpha = 0^o\right) = c_1 + c_2 \left\langle\left\langle\cos^2\theta\right\rangle\right\rangle(t_d) + c_3\left\langle\left\langle\sin^2 2\theta\right\rangle\right\rangle(t_d)$. Using their planar model, the signal for perpendicular polarization reads $S\left(t_d; \alpha = 90^o\right) = c_1 + c_2\left[1 - \left\langle\left\langle\cos^2\theta\right\rangle\right\rangle(t_d)\right] + c_3\left\langle\left\langle\sin^2 2\theta\right\rangle\right\rangle(t_d)$, clearly showing that the modulation depth remains constant for two polarizations. This result disagrees with their experimental data, where the modulation depth of perpendicular polarization is a half of that for parallel polarization. However, they did not fit their experimental data for perpendicular polarization, with their formula.

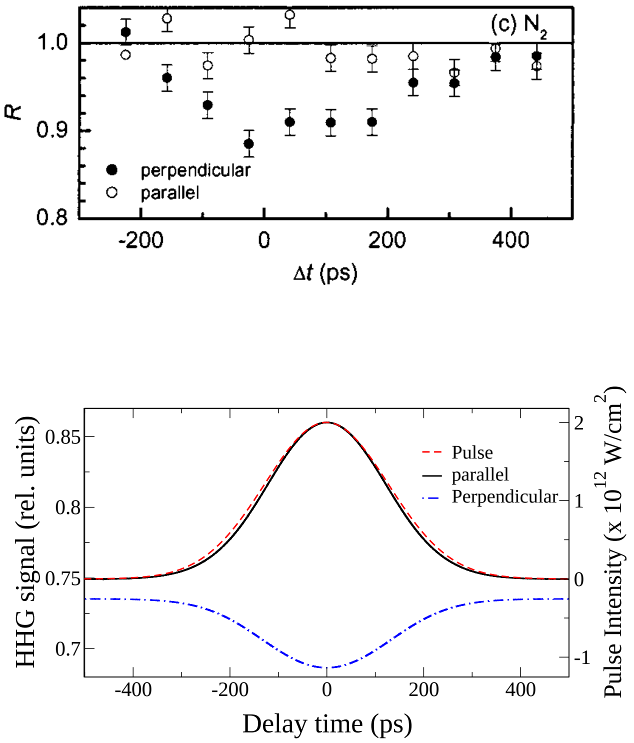

Figure 7.14: Experimental (upper panel) (from [67, 141, 142]) and theoretical (lower panel) dynamic signal of 9th harmonic signal of N_2 for various pump-probe polarizations angle $\alpha = 0^o$ and $\alpha = 90^o$; pump intensity $I = 2 \times 10^{12}$W/cm^2, duration 300 ps; probe intensity, $I = 5 \times 10^{14}$ W/cm^2, duration 70 fs, and wavelength 798 nm; Boltzmann temperature 25 K.

A good agreement between the theoretical and the experimental HHG spectrum of adiabatically and non-adiabatically aligned ensemble, supports the application of the present theory to the HHG spectrum of ensemble aligned by using turn-off schema, which has not been investigated theoretically and experimentally. In Fig. 7.15, we show the calculated results for HHG spectrum of N_2 aligned by using turn-off schema. Fig. 7.15(a) presents the dynamic signal as a function of delay time between the pump and the probe pulse. From the figure, we see that the HHG signal mimics the profile of long pump pulse, until it was turned off. After the long pulse is turned off, the signal recurrence with period $T_{rev} = 8.4$ ps, as in non-adiabatic case. This phenomena is kept for any relative polarization angle α, except that the signal with perpendicular polarization has opposite phase with respect to that with parallel polarization. In Fig. 7.15(b), we show the dependence of the top-, average-, and anti-top-signal on relative polarization angle α. It shows a 'magic' angle, $\alpha_c \approx 54.7^o$, in which the dynamic signal is time-independent. Fig. 7.15(c) shows the frequency spectra of dynamic alignment with parallel polarization. It is obtained by Fourier transforming the dynamic signal in a delay time 11 ps $\leq t_d \leq$ 19.4 ps. The spectrum shows series I:

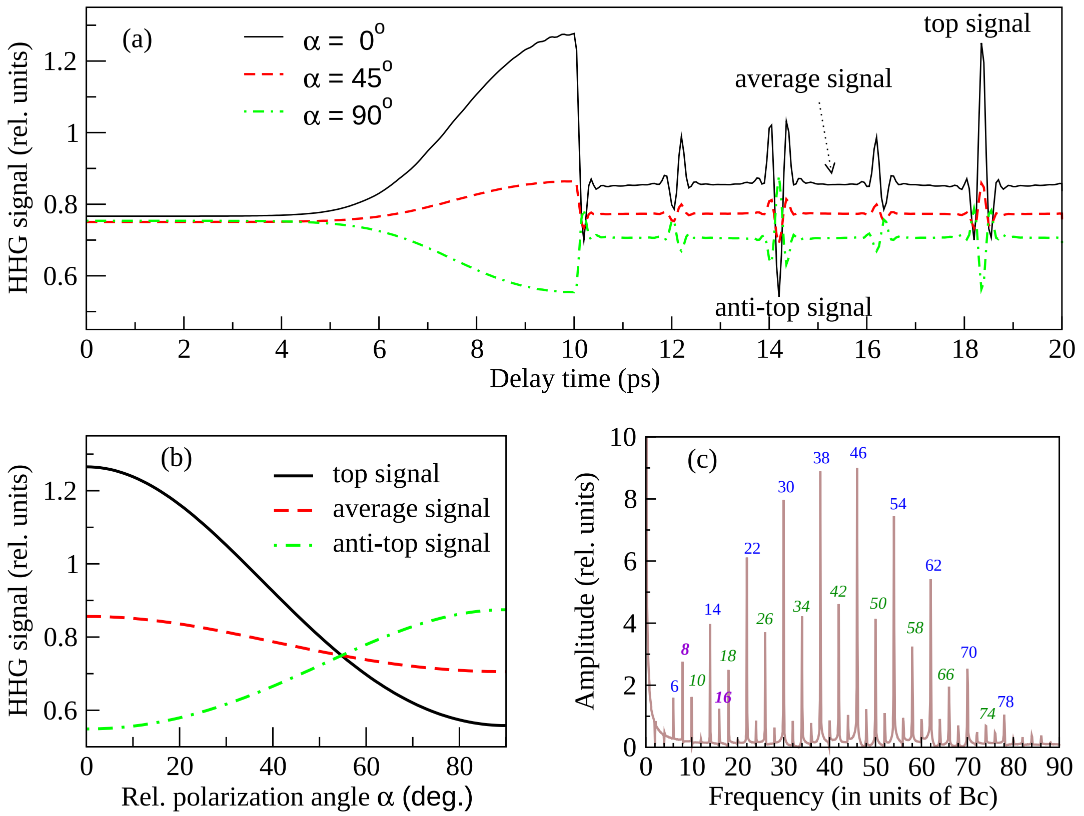

Figure 7.15: Theoretical 19th harmonic signal of molecule aligned by using turn-off method. (a) Dynamic alignment for various relative polarization angle α. (b) α-dependent HHG signal for various delay time. (c) Fourier spectrum for HHG signal with $\alpha = 0^o$. We use $I_{pump} = 0.8 \times 10^{14}\mathrm{W/cm^2}$ with $\tau_{on} = 2.6547\,\mathrm{ps}$ and $\tau_{off} = 24\,\mathrm{fs}$, $I_{probe} = 1.7 \times 10^{14}\mathrm{W/cm^2}$ with $\tau = 24\,\mathrm{fs}$ and wavelength 800 nm, and Boltzmann temperature 200 K.

$(6, 14, 22, 30, 38, ..)\,Bc$ (blue mark), series II: $(\mathit{10}, \mathit{18}, \mathit{26}, \mathit{34}, \mathit{42}, ..)\,Bc$ (green mark), series III: $(\mathbf{20}, \mathbf{28}, \mathbf{36}, \mathbf{44}, \mathbf{52}, \mathbf{60}, ..)Bc$ (without mark), and series IV: $(\boldsymbol{\mathit{4}}, \boldsymbol{\mathit{8}}, \boldsymbol{\mathit{12}}, \boldsymbol{\mathit{16}}, \boldsymbol{..})Bc$ (violet mark), as observed in non-adiabatic case.

In spite of some similarities, we remark the different character of the HHG signal from the turn-off schema. First, comparing to the non-adiabatic case, the switched-off schema has a benefit that it gives a greater top signal, a smaller anti-top signal, and as a consequence a greater modulation depth. Second, the peak of intensity of Fourier spectrum occurs at $J_{max} = 10$. With the same pulse parameter (except that $\tau_{on} = \tau_{off}$ for non-adiabatic alignment), the non-adiabatic signal has $J_{max} = 8$.

Chapter 8

Summary and Outlook

In this work, we have developed an intense-field theory for investigating high harmonic generation (HHG) signals from pump-probe experiments with intense ultrashort femtosecond lasers from aligned linear symmetric-top molecules. The present theory distinguishes itself significantly from the earlier ad hoc models. First, the present theory is derived systematically from the Schrödinger equation of the interacting system starting with the Born-Oppenheimer Hamiltonian of the total system. Second, the dipole expectation value is evaluated from the approximate intense-field expansion of the wavefunction of the considered system, which is a combination of the molecular coherent rotational wave function and the electronic wavefunction. Third, the coherent HHG emission is recognized as due to the virtual ionization of the electron by absorption of n photons and its recombination into the same state of the system from which it starts. The signal for a pure initial state is given by the norm square of the Fourier transform of the total dipole expectation value. The total HHG signal is obtained by averaging the signals from all single initial rotational wavepacket states with the Boltzmann weights corresponding to the initial temperature T. Fourth, in real computations, we use the asymptotic wave functions of the molecular orbitals, which provide an analytical expression of the dependence of HHG signal of aligned molecules on their alignment angle as a function of delay time between the pump and the probe pulse. Finally, the signal derived here has a simple structure that can be readily generalized to any relative angle between the polarization directions of the the pump and the probe pulse.

The theory is applied to the diatomic (N_2 and O_2) (chapter 4) and three-atomic (CO_2) (chapter 5) molecules. The calculated results for experimentally accessible laser parameters are presented both for the differential and the integrated total signals as a function of harmonic order and delay time between pump and probe pulse, and compared with available given experimental data. The behavior of harmonic signal is shown to depend on the molecular symmetry. For N_2, the harmonic emission signal is maximized when the pump pulse is parallel to the molecular axis, whereas the dynamic signal mimics the expectation value of the alignment measure: $\langle\langle \cos^2\theta \rangle\rangle (t_d)$. On the other hand, the harmonic signal of O_2 is maximum when the pump pulse makes an angle $\theta_{peak} \approx 40^o$ with respect to the molecular axis, whereas its dynamic signal is given by the leading term $\left\langle \left\langle \sin^2\theta\cos^2\theta \right\rangle^2 \right\rangle (t_d)$. The behavior predicted for N_2 should be applicable to other molecule with σ_g HOMO symmetry, while the behavior for O_2 should be applicable to other molecules with π_g HOMO symmetry. The present theory also predicts the existence of higher order terms, providing a good explanation on the rich properties of the dynamic signals. In addition, the harmonic spectra also show minima, which depend on angular momentum components of the recombination matrix element and thus strongly speak of the importance of the recombination process in HHG.

The three-atomic molecule CO_2 has a similar HOMO as O_2, except that the first has a longer internuclear distance and therefore its wavefunction has more significant contribution of electron with higher linear momentum state. It causes the harmonic signal of CO_2 to have the following properties. (i) The peak HHG signal θ_{peak} can be greater or smaller than that of O_2. (ii) The dynamic signal has more terms, gives the leading term $c_{11}\left\langle \left\langle \sin^2\theta\cos^2\theta \right\rangle^2 \right\rangle (t_d) + c_{12}\left\langle \left\langle \sin^2\theta\cos^2\theta \right\rangle \left\langle \sin^2\theta\cos^4\theta \right\rangle \right\rangle (t_d)$. (iii) The harmonic order with a greater θ_{peak} tends to have c_{12} to be negative, that causes an inverted modulation, where the dynamic HHG signal has an opposite phase with respect to that of its alignment degree $\left\langle \left\langle \cos^2\theta \right\rangle \right\rangle (t_d)$. The inverted modulation depends on the pump and the probe parameters and it is indicated by (a) a stronger signal at $\theta_{anti\,top}$ than the one at θ_{top} or (b) θ_{peak} is closer to $\theta_{anti\,top}$, than to θ_{top}. The behavior predicted for CO_2 should be applicable to other molecule with π_g HOMO symmetry with long internuclear distances, as seen in the recent experiment with organic molecules [158].

The validity of the present theory is then further investigated by the following.

- Investigating the Fourier spectra of the dynamic signal, which provides more precises discrete information of the spectral lines and shows detailed agreements between the theoretical and the observed spectra (chapter 6). The extra ‘anomalous’ series observed in experiment with O_2 is correctly generated by the present theory while the earlier ad hoc models fail to do so (see § 6.5). The frequency spectra also distinguish the present theory from the other ad hoc models. The Fourier spectrum also provides a way of determining otherwise difficult to determine the initial temperature of the gas jet (§ 6.4).

- Generalizing the theory for arbitrary relative polarization angle between the pump and the probe pulse, α (chapter 7). The observed dependence of the HHG signal on α which could not be reproduced by the earlier ad hoc models, is well reproduced by the present theory. By controlling α, it is shown to be possible to obtain a control over HHG signal with a maximum or a minimum modulation depth.

- The present theory predicts the existence a single ‘magic angle’ $\alpha_c = arc\cos\left(\sqrt{\frac{1}{3}}\right) \approx 54.7^o$ for linear symmetric-top molecules with σ_g HOMO symmetry, where the signals become independent of the delay, whereas a ‘crossing-neighborhood’ near $\alpha_c \approx 54.7^o$

is predicted for linear molecules with π_g HOMO symmetry (§ 7.5). Existence of such ‘magic angles’ and ’crossing neighborhood’ have recently been confirmed experimentally [166, 158].

We conclude that the theory developed and tested in this work is expected to provide a powerful analytical tool for the analysis of the phenomena of molecular HHG radiation and molecular alignments that are currently being rigorously pursued in various word wide various laboratories.

With increasing in the experimental interest in more complex systems, such as the organic molecules and for much shorter time scales, such as given by attosecond laser pulses, the present theory needs to be and could be extended to investigate them fruitfully in the future. This could be done without having to change the basic framework of the theory laid down in this work.

Bibliography

[1] J.H. Posthumus. The dynamics of small molecules in in intense laser fields. *Rep. Prog. Phys.*, 67(5):623 – 666, May 2004.

[2] A. Becker and F.H.M. Faisal. Intense-field Many-body S-matrix Theory. *J. Phys. B: At. Mol. Opt. Phys.*, 38(3):R1 – R56, Feburary 2005.

[3] P. Agostini and L.F. DiMauro. The physics of attosecond lights. *Rep Prog. Phys.*, 67(6):813 – 855, June 2004.

[4] J. Levesque and P.B. Corkum. Attosecond and science and technology. *Can. J. Phys.*, 84(1):1 – 18, January 2006.

[5] P.B. Corkum and F. Krausz. Attosecond sience. *Nature Physics*, 3(6):381 – 387, Juni 2007.

[6] X.F. Li, M. Ferray, L.A Lompre, and G. Mainfray. Multiple-harmonic generation in rare gases at high laser intensities. *Phys. Rev. A*, 39(11):5751–5761, June 1989.

[7] R.S. Judson and H. Rabitz. Teaching lasers to control molecule. *Phys. Rev. Lett.*, 68(10):1500 – 1503, March 1992.

[8] A.H. Zewail. Femtochemistry: Atomic-scale dynamics of the chemical bond. *J. Phys. Chem. A*, 104(24):5660 – 5694, June 2000.

[9] H. Stapelfeldt and T. Seideman. Colloquium: Aligning molecules with strong laser pulses. *Rev. Mod. Phys.*, 75(2):543 – 557, April 2003.

[10] T. Seideman and E. Hamilton. Nonadiabtic alignment by intense pulse. Concepts, theory, and directions. *Adv. in Atomic, Mol, and Opt. Phys.*, 52:289 – 329, April 2006.

[11] H Stapelfeldt. Laser aligned molecules: Application in physics and chemistry. *Phys. Scr.*, T110:132 – 136, 2004.

[12] S. Fleischer, I. Sh. Averbukh, and Y. Prior. Isotope-selective laser molecular-alignment. *Phys. Rev. A*, 74(4):041403, October 2006.

[13] J. Itatani, J. Levesque, D. Zeidler, H. Niikura, H. Pepin, J.C. Kieffer, P.B. Corkum, and D.M. Villeneuve. Tomographic imaging of molecular orbitals. *Nature*, 432(7019):867 – 871, December 2004.

[14] R. J. Gordon, L. C. Zhu, W. A. Schroeder, and T. Seideman. Nanolithography using molecular optics. *J. Appl. Phys.*, 94(1):669 – 676, July 2003.

[15] R. A. Bartels, T.C. Weinacht, N. Wagner, M. Baerthschy, C. H. Greene, M. M. Murname, and H. Kapteyn. Phase modulation of ultrashort light pulses using molecular rotational wave packets. *Phys. Rev. Lett.*, 88(1):013903, December 2002.

[16] K.F. Lee, D.M. Villeneuve, P.B. Corkum, and E. A. Shapiro. Phase control of rotational wave packets and quantum information. *Phys. Rev. Lett.*, 93(23):233601, November 2004.

[17] B. Zon and B. Katsnelson. Nonresonant scattering of intense light by a molecule. *Zh. Exp. Teor. Fiz.*, 69:1166 – 1178, October 1975. [Sov. Phys. JETP. 42(4), 595 – 601 (1976)].

[18] J.P. Heritage, T.K. Gustafson, and C.H. Lin. Observation of coherent transient birefringence in CS_2. *Phys. Rev. Lett.*, 34(21):1299 –1302, May 1975.

[19] D. P. Pullmann, B. Friedrich, and D.R. Herschbach. Collisional alignment of molecular rotation - simple models and trajectory analysis. *J. Phys. Chem.*, 99(19):7407 – 7415, May 1995.

[20] H.J. Loesch and A. Remscheid. Bruto force in molecular reaction dynamics: A novel technique for measuring steric effects. *J. Chem. Phys.*, 93(4):4779 – 4790, October 1990.

[21] B. Friedrich and D. Herschbach. Alignment and trapping of molecules in intense laser fields. *Phys. Rev. Lett.*, 74(23):4623 – 4626, June 1995.

[22] T. Seideman. Rotational excitation and molecular alignment in intense laser field. *J. Chem. Phys.*, 103(18):7887 – 7896, November 1995.

[23] T. Seideman. Revival structure of aligned rotational wave packets. *Phys. Rev. Let.*, 83(24):4971 – 4974, December 1999.

[24] Z. C. Yan and T. Seideman. Photomanipulation of external molecular modes: A time-dependent-self-consistent-field approach. *J. Chem. Phys.*, 111(9):4113 – 4120, September 1999.

[25] F. Rosca-Pruna and M. J. J. Vrakking. Experimental Observation of Revival Structures in Picosecond Laser-Induced Alignment of I_2. *Phys. Rev. Lett.*, 87(15):153902, September 2001.

[26] I.V. Litvinyuk, K.F. Lee, P.W. Dooley, D.M. Rayner, D.M. Vileneuve, and P.B. Corkum. Alignment-dependent strong field ionization of molecules. *Phys. Rev. Lett.*, 90(23):233003, June 2003.

[27] P. W. Dooley, I. V. Litvinyuk, K. F. Lee, D. M. Rayner, M. Spanner, D. M. Villeneuve, and P. B. Corkum. Direct imaging of rotational wave-packet dynamics of diatomic molecules. *Phys. Rev. A*, 68(2):023406, August 2003.

[28] V. Renard, M. Renard, A. Rouzee, S. Guerin, H.R. Jauslin, B. Lavorel, and O. Faucher. Noninterusive monitoring and qualitative analysis of strong laser-field-induced impulsive alignment. *Phys. Rev. A*, 70(3):033420, September 2004.

[29] D. Pinkham and R.R. Jones. Intense laser ionization of transiently aligned CO. *Phys. Rev. A*, 72(2):023418, August 2005.

[30] K.F. Lee, F. Legare, D.M. Villeneuve, and P.B. Corkum. Measured field-free alignment of deuterium by few-cycle pulses. *J. Phys. B: At. Mol. Opt. Phys.*, 39(20):4081 –4086, October 2006.

[31] W. Kim and P.M. Felker. Spectroscopy of pendular states in optical-field-aligned gas. *J. Chem. Phys.*, 104(3):1147 –1150, January 1996.

[32] B.J. Sussman, J.G. Underwood, R. Lausten, M.Y. Ivanov, and A. Stolllow. Quantum control via the dynamic Strak effect: Application to switch rotational wave packets and molecular axis alignment. *Phys. Rev. A*, 73(5):053403, May 2006.

[33] M. Leibscher, I. Sh. Averbukh, and H. Rabitz. Molecular alignment by trains of short laser pulses. *Phys. Rev. Lett.*, 90(21):213001, May 2003.

[34] M. Leibscher, I. Sh. Averbukh, and H. Rabitz. Enhanced molecular alignment by short laser pulses. *Phys. Rev. A*, 69(1):013402, January 2004.

[35] K.F. Lee, I.V. Litvinyuk, P.W. Dooley, M. Spanner, D.M. Villaneuve, and P.B. Corkum. Two-pulses alignment of molecules. *J. Phys. B: At. Mol. Opt. Phys.*, 37(3):L43 – L48, February 2004.

[36] C. Z. Bisgaard and S. S. Viftrup. Alignment enhancement of a symmetric top molecule by two short laser pulses. *Phys. Rev. A*, 73(5):053410, May 2006.

[37] M.D. Poulsen, T. Ejdrup, and H. Stapelfeldt. Alignment enhancement by the combination of a short and long laser pulse. *Phys. Rev. A*, 73(3):033405, March 2006.

[38] B. Friedrich and D.R. Herschbach. Manipulating molecules via combined static and laser fields. *J. Phys. Chem. A*, 103(49):10280 – 10288, December 1995.

[39] B. Friedrich and D. Herschbach. Enhanced orientation of polar molecules by combined electrostatic and nonresonant induced dipole forces. *J. Chem. Phys.*, 111(14):6157 – 6160, October 1999.

[40] L. Cai, J. Marango, and B. Friedrich. Time-dependent alignment and orientation of molecules in combined electrostatic and pulsed nonresonant laser fields. *Phys. Rev. Lett.*, 86(5):775 – 778, January 2001.

[41] C.A. Arango, W.K. Kennerly, and G.S. Ezra. Quantum monodromy for diatomic molecules in combined electrostatic and pulsed nonresonant laser fields. *Chem. Phys. Lett.*, 392(4-6):486 – 492, July 2004.

[42] T. Kiljunen, B. Schmidt, and N. Schwentner. Intense-field alignment of molecules confined in octohedral fields. *Phys. Rev. Lett.*, 94(12):123003, March 2005.

[43] T. Kanai, S. Minemoto, and H. Sakai. Quantum interference during high-order harmonic generation from aligned molecule. *Nature*, 435(7041):470 – 474, May 2005.

[44] F. Rosca-Pruna and M. J. J. Vrakking. Revival structures in picosecond laser-induced alignment of I_2 molecules. I. Experimental results. *J. Chem. Phys.*, 116(15):6567 – 6578, April 2002.

[45] F. Rosca-Pruna and M. J. J. Vrakking. Revival structures in picosecond laser-induced alignment of I_2 molecules. II. Numerical modeling. *J. Chem. Phys.*, 116(15):6579 – 6588, April 2002.

[46] R. Torres, R. de Nalda, and J.P. Marangos. Dynamics of laser-induced molecular alignment in the impulsive and adiabatic regime: A direct comparison. *Phys. Rev. A*, 72(2):023420, August 2005.

[47] D. Daems, S. Guerin, E. Hertz, H.R. Jauslin, B. Lavorel, and O. Faucher. Field-free two-direction alignment of linear molecules by elliptic laser pulses. *Phys. Rev. Lett.*, 95(6):063005, August 2005.

[48] H. Tanji, S. Minemoto, and H. Sakai. Three-dimensional molecular orientation with combined electrostatic and elliptically polarized laser fields. *Phys. Rev. A*, 72(6):063401, December 2005.

[49] K.F. Lee, D.M. Villeneuve, P.B. Corkum, A. Stolow, and J.G. Underwood. Fild-free three dimensional alignment of polyatomic molecules. *Phys. Rev. Lett.*, 97(17):173001, October 2006.

[50] A. McPherson, G. Gibson, H. Jara, U. Johann, T. S. Luk, I. A. McIntyre, K. Boyer, and C. K. Rhodes. Studies of multiphoton production of vacuum-ultraviolet radiation in the rare gases. *J. Opt. Soc. Am. B*, 4(4):595 – 601, April 1987.

[51] M Ferray, A L'Huillier, X F Li, L A Lompre, G Mainfray, and C Manus. Multiple-harmonic conversion of 1064 nm radiation in rare gases. *J. Phys. B: At. Mol. Opt. Phys.*, 21(3):L31, February 1988.

[52] F.H.M. Faisal. *Theory of Multiphoton Processes.* Plenum Press, New York, 1987.

[53] J.L. Krause, K.J. Schafer, and K.C. Kulander. High-order harmonic generation from atoms and ions in the high intensity regime. *Phys. Rev. Lett.*, 68(24):3535 – 3538, March 1992.

[54] P.B. Corkum. Plasma perspective on strong-field multiphoton ionization. *Phys. Rev. Lett.*, 71(13):1994 – 1997, February 1993.

[55] K.C. Kulander, K.J. Schafer, and J.L. Krause. *Dynamics of short-pulse excitation and ionization and harmonic generation.* Plenum Press, 1993.

[56] M. Lewenstein, Ph. Balcou, M. Yu. Ivanov, A. L'Huillier, and P.B. Corkum. Theory of high-harmonic generation by low-frequency laser fileds. *Phys. Rev. A*, 49(3):2117 – 2132, March 1994.

[57] L.V. Keldysh. Ionization in the field of a strong electromagnetic wave. *Sov. Phys. JETP*, 20:1307, 1965.

[58] Y. Liang, S. Augst, S.L. Chin, Y. Beaudoin, and M. Chaker. High harmonic generation in atomic and diatomic molecular gases using intense picosecond laser pulses - a comparison. *J. Phys. B: At. Mol. Opt Phys.*, 27(28):5119 – 5130, October 1994.

[59] H. Sakai and K. Miyazaki. High-order harmonic generation in nitrogen molecule with subpicosecond visible dye-laser pulse. *Appl. Phys. B: Lasers Opt.*, 61(5):493 – 498, November 1995.

[60] B. Shan, X.M. Tong, Z. X. Zhao, Z. Chang, and C.D. Lin. High-order harmonic cut-off extension of the O_2 molecule due to ionization suppression. *Phys. Rev. A*, 66(6):061401(R), 2002.

[61] C. Altucci, R. Vellota, J.P. Marangos, E. Hessel, E. Springate, M. Pascolini, L. Poletto, P. Villloresi, C. Vozzi, G. Sansone, M. Anscombe, J-P. Caumes, S. Stagira, and M. Nisoli. Dependence upon the molecular and atomic ground state of higher-order harmonic generation in few-optical-cycle regime. *Phys. Rev. A*, 71(1):013409, January 2005.

[62] V. Renard, M. Renard, S. Guerin, Y. T. Pashayan, B. Lavorel, O. Faucher, and H.R. Jauslin. Postpulse molecular alignment measured by a weak field polarization technique. *Phys. Rev. Lett.*, 90(15):153601, April 2003.

[63] M. Renard, E. Hertz, S. Guerin, H.R. Jauslin, B. Lavorel, and O. Faucher. Control of field-fre molecular alignment by phase-shaped laser pulse. *Phys. Rev. A*, 72(2):025401, August 2005.

[64] M. Tsubouchi and T. Suzuki. Photoionization of homonuclear diatomic molecules aligned by an intense femtosecond laser pulse. *Phys. Rev. A*, 72(2):022512, 2005.

[65] T. K. Kjeldsen and L. B. Madsen. Alignment-dependent above-threshold ionization of molecules. *J. Phys. B: At. Mol. Opt. Phys.*, 40(1):237 – 245, January 2007.

[66] C.B. Madsen, A.S. Mouritzen, T.K. Kjeldsen, and L.B. Madsen. Effects of orientation and alignment in high-harmonic generation and above threshold ionization. *Arxiv/physics*, -:0703234, March 2007.

[67] R. Vellota, N. Hay, M.B. Mason, M. Castillejo, and J.P. Marangos. High-order harmonic generation in aligned molecules. *Phys. Rev. Lett.*, 87(18):183901, October 2001.

[68] R. de Nalda, E. Hessel, M. Lein, N. Hay, R. Vellota, E. Springate, M. Castillejo, and J.P. Marangos. Role of orbital symmetry in high-order harmonic generation from aligned molecules. *Phys. Rev. A*, 69(3):031804, March 2004.

[69] M. Kaku, K. Masuda, and K. Miyazaki. Observation of revival structure in femtosecond laser indiced alignment of N_2 with high-order harmonic generation. *Japan. J. Appl. Phys.*, 43(4B):L591 – 593, April 2004.

[70] J. Itatani, D. Zeidler, J. Levesque, M. Spanner, D.M. Villaneuve, and P.B. Corkum. Controlling high harmonics generation with molecular wave packets. *Phys. Rev. Lett.*, 94(12):123902, March 2005.

[71] K. Miyazaki, M. Kaku, G. Miyaji, A. Abdurrouf, and F.H.M. Faisal. Field-free alignment of molecules observed with high-order harmonic generation. *Phys. Rev. Lett.*, 95(24):243903, December 2005.

[72] M. Kaku, R. Morichi, G. Miyaji, and K. Miyazaki. High harmonic generation from femtosecond-laser aligned N_2, O_2, and CO_2 molecules. In *IEEE on Quantum Electronic Conference 2005*, pages 1036 – 1037, July 2005.

[73] C. Vozzi, F. Calegari, E. Benedetti, R. Berlasso, G. Sansone, S. Stagira, M. Nisoli, C. Altucci, R. Velotta, R. Torres, E. Hessel, N. Kajumba, and J.P. Marangos. Probing two-centre interference in molecular high harmonic generation. *J. Phys. B: At. Mol. Opt. Phys.*, 39(13):S457 – S466, July 2006.

[74] T. Kanai, S. Minemoto, and H. Sakai. Ellipticity dependence of high-order harmonic generation from aligned molecules. *Phys. Rev. Lett.*, 98(5):053002, February 2006.

[75] C. Altucci, R. Vellota, R. Torres, E. Heesel, N. Kajumba, J.P. Marangos, C. Vozzi, F. Calegari, E. Benedetti, G. Sansone, S. Stagira, and M. Nisoli. Probing electron dynamics by ellipticity effects in molecular high harmonic generation. *J. Mod. Opt.*, 54(7):1063 – 1074, May 2007.

[76] J. Levesque, J. Itatani, D. Zeidler, H. Pepin, J.C. Kiefer, P.B. corkum, and D.M. Villeneuve. Probing electronic structure of molecules with high harmonics. *J. Mod. Opt.*, 53(1-2):165 – 192, January 2006.

[77] S. Patchkovskii, Z. Zhao, T. Brabec, and D.M. Villeneuve. High harmonic generation and molecular orbital tomography in multielectron system. *J. Chem. Phys.*, 126(11):114306, March 2007.

[78] S. Patchkovskii, Z. Zhao, T. Brabec, and D.M. Vileeneve. High harmonic generation and molecular orbital tomography in multielectron system. *Phys. Rev. Lett.*, 97(2):123003, September 2006.

[79] S. Baker, J.S. Robinson, C.A. Haworth, H. Teng, R.A. Smith, C.C. Chirila, M. Lein, J.W.G. Tisch, and J.P. Marangos. Probing proton dynamics in molecules on an attosecond time scale. *Science*, 312:424 –427, 2006.

[80] N. L. Wagner, A. Wüest, I. P. Christov, T. Popmintchev, X. Zhou, M. M. Murname, and H. C. Kapteyn. Monitoring molecular dynamics using coherent electron from high harmonic generation. *PNAS*, 5(103):13279 – 13285, September 2006.

[81] H. Wabnitz, Y. Maisere, L.J. Frasinski, M. Stankiewicz, W. Boutu, P. Breger, P. Johnsson, H. Merdji, P. Monchicourt, P. Salieres, K. Varju, M. Vitteau, and B. Carre. Generation of attosecond pulses in molecular nitrogen. *Eur. Phys. J. D*, 40(2):305 – 311, November 2006.

[82] K. Miyazaki, M. Kaku, R. Morichi, G. Miyaji, A. Abdurrouf, and F.H.M. Faisal. Field-free molecular alignment observed with high-order harmonic generation. In 14^{th} *Laser Physics Conference 2005*, July 2005.

[83] R. Kopold, W. Becker, and M. Kleber. Model calculations of high-harmonic generation in molecular ions. *Phys. Rev. A*, 5(5):4022 – 4038, November 1998.

[84] D. G. Lappas and J.P. Marangos. Orientation dependence of high-order harmonic generation in hydrogen molecular ions. *J. Phys. B: At. Mol. Opt. Phys.*, 33(21):4679 – 4689, 2000.

[85] M. Lein, N. Hay, R. Velotta, J.P. Marangos, and P. L. Knight. Role of intramolecular phase in high-harmonic generation. *Phys. Rev. Lett.*, 88(18):183903, 2002.

[86] M. Lein, N. Hay, R. Velotta, J.P. Marangos, and P. L. Knight. Interference effects in high-order harmonic generation with molecules. *Phys. Rev. A*, 66(2):023805, April 2002.

[87] X.X. Zhou, X.M. Tong, Z.X. Zhao, and C.D. Lin. Role of molecular orbital on the alignment dependence of high-order harmonic generation with molecules. *Phys. Rev. A*, 71(6):061801(R), June 2005.

[88] X.X. Zhou, X.M. Tong, Z.X. Zhao, and C.D. Lin. Alignment dependence of high-order harmonic generation from N_2 and O_2 molecules in intense laser fields. *Phys. Rev. A*, 72(3):033412, September 2005.

[89] C.B. Madsen and L.B. Madsen. High-harmonic generation from arbitrarily oriented diatomic molecules including nuclear motion and field-free alignmnet. *Phys. Rev. A*, 74(2):023403, August 2006.

[90] J.D. Jackson. *Clasical Electrodyanamics.* John Wiley and Sons, New York, 1962.

[91] F.H.M. Faisal and A. Becker. 'Intense-Field Many Body S-Matrix Theory' and mechanism of laser induced double ionization of Helium. In D.H. Campbell and H. Kleinpoppen, editors, *Selected Topics on Electron Physics*, pages 397 – 410. Plenum Press, New York, 1996.

[92] A. Becker and F.H.M. Faisal. S-matrix theory of two-electron momentum distribution produced by double ionization in intense laser fields. *Opt. Express*, 8(7):383 – 394, March 2001.

[93] B.H. Bransden and C.J. Joachain. *Physics of Atoms and Molecules.* Longman, London, 1995.

[94] F.H.M. Faisal, A. Abdurrouf, K. Miyazaki, and G. Miyaji. Origin of anomalous spectra of dynamic alignments observed in n_2 and o_2. *Phys. Rev. Lett.*, 98(14):143001, April 2007.

[95] J. Ortigoso, M. Rodriguez, M. Gupta, and B. Friedrich. Time evolution of pendular states created by the interaction of molecular polarizability with a pulsed nonresonant laser field. *J. Chem. Phys.*, 110(8):3870 – 3875, February 1999.

[96] F.H.M. Faisal. Multiple absorption of laser photons by atoms. *J. Phys. B: At. Mol. Opt. Phys.*, 6(4):L89 – L92, April 1973.

[97] H.R. Reiss. Effect of an intense electromagnetic field on a weakly bound system. *Phys. Rev. A*, 22(5):1786 – 1813, November 1980.

[98] D.M. Chase. Adiabatic approximation for scattering processes. *Phys. Rev.*, 104(3):838 – 842, November 1956.

[99] F.W.J. Olver. *Asymptotic and Special Functions.* Academic Press, New York, 1974.

[100] A. Erdelyi. *Asymptotic expansions.* Dover, 1956.

[101] F.E. Harris and H.H. Michels. Multicenter integrals in quantum mechanics. I. Expansion of Slater-type orbitals about a new origin. *J. Chem. Phys.*, 43(10):S165 – S169, November 1965.

[102] F.H.M. Faisal. Electrons-molecule interaction: I. *J.Phys. B*, 3(5):636 – 640, May 1970.

[103] D.A. Varshalovich, A.N. Moskalev, and V.K. Khersonski. *Quantum Theory of Angular Momentum.* Word Scientific, Singapore, 1988.

[104] R. N. Zare. *Angular Momentum, Understanding Aspects in Chemistry and Physics.* John Wiley & Sons, New York, 1988.

[105] X.M. Tong, Z.X. Zhao, and C.D. Lin. Theory of molecular tunneling ionization. *Phys. Rev. A*, 66(3):033402, September 2002.

[106] T.K. Kjeldsen and L.B. Madsen. Strong-field ionization of diatomic molecules and companion atoms: strong-field approximation and tunneling theory including nuclear motion. *Phys. Rev. A*, 71(2):023411, February 2005.

[107] I.S. Gradshsteyn and I.M. Rhysik. *Table of integral, series, and product.* Academic Press, New York, 1965.

[108] G. Arfken and H.J. Weber. *Mathematical Methods for Physicists.* Elsevier Inc., 2005.

[109] M.W. Schmidt, K.K. Baldridge, J.A. Boatz, S.T. Elbert, M.S. Gordon, J.H. Jensen, S. Koseki, N. Matsunaga, K.A. Nguyen, S. Su, T.L. Windus, M. Dupuis, and J.A. Motgomery Jr. General atomic and molecular electronic structure system. *J. Compt. Chem.*, 14(11):1347 – 1363, November 1993.

[110] A.T. Le, X.M. Tong, and C.D. Lin. Evidence of two-center interference in high-order harmonic generation from CO_2. *Phys. Rev. A*, 73(4):041402(R), April 2006.

[111] J.P. Marangos, C. Altucci, R. Vellota, E. Hessel, E. Springate, M. Pascolini, L. Poletto, P. Villloresi, C. Vozzi, G. Sansone, M. Anscombe, J-P. Caumes, S. Stagira, and M. Nisoli. Molecular orbital dependence of high-order harmonic generation. *J. Mod. Opt.*, 53(1-2):97 – 111, January 2006.

[112] C.B. Madsen and L.B. Madsen. Theoretical studies of high-harmonic generation:Effect of symmetry, degeneracy, and orientation. *Arxiv/physics*, -:07063306v1, June 2007.

[113] C.M. Dion, A. Keller, O. Atabek, and A.D. Bandrauk. Laser-induced alignment dynamics of HCN: Roles of the permanent dipole moment and polarizability. *Phys. Rev. A*, 59(2):1382 – 1391, February 1999.

[114] B. Friedrich. Recurring molecular alignment induced by pulsed nonresonant laser fields. *Collect. Czeh. Chem. Commun.*, 66(7):991–1004, July 2001.

[115] P.F. Bernath. *Spectra of Atoms and Molecules.* Oxford University Press, Oxford, 1995.

[116] W.H. Press, B.P. Flannery, S.A. Teukolsky, and W.T. Vetterling. *Numerical Recipes: The Art of Scientific Computing.* Cambridge University Press, 1986.

[117] G. Herzberg. *Molecular Spectra and Molecular Structure, Vol I : Spectra of Diatomic Molecules.* Van Nostrand Reinhold, Ltd., London, 1950.

[118] J.O. Hirshfelder and C.F. Curtis. *Molecular Theory of Gases and Liquids.* Wiley, New York, 1954.

[119] K.J. Miller. Additivity methods in molecular polarizaility. *J. Am. Chem. Soc.*, 112(23):8533 – 8542, November 1990.

[120] K.J. Miller. Calculation of the molecular polarizability tensor. *J. Am. Chem. Soc.*, 112(23):8543 – 8551, November 1990.

[121] A.M. James and M.P. Lord. *Chemical Physical Data.* MacMillan, London, 1992.

[122] D.A. McQuarrie and J.D. Simon. *Physical Chemistry, A Molecular Approach.* University Sience Books, California, 1997.

[123] M. Spanner. *Field Free Alignment and Strong Field Control of Molecule Rotors.* PhD thesis, University of Waterloo, Ontorio, Canada, 2004. $< http : //etd.uwaterloo.ca/etd/mspanner2004.pdf >$.

[124] T. Seideman. On the dynamics of rotationally broad, spatially aligned wave packets. *J. Chem. Phys.*, 115(13):5965 – 5973, October 2001.

[125] M. Machholm. Postpulse alignment of molecules robust to thermal averaging. *J. Chem. Phys.*, 115(23):10724 – 10730, December 2001.

[126] C.M. Dion, A Keller, and O. Atabek. Orienting molecules using half-cycle pulses. *Eur. Phys. J. D.*, 14(1):249 – 255, May 2001.

[127] I. Sh. Averbukh and N.F. Parelman. Fractional revivals: Universality in the long-term evolution of quantum wave packets beyond the correspondence principle dynamics. *Phys. Lett. A*, 139(9):449 – 453, August 1989.

[128] M. J. J. Vrakking, D. M. Villeneuve, and A. Stolow. Observation of fractional revivals of a molecular wave packet. *Phys. Rev. A*, 54(1):R37 – R40, July 1996.

[129] R. Bluhm, V.A. Kostelecky, and J.A. Porter. Time evolution and revival structure of localized quantum wave packets. *Am. J. Phys.*, 64(7):944 – 953, July 1996.

[130] M. Lein, P.P. Corso, J.P. Marangos, and P.L. Knight. Orientation dependence of high-order harmonic generation in molecules. *Phys. Rev. A*, 67(2):023819, February 2003.

[131] C. Z. Bisgaard, M. D. Poulsen, E. Peronne, S. S. Viftrup, and H. Stapelfeldt. Observation of enhanced field-free molecular alignment by two laser pulses. *Phys. Rev. Lett.*, 92(17):173004, April 2004.

[132] S. Ramakrishna and T. Seideman. Intense laser alignment in dissipative media as a route to solvent dynamics. *Phys. Rev. Lett.*, 95(11):113001, September 2005.

[133] D. Zeidler, J. Levesque, J. Itatani, K. Lee, P.W. Dooley, I Litvinyuk, D.M. Villeneuve, and P.B. Corkum. *Ultrafast Otics IV*. Springer, New York, 2004. p. 147.

[134] G.H. Lee, H.T. Kim, J.Y. Park, and C.H. Nam. Revival structures of linear molecules in a field-free alignment condition as probed by high-order harmonic generation. *J. Korean Phys. Soc.*, 49(1):S337 – S341, July 2006.

[135] G. Miyaji, M. Kaku, and K. Miyazaki. Frequancy spectra in field-free revival structure of fs-laser aligned molecules. In *IEEE on Quantum Electronic Conference 2005*, pages 1038 – 1039, July 2005.

[136] W.L. Jorgensen and L. Salem. *The Organic Chemist's Book of Orbitals.* Academic Press, New York, 1973.

[137] B. Zimmermann, M. Lein, and J.M. Rost. Analysis of recombination in high-order harmonic generation in molecules. *Phys. Rev. A*, 71(3):033401, 2005.

[138] K. Miyazaki. Private communication, 2006.

[139] V. Kumarappan, C.Z. Bisgaard, S.S. Viftrup, L. Holmegaard, and H. Stapelfeldt. Role of rotational temperature in adiabatic molecular alignment. *J. Chem. Phys.*, 125(19):194309, November 2006.

[140] F. Rosca-Pruna. *Alignment of Diatomic Molecules Induced by Intense Laser Fields.* December, Vrije Universiteit, 2001. $< http : //www.amolf.nl/publications/theses/rosca/index.html?rosca.html >$.

[141] N. Hay, R. Vellota, M. Lein, R. de. Nalda, E. Hessel, M. Castillejo, and J.P. Marangos. High-order harmonic generation in laser-aligned molecules. *Phys. Rev. A*, 65(5):053805, April 2002.

[142] N. Hay, M. Lein, R. Vellota, R. de. Nalda, E. Hessel, M. Castillejo, P.L. Knight, and J.P. Marangos. Investigation of electron wave-packet dynamics and high-order harmonic generation in laser-aligned molecules. *J. Mod. Opt.*, 50(3-4):561 – 577, March 2003.

[143] L. Cui, J. Zhao, Y.J. Hu, X.H. Zeng, and B. Gu. Effect of different laser polarization direction on high order harmonic gneration of N_2 and H_2. *Appl. Phys. Lett.*, 89(21):211103, November 2006.

[144] C. Vozzi, F. Calegari, E. Benedetti, J.-P. Caumes, G. Sansone, S. Stagira, M. Nisoli, R. Torres, E. Hessel, N. Kajumba, J.P. Marangos, C. Altucci, and R. Velotta. Controlling two-centre interference in molecular high harmonic generation. *Phys. Rev. Lett.*, 95(15):153902, October 2005.

[145] H. Merdji, W. Boutu, R. Fitour, P. Monchicourt, P. Breger, B. Carre, and P. Salieres. Measurements of attosecond pulses from aligned molecules. In *KITP Conference: Attosecond Science Workshop (Jul 31 - Sep 15, 2006)*, 2006. $< http : //online.itp.ucsb.edu/online/atto\_c06 >$.

[146] J.P. Marangos. Molecular stucture in an instants. *Nature*, 435(7041):435, May 2005.

[147] J. Muth-Böhm, A. Becker, and F.H.M. Faisal. Suppressed molecular ionization for a class of diatomics in intense femtosecond laser fields. *Phys. Rev. Lett.*, 85(11):2280 – 2283, February 2000.

[148] J. Muth-Böhm. *Theoretische Untersuchungen zur Ionisationsdynamik von Molekülen in intensiven Laserfeldern.* PhD thesis, Faculty of Physics, University of Bielefeld, Bielefeld, Germany, June 2001.

[149] F. Grasbon, G.G. Paulus, S.L. Chin, H. Walther, J. Muth-Böhm, A. Becker, and F.H.M. Faisal. Signature of symmetry-induced quantum-interference effects observed in abive-threshold-ionization spectra of molecules. *Phys. Rev. A*, 63(4):041402(R), April 2001.

[150] G. L. Kamta, A.D. Bandrauk, and P.B. Corkum. Asymmetry in the harmonic generation from nonsymmetric molecules. *J. Phys. B: At. Mol. Opt. Phys.*, 38(20):L339 – L346, October 2005.

[151] M. Lein, R. de. Nalda, E. Hessel, N. Hay, E. Springate, R. Vellota, M. Castillejo, P.L. Knight, and J.P. Marangos. Signature of molecular structure in the strong-field response of aligned molecules. *J. Mod. Opt.*, 52(2-3):465, January 2005.

[152] A.T. Le, X.M. Tong, and C.D. Lin. Alignment dependence of high-order harmonic generation form CO_2. *J. Mod. Opt.*, 54(7):967 – 980, May 2007.

[153] M.A. Blanco, M. Florez, and M. Bermejo. Evaluation of the rotation matrices in the basis of real sherical harmonics. *J. Mol. Struc.*, 419(1-3):19 – 27, December 1997.

[154] P. Linstrom and W. Mallard, editors. *NIST Chemistry Webbook, NIST Standard Reference Database Number 69.* National Institute of Standards and Technology, Gaithersburg. MD, 2005.

[155] A. Flettner, J König, M.B. Mason, T. Pfeifer, U. Weichmann, R. Düren, and G. Gerber. Ellipticity dependence of atomic and molecular high harmonic generation. *Eur. Phys. J. D*, 21(1):115 – 119, October 2002.

[156] A. Flettner, J König, M.B. Mason, T. Pfeifer, U. Weichmann, and G. Gerber. Atomic and molecular high-harmonic generation: A comparison of ellipticity dependence based on the three-step model. *J. Mod. Opt.*, 50(3 - 4):529 – 537, March 2003.

[157] N. Kajumba, R. Torres, S. Baker, J.S. Robinson, J.G.W. Tisch, J.G. Underwood, R. de Nalda, C. Altucci, R. Velotta, W.A. Bryan, and I.C.E. Turcu. High harmonic generation from laser aligned organic molecules. Annual Report 2005 - 2006, Central Laser Facility, Rutherford Appleton Laboratory, Chilton, Didcot, Oxfordshire, OX11 0QX, 2006. $< http://www.clf.rl.ac.uk/reports/2005-2006/pdfs/Kajumba.pdf >$.

[158] R. Torres, N. Kajumba, J.G. Underwood, J.S. Robinson, S. Baker, J.W.G. Tisch, R. de Nalda, W.A. Bryan, R. Velotta, C. Altucci, I.C.E. Turcu, and J.P. Marangos. Probing orbital structure of polyatomic molecules by high-order harmonic generation. *Phys. Rev. Lett.*, 98(20):203007, May 2007.

[159] A. Rouzee, S. Guerin, V. Boudon, B. Lavorel, and O. Faucher. Field-free one-dimensiaonal alignment of ethylene molecule. *Phys. Rev. A.*, 73(3):033418, 2006.

[160] N. Xu, C. Wu, R. Ma, J. Huang, Z. Wu, Q. Liang, H. Yang, and Q. Gong. Dynamic alignment of C_2H_4 investigated by using two linearly polarized femtosecond laser pulses. *J. Am. Soc. Mass. Spectrom.*, 17(12):1717 – 1724, December 2006.

[161] J.G. Underwood, B.J. Sussman, and A. Stollow. Field-free three dimensional molecular axis alignment. *Phys. Rev. Lett.*, 94(14):143002, 2005.

[162] T.K. Kjeldsen, C.Z. Bisgaard, L.B. Madsen, and H. Stapelfeldt. Influecce of molecular symmetry on strong-field ionization: Studies on ethylene,benzena, fluorobenzena,and chlorofluorobenzena. *Phys. Rev. A*, 71(1):013418, January 2005.

[163] V. G. Stavros, E. Harel, and S.R. Leone. The influence of intense control laser pulses on homodyne-detected rotational wave packet in O_2 by degenarate four-wave mixing. *J. Chem. Phys.*, 122(6):064301, February 2005.

[164] J.J. Larsen. *Laser Induced Alignment of Neutral Molecules.* PhD thesis, Institut of Physics and Astronomy, University of Aarhus, Aarhus, Denmark, 2000. < *http://www.phys.au.dk/main/publications/PhD/Jakob_Juul_Larsen.pdf* >.

[165] A. Scrinzi, M. Yu Ivanov, R. Kienberger, and D.M. Villeneuve. Attosecond physics. *J. Phys. B: At. Mol. Opt. Phys.*, 39(1):R1 – R37, January 2006.

[166] K Yoshii, G. Miyaji, K. Miyazaki, A. Abdurrouf, and F.H.M. Faisal. Angle-dependent high-harmonic generation from field-free aligned molecules. In *The 7th Pasicif Rim Conference on Laser and Electro-Optics (CLEO /Pacific Rim 2007), Seoul, Korea*, 2007.

Appendix A

List of Publication

Most of the work presented in this dissertation is (or will be) published or presented in :

1. K. Miyazaki, M. Kaku, G. Miyaji, A. Abdurrouf, and F.H.M. Faisal, *Field-Free Alignment of Molecules Observed with High-Order Harmonic Generation*, Phys. Rev. Lett. **95**, 243903 (2005)
2. F.H.M. Faisal, A.Abdurrouf, K. Miyazaki, and G. Miyaji, *Origin of Anomalous Spectra of Dynamic Alignments Observed in N_2 and O_2,* Phys. Rev. Lett. **98**, 143001 (2007)
3. F.H.M. Faisal and A.Abdurrouf, *Interplay of polarization geometry and rotational dynamics in high harmonic generation from coherently rotating linear molecules,* arXiv:0707.2184v1 and Phys. Rev. Lett. (submitted, 2007)
4. F.H.M. Faisal, A.Abdurrouf, K. Miyazaki, and G. Miyaji, *A theory of molecular high harmonic generation from coherently rotating molecules and interpretation of recent pump-probe experiments,* The 7th Pacific Rim Conference on Lasers and Electro-Optics (Seoul, Korea), *Technical Digest* (*IEEE Catalog Number 07TH8953C*) pp. 267 - 268, August, 2007
5. K. Miyazaki, K. Yoshii, G. Miyaji, F.H.M. Faisal, and A.Abdurrouf, *Rotational coherence in high-order harmonic generation from nonadibatically aligned molecules,* The 7th Pacific Rim Conference on Lasers and Electro-Optics (Seoul, Korea), *Technical Digest* (*IEEE Catalog Number 07TH8953C*) pp. 273 - 274, August, 2007
6. K. Yoshii, G. Miyaji, K. Miyazaki, A. Abdurrouf, and F.H.M. Faisal, *Angle-dependent high-harmonic generation from field-free aligned molecules,*The 7th Pacific Rim Conference on Lasers and Electro-Optics (Seoul, Korea), *Technical Digest* (*IEEE Catalog Number 07TH8953C*) pp. 660 - 661, August, 2007

7. K. Miyazaki, M. Kaku, G. Miyaji, A. Abdurrouf, and F.H.M. Faisal, *Field-free molecular alignment observed with high-order harmonic generation*, The 14th Laser Physics Workshop (LPHYS '05), Kyoto, Japan
8. A. Abdurrouf and F.H.M. Faisal, *A theory of intense-field pump-probe high harmonic generation signals from coherently rotating molecules*, in preparation.

Appendix B

Field-Free Alignment of Molecules Observed with High-Order Harmonic Generation

K. Miyazaki, M. Kaku, G. Miyaji, A. Abdurrouf, and F.H.M. Faisal
Phys. Rev. Lett. **95**, 243903 (2005)

PRL **95**, 243903 (2005) PHYSICAL REVIEW LETTERS week ending 9 DECEMBER 2005

Field-Free Alignment of Molecules Observed with High-Order Harmonic Generation

K. Miyazaki,[1,*] M. Kaku,[1] G. Miyaji,[1] A. Abdurrouf,[2] and F. H. M. Faisal[2]

[1]*Institute of Advanced Energy, Kyoto University, Gokasho, Uji, Kyoto 611-0011, Japan*
[2]*Fakultät für Physik, Universität Bielefeld, D-33615 Bielefeld, Germany*

(Received 22 June 2005; published 8 December 2005)

High-order harmonic generation is demonstrated to provide a sensitive way for an extensive study of dynamic processes in the field-free alignment of strong-field-induced molecular rotational wave packets. The time-dependent harmonic signal observed from field-free-aligned N_2, O_2, and CO_2 has been found to include two sets of beat frequency for pairs of coherently populated rotational states. One of them is the well-known frequency component characterizing the field-free alignment of molecules, and the other is ascribed to the beat that arises from coherence embedded in the wave packet. We discuss the effect of each frequency component on the revival signal observed with the harmonic generation.

DOI: 10.1103/PhysRevLett.95.243903 PACS numbers: 42.65.Ky, 33.15.Mt, 33.90.+h

The interaction of an intense ultrashort laser pulse with molecules has theoretically been shown to create a superposition of coherently excited rotational states or a rotational wave packet [1]. This wave packet gives rise to transient alignment of molecules that is recurrent under field-free conditions. There has been much interest in this field-free alignment of molecules, because it provides a promising and versatile way to control molecules with an external field for a variety of applications [2]. The revival structure in the field-free molecular alignment was first observed with the Coulomb explosion imaging by Rosca-Pruna and Vrakking [3]. The fundamental behavior and dynamics of the alignment have been extensively studied so far using the imaging [4,5] and polarization spectroscopy [6,7].

Recently the present authors [8] and Zeidler *et al.* [9] have reported the first observation of high-order harmonic generation (HHG) from the rotational wave packet with an intense femtosecond (fs) laser pulse. In contrast to the HHG from randomly oriented molecules observed so far [10], the harmonic yield was very sensitive to the molecular alignment [11] and strongly modulated by the temporal evolution. The characteristic HHG observed demonstrates an effective approach to an extensive study of wave packet dynamics through the high-order nonlinear optical process [8,9,12–14], while suggesting a possible new area of nonlinear optics using the molecular wave packet to control the strong-field interaction.

The purpose of this Letter is to show a new aspect in the field-free molecular alignment that emerges in the HHG and to discuss the detailed structure and formation process of rotational wave packets in time and frequency domains. We focus our attention on temporal evolutions of harmonic yield from the wave packet in N_2, O_2, and CO_2 and their frequency spectra. The results have shown that the time-dependent harmonic signal includes two sets of beat frequency for pairs of rotational states making up a wave packet. One of them is well known to characterize the field-free alignment of molecules with a full revival period of $T_{\rm rev} = 1/(2Bc)$, where B is the rotational constant. The other is ascribed to the beat that results from coherence embedded in the wave packet and creates the revival signal with a period of $T_{\rm rev}/2$.

We consider a pump-probe experiment for simple linear molecules such as N_2 and O_2, using nonresonant, linearly polarized ultrashort laser pulses. The pump pulse forms a ground-state rotational wave packet $\Psi_g(t) = \sum_J a_J \psi_{JM} \exp(-iE_J t/\hbar)$ that brings about molecular alignment and its field-free revivals, where ψ_{JM} is the field-free rotor wave function, pertaining to the eigenenergy E_J, for the rotational state with the angular momentum J and its projection M on the field direction, and the coefficient a_J depends on the interaction strength and should almost be independent on time after the end of interaction [1]. As theoretically discussed in detail, the degree of alignment is characterized by the expectation value $\langle \cos^2\theta \rangle$, which is calculated using $\Psi_g(t)$, with the angle θ between the molecular axis and the field direction [1]. It is well known that the time-dependent behavior of $\langle \cos^2\theta \rangle$ is dominated by beats between any pair of rotational states populated through the transition, $\Delta J \equiv J\text{-}J' = 0, \pm 2$ with $\Delta M = 0$. For the rotational states with $E_J = 2\pi\hbar BcJ(J+1)$, the beat frequency is calculated as $\omega_1 = 2\pi Bc(4J+6)$ for a pair of J and $J \pm 2$. This beat usually leads to four transient peaks of $\langle \cos^2\theta \rangle$ in a revival period $T_{\rm rev} = 1/(2Bc)$ [3–7].

In the pump-probe experiment, the delayed probe pulse generates high harmonic radiation from the wave packet, and the harmonic signal is observed as a function of time delay Δt between the pump and probe pulses. The HHG from a single molecule is illustrated well by a semiclassical model consisting of three steps of ionization, acceleration of freed electron, and recombination to emit a harmonic photon [15]. This harmonic generation process is essentially a single-cycle event in the laser field. In contrast, the temporal change in the harmonic signal to be observed is very slow and predominantly governed by the beat at ω_1 as for $\langle \cos^2\theta \rangle$.

The experimental procedure was almost the same as in our recent work [8]. Briefly, the laser can produce pulse energy of 40 mJ in 40 fs pulses at 800 nm. The linearly polarized output was split into two beams to produce a variable time delay Δt between the pump and probe pulses. The two beams were recombined collinearly and focused with a 50 cm focal-length lens into a pulsed molecular beam jetted from a 1 mm diameter nozzle. The gas jet pressure was typically 10 Torr. The accurate time delay of $\Delta t = 0$ was determined by the second-harmonic autocorrelation signal produced with a small portion of the combined pulses. The pump pulse intensity in the gas jet was in a range of $(4\text{–}8) \times 10^{13}$ W/cm^2, while the probe intensity for the HHG was slightly higher than the pump. The harmonic radiation was detected by an electron multiplier mounted on a vacuum ultraviolet monochromator, and the signal processed by a boxcar averager was stored on a personal computer. The probe pulse polarization was fixed to the direction along the monochromator slit, while the pump polarization was usually parallel to the probe and rotated by an angle α if necessary.

In the preliminary experiment we observed the time-dependent signal for all orders of harmonic higher than the 15th for which the semiclassical model [15] would be valid. Since their revival structures represented no fundamental difference, for the present study we selected the 19th harmonic ($\lambda \sim 42.1$ nm) with a good signal to noise ratio.

Figure 1 shows (a) a typical example of the harmonic signal observed for N_2 as a function of Δt and (b) the temporal evolution of $\langle\cos^2\theta\rangle$ simulated under the same pump pulse conditions as in the experiment. The observed time-dependent harmonic signal is well reproduced by the simulated result of $\langle\cos^2\theta\rangle$, except for the signal at $\Delta t \sim 0$. This demonstrates that the harmonic is most efficiently produced with N_2 molecules aligned parallel to the probe pulse field and suppressed with those aligned perpendicularly, as reported so far [8,9,13]. The detailed revival structure is seen comparing the observed signal with the simulated $\langle\cos^2\theta\rangle$. The large signal drop at $\Delta t \sim 0$ is due to strong ionization induced by the high intensity of superimposed pump and probe pulses, which is not taken into account in the simulation. The onset of alignment is shown by the first peak at $\Delta t \sim 0.2$ ps after the pump pulse interaction [16]. This signal peak rapidly decreases due to dephasing of rotational states in the wave packet, but the background signal from randomly oriented molecules is kept higher than that at $\Delta t < 0$. This enhanced background at $\Delta t > 0$ is seen also in the simulated result, whereas $\langle\cos^2\theta\rangle = 1/3$ for the isotropic distribution at $\Delta t < 0$, and attributed to the effect of the time-independent component for $\Delta J = 0$. The full revival of alignment is observed at $\Delta t \sim 8.5$ ps, corresponding to $T_{\text{rev}} = 8.3$ ps with $B = 2$ cm^{-1} for N_2, where the rapid signal modulation is due to the rotation of aligned molecules.

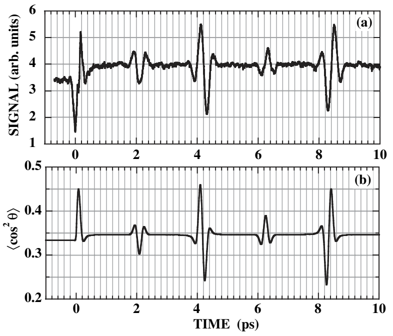

FIG. 1. (a) The 19th harmonic signal observed for N_2 as a function of time delay between the pump and probe pulses at the intensities of 0.8 and 1.7×10^{14} W/cm^2, respectively, and (b) temporal evolution of $\langle\cos^2\theta\rangle$ simulated under the same pump pulse conditions, where $T_{\text{rot}} = 300\,^\circ$K is assumed so as to give the same J value for the peak amplitude as in Fig. 2.

With the Fourier transform we analyzed the observed time-dependent harmonic signal to see the structure, and the result is shown in Fig. 2. The spectrum is mainly composed of beat frequencies at ω_1 with a separation $\Delta\omega_1/2\pi = 4Bc$, as expected. The spectral amplitude is larger for the even J and weaker for the odd J, representing the intensity alternation that originates from the population ratio 2:1 between the even- and odd-J states of N_2 [17]. Making the inverse Fourier transform for each, we have confirmed that the even- and odd-J states contribute in antiphase to the revival signals at $T_{\text{rev}}/4$ and $3T_{\text{rev}}/4$ to produce the small peak owing to the population difference, as discussed by Dooley *et al.* [4].

The spectrum shown in Fig. 2 includes another set of weak frequency component with a separation of $8Bc$. This

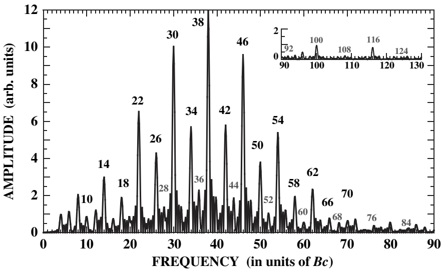

FIG. 2. Frequency spectrum of the time-dependent 19th harmonic signal shown in Fig. 1(a). The inset is the extended spectrum in the higher frequency region. The number on each peak denotes the frequency $4J + 6$ (in black) at ω_1 and $8J + 20$ (in gray) at ω_2.

component is definitely ascribed to the beat frequency $\omega_2 = (E_{J+4} - E_J)/\hbar = 2\pi Bc(8J + 20)$ for a pair of rotational states J and $J \pm 4$. We note that the rotational wave packet includes such additional coherence as to be detected with the HHG, while $\langle \cos^2\theta \rangle$ is not allowed to contain the ω_2 component due to the selection rule. This coherence between the states for $\Delta J = \pm 4$ would be created by multistep transitions during the wave packet formation process, and then the spectral amplitude at ω_2 should be much weaker than that at ω_1, as seen in Fig. 2. The time-dependent signal from the ω_2 component is easily shown to have the revival period of $T_{\mathrm{rev}}/2 = 1/(4Bc)$. Since it is difficult to see the effect of the ω_2 component on the revival signal in Fig. 1(a), we discuss it in detail for O_2.

Figure 3 shows (a) the time-dependent 19th harmonic signal for O_2 and (b) its frequency spectrum. The full revival is seen at $T_{\mathrm{rev}} \sim 11.6$ ps, corresponding to $B = 1.44\ \mathrm{cm}^{-1}$ for O_2. The revival signals at multiples of $T_{\mathrm{rev}}/4$ represent almost the same amplitude, since only odd-J states are populated in the ground state of O_2 with no nuclear spin. The observed harmonic yield as well as the revival signal was much smaller than that for N_2. The low HHG efficiency would result from the antisymmetric structure of molecular orbital [18]. We tried to find a different angle α between the pump and probe field directions to produce a larger revival signal, but the best signal modulation was observed at $\alpha \sim 0°$, as well as the highest harmonic yield. This appears to be inconsistent with the previous conclusion [13] that the HHG from aligned O_2 is peaked at $\theta \sim 45°$ and minimized at $\theta \sim 0°$ and $90°$, while θ might be different from α, and the phase matching consideration is not involved.

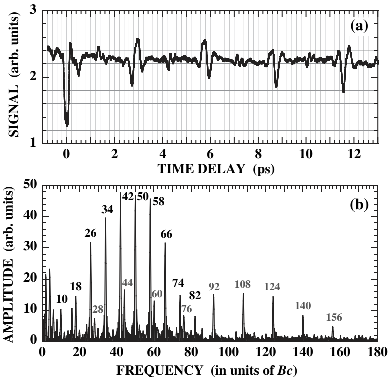

FIG. 3. (a) The 19th harmonic signal observed for O_2 as a function of time delay and (b) its frequency spectrum, in which the number on each spectral peak denotes the frequency $4J + 6$ (in black) at ω_1 and $8J + 20$ (in gray) at ω_2. The pump and probe pulse intensities are 0.5 and $1.2 \times 10^{14}\ \mathrm{W/cm}^2$, respectively.

The frequency spectrum shown in Fig. 3(b) consists of the strong component at ω_1 and the weak at ω_2 for only odd J. It is noted that the spectral peaks at $\omega_1/2\pi =$ (42–58)Bc correspond to those at $\omega_2/2\pi =$ (92–124)Bc for almost the same values of $J =$ 9–13. This confirms that the ω_2 component certainly originates from the beat between the rotational states J and $J \pm 4$ that are coherently populated in the wave packet.

To see the excitation process to form the wave packet in O_2, we have simulated the ensemble averages of $\langle \cos^2\theta \rangle$ at different rotational temperatures T_{rot}. The results have shown that the ω_1 component is peaked for $J = 5$ and 11 at $T_{\mathrm{rot}} = 90$ and $300\,°\mathrm{K}$, respectively. Since T_{rot} in the supersonic O_2 gas jet would be less than $100\,°\mathrm{K}$ [19], the spectral peaks for $J =$ 9–13 in Fig. 3(b) indicate that the multistep Stokes transitions preferentially take place to shift the initial rotational distribution and form the wave packet, due mainly to the restriction of $\Delta M = 0$ for $|M| \leq J$.

The spectrum shown in Fig. 3(b) appears to involve a different series of the weak ω_2 component at (28–76)Bc with a subpeak for $J = 3$. We believe that this series of the ω_2 in the low frequency region accounts for the initial low temperature T_{rot} in the supersonic gas jet. Our simulation has shown that the spectral peak for $J = 3$ corresponds to $T_{\mathrm{rot}} =$ 25–50 °K.

The above discussion on the ω_2 component in the high and low frequency regions is valid also for the N_2 spectrum shown in Fig. 2.

The effect of the ω_2 component on the time-dependent harmonic signal can be seen in Fig. 3(a), where the signal includes weak revival signals at $(2m - 1)T_{\mathrm{rev}}/8$ with positive integer m. The 1/8-partial revival signals are shown to arise from the ω_2 component as follows. With the inverse Fourier transform we reconstructed the time-dependent harmonic signal, using one of two components at ω_1 and ω_2 [20]. The results presented in Fig. 4 demonstrate that the ω_1 component certainly creates the revival signals at $mT_{\mathrm{rev}}/4$, while the ω_2 component produces the small revival signals at $mT_{\mathrm{rev}}/8$ with the full revival period of $T_{\mathrm{rev}}/2$. We note that the time-dependent harmonic signal observed is the simple superposition of those arising from two components at ω_1 and ω_2.

Theoretically, the temporal evolution of $\langle \cos^2\theta \rangle$ does not include the ω_2 component, as discussed above. This suggests that the coherence for the beat at ω_2 is embedded in the wave packet, while detected through the anisotropic electronic response to the linearly polarized probe pulse used for the HHG. The 1/8-revival signals for O_2 were also observed so far with the Coulomb explosion imaging [4], where $\langle \cos^2 m\theta \rangle$ was used to analyze the fractional revivals. On the other hand, the analysis with $\langle \sin^2 2\theta \rangle$ was proposed to reproduce the time-dependent harmonic signal for O_2 [13]. The temporal evolution of $\langle \sin^2 2\theta \rangle$ is certainly able to

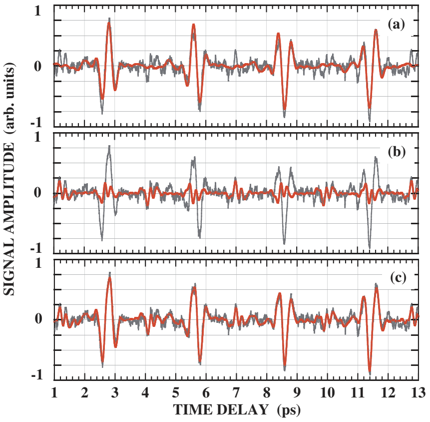

FIG. 4 (color). Time-dependent 19th harmonic signals (red solid lines) reproduced using (a) the frequency component at ω_1, (b) at ω_2, and (c) both at ω_1 and ω_2. For comparison, each trace includes the observed signal given by the gray solid line.

include the ω_2 component that leads to the revival signals at $mT_{\mathrm{rev}}/8$, so that this analysis appears to reconcile with the present picture for the revival signals.

The time-dependent 19th harmonic signal was also measured for CO_2 having only even-J states, where the revival period of 42.7 ps was in good agreement with T_{rev} for $B = 0.39\ \mathrm{cm}^{-1}$, and the frequency spectrum was also observed to consist of the ω_1 and ω_2 components. In contrast to those for N_2 and O_2, however, the onset of alignment was observed with a signal minimum at $\Delta t \sim 0.3$ ps that was clearly separated from the signal drop at $\Delta t \sim 0$. Corresponding to the first negative peak, the revival signal phase was completely reversed from those in Figs. 1(a) and 3(a). The temporal evolution of $\langle \cos^2\theta \rangle$ simulated for CO_2 represented the same amplitude phase as those for N_2 and O_2. These results suggest that the 19th harmonic is minimized with CO_2 aligned along the pump pulse polarization and peaked with those aligned perpendicularly. This might be induced by the destructive interference of recombining electron wave [21,22] and/or by the θ-dependent HHG process characteristic to CO_2 molecules. The experimental results on the harmonic signal phase will be presented and discussed in a separate paper.

In summary, the results of time-dependent HHG from rotational wave packets and its frequency analysis have shown a new aspect in the revival structure of field-free molecular alignment. The present results are useful for controlling rotational wave packets with ultrashort laser pulses [23] and nonlinear optical processes in molecules.

*Electronic address: miyazaki@iae.kyoto-u.ac.jp

[1] J. Ortigoso *et al.*, J. Chem. Phys. **110**, 3870 (1999); T. Seideman, Phys. Rev. Lett. **83**, 4971 (1999); J. Chem. Phys. **115**, 5965 (2001); L. Cai, J. Marango, and B. Friedrich, Phys. Rev. Lett. **86**, 775 (2001); M. Macholm, J. Chem. Phys. **115**, 10 724 (2001).
[2] H. Stapelfeldt and T. Seideman, Rev. Mod. Phys. **75**, 543 (2003), and references therein.
[3] F. Rosca-Pruna and M. J. J. Vrakking, Phys. Rev. Lett. **87**, 153902 (2001); J. Chem. Phys. **116**, 6567 (2002); **116**, 6579 (2002).
[4] P. W. Dooley *et al.*, Phys. Rev. A **68**, 023406 (2003).
[5] I. V. Litvinyuk *et al.*, Phys. Rev. Lett. **90**, 233003 (2003).
[6] M. Comstock, V. V. Lozovoy, and M. Dantus, Chem. Phys. Lett. **372**, 739 (2003).
[7] V. Renard *et al.*, Phys. Rev. Lett. **90**, 153601 (2003); Phys. Rev. A **70**, 033420 (2004).
[8] M. Kaku, K. Masuda, and K. Miyazaki, Jpn. J. Appl. Phys. **43**, L591 (2004).
[9] D. Zeidler *et al.*, in *Ultrafast Optics IV*, edited by F. Krausz *et al.* (Springer, New York, 2004), p. 247.
[10] H. Sakai and K. Miyazaki, Appl. Phys. B **61**, 493 (1995); Y. Liang *et al.*, J. Phys. B **27**, 5119 (1994).
[11] R. Velotta, N. Hay, M. B. Mason, M. Castillejo, and J. P. Marangos, Phys. Rev. Lett. **87**, 183901 (2001); N. Hay *et al.*, Phys. Rev. A **65**, 053805 (2002).
[12] J. Itatani *et al.*, Nature (London) **432**, 867 (2004).
[13] J. Itatani *et al.*, Phys. Rev. Lett. **94**, 123902 (2005).
[14] K. Miyazaki *et al.*, in *Ultrafast Phenomena XIV*, edited by T. Kobayashi *et al.* (Springer, New York, 2005), p. 195.
[15] P. B. Corkum, Phys. Rev. Lett. **71**, 1994 (1993).
[16] K. Miyazaki, T. Shimizu, and D. Normand, J. Phys. B **37**, 753 (2004).
[17] G. Herzberg, *Molecular Spectra and Molecular Structure, I. Spectra of Diatomic Molecules* (Van Nostrand Reinhold, New York, 1950), Chap. III.
[18] A. Jarón-Becker, A. Becker, and F. H. M. Faisal, Phys. Rev. A **69**, 023410 (2004); B. Shan, X. M. Tong, Z. Zhao, Z. Chang, and C. D. Lin, Phys. Rev. A **66**, 061401(R) (2002).
[19] A. Owyoung, R. A. Hill, and P. Esherick, Opt. Lett. **8**, 425 (1983).
[20] For the inverse Fourier transform, we ignored the low frequency components less than 0.6 THz, because the time-dependent second-harmonic autocorrelation signal has shown that such components came from the fluctuation of the laser output.
[21] M. Lein, N. Hay, R. Velotta, J. P. Marangos, and P. L. Knight, Phys. Rev. A **66**, 023805 (2002); R. de Nalda *et al.*, Phys. Rev. A **69**, 031804(R) (2004).
[22] T. Kanai, S. Minemoto, and H. Sakai, Nature (London) **435**, 470 (2005).
[23] M. Spanner, E. A. Shapiro, and M. Ivanov, Phys. Rev. Lett. **92**, 093001 (2004); C. Z. Bisgaard, M. D. Poulsen, E. Peronne, S. S. Viftrup, and H. Stapelfeldt, Phys. Rev. Lett. **92**, 173004 (2004); K. F. Lee, D. M. Villeneuve, P. B. Corkum, and E. A. Shapiro, Phys. Rev. Lett. **93**, 233601 (2004).

Appendix C

Origin of Anomalous Spectra of Dynamic Alignments Observed in N_2 and O_2

F.H.M. Faisal, A.Abdurrouf, K. Miyazaki, and G. Miyaji
Phys. Rev. Lett. **98**, 143001 (2007)

PRL **98,** 143001 (2007) PHYSICAL REVIEW LETTERS week ending 6 APRIL 2007

Origin of Anomalous Spectra of Dynamic Alignments Observed in N_2 and O_2

F. H. M. Faisal,[1,2] A. Abdurrouf,[1] K. Miyazaki,[3] and G. Miyaji[3]

[1]*Fakultät für Physik, Universität Bielefeld, Postfach 100131, D-33501 Bielefeld, Germany*
[2]*ITAMP, Harvard-Smithsonian Center for Astrophysics, 60 Garden St., Cambridge, Massachusetts 02138, USA*
[3]*Institute of Advanced Energy, Kyoto University, Gokasho, Uji, Kyoto 611-0011, Japan*

(Received 5 July 2006; published 2 April 2007)

Recent pump-probe experiments with intense femtosecond laser pulses and diatomic molecules N_2 and O_2, have revealed the presence of Raman-forbidden anomalous series and lines in the Fourier spectrum of HHG (high harmonic generation) signals. A theoretical analysis of the problem is made by deriving a general expression of the angle dependent HHG operator that governs the dynamic alignment signals in linear molecules, and applying them to the experiments in N_2 and O_2. A unified interpretation of the origin of the observed Raman-allowed *and* the anomalous spectral features is given. The results are also used to estimate the molecular temperature in the experiments.

DOI: 10.1103/PhysRevLett.98.143001 PACS numbers: 32.80.Rm, 32.80.Fb, 42.50.Hz

Much interest has recently been generated by the observation [1–7] of dynamic alignments [8,9] of the linear molecules N_2 and O_2, that are monitored by the nondestructive high harmonic generation (or HHG) signals induced by a delayed probe pulse. The observed signal from N_2 was found to mimic the usual measure (e.g., [8–10]) of alignment, $A(t_d)$, of the molecular axis, and the associated fractional revival structures (e.g., [9]), given by the ensemble averaged expectation value of $\cos^2\theta$: $A(t_d) = \langle\langle\cos^2\theta\rangle\rangle(t_d)$, where θ is the angle between the polarization direction and the molecular axis, t_d is the delay between the pump and the probe pulse; the inner brackets stand for the expectation value with respect to the rotational wave packet excited by the pump pulse, and the outer brackets, for the thermal average with respect to the Boltzmann distribution of the molecular ensemble. As expected, the Fourier spectrum of the HHG signal of N_2 was found to show the rotational lines associated with $A(t_d)$ that were consistent with the Raman selection rules $\Delta J = 0, \pm 2$. Recently, Miyazaki *et al.* reported [6] the surprising observation of a weak sequence of lines in N_2 that is Raman forbidden. A similar Raman-forbidden series, or the associated $\frac{1}{8}$-revival in the time domain, has been also observed for O_2, and several empirical ansatz have been made to fit the data (e.g., [4–6]). Finally, a careful examination of the experimental spectra of the HHG signals [6] for N_2 and O_2 reveals the presence of still another puzzling sequence of lines that does *not* belong either to the usual Raman-allowed or the Raman-forbidden series, mentioned above.

The purpose of this Letter is to analyze the Raman-allowed and the anomalous spectral features of the HHG signals observed for N_2 and O_2, and to give a unified theoretical interpretation of their origin. To this end, we first derive an explicit expression of the *operator* governing the pump-probe HHG signal for linear molecules and obtain the corresponding expressions for the dynamic (delay-time dependent) HHG signals for N_2 and O_2.

The total Hamiltonian of the molecular system interacting with a pump pulse (L_1) at a time t and a probe pulse (L_2) at a delayed time $t - t_d$, within the Born-Oppenheimer approximation (we use atomic units, unless stated otherwise: $e = \hbar = m = \alpha c = 1$) is:

$$H_{\mathrm{tot}}(t) = H_N^{(0)} + V_{N-L_1}(t) + H_e^{(0)} + V_{e-L_2}(t - t_d), \quad (1)$$

where $H_N^{(0)}$ is the nuclear Hamiltonian, $H_e^{(0)}$ is the electronic Hamiltonian, and $V_{N-L_1}(t) = -\frac{1}{2}\sum_{i,j}F_{1i}(t)\alpha_{ij}F_{1j}(t)$ is the interaction of the nuclear motion with the pump pulse $\boldsymbol{F}_1(t)$ (polarizability tensor $\boldsymbol{\alpha}$); $V_{e-L_2}(t - t_d) = -\boldsymbol{F}_2(t - t_d)\cdot\boldsymbol{d}_e$ (dipole operator $\boldsymbol{d}_e$) is the delayed interaction of the molecule with the probe pulse $\boldsymbol{F}_2(t - t_d)$. The pump pulse produces a rotational wave packet, evolving from an initial rotational state $|J_0M_0\rangle$:

$$|\Phi_{J_0M_0}(t)\rangle = \sum_{JM} C_{JM}^{J_0M_0}(t)e^{-iE_{JM}t}|JM\rangle, \quad (2)$$

where the coefficients $C_{JM}^{J_0M_0}(t)$ are determined by solving the equations for the nuclear motion (e.g., [9]),

$$i\frac{\partial}{\partial t}C_{JM}^{J_0M_0}(t) = \sum_{J'M'}\langle JM|V_{N-L_1}(t)|J'M'\rangle C_{J'M'}^{J_0M_0}(t). \quad (3)$$

Using Eq. (2) and the well-known Volkov Green's function of the active electron (e.g., [11]) we have constructed the wave function of the interacting total system, within the molecular Keldysh-Faisal-Reiss approximation (cf. [11,12]), and used it to evaluate the expectation value (cf. [13]) of the dipole operator and to derive the matrix element of the HHG transition operator for the nth harmonic with respect to the reference wave packet state $\Phi_{J_0M_0}(t_d)$. Finally, modulo-squaring it to obtain the corresponding probability and taking, as usual, the Boltzmann average of the independent probabilities [14], we obtain the scaled dynamic HHG *signal* "per molecule", as a function of t_d:

0031-9007/07/98(14)/143001(4) 143001-1

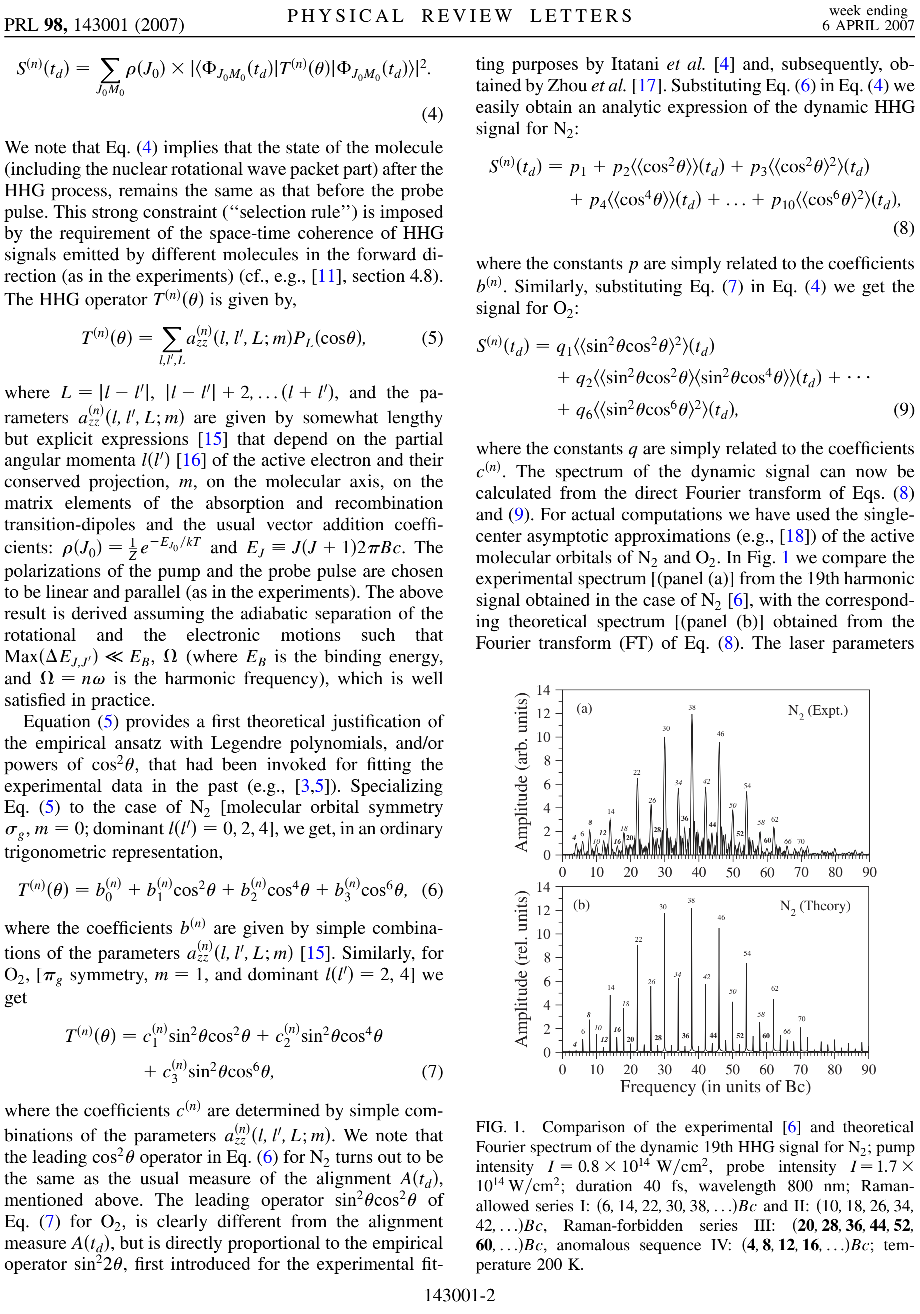

$$S^{(n)}(t_d) = \sum_{J_0M_0} \rho(J_0) \times |\langle \Phi_{J_0M_0}(t_d)|T^{(n)}(\theta)|\Phi_{J_0M_0}(t_d)\rangle|^2. \tag{4}$$

We note that Eq. (4) implies that the state of the molecule (including the nuclear rotational wave packet part) after the HHG process, remains the same as that before the probe pulse. This strong constraint ("selection rule") is imposed by the requirement of the space-time coherence of HHG signals emitted by different molecules in the forward direction (as in the experiments) (cf., e.g., [11], section 4.8). The HHG operator $T^{(n)}(\theta)$ is given by,

$$T^{(n)}(\theta) = \sum_{l,l',L} a_{zz}^{(n)}(l, l', L; m)P_L(\cos\theta), \tag{5}$$

where $L = |l - l'|$, $|l - l'| + 2, \ldots (l + l')$, and the parameters $a_{zz}^{(n)}(l, l', L; m)$ are given by somewhat lengthy but explicit expressions [15] that depend on the partial angular momenta $l(l')$ [16] of the active electron and their conserved projection, m, on the molecular axis, on the matrix elements of the absorption and recombination transition-dipoles and the usual vector addition coefficients: $\rho(J_0) = \frac{1}{Z}e^{-E_{J_0}/kT}$ and $E_J \equiv J(J + 1)2\pi Bc$. The polarizations of the pump and the probe pulse are chosen to be linear and parallel (as in the experiments). The above result is derived assuming the adiabatic separation of the rotational and the electronic motions such that $\mathrm{Max}(\Delta E_{J,J'}) \ll E_B$, Ω (where E_B is the binding energy, and $\Omega = n\omega$ is the harmonic frequency), which is well satisfied in practice.

Equation (5) provides a first theoretical justification of the empirical ansatz with Legendre polynomials, and/or powers of $\cos^2\theta$, that had been invoked for fitting the experimental data in the past (e.g., [3,5]). Specializing Eq. (5) to the case of N_2 [molecular orbital symmetry σ_g, $m = 0$; dominant $l(l') = 0, 2, 4$], we get, in an ordinary trigonometric representation,

$$T^{(n)}(\theta) = b_0^{(n)} + b_1^{(n)}\cos^2\theta + b_2^{(n)}\cos^4\theta + b_3^{(n)}\cos^6\theta, \tag{6}$$

where the coefficients $b^{(n)}$ are given by simple combinations of the parameters $a_{zz}^{(n)}(l, l', L; m)$ [15]. Similarly, for O_2, [π_g symmetry, $m = 1$, and dominant $l(l') = 2, 4$] we get

$$\begin{aligned} T^{(n)}(\theta) = {} & c_1^{(n)}\sin^2\theta\cos^2\theta + c_2^{(n)}\sin^2\theta\cos^4\theta \\ & + c_3^{(n)}\sin^2\theta\cos^6\theta, \end{aligned} \tag{7}$$

where the coefficients $c^{(n)}$ are determined by simple combinations of the parameters $a_{zz}^{(n)}(l, l', L; m)$. We note that the leading $\cos^2\theta$ operator in Eq. (6) for N_2 turns out to be the same as the usual measure of the alignment $A(t_d)$, mentioned above. The leading operator $\sin^2\theta\cos^2\theta$ of Eq. (7) for O_2, is clearly different from the alignment measure $A(t_d)$, but is directly proportional to the empirical operator $\sin^2 2\theta$, first introduced for the experimental fitting purposes by Itatani *et al.* [4] and, subsequently, obtained by Zhou *et al.* [17]. Substituting Eq. (6) in Eq. (4) we easily obtain an analytic expression of the dynamic HHG signal for N_2:

$$\begin{aligned} S^{(n)}(t_d) = {} & p_1 + p_2\langle\langle\cos^2\theta\rangle\rangle(t_d) + p_3\langle\langle\cos^2\theta\rangle^2\rangle(t_d) \\ & + p_4\langle\langle\cos^4\theta\rangle\rangle(t_d) + \ldots + p_{10}\langle\langle\cos^6\theta\rangle^2\rangle(t_d), \end{aligned} \tag{8}$$

where the constants p are simply related to the coefficients $b^{(n)}$. Similarly, substituting Eq. (7) in Eq. (4) we get the signal for O_2:

$$\begin{aligned} S^{(n)}(t_d) = {} & q_1\langle\langle\sin^2\theta\cos^2\theta\rangle^2\rangle(t_d) \\ & + q_2\langle\langle\sin^2\theta\cos^2\theta\rangle\langle\sin^2\theta\cos^4\theta\rangle\rangle(t_d) + \cdots \\ & + q_6\langle\langle\sin^2\theta\cos^6\theta\rangle^2\rangle(t_d), \end{aligned} \tag{9}$$

where the constants q are simply related to the coefficients $c^{(n)}$. The spectrum of the dynamic signal can now be calculated from the direct Fourier transform of Eqs. (8) and (9). For actual computations we have used the single-center asymptotic approximations (e.g., [18]) of the active molecular orbitals of N_2 and O_2. In Fig. 1 we compare the experimental spectrum [(panel (a)] from the 19th harmonic signal obtained in the case of N_2 [6], with the corresponding theoretical spectrum [(panel (b)] obtained from the Fourier transform (FT) of Eq. (8). The laser parameters

FIG. 1. Comparison of the experimental [6] and theoretical Fourier spectrum of the dynamic 19th HHG signal for N_2; pump intensity $I = 0.8 \times 10^{14}$ W/cm^2, probe intensity $I = 1.7 \times 10^{14}$ W/cm^2; duration 40 fs, wavelength 800 nm; Raman-allowed series I: (6, 14, 22, 30, 38, ...)Bc and II: (10, 18, 26, 34, 42, ...)Bc, Raman-forbidden series III: (**20**, **28**, **36**, **44**, **52**, **60**, ...)Bc, anomalous sequence IV: (**4**, **8**, **12**, **16**, ...)Bc; temperature 200 K.

are chosen to be the same in the calculations as in the experiment: peak intensity $I = 0.8 \times 10^{14}\ \mathrm{W/cm^2}$ for pump pulse, and $I = 1.7 \times 10^{14}\ \mathrm{W/cm^2}$ for probe pulse; duration and wavelength of both pulses are 40 fs and 800 nm. It can be seen from the figure that the experimental spectrum [(panel (a)] exhibits two prominent series I: $(6, 14, 22, 30, 38, \ldots)Bc$, and II: $(10, 18, 26, 34, 42, \ldots)Bc$, which are also present in the theoretical spectrum [(panel (b)]. They are easily understood to arise from the FT of the $\langle\langle \cos^2\theta \rangle\rangle$ term in Eq. (8). Since the matrix elements of $\cos^2\theta$ between the rotational states are zero except for the Raman transitions $\Delta J = 0, \pm 2$, one gets (besides the zero frequency contribution) a sequence of lines at $(E_{J+2} - E_J)/2\pi = (4J + 6)Bc$. This gives the series I: $(6, 14, 22, 30, 38, \ldots)Bc$ for even values of J, and series II: $(10, 18, 26, 34, 42, \ldots)Bc$, for odd values of J. We may recall that both the even and the odd J levels are permitted for N_2 by the nuclear spin of 1 for the N atoms. The relative prominence of the even series I over the odd series II, in both the panels in Fig. 1, could be understood as the 2:1 ratio of the nuclear spin statistics giving the same ratio of even:odd J values in N_2 (e.g., [19,20]). The weakly resolved series III: $(\mathbf{20}, \mathbf{28}, \mathbf{36}, \mathbf{44}, \mathbf{52}, \mathbf{60}, \ldots)Bc$ [6] in Fig. 1(a) is the unexpected Raman-forbidden series of N_2 mentioned at the outset; it cannot be produced by the FT of the alignment signal $A(t_d)$. A careful examination of the experimental spectrum, Fig. 1(a), also shows the presence of an additional anomalous sequence of lines IV: $(\mathbf{4}, \mathbf{8}, \mathbf{12}, \mathbf{16}, \ldots)Bc$, which does not belong to the usual Raman-allowed or the Raman-forbidden series mentioned above. We note that the series III, although relatively weak, is certainly also present in the calculated spectrum [Fig. 1(b)]. The anomalous sequence IV also can be seen in the theoretical spectrum [(panel (b)]. To interpret their origin, we therefore consider the two higher order terms involving $\langle\langle \cos^4\theta \rangle\rangle(t_d)$ and $\langle\langle \cos^2\theta \rangle^2\rangle(t_d)$ in Eq. (8). From the rotational matrix elements of the operator $\cos^4\theta$, which vanishes unless $\Delta J = 0$, ± 2, and ± 4, we see that its expectation value allows not only the Raman-allowed transitions discussed above but also the Raman-forbidden transitions with $\Delta J = \pm 4$. The Raman-allowed transitions simply overlap with the series I and II (and strengthen them). But the Raman-forbidden transitions produce the sequence: $(E_{J+4} - E_J)/2\pi = (8J + 20)Bc$. For integer values of J, this yields the series $(20, 28, 36, 44, 52, 60, \ldots)Bc$, which agrees with the Raman-forbidden series III in Fig. 1(a). Next, we consider the product term $\langle\langle \cos^2\theta \rangle^2\rangle \times (t_d)$. From the $\Delta J = 2$ and $\Delta J' = 0$ transitions, this term produces the combination frequencies $\{(4J + 6) \pm (0)\}Bc$. However, the resulting series for the even and odd values of J, overlap with the Raman-allowed series I and II, and give no new spectral lines. But, from the transitions $\Delta J = 2$ and $\Delta J' = 2$, the cross term can produce the sum and difference (or combination) frequencies, $\{(E_{J+2} - E_J) \pm (E_{J'+2} - E_{J'})\}/2\pi \equiv [4(J + J') + 12]Bc$ and $[4(J - J')Bc] > 0$, respectively. For integer values of J and J', together they yield the sequence of lines: $(4, 8, 12, 16, 20, 24, 28, \ldots)Bc$. Note that the alternative values of the sequence, starting with $20Bc$, are identical, and hence overlap, with the Raman-forbidden series III: $(\mathbf{20}, \mathbf{28}, \mathbf{36} \ldots)Bc$. Moreover, the remaining members of the sequence produce the anomalous sequence IV: $(\mathbf{4}, \mathbf{8}, \mathbf{12}, \mathbf{16}, \ldots)Bc$, found in the experimental spectrum in Fig. 1(a) as well as in the theoretical spectrum in Fig. 1(b). Thus, the present theory is seen to provide a unified interpretation of the origin of the Raman-allowed series I and II, the Raman-forbidden series III, and the additional anomalous lines IV, that had been observed experimentally for N_2. We may point out that during the test calculations, the relative strengths of the lines in a calculated spectrum were found to depend significantly on the assumed molecular temperature (which is rather difficult to determine experimentally); Figs. 1(b) and 2(b), have been calculated for an illustrative temperature of 200 K. In Fig. 2 we compare the experimental spectrum [(panel (a)] for O_2 [6] with the theoretical spectrum [(panel (b)] calculated from Eq. (9). They correspond to a pump intensity $I = 0.5 \times 10^{14}\ \mathrm{W/cm^2}$ and a probe intensity $I = 1.2 \times 10^{14}\ \mathrm{W/cm^2}$, and for the same duration and wavelength as in Fig. 1. Both the experimental and the theoretical spectra in Fig. 2 [panel (a), and panel (b), respectively] show the Raman-allowed series II: $(10, 18, 26, 34, 42, \ldots)Bc$, but not the series I: $(6, 14, 22, 30, 38, \ldots)Bc$. The latter fact is easily understood as due to the nuclear spin of O atoms, which is 0, that strictly forbids any even J rotational state for O_2, as required by the overall symmetry of the total

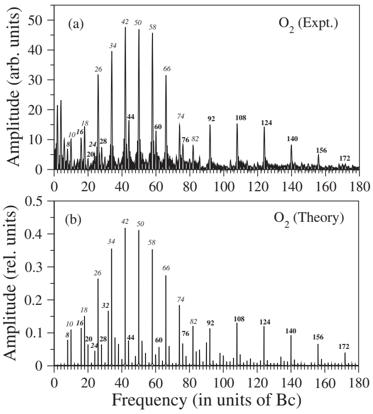

FIG. 2. Comparison of the experimental [6] and theoretical Fourier spectrum of the dynamic 19th HHG signal for O_2; pump intensity $I = 0.5 \times 10^{14}\ \mathrm{W/cm^2}$, probe intensity $I = 1.2 \times 10^{14}\ \mathrm{W/cm^2}$; other parameters are as in Fig. 1; Raman-allowed series II: $(10, 18, 26, 34, 42, \ldots)Bc$, forbidden series III: $(\mathbf{20}, \mathbf{28}, \mathbf{36}, \mathbf{44}, \mathbf{52}, \mathbf{60}, \ldots)Bc$, another anomalous sequence V: $(\mathbf{8}, \mathbf{16}, \mathbf{24}, \ldots)Bc$; temperature 200 K.

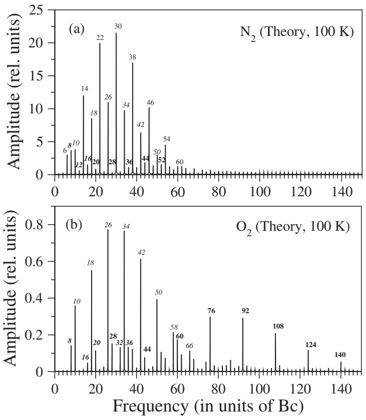

FIG. 3. Calculated spectra for N$_2$ (a) and O$_2$ (b) at Boltzmann temperature 100 K; laser parameters as in Fig. 1, for N$_2$ and, as in Fig. 2 for O$_2$.

wavefunction for O$_2$ (e.g., [19,20]). The forbidden series III: $(\mathbf{20}, \mathbf{28}, \mathbf{36}, \mathbf{44}, \mathbf{52}, \mathbf{60}, \ldots)Bc$, discussed in the case of N$_2$ above, appears for O$_2$ as well. Finally, another anomalous sequence V: $(\mathbf{8}, \mathbf{16}, \mathbf{24}, \ldots)Bc$ can be seen to be present in the data for O$_2$ in Fig. 2(a). To interpret the origin of the observed series in O$_2$ we first consider the HHG operator $T^{(n)}$, given by Eq. (7). Noting that the leading term of $T^{(n)}$ can be split in the form: $\sin^2\theta\cos^2\theta = \cos^2\theta - \cos^4\theta$, it becomes clear that the leading term of the signal, Eq. (9), would contain product of expectation values of the form $\langle\langle\cos^2\theta\rangle^2\rangle$, as in the case of N$_2$, as well as higher order terms. The product term gives as before the combination frequencies, from the transitions $\Delta J(J') = 2(0)$, at $[(4J+6) \pm (0)]Bc$. For odd values of J, this produces the Raman-allowed series II: $(10, 18, 26, \ldots)Bc$ in Fig. 2, and, as noted already, due to the absence of the even J levels in O$_2$, the corresponding Raman-allowed series I: $(6, 14, 22, 30, 38, \ldots)Bc$ can not occur. This is consistent with the experimental data [(panel a)] and the theoretical spectrum [(panel (b)]. The product term produces also the combination frequencies from the transitions $\Delta J(J') = 2(2)$, at $\{(E_{J+2} - E_J) \pm (E_{J'+2} - E_{J'})\}/2\pi \equiv [4(J + J') + 12]Bc$ and $[4(J - J')Bc] > 0$, respectively. For the odd $J(J')$ values, appropriate for O$_2$, the sum frequencies yield the forbidden series III: $(\mathbf{20}, \mathbf{28}, \mathbf{36}, \mathbf{44}, \ldots)Bc$, and the difference frequencies yield the another anomalous sequence V: $(\mathbf{8}, \mathbf{16}, \mathbf{24}, \ldots)Bc$, as seen in Fig. 2. The remaining higher order terms in Eq. (9) contribute, generally weakly, to the same series as above or to some additional lines that can be seen in Fig. 2(b), but hardly resolved in Fig. 2(a). Finally, we may point out that the heights of the few lowest frequency lines in the data in Fig. 2(a) for O$_2$ are due to the fluctuation of the laser outputs (footnote [19] of [6]). Before concluding, we compare the spectra in Fig. 3 for N$_2$ [(panel (a)] and O$_2$ [(panel (b)] calculated at 100 K, with the spectra in Figs. 1(b) and 2(b), calculated for 200 K. Note that the maximum of the spectrum for N$_2$ moves from the position 38 at 200 K, to 30 at 100 K, and that for O$_2$, from 42 to 26. Comparisons with the respective experimental spectra show a better overall agreement for 200 K than for 100 K, which suggests an effective molecular temperature near 200 K; it is higher than what one might expect from a supersonic beam.

To summarize, we give an *ab initio* theory of molecular HHG that provides a unified interpretation of the recently observed anomalous series and lines in the Fourier spectrum of the dynamic HHG signals from N$_2$ and O$_2$.

This work was supported partially by NSF through a grant for ITAMP at Harvard University and Smithsonian Astrophysical Observatory.

[1] K. Miyazaki, Jpn. J. Appl. Phys. **43**, L591 (2004).
[2] Zeidler *et al.*, in *Ultrafast Optics IV*, edited by F. Krauz *et al.* (Springer, New York, 2004), Vol. 432, p. 247.
[3] J. Itatani *et al.*, Nature (London) **432**, 867 (2004).
[4] J. Itatani *et al.*, Phys. Rev. Lett. **94**, 123902 (2005).
[5] T. Kanai *et al.*, Nature (London) **435**, 470 (2005).
[6] K. Miyazaki *et al.*, Phys. Rev. Lett. **95**, 243903 (2005).
[7] J. Levesque *et al.*, J. Mod. Opt. **53**, 185 (2006).
[8] J. Ortigoso *et al.*, J. Chem. Phys. **110**, 3870 (1999); T. Seideman, Phys. Rev. Lett. **83**, 4971 (1999); L. Cai *et al.*, Phys. Rev. Lett. **86**, 775 (2001).
[9] H. Stapelfeldt and T. Seideman, Rev. Mod. Phys. **75**, 543 (2003).
[10] F. Rosca-Pruna and M. J. J. Vrakking, Phys. Rev. Lett. **87**, 153902 (2001).
[11] A. Becker and F. H. M. Faisal, J. Phys. B **38**, R1 (2005).
[12] J. Muth-Böhm *et al.*, Phys. Rev. Lett. **85**, 2280 (2000).
[13] M. Lewenstein *et al.*, Phys. Rev. A **49**, 2117 (1994).
[14] Note that the wave packet states $\Phi_{J_0M_0}(t)$ are in *one-to-one* correspondence with the eigenstates $|J_0M_0>(t) = e^{-iE_{J_0}t}|J_0M_0>$ having weights $\rho(J_0)$.
[15] A. Abdurrouf and F. H. M. Faisal (to be published).
[16] F. E. Harris and H. H. Michels, J. Chem. Phys. **43**, S165 (1965); F. H. M. Faisal, J. Phys. B **3**, 636 (1970).
[17] X. X. Zhou *et al.*, Phys. Rev. A **71**, 061801(R) (2005); **72**, 033412 (2005).
[18] X. M. Tong, Z. X. Zhao, and C. D. Lin, Phys. Rev. A **66**, 033402 (2002); T. K. Kjeldsen and L. B. Madsen, Phys. Rev. A **71**, 023411 (2005).
[19] P. W. Dooley *et al.*, Phys. Rev. A **68**, 023406 (2003).
[20] G. Herzberg, *Molecular Spectra and Molecular Structure, I.* (Van Nostrand, New York, 1950), Chap. III.

Appendix D

Interplay of polarization geometry and rotational dynamics in high harmonic generation from coherently rotating linear molecules

F.H.M. Faisal and A.Abdurrouf
arXiv:0707.2184v1 and Phys. Rev. Lett. (submitted, 2007)

Interplay of polarization geometry and rotational dynamics in high harmonic generation from coherently rotating linear molecules

F.H.M. Faisal[1,2] and A. Abdurrouf[1]
[1]*Fakultät für Physik, Universität Bielefeld, Postfach 100131, D-33501 Bielefeld, Germany and*
[2]*ITAMP, Harvard-Smithsonian Center for Astrophysics, 60 Garden St., Cambridge, MA 02138, USA*

Recent reports on intense-field pump-probe experiments for high harmonic generation from coherently rotating linear molecules, have revealed remarkable characteristic effects of the simultaneous variation of the polarization geometry and the time delay on the high harmonic signals. We analyze the effects and give a unified theoretical account of the experimental observations.

PACS numbers: 32.80.Rm,32.80.Fb,34.50.Fk,42.50.Hz

The phenomenon of high harmonic generation (HHG) from atoms or molecules in intense laser fields can be thought of as a "fusion" of n laser photons, each of energy $\hbar\omega$, into a *single* harmonic photon of an enhanced energy $\hbar\Omega = n\hbar\omega$. This might seem surprising at first since the photons do *not* interact with each other and therefore can not "fuse" on their own. However, a bound electron interacting with a laser pulse can absorb n photons from the laser field, go into highly excited virtual states and can return to the same bound state by releasing precisely the excitation energy ($n\hbar\omega$) as a single harmonic photon. Note that at the end of the coherent process the electron does not change its state – it merely acts as a "catalyst" of the process. The phenomenon is currently being vigorously investigated, both experimentally and theoretically, specially in connection with dynamic alignments of molecules (e.g. [1]).

Recently a number of remarkable pump-probe experiments for high harmonic generation with intense femtosecond laser pulses from coherently rotating linear molecules (e.g. N_2, O_2, CO_2, HC≡CH) have been reported in this journal and elsewhere (e.g. [2, 3, 4, 5, 6, 7]). These experiments measure the HHG signals as a function of the delay-time, t_d, between a pump pulse that sets the molecule in coherent rotation, and a probe pulse that generates the high harmonic signal from the rotating molecule. The changes in the dynamic signals are then recorded by varying the angle, α, between the polarizations of the two pulses. Fig. 1 shows a schematic diagram of the various vectors involved in the pump-probe experiments. The geometric angle α is the operational angle in the laboratory, although at times it is erroneously identified with the angle θ (or θ'); the latter is a quantum variable, not measured in these experiments. Here we derive an explicit theoretical expression for the HHG signal as a simultaneous function of the geometric angle α and the delay-time t_d and analyze the experimental observations. The results provide a unified theoretical account of the observed effects.

Let the total Hamiltonian of the molecular system interacting with a pump pulse L_1 at a time t, and a probe pulse L_2 applied after a delay-time t_d, be written, within the Born-Oppenheimer approximation as (e.g. [8, 9]):

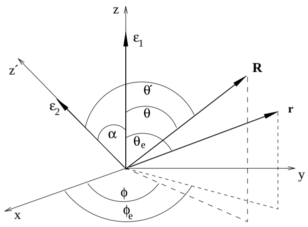

Figure 1: A schematic diagram defining: molecular axis, $\boldsymbol{R}$, electron position $\boldsymbol{r}$, pump polarization $\boldsymbol{\epsilon}_1$, probe polarization $\boldsymbol{\epsilon}_2$; z and z' axes lie on common z-z'-x plane; fields propagate along y-axis.

$$H_{tot}(t) = H_N^{(0)} + V_{N-L_1}(t) + H_e^{(0)} + V_{e-L_2}(t - t_d) \quad (1)$$

where the subscripts N and e stand for the nuclear and the electronic subsystems, respectively. An intense femtosecond pump-pulse is assumed to interact with the molecular polarizability, via $V_{N-L_1}(t)$, and sets it into coherent free rotation.

The coherent rotational motion [10] is described by the nuclear wavepacket states created by the pump pulse:

$$|\Phi_{J_0M_0}(t)\rangle = \sum_J C_{JM}^{J_0M_0}(t) e^{-\frac{i}{\hbar}E_{JM}t} |JM\rangle . \quad (2)$$

Each wavepacket state (2) evolves *one-to-one* from an initially occupied ensemble of eigen states, $|J_0M_0\rangle$, populated with a Boltzmann distribution $\rho(J_0) = \frac{1}{Z_P} e^{-E_{J_0M_0}/kT}$, where Z_P is the partition function. Thus, after the pump pulse, the initial state of the molecule is characterized by the ensemble of product states, $|\chi_i(t)\rangle$, with $i \equiv \{e, J_0, M_0\}$, composed of the ground electronic state $\left|\phi_e^{(0)}(t)\right\rangle$ and the coherent wavepackets $|\Phi_{J_0M_0}(t)\rangle$:

$$|\chi_i(t)\rangle = \left|\phi_e^{(0)}(t)\right\rangle |\Phi_{J_0M_0}(t)\rangle . \quad (3)$$

Generalizing the well-known strong-field KFR (Keldysh-Faisal-Reiss) approximation (e.g. [11]) to the present

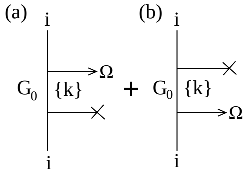

Figure 2: Quantum amplitude for coherent emission of a high harmonic photon (frequency Ω) is the sum of two diagrams, (a) direct, and (b) time-reversed; probe-interaction (line-×), photon emission (arrow); intermediate propagators, G_0; Volkov wave-vector $\boldsymbol{k}$; $i \equiv$ Eq.(3).

molecular case, we write the wavefunction of the system, evolving from each of the ensemble of the initial states (3) as:

$$|\Psi(t)\rangle = |\chi_i(t)\rangle + \int dt' G_0(t,t') V_{e-L2}(t'-t_d)\,|\chi_i(t')\rangle \tag{4}$$

where, the Green's function $G_0(t,t')$ of the system is given by

$$\begin{aligned} G_0(t,t') &= -\frac{i}{\hbar}\theta(t-t') \sum_{j\boldsymbol{p}JM} \left|\phi_j^{(+)}\right\rangle |\phi_{\boldsymbol{p}}(t-t_d)\rangle \\ &\quad \times |\Phi_{JM}(t)\rangle\, e^{-\frac{i}{\hbar}E_j^{+}(t-t')} \langle \Phi_{JM}(t')| \\ &\quad \times \langle \phi_{\boldsymbol{p}}(t'-t_d)| \left\langle \phi_j^{(+)}\right| \end{aligned} \tag{5}$$

where, $\left|\phi_j^{(+)}\right\rangle$ are ionic orbitals and $|\phi_{\boldsymbol{p}}(t)\rangle$ are Volkov states (e.g. [11]).

The quantum transition amplitude for the coherent emission of a harmonic photon of energy $\hbar\Omega = n\hbar\omega$, from an initial state (3) evolving into (4) and recombining back into the same state (3), is given by the sum of a 'direct' and a 'time reversed' diagram for the photon emission process (cf. Fig. 2). Writing out the amplitude analytically using Eqs. (2) to (5), assuming the "adiabatic nuclei" condition, $Max(\Delta E_{J,J'}) \ll E_e$, carrying out the lengthy algebra, and modulo-squaring the result, we obtain the coherent HHG emission probability for each initial state (3). Taking the statistical average of the independent probabilities for the ensemble of initial states (3), we obtain the scaled HHG signal "per molecule", as an explicit function of α and t_d:

$$\begin{aligned} S^{(n)}(t_d,\alpha) &= \sum_{J_0M_0} \rho(J_0) \Big| \langle \Phi_{J_0M_0}(t_d)| \, T^{(n)}(\theta,\phi;\alpha) \\ &\quad \times |\Phi_{J_0M_0}(t_d)\rangle \Big|^2 \end{aligned} \tag{6}$$

where

$$\begin{aligned} T^{(n)}(\theta,\phi;\alpha) &= \sum_{L,M,l,l'} a^{(n)}_{z'z'}(l,l',L;m) \frac{4\pi}{2L+1} Y_{LM}(\alpha,0) \\ &\quad \times Y_{LM}(\theta,\phi) \end{aligned} \tag{7}$$

with, $L = (|l-l'|,(l+l'))$, $M = (-L,L)$; the parameters $a^{(n)}_{z'z'}(l,l',L;m)$ are given by rather lengthy but explicit expressions [9] that depend on the partial angular momenta $l(l')$ of the active electron and their conserved projection, m, on the molecular axis, on the matrix elements of the absorption and recombination transition-dipoles, and on the usual vector addition coefficients.

Specializing Eq. (7) to the case of N_2 (molecular orbital symmetry σ_g, $m = 0$; dominant $l(l') = 0,2,4$), we get, in an ordinary trigonometric representation, an analytic expression of the dynamic HHG signal for N_2:

$$\begin{aligned} S^{(n)}(t_d,\alpha) &= p_1 + p_2 \left\langle\left\langle \cos^2\theta' \right\rangle\right\rangle (t_d) \\ &\quad + p_3 \left\langle\left\langle \cos^2\theta' \right\rangle \left\langle \cos^2\theta' \right\rangle\right\rangle (t_d) \\ &\quad + p_4 \left\langle\left\langle \cos^4\theta' \right\rangle\right\rangle (t_d) + \cdots \\ &\quad + p_{10} \left\langle\left\langle \cos^6\theta' \right\rangle \left\langle \cos^6\theta' \right\rangle\right\rangle (t_d) \end{aligned} \tag{8}$$

where $\cos\theta' = \cos\alpha\cos\theta + \sin\alpha\sin\theta\cos\phi$. Similarly, for O_2, (π_g symmetry, $m = 1$, and dominant $l(l') = 2,4$) we get,

$$\begin{aligned} S(t_d,\alpha) &= q_1 \left\langle \left\langle \sin^2\theta' \cos^2\theta' \right\rangle^2 \right\rangle (t_d) \\ &\quad + q_2 \left\langle \left\langle \sin^2\theta' \cos^2\theta' \right\rangle \right. \\ &\quad \times \left. \left\langle \sin^2\theta' \cos^4\theta' \right\rangle \right\rangle (t_d) \\ &\quad + \cdots + q_6 \left\langle \left\langle \sin^2\theta' \cos^6\theta' \right\rangle^2 \right\rangle (t_d)\,. \end{aligned} \tag{9}$$

The coefficients p's and q's are determined by simple combinations of the parameters $a^{(n)}_{z'z'}(l,l',L;m)$ [9]. We note that for α =0, Eqs. (8) and (9) reduce correctly to the special limits [8].

In Fig. 3 we show the results of computations using Eq. (8) for the dynamic signals from N_2 as a function

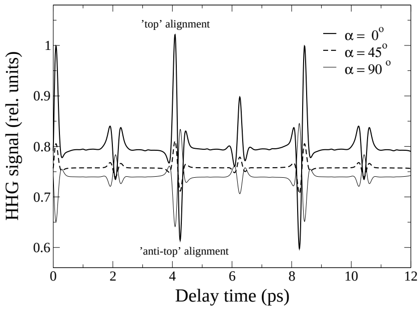

Figure 3: Calculated 19th harmonic dynamic signal for N_2 for various pump-probe polarization angles, i.e. $\alpha = 0^o$, $\alpha = 45^o$, and $\alpha = 90^o$; pump intensity $I = 0.8 \times 10^{14}\,\mathrm{W/cm^2}$, probe intensity, $I = 1.7 \times 10^{14}\,\mathrm{W/cm^2}$, duration 40 fs, and wavelength 800 nm; Boltzmann temperature 200 K.

of the delay time t_d, at three different relative polarization angles, $\alpha = 0^o$, 45^o, and 90^o. The results show the full revival with a period $T_{rev} \equiv \frac{1}{2Bc} = 8.4\,\mathrm{ps}$, and the fractional $\frac{1}{2}$ and $\frac{1}{4}$ revivals, for all three α values. The $\langle\langle\cos^2\theta\rangle\rangle(t_d)$ term is known to govern the $\frac{1}{2}$ and $\frac{1}{4}$ revivals and the associated Raman allowed spectral lines (e.g.[1, 8]). Remarkably, the signals for $\alpha = 0^o$ and $\alpha = 90^o$ are found to be in opposite phase, while that for $\alpha = 0^o$ and $\alpha = 45^o$ are in the same phase. Exactly the same phase relation between the α-dependence of the t_d-signal from N_2 has been observed in recent experiments (e.g. [3, 4, 5]).

To analyze their origin, we consider the leading term of Eq. (8) for N$_2$, more explicitly. (Below, we omit the argument (t_d) for the sake of brevity.) Noting that $\langle\cos^2\theta'\rangle = \frac{1}{2}\sin^2\alpha + (\cos^2\alpha - \frac{1}{2}\sin^2\alpha)\langle\cos^2\theta\rangle$ we get:

$$S(t_d;\alpha) \approx \left(p_1 + p_2\frac{1}{2}\sin^2\alpha\right) + p_2\left(\cos^2\alpha - \frac{1}{2}\sin^2\alpha\right) \times \langle\langle\cos^2\theta\rangle\rangle + \cdots \quad (10)$$

Therefore, for the parallel polarizations we have, $S(t_d;0^o) \approx p_1 + p_2\langle\langle\cos^2\theta\rangle\rangle$ and for the perpendicular polarization, $S(t_d;90^o) \approx \left(p_1 + \frac{1}{2}p_2\right) - \frac{1}{2}p_2\langle\langle\cos^2\theta\rangle\rangle$. Clearly due to the opposite sign of the $\langle\langle\cos^2\theta\rangle\rangle$ term, they vary in *opposite* phase to each other from their respective bases. In contrast, the signal at $\alpha = 45^o$, $S(t_d, 45^o) \approx \left(p_1 + \frac{1}{4}p_2\right) + \frac{1}{4}p_2\langle\langle\cos^2\theta\rangle\rangle$, has the same sign of the $\langle\langle\cos^2\theta\rangle\rangle$ term as for $\alpha = 0$, which makes them to vary *in* phase. These behaviors are what can be seen in the full calculations in Fig. 3, and they also agree with the recent experimental observations (e.g. [2, 3, 4, 5]). The simple formula (10) predicts further that the extrema of the signal should occur for $\sin\alpha\cos\alpha = 0$, with a maximum at $\alpha = 0^o$ and a minimum at $\alpha = 90^o$. This is also what has been seen experimentally [2, 5]. Finally, (10) predicts a "magic angle" $\alpha_c = \arcsin\sqrt{\frac{2}{3}} \approx 54.7^o$, given by the condition $(\cos^2\alpha_c - \frac{1}{2}\sin^2\alpha_c) = 0$ at which the HHG signals become essentially independent of the delay t_d between the pulses. Exactly such a "magic" crossing angle for N$_2$ signals has been observed experimentally [5]. We may point out that this geometry can be used in femtosecond pulse-probe experiments to generate an essentially steady HHG signal from freely rotating N$_2$.

In Fig. 4 we present the results of full calculations for O$_2$, using Eq. (9), for the three geometries, $\alpha = 0^o$, 45^o, and 90^o. The signals are seen to be characterized by a full revival at $T_{rev} = \frac{1}{2Bc} = 11.6\,\mathrm{ps}$ and also by the fractional $\frac{1}{2}$ and $\frac{1}{4}$ revivals, like in N$_2$, as well as an additional $\frac{1}{8}$-revival, for all the three geometries; the same characteristics have been observed experimentally (e.g. [4, 5]). The existence of the $\frac{1}{8}$-revival is due mainly to the presence of higher powers and moments than $\langle\langle\cos^2\theta\rangle\rangle$, that couple the Raman-forbidden ($\Delta J = \pm 4$) and the "anomalous" transitions ($|\Delta J| > 4$) between the rotational states [8].

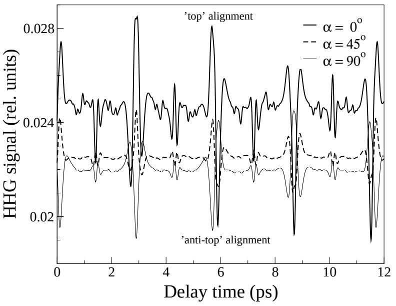

Figure 4: Calculated 19*th* HHG spectrum of O$_2$ for various pump-probe polarizations angle, i.e. $\alpha = 0^o$, $\alpha = 45^o$, and $\alpha = 90^o$; pump intensity $I = 0.5 \times 10^{14}\mathrm{W/cm^2}$, probe intensity, $I = 1.2 \times 10^{14}$ W/cm^2, duration 40 fs, and wavelength 800 nm; Boltzmann temperature 200 K.

We may express the contribution from the first term of Eq. (9) more explicitly as:

$$\begin{aligned} S(t_d;\alpha) \approx \frac{q_1}{64}\Big\langle\big\{&\left(3 - 30\cos^2\alpha + 35\cos^4\alpha\right) \\ &\times\langle\sin^2\theta\cos^2\theta\rangle \\ &- \left(1 - 6\cos^2\alpha + 5\cos^4\alpha\right)\langle\cos^2\theta\rangle \\ &+ \left(4\sin^2\alpha - 3\sin^4\alpha\right)\big\}^2\Big\rangle + \cdots. \end{aligned} \quad (11)$$

For $\alpha = 0^o$, this gives, $S(t_d;\alpha) \approx q_1\left\langle\langle\sin^2\theta\cos^2\theta\rangle^2\right\rangle$ and, for $\alpha = 90^o$, $S(t_d;\alpha) \approx q_1(\frac{3}{8})^2\left\langle\left\{\langle\sin^2\theta\cos^2\theta\rangle - \frac{1}{3}\langle\cos^2\theta\rangle + \frac{1}{3}\right\}^2\right\rangle$. A comparison of the above expressions suggests that for $\alpha = 0^o$ and 90^o, the signals at the full, $\frac{1}{2}$ and $\frac{1}{4}$ revivals would be in opposite phase, and that at the $\frac{1}{8}$ revival would be in phase. A direct comparison of the calculations using the above abbreviated formulas with the full calculation in Fig. 4 and the experimental observations in O$_2$ (e.g. [4, 5]), fully confirm the above expectations.

In Fig. 5 we show the calculated results of the dynamical signals for N$_2$ (upper panel) and O$_2$ (lower panel), as a continuous function of α, between 0^o to 90^o, at three different delay-times t_d near the $\frac{1}{2}$ revival period. In the upper panel for N$_2$, a remarkable coincidence of the three signals is seen to occur at the "magic angle" $\alpha_c = \arcsin\sqrt{\frac{2}{3}} \approx 54.7^o$ as predicted above. Moreover, the signal at the "top"-alignment time $t_d = 4.05\,\mathrm{ps}$ (solid curve) is seen to lie above the signal at the "anti-top" alignment time $t_d = 4.3\,\mathrm{ps}$ (dash-dot curve), for all $\alpha < \alpha_c$, and they invert their relative strengths for all $\alpha > \alpha_c$. This is again in agreement with the recent observations (e.g. [2, 3]). The corresponding signals for O$_2$ (lower panel) does not show a single crossing point,

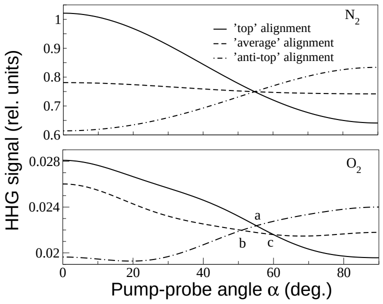

Figure 5: Variation of dynamic HHG signal as a function of pump-probe angle α, near the first half-revival, for N_2 and O_2. The pulse parameters are the same as in Fig. (3) for N_2 and Fig. (4) for O_2.

rather they cross at three different points a, b, and c in the neighborhood of the magic angle $\alpha_c \approx 54.7^o$. Such a crossover-neighborhood around the magic angle $\approx 54.7^o$ for O$_2$ is recently confirmed experimentally [5]. The absence of a single crossing point for O$_2$ is due mainly to the non-negligible contribution of the moment $\langle\langle \cos^4\theta \rangle\rangle$ to the O$_2$ signal (cf. Eq. (11)).

Before concluding, we may make a few qualitative remarks on the α dependence of the dynamic signals for the more complex triatomic molecule CO$_2$ [5], and the organic molecule acetylene (π symmetry), that are mesured recently [6, 7]. The structure of the operator (7) shows, even without a detailed calculation, that the CO$_2$ and acetylene (HC≡CH), due to their linear structure, would show a similar crossover at or near $\alpha_c \approx 54.7^o$. A direct perusal of the experimental data [5, 6] confirms this general expectation from the present theory – both CO$_2$ and acetylene exhibit the crossover effect, and indeed near the "magic angle" $\alpha_c = \arcsin\sqrt{\frac{2}{3}} \approx 54.7^o$.

To summarize: The simultaneous dependence of the dynamic HHG signals from coherently rotating linear molecules, on the relative polarization angle, α, and the time delay, t_d, between a pump and a probe pulse, is investigated theoretically. A general formula for the dynamic signals for linear molecules is derived (Eqs. (6) and (7)). It is used to analyze the recently observed characteristics of the HHG signals from N$_2$ and O$_2$. Among other things, a "magic angle" $\alpha_c = \arcsin\sqrt{\frac{2}{3}} \approx 54.7^o$ for the crossing of the dynamic signals for N$_2$, and a crossover-neighborhood around the "magic angle", for O$_2$, are predicted by the theory and confirmed by the available experimental data. The presence of analogous crossovers for the more complex linear molecules, CO$_2$, HC≡CH (acetylene), are also suggested by the present theory, and are corroborated by the recent observations.

We thank Prof. K. Miyazaki for the private communications and fruitful discussions. This work was partially supported by NSF through a grant for ITAMP at Harvard University and Smithsonian Astrophysical Observatory.

[1] F. Rosca-Pruna and M.J.J. Vrakking, Phys. Rev. Lett. **87**, 153902 (2001); R. Velotta et al., Phys. Rev. Lett. **87**, 183901 (2001); N. Hay et al., Phys. Rev. A **65**, 053805 (2002); N. Hay et al., J. Mod. Opt. **50**, 561 (2003); P.W. Dooley et al., Phys. Rev. A **68**, 023406 (2003); M. Lein et al., Phys. Rev. A **67**, 023819) (2003); J. Itatani et al., Nature **432**, 867 (2004); R. de Nalda et al., Phys. Rev. A **69**, 031804 (2004); M. Kaku et al., Japan J. Appl. Phys. **43**, L591 (2004). Zeidler et al. in Ultrafast Optics, IV, ed. F. Krauz et al.,(Springer, New York, 2004); M. Lein et al., J. Mod. Opt. **52**, 465 (2005); C. Vozzi et al., Phys. Rev. Lett, **95**, 153902 (2005); X.X. Zhou et al., Phys. Rev. A **72**, 033412 (2005); C.B. Madsen and L.B. Madsen, Phys. Rev. A **74**,023403(2006). C. Vozzi et al., J.Phys. B. **39**, S457 (2006).

[2] J. Itatani et al., Phys. Rev. Lett. **94**, 123902 (2005).

[3] K. Miyazaki et al., Phys. Rev. Lett. **95**, 243903 (2005).

[4] T. Kanai et al., Nature **435**, 470 (2005).

[5] K. Miyazaki et al., IEEE-CLEO-PR-2007 Conf. Rep. (submitted, 2007).

[6] N. Kajumba et al., *Central Laser Facility Ann. Rep., 2005/2006*, p. 80, Rutherford Appleton Lab. U.K. (2006).

[7] R. Torres et al., Phys. Rev. Lett., **98**, 203007 (2007).

[8] F.H.M. Faisal, A. Abdurrouf, G. Miyaji, and K. Miyazaki, Phys. Rev. Lett., **98**, 143001 (2007).

[9] A. Abdurrouf and F.H.M. Faisal, Phys. Rev. A (to be submitted, 2007).

[10] H. Stapelfeldt and T. Seideman, Rev. Mod. Phys. **75**, 543 (2003).

[11] A. Becker and F.H.M. Faisal, J. Phys. B **38**, R1 (2005).

[12] G. Herzberg, *Molecular Spectra and Molecular Structure, II* (Van Nostard Reinhold, New York, (1950).

Appendix E

A theory of molecular high harmonic generation from coherently rotating molecules and interpretation of recent pump-probe experiments

F.H.M. Faisal, A.Abdurrouf, K. Miyazaki, and G. Miyaji
The 7th Pacific Rim Conference on Lasers and Electro-Optics (Seoul, Korea), *Technical Digest* (*IEEE Catalog Number 07TH8953C*) pp. 267 - 268, August, 2007

A theory of molecular high harmonic generation from coherently rotating molecules and interpretation of recent pump-probe experiments

F.H.M. Faisal[1,2], **A. Abdurrouf**[1], **K. Miyazaki**[3], **and G. Miyaji**[3]
[1]Fakultät für Physik, Universität Bielefeld, Postfach 100131, D-33501 Bielefeld, Germany
[2]ITAMP Harvard-Smithsonian Center for Astrophysics, Cambridge, MA 02138, USA
[3]Institute of Advanced Energy, Kyoto University, Gokasho, Uji, Kyoto 611-0011, Japan
Email:ffaisal@harvard.cfa.edu

Abstract: A general theory of molecular high harmonic generation in intense femtosecond pump-probe experiments is presented. It provides explicit analytical expressions correlating the harmonic signals with the dynamical alignment of linear molecules. Recent experimental data from pump-probe experiments are analyzed and a unified interpretation of the diverse observations is given.

1. Introduction

In this paper we present a general theory of molecular high harmonic generation by an intense femtosecond probe-pulse, interacting with coherently rotating linear molecules, that are set in free-motion at an earlier time, by another intense femtosecond pump-pulse. The theory is applied to establish the nature of the correlation between the time-dependent recurrent alignments of the freely rotating molecules (starting from a thermally populated ensemble) and the modulation of the observed high harmonic generation (HHG) signals [1,2,3], as well as their Fourier-spectra [4]. We also analyze the dependence of the signals on the controllable geometrical angle, α, between the polarizations of the pump- and the probe-pulse [3,5]. Finally, we have computed and analyzed the (Raman) allowed, forbidden, and anomalous spectral series and lines that are observed recently in the Fourier spectra of the alignment signals from a number of linear molecules, e.g. N_2, O_2 and CO_2 (e.g. [4,6]). A remarkable agreement between the data and the theory is found and a unified interpretation of their origin is given.

2. Theory

The total Hamiltonian of a molecule interacting with a pump pulse (L_1) at a time t and a probe pulse (L_2) after a delay t_d, can be written (in Born-Oppenheimer approximation) (in a.u.: $e = \hbar = m = \alpha c = 1$) as,

$$H_{tot}(t) = H_N + V_{N-L_1}(t) + H_e + V_{e-L_2}(t - t_d) \qquad (1)$$

where H_N is the nuclear Hamiltonian, $V_{N-L_1}(t) = -\boldsymbol{\mu}.\boldsymbol{F}_1(t) - \frac{1}{2}\boldsymbol{F}_1(t) : \boldsymbol{\alpha} : \boldsymbol{F}_1(t)$ where $\boldsymbol{\mu}$ is the permanent molecular dipole (if a polar molecule), H_e is the electronic Hamiltonian, and $V_{e-L_2}(t) = -\boldsymbol{F}_2(t).\boldsymbol{d}_e$ where $\boldsymbol{d}_e$ is the electronic dipole operator.

We generalize the well-known intense-field KFR-approximation for laser-atom interaction to the molecular Hamiltonian (Eq. [1]) and derive fully theoretical expressions of molecular HHG signals for intense-field pump-pulse experiments. Thus, for the general case of an arbitrary angle α between the pump and probe polarizations, we obtain, for example for N_2, the nth harmonic emission signal:

$$S^{(n)}(t_d;\alpha) = c_{00}^{(n)} + c_{01}^{(n)}\left\langle\left\langle\cos^2\theta'\right\rangle\right\rangle(t_d) + c_{11}^{(n)}\left\langle\left\langle\cos^2\theta'\right\rangle^2\right\rangle(t_d) + \ldots c_{33}^{(n)}\left\langle\left\langle\cos^6\theta'\right\rangle^2\right\rangle(t_d) \qquad (2)$$

In above, θ' is the direction of the molecular axis with respect to the probe polarization, given by

$$\cos\theta' = \cos\theta\cos\alpha + \sin\theta\sin\alpha\cos\phi \qquad (3)$$

where (θ,ϕ) is the direction of the molecular axis with respect to the pump polarization. The $c_{ij}^{(n)}$ coefficients are obtained analytically and are to be presented elsewhere. The angle-brackets stand for the quantum expectation value (inner brackets) with respect to the rotational wavepacket states, $\Phi_{J_0M_0}(t_d)$, created by the pump pulse, and the outer angle brackets stand for the Boltzmann average over the initial occupation of the rotational states. Similarly, for O_2 we get,

$$S^{(n)}(t_d;\alpha)= c_{11}^{(n)}\left\langle\left\langle \sin^2\theta'\cos^2\theta'\right\rangle^2\right\rangle(t_d)+c_{12}^{(n)}\left\langle\left\langle \sin^2\theta'\cos^2\theta'\right\rangle\left\langle \sin^2\theta'\cos^4\theta'\right\rangle\right\rangle(t_d)+\dots \qquad (4)$$

We present a number of illustrative results of the theoretical predictions, regarding the dynamic signals for N_2 and O_2 and their α-dependence. We also show a comparison between the calculated and the observed Fourier-spectra of the dynamic alignment in O_2. These and other results will be reported and discussed in greater details.

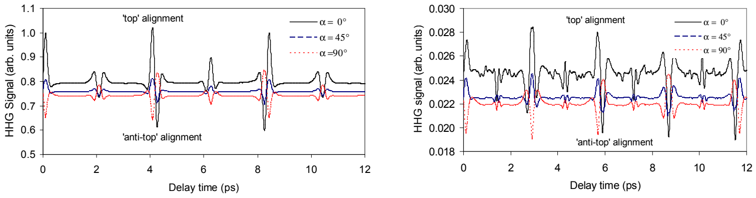

Fig 1. Dynamic HHG signal from N_2 (left panel) and O_2 (right panel) for different relative angles α, between the pump and probe polarizations.

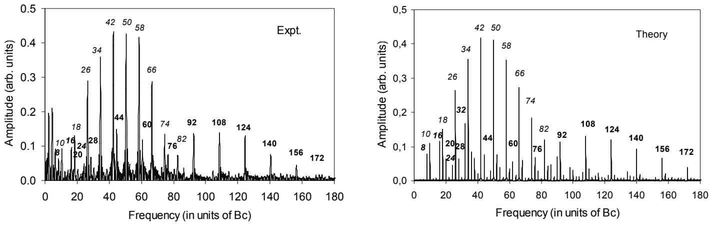

Fig 2. Comparison of experimental [4] and theoretical Fourier spectrum of n=19th harmonic signal for dynamical alignment of O_2; pump- $I = 0.5x10^{14}$ W/cm^2, probe- $I = 1.2x10^{14}$ W/cm^2; $\tau = 40$ fs, $\lambda = 800$ nm, $T = 200$ K. Raman allowed series II: $(10,18,26,34,42,....)Bc$, Raman forbidden series III: $(\mathbf{20,28,36,44,52,60},....)Bc$, `anomalous' sequence V: $(\mathbf{8,16,24},....)Bc$.

3. Acknowledgment

This work was partially supported by NSF through a grant for ITAMP at Harvard University and Smithsonian Astrophysical Observatory.

4. Reference

[1] M. Kaku, K. Masuda, and K. Miyazaki, "Observation of revival structure in femtosecond-laser-induced alignment of N_2 with high-order harmonic generation", Japan J. Appl. Phys. **43**, L591 (2004)

[2] J. Itatani, D. Zeidler, J. Levesque, M. Spanner, D.M. Villeneuve and P.B. Corkum, "Controlling high harmonic generation with molecular wave packets", Phys. Rev. Lett. **94**, 123902 (2005).

[3] T. Kanai, S. Minemoto and H. Sakai, "Quantum interference during high-order harmonic generation from aligned molecules", Nature **435**, 470 (2005).

[4] K. Miyazaki, M. Kaku, G. Miyaji, A. Abdurrouf, and F.H.M. Faisal, "Field-free alignment of molecules observed with high-order harmonic generation", Phys. Rev. Lett. **95**, 243903 (2005).

[5] M. Kaku, R. Morichi, G. Miyaji, and K. Miyazaki, "High harmonic generation from femtosecond-laser aligned N_2,O_2, and CO_2 molecules", IEEE quantum electronics conference 2005 (IEEE, 2005), pp. 1036-7.

[6] F.H.M. Faisal, A. Abdurrouf, K. Miyazaki, and G. Miyaji, "Origin of anomalous spectra of dynamic alignments observed in N_2 and O_2", Phys. Rev. Lett. (2007), in press.

Appendix F

Rotational coherence in high-order harmonic generation from monadibatically aligned molecules

K. Miyazaki, K. Yoshii, G. Miyaji, F.H.M. Faisal, and A.Abdurrouf

The 7th Pacific Rim Conference on Lasers and Electro-Optics (Seoul, Korea), *Technical Digest* (*IEEE Catalog Number 07TH8953C*) pp. 273 - 274, August, 2007

Rotational coherence in high-order harmonic generation from nonadiabatically aligned molecules

K.Miyazaki,[1] K.Yoshii,[1] G.Miyaji,[1] F.H.M.Faisal,[2] and A.Abdurrouf[2]

[1]*Institute of Advanced Energy, Kyoto University, Gokasho, Uji, Kyoto 611-0011, Japan*

[2]*Fakultät für Physik, Universität Bielefeld, D-33615 Bielefeld, Germany*

miyazaki@iae.kyoto-u.ac.jp

Abstract: This paper discusses rotational coherence created in wave packets of N_2, O_2 and CO_2 with intense ultrashort laser pulses and observed with high-order harmonic generation. We identify the origin of several sets of frequency component included in the time-dependent harmonic signal and its effect on the revival structure.

1. Introduction

There has been much interest in molecular alignment that is nonadiabatically induced with intense ultrashort laser pulses, since the laser-induced alignment would be a promising approach to control molecules for a variety of applications in molecular and/or material science. We have demonstrated that high-order harmonic generation (HHG) is a sensitive way to probe the dynamic alignment of molecules, and the characteristic harmonic signal in time and frequency domains clearly reveals coherence included in the rotational wave packet [1,2]. In this paper, we report the complete identification of frequency components according to a theory that has recently been developed to elucidate fundamental properties of the harmonic signal from aligned molecules [3], where we focus our attention on the revival structure in the field-free alignment of N_2, O_2 and CO_2.

2. Experimental

We made a pump-probe experiment with nonresonant, linearly polarized ultrashort laser pulses, where the pump pulse forms a wave-packet, and the delayed probe pulse generates high harmonic radiation from the wave packet that aligns molecules. The linearly polarized output in 40 fs pulses at 800 nm from a Ti:sapphire laser was split into two beams to produce a variable time delay Δt between the pump and probe pulses. The two beams were recombined collinearly and focused with a 50-cm focal-length lens into a pulsed molecular beam jetted from a 1-mm-diameter nozzle. The harmonic radiation was detected by an electron multiplier mounted on a VUV monochromator, and the signal processed by a boxcar averager was stored on a personal computer.

2. Results and discussion

Figure 1 shows a typical example of frequency spectrum for the 19th harmonic signal observed for O_2 as a function of Δt. The time-dependent signal shown in the inset of Fig.1 is often reproduced well by the expectation values $\langle\cos^2\theta\rangle$ and/or $\langle\sin^2 2\theta\rangle$ with the angle θ between the molecular axis and the field direction, where $\langle\cos^2\theta\rangle$ represents the degree of alignment with the revival period of $1/(2Bc)$ with the rotational constant B, while $\langle\sin^2 2\theta\rangle$ is empirical. The result shown in Fig.1 demonstrates that the major coherence in the harmonic signal is created through the Raman transition induced by the pump pulse, which is seen with the frequency component at $\omega_1 = (E_{J+2} - E_J)/\hbar = 2\pi Bc(4J+6)$ that give rise to a series (10, 18, 26, 34, 42, ---) for a pair of odd J and $J\pm2$ states of O_2. This Raman-allowed series certainly arises from $\langle\cos^2\theta\rangle$. The spectrum includes additional sets of component at $\omega_2 = (E_{J+4} - E_J)/\hbar = 2\pi Bc(8J+20)$ with a series (28, 44, 60, 76, 92, ---). This coherence between the rotational states J and $J\pm4$ arises from the expectation value $\langle\cos^4\theta\rangle$ and would be created by multi-step Raman transitions during the wave packet formation. The third set of frequency component is identified to $\omega_3 = 2\pi Bc[4(J-J')]$ and $\omega_3 = 2\pi Bc[4(J+J')+12]$, which leads to a series (8, 16, 24, 32, 40,---) with the former and a weak one (12, 20, 28, 36,---) with the latter. This anomalous series originates from the expectation of the form $\langle\cos^2\theta\rangle\langle\cos^2\theta\rangle$, as shown by the theory [3]. The relatively large amplitude for $4(J-J') = 8$ represents the coherence between the adjacent rotational states J and J'. Higher order coherence is also seen with a series (6, 14, 22, 30, 38, ---), which comes from $\langle\cos^2\theta\rangle\langle\cos^4\theta\rangle$.

These frequency components observed are consistent with the theoretical result [3] that the time-dependent harmonic signal for O_2 is dominated by the term proportional to $\langle\langle\cos^2\theta\,\sin^2\theta\rangle^2\rangle(\Delta t)$. The experimental results for N_2 and CO_2 have also been compared with the theoretical.

References

[1] M.Kaku, K.Masuda, and K.Miyazaki: "*Observation of Revival Structure in Femtosecond-Laser-Induced Alignment of N_2 with High-Order Harmonic Generation*", Jpn. J. Appl. Phys. **43**, L591-L593 (2004).

[2] K.Miyazaki, M.Kaku, G.Miyaji, A.Abdurrouf, and F.H.M.Faisal: "*Field-Free Alignment of Molecules Observed with High-Order Harmonic Generation*", Phys. Rev. Lett. **95**, 243903 (2005).

[3] F.H.M.Faisal, A.Abdurrouf, K.Miyazaki, and G.Miyaji, "*Origin of Anomalous Spectra of Dynamic Alignment Observed in N_2 and O_2*", Phys. Rev. Lett. (2007), in press.

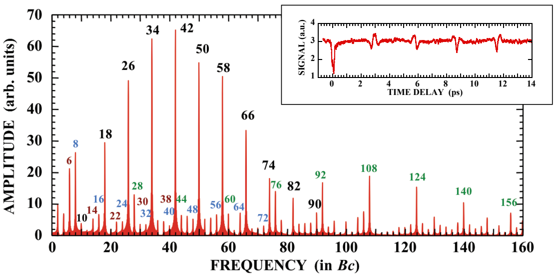

Fig.1. Example of frequency spectrum of the time-dependent 19th harmonic signal for O_2. The number for each peak denotes the frequency in *Bc*. The inset is the time-dependent signal observed at the pump intensity of 0.71×10^{14} W/cm^2 and the probe of 1.1×10^{14} W/cm^2.

Appendix G

Angle-dependent high-harmonic generation from field-free aligned molecules

K. Yoshii, G. Miyaji, K. Miyazaki, A. Abdurrouf, and F.H.M. Faisal
The 7th Pacific Rim Conference on Lasers and Electro-Optics (Seoul, Korea), *Tecnical Digest* (*IEEE Catalog Number 07TH8953C*) pp. 660 - 661, August, 2007)

Angle-dependent high-harmonic generation from field-free aligned molecules

K.Yoshii,[1] G.Miyaji, [1] K.Miyazaki, [1] A.Abdurrouf,[2] and F.H.M.Faisal[2]

[1]*Institute of Advanced Energy, Kyoto University, Gokasho, Uji, Kyoto 611-0011, Japan*

[2]*Fakultät für Physik, Universität Bielefeld, D-33615 Bielefeld, Germany*

miyazaki@iae.kyoto-u.ac.jp

Abstract: High-order harmonic generation from field-free aligned molecules has been measured as a function of the angle between polarization directions of femtosecond pump and probe pulses. The results are compared with the recent theoretical prediction for N_2, O_2 and CO_2 molecules.

1. Introduction

Intense ultrashort laser pulses are able to non-adiabatically induce alignment of molecules that is recurrent under field-free conditions. The field-free alignment of molecules provides a promising approach to control linear and nonlinear optical properties of molecules. Recently we have demonstrated that high-order harmonic generation (HHG) is able to detect the dynamic alignment of molecules at a high sensitivity, suggesting possible control of the HHG with the molecular alignment [1.2]. In this paper we report the HHG efficiency for the aligned molecules that were measured as a function of the angle α between the pump and probe polarization directions. We discuss the results for N_2, O_2 and CO_2 molecules by comparing with theoretical predictions [3,4] .

2. Experimental

We used linearly polarized 40-fs, 800-nm laser pulses in the measurement using a pump and probe technique, where the pump pulse forms a rotational wave packet for alignment of molecules, and the delayed probe generates high-order harmonic radiation from the aligned molecules. The pump and the probe with a time delay Δt were focused into a pulsed molecular beam jet. The pump intensity in the gas jet was in a range of $(4 \sim 8) \times 10^{13}$ W/cm^2, and the probe intensity was slightly higher than the pump. The harmonic radiation was detected by an electron multiplier mounted on a VUV monochromator. For the angle-dependent HHG, the probe pulse polarization was fixed to the direction along the entrance slit of the monochromator, while the pump polarization was rotated by an angle α.

3. Results and discussion

We observed the time-dependent harmonic signals of most of all harmonic orders at $\alpha = 0 \sim 90^\circ$ that could be observed for N_2, O_2 and CO_2 with our experimental apparatus. Figure 1 shows (a) examples of the time-dependent 19th-harmonic signal observed around the half revival time $T_{rev}/2 = 1/(4Bc)$ at different angles α for N_2, where B is the rotational constant. In Fig.1(b) are plotted the modulation amplitude $S_1 - S_2$, as well as $S_1 - S_0$ and $S_2 - S_0$, where S_1, S_2, and S_0 are the harmonic signals measured at the top-alignment, at the anti-top alignment, and at the random alignment in the time-dependent degree of alignment $<\cos^2\theta>$ with the angle θ between the molecular axis and the field direction, respectively, as illustrated in the inset. The modulation $S_1 - S_2$ is peaked and minimized at $\alpha = 0°$ and $90°$, respectively. The α-dependent modulation demonstrates that the 19th harmonic radiation is most efficiently produced at the top alignment where molecules are parallel to the probe pulse field and suppressed at the anti-top alignment, though α does not always coincide with θ. It should be noted in Fig.1 that the modulation phase is reversed at $\alpha \sim 55°$, where the harmonic signal is independent of the time delay. These α-dependent high-harmonic signals observed are well reproduced with the theory that has recently been developed for N_2 and O_2 [3,4].

The similar angle dependences of harmonic signals were measured for different molecules. The experimental results will be discussed by comparing with the theoretical.

References

[1] M.Kaku, K.Masuda, and K.Miyazaki: "*Observation of Revival Structure in Femtosecond-Laser-Induced Alignment of N_2 with High-Order Harmonic Generation*", Jpn. J. Appl. Phys. **43**, L591-L593 (2004).
[2] K.Miyazaki, M.Kaku, G.Miyaji, A.Abdurrouf, and F.H.M.Faisal: "*Field-Free Alignment of Molecules Observed with High-Order Harmonic Generation*", Phys. Rev. Lett. **95**, 243903 (2005).
[3] F.H.M.Faisal, A.Abdurrouf, K.Miyazaki, and G.Miyaji, "*Origin of Anomalous Spectra of Dynamic Alignment Observed in N_2 and O_2*", Phys. Rev. Lett. (2007), in press.
[4] F. H. M. Faisal and A. Abdurrouf: unpublished.

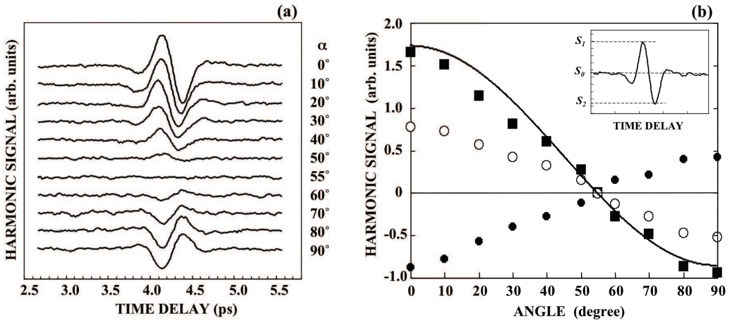

Fig.1. (a) Time-dependent 19th harmonic signals observed at the different angle α between the pump and probe filed directions and (b) the signal modulations $S_1 - S_2$ (solid square), $S_1 - S_0$ (white circle), and $S_2 - S_0$ (solid circle) as a function of α around $T_{rev}/2$ for N_2, where S_1, S_2 and S_0 are defined as in the inset, and the solid line represents the modulation $S_1 - S_2$ calculated for the same conditions as for the experiment. The pump and probe intensities are 0.8 and 1.7 x 10^{14} W/cm^2, respectively.

Acknowledgements

All praise are due to God the almighty, the most gracious and the most merciful. Without His Consent this work never become real.

I started this work with little confidence that it would be worthy to be recognized. The completion of this thesis is due to nothing more than the tremendous support from the people, whom I would like to thank.

First, I would like to express my deepest gratitude to my supervisor Prof. F.H.M. Faisal, Ph.D. for giving me a chance to join his group, for giving me an interisting theoretical problem, and for guiding me with enthusiastically stimulating discussions with his experience and intuitions. I appreciate his efforts in trying to improve every aspect of my scientific research and my life. I am deeply indebted to his guidance and all outstanding support during all stages of my work.

I would like to thank Prof. Dr. J. Schnack for agreeing to be the second referee of my Ph.D. dissertation. Many thanks are also addressed to Prof. Dr. H. Steidl and Prof. Dr. D. Bödeker for agreeing to be members in the jury.

I would like to thank to Prof. K. Miyazaki for his stimulating and interesting discussions regarding the recent experiments on this field. Some of the figures appear in this work (Figs 5.4 (upper panel), 6.3 (upper panel), and 7.3 (left panel)) are due to his courtesy.

I would like to express my gratefulness to all member of the Theoretical Atomic, Molecular, and Laser Physics group at the Bielefeld University: Dr. M. Nurhuda (for encouraging me to pursue this degree and for the discussion on the numerical recipes), Dr. A. Becker (for his contacts and the papers I received before I came to Bielefeld), Dr. A. Requate (for the discussion on GAMESS), and N. Takemoto (for discussion on the Fourier transform). Thanks to Mrs. Susi von Reder and Mrs. Gudrun Eickmeyer for all the help and support I received from them in various circumstances. I can not forget all the colleagues and friends in D6/E6 for the very nice and pleasant atmosphere created by them during my studies.

I thank the Physics Department, Brawijaya University, who gave me the opportunity to undertake my work. I immensely benefited from the TPSDP project. Many thanks to the people involved in this project.

I want to thanks also to all friends around me: Wiryana and his family, Jesch and his family, A. Tarigan, I. Amin, E. Nugoho, N. Wibowo, Y. Krisnawati, and all the Indonesian families in Bielefeld.

Finally, my family is my best supporter. My wife Yuni, my daughters Ifti and Biba who give me unconditional loves and funny smiles to push me forward toward my work. My mother, my father, my sisters, and my brothers for their praying along the night. Thanks for their infinite support and encouragements. I could not find any words to express my gratitude, except dedicating this work to them. My grandfather and grandmother, I am sorry to be not able to come in your burial due to this study.

Selbtändigkeitserklärung

Hiermit erkläre ich, die vorliegende Artbeit selbständig verfasst und nur die angegeben Literatur verwendet zu haben.

Bielefeld, 24. September 2007

Abdurrouf